

Some theoretical aspects of black holes and compact stars



Some theoretical aspects of black holes and compact stars

Thesis submitted for the award
of the degree of

**Doctor of Philosophy
(Science)**

by

Monimala Mondal

Under the guidance of

Prof. Farook Rahaman



Department of Mathematics
Jadavpur University
Kolkata-700032, India

2024

Dedicated to
My beloved Husband
Dr. Subhas Khajanchi
&
my lovely daughter
Shanaya Khajanchi

Prof. Dr. Farook Rahaman
Fellow of Royal Astronomical Society
(F R A S, London)



Department of Mathematics
JADAVPUR UNIVERSITY
KOLKATA- 700032, India.

Ref.

Date 27.3.24

CERTIFICATE FROM THE SUPERVISOR

This is to certify that the thesis entitled “Some theoretical aspects of black holes and compact stars” Submitted by **Smt. Monimala Mondal** who got her name registered on 02/12/2021 (Index No.: 131/21/Maths./27) for the award of Ph. D. (Science) Degree of Jadavpur University, is absolutely based upon his own work under the supervision of **Prof. (Dr.) Farook Rahaman** and that neither this thesis nor any part of it has been submitted for either any degree / diploma or any other academic award anywhere before.

Farook Rahaman

(Signature of the Supervisor date with official seal)

DR. FAROOK RAHAMAN
Professor
Department of Mathematics
JADAVPUR UNIVERSITY
Kolkata - 700032, W.B., INDIA

Corresponds at : KHODAR BAZAR, BARUIPUR, KOLKATA-700144 WEST BENGAL, INDIA
WAP+Mob. No.- 9831907279 (Residence), (+91) (033) 24572716
E-mail : farook_rahaman@yahoo.com, rahaman@associates.iucaa.in, farookrahaman@gmail.com

Declaration

I, **Monimala Mondal**, research scholar hereby declare that the thesis titled "**Some theoretical aspects of black holes and compact stars** " which is submitted by me to the Jadavpur University in partial fulfilment of the requirement for the award of the degree of Doctor of Philosophy in Science is my own work and complete in all parts under the supervision of **Prof. Farook Rahaman**, Department of Mathematics, Jadavpur University, Kolkata, West Bengal, India. Also I declare that the thesis fulfilled all the guidelines regarding PhD degree.

Finally, I declare that any part of it has not been submitted for any degree/diploma at any other institute/university.

Monimala Mondal 27.03.24

(Monimala Mondal)

List of Publications

This thesis is the result of research done at the Department of Mathematics at Jadavpur University in Kolkata, West Bengal, India (700032). The following publications form the foundation of this thesis:

1. Null geodesics and QNMs in the field of regular black holes.

Monimala Mondal, Anil Kumar Yadav, Parthapratim Pradhan, Sayeedul Islam and Farook Rahaman.

International Journal of Modern Physics D, Vol. 30, No. 12, 2150095 (2021).

2. Geodesic stability and quasi normal modes via Lyapunov exponent for Hayward black hole.

Monimala Mondal, Parthapratim Pradhan, Farook Rahaman and Indrani Karar.

Modern Physics Letters A, 2050249 (2020).

3. Tolman VI Fluid Sphere in $f(R, T)$ Gravity.

Monimala Mondal and Farook Rahaman.

Universe **2023**, **9**, 122.

4. Solar system tests in Rastall gravity.

Tuhina Manna, **Monimala Mondal** and Farook Rahaman.

Modern Physics Letters A, 2050034 (2019).

5. Singularity-free non-exotic compact star in $f(R, T)$ gravity system.

Anil Kumar Yadav, **Monimala Mondal** and Farook Rahaman.

Pramana J. Phys. **94**, 90(2020).

6. A new model for dark matter fluid sphere.

Shyam Das, Nayan Sarkar, **Monimala Mondal**, and Farook Rahaman.

Modern Physics Letters A, **35**, 2050280 (2020).

7. Lyapunov exponent, ISCO and Kolmogorov-Senai entropy for Kerr-Kiselev BH.

Monimala Mondal, Farook Rahaman, Ksh. Newton Singh.

Eur. Phys. J. C, **35**, 2050280 (2020).

Acknowledgments

In the course of my Ph.D. research work, several people have directly or indirectly provided me a lot of support and encouragement. I am glad to acknowledge them for their support during this phase of my research career, which has led to the completion of the present thesis.

First and foremost, I owe a deep debt of gratitude to my supervisor Prof. Farook Rahaman, Department of Mathematics, Jadavpur University for providing me the research opportunity with him. In spite of a government, he accepted me under his supervision with open handed, giving me first priority to admit for Ph.D. I consider myself fortunate to have had his excellent, untiring supervision and guidance throughout my research career. I further thank him for his coolness, meticulous attention.

I am incredibly appreciative of the Jadavpur University, Department of Mathematics for their academic support and for providing the facilities needed to do the research.

I would like to sincerely thank to all the faculty members of the Department of Mathematics, Jadavpur University for their insightful advice and assistance in a variety of circumstances and motivation made me reach this stage.

I would like to thank my labmates and friends Dr. Ksh. Newton Singh, Tuhina Ghorui, Somi Aktar, Bidisha Samanta, Tanmoy Chowdhury, Anikul Islam, Shreya Majumder, Anupama Roy Chowdhury, Anntara Mapdar, Iftikar H Sardar, Lipi Baskey, Naeem Ahmad Pundeer, Bikramarka Samadder Choudhury, for being such well wishers. Their lots of love, valuable suggestion and motivations made me reach this stage.

I owe to express my gratitude to my collaborators Dr. Ksh. Newton Singh, Prof. G.R.P. Teruel, Dr. Rajibul Shaikh, Dr. Anil Kumar Yadav, Dr. Parthapratiim Pradhan, Dr. Sayeedul Islam, Dr. Shyam Das, Dr. Nayan Sarkar, Dr. Tuhina manna, Dr.

Indrani Karar.

I would like to thanks to the Head mistress Sujata Dutta and all of my colleagues of Bansberia Girls' High School (H.S) for their absolute love and support.

A ton of thanks to my husband-cum-best friend Dr. Subhas Khajanchi and my little princes Shanaya Khajanchi for giving me unlimited love, space and time. At every stage of my life they both have inspired me for the betterment and thus have illuminated my path to the success. Without their help and support, I was unable to complete my research work.

Last but not the least, I would like to thank my mother Kalosona Miondal, father Kalipada Mondal, father-in-law Rabindranath Khajanchi, mother-in-law Subhadra Khajanchi, sister Jhinukmala Mondal, Chinu Biswas, brother Ramprasad Mondal, sister-in-law Gouri Mondal, Basanti Mondal, niece Shruti Mondal, nephew Tarak Mondal for their unconditionl love, support and encouragement. That was a huge contribution! I feel very lucky to have such members in my family and their great affection, good care and blessing made my journey smooth. Their love and sacrifice always give me the strength to overcome all the hindrance that came into my journey.

Place- Kolkata

Date- 27.03.24

Monimala Mondal
Monimala Mondal

Farooq Rahaman
27/3/24

DR. FAROOK RAHAMAN
Professor
Department of Mathematics
JADAVPUR UNIVERSITY
Kolkata - 700032, W.B., INDIA

Abstract

The purpose of this thesis is to construct a number of physically plausible models of black holes and compact stars based on Einstein's theory of General Relativity and then forecast the unknown interior features of these phenomena. The problems have been analysed/solved by employing some analytical as well as numerical techniques. We organize the whole thesis into nine chapters, described as follows:

The **first chapter** contains the introductory portion of the thesis in which the contents of the certain relevant topics namely, General theory of relativity, the modified theory of gravity, black holes, compact stars and concerning the problems in the subsequent chapters are briefly described.

In the **second chapter**, we analyze the null geodesics of regular black holes. As an application of null geodesics, we calculate the radius of photon sphere, gravitational bending of light, the angle of deflection for the photons and the shadow of BH. As an application of time-like geodesics we compute the innermost stable circular orbit (ISCO) and marginally bound circular orbit (MBCO) of the regular BHs .

In the **third chapter**, we derive proper-time Lyapunov exponent (λ_p) , coordinate-time Lyapunov exponent (λ_c) and compute their ratio ($\frac{\lambda_p}{\lambda_c}$) for a regular Hayward class of black hole. We show that, in the eikonal limit, the real and imaginary parts of quasi-normal modes (QNMs) is specified by the frequency and instability time scale of the null circular geodesics. Furthermore, we discuss the unstable photon sphere and radius of shadow for this class of black hole.

Of concern in the **forth chapter**, we analyze the behavior of relativistic spherical objects within the context of modified $f(R, T)$ gravity considering Tolman VI spacetime. For this investigation, we have chosen three compact stars namely PSR J1614-2230, Vela X-1 and 4U 1538-52. In this theory the equation of pressure isotropy is identical to standard Einstein's theory. We have investigated the effort of coupling parameter (β) on the local matter distribution.

In the **fifth chapter**, we have investigated the classical tests of General Relativity like precession of perihelion, deflection of light and time delay by considering a phenomenological astrophysical object like Sun, as a neutral regular Hayward black hole in Rastall gravity. We have tabulated all our results for some appropriate values

of the parameter σ . We have compared our values with $\sigma = 0$, which correspond to the Schwarzschild case.

In the [sixth chapter](#), we have searched the existence of anisotropic and non-singular compact star in the $f(R, T)$ gravity by taking into account the non-exotic equation of state (EoS). We assume the well known barotropic form of EoS that yields the linear relation between pressures and energy density.

The aim of the [seventh chapter](#) is to develop a new model for a spherically symmetric dark matter fluid sphere containing two regions: **(i)** Isotropic inner region with constant density and **(ii)** Anisotropic outer region. We solve the system of field equation by assuming a particular density profile along with a linear equation of state. The obtained solutions are well-behaved and physically acceptable which represent equilibrium and stable matter configuration.

In the [eighth chapter](#), we calculate the principle Lyapunov exponent (LE) and Kolmogorov-Senai (KS) entropy for our rotating Kerr-Kiselev (KK) black hole. We found that the null circular geodesics has larger angular frequency than time-like circular geodesics ($Q_o > Q_\sigma$) and has shortest orbital period ($T_{photon} < T_{ISCO}$) among the all possible circular geodesics.

Finally, in the [ninth chapter](#), we have discussed the summary and future scopes for all above chapters.

Contents

List of Figures	vii
List of Tables	xv
1 Introduction	1
1.1 Einstein's Theory of Relativity	1
1.1.1 Postulates of General Relativity	2
1.1.2 Einstein's Field Equations	3
1.1.3 Consequences of Einstein's General Relativity	4
1.1.4 Limitation of Einstein's General Relativity	5
1.2 Modified Theories of Gravity	5
1.2.1 $f(R)$ Theories of Gravity	6
1.2.1.1 Einstein's Field Equations in metric $f(R)$ Gravity .	6
1.2.1.2 Einstein's Field Equations in Palatini $f(R)$ Gravity	7
1.2.1.3 Some Consequences of $f(R)$ Theories of Gravity . .	8
1.2.2 $f(R, T)$ Theories of Gravity	8
1.2.2.1 Einstein' field equation corresponding to $f(R, T) = R +$ $2 f(T)$	9
1.2.2.2 Einstein' field equation corresponding to $f(R, T) =$ $f_1(R) + f_2(T)$	9
1.2.2.3 Einstein' field equation corresponding to $f(R, T) =$ $f_1(R) + f_2(R)f_3(T)$	10
1.2.2.4 Some consequence of $f(R, T)$ Theories of Gravity . .	10
1.3 Compact stars	10
1.3.1 White dwarfs	11
1.3.2 Neutron stars	12
1.3.3 Black Hole	12

1.3.3.1	Black Holes in General Relativity	13
1.3.3.2	Different Black Hole	13
1.3.3.3	Black Hole solutions	14
1.3.3.4	Non-rotating black holes:	14
1.3.3.5	Rotating Black Hole:	16
1.3.3.6	Black Hole in modified gravity	18
1.3.3.7	Regular Black Hole	19
1.4	Lyapunov Exponent	20
1.4.1	The maximal Lyapunov exponent(MLE)	20
1.4.2	Lyapunov spectrumt	20
1.5	Shadow of the black hole	21
1.5.1	Radius of shadow	22
1.6	Photon sphere	22
1.6.1	Photon sphere for non-rotating black hole:	22
1.6.2	Photon sphere for rotating black hole:	23
1.7	Equating of ISCO	23
2	Null geodesics and QNMs in the field of regular black holes	25
2.1	Introduction	25
2.2	Introduction of Regular BHs	28
2.3	Action and field equations	30
2.3.1	Circular orbits in the Equatorial Plane	31
2.4	Null Geodesics of Regular BHs	32
2.4.1	Radial null geodesics:	33
2.4.2	Geodesics with angular momentum($L \neq 0$):	34
2.4.3	Radius of photon sphere :	36
2.4.4	Shadow of the BH:	38
2.4.5	Dependence of shadow radius R_s on various parameters: . . .	39
2.4.6	Gravitational Bending of light	42
2.5	Basic equation for the perturbation of the regular BH :	43
2.6	Massive scalar perturbations:	47
2.7	Unstable null geodesics and quasinormal modes of massless scalar field in the eikonal limit	48
2.8	Time-like Geodesics of Regular BHs	51

Contents

2.8.1	The Effective Potential	51
2.8.2	Marginally bound circular orbit (MBCO):	54
2.8.3	Equation of ISCO:	55
2.9	Conclusion and future work:	55
3	Geodesic stability and quasi normal modes via Lyapunov exponent for Hayward black hole	61
3.1	Introduction	61
3.2	Proper time Lyapunov exponent, Coordinate time Lyapunov exponent and Geodesic stability	64
3.3	Equatorial Circular Geodesics in Spherically Symmetric metric Hayward Space-time	68
3.3.1	Circular orbits	69
3.3.1.1	Time-like geodesics	70
3.3.1.2	Null geodesics	71
3.3.2	Bending of light	72
3.3.2.1	Radius of the Shadow	73
3.3.3	Lyapunov exponent	75
3.3.3.1	Time-like case	75
3.3.3.2	Null geodesics	77
3.4	Null Circular Geodesic and QNMs for Hayward BH in the Eikonal limit	78
3.5	Conclusions	81
4	Tolman VI Fluid Sphere in $f(R, T)$ Gravity	83
4.1	Introduction	83
4.2	Mathematics behind $f(R, T)$ gravity	86
4.3	Interior space-time and the realistic viable $f(R, T)$ gravity models: . .	87
4.4	Exterior space-time and boundary condition:	91
4.5	Physical properties of the present model:	94
4.6	Discussion and concluding remarks	99
5	Solar system Tests in Rastall gravity	103
5.1	Introduction	103
5.2	Neutral regular black hole solution in Rastall gravity	106
5.3	Classical Tests of General Relativity	107
5.3.1	Precession of Perihelion	107

5.3.2	Gravitational Lensing	111
5.3.3	Time Delay	114
5.4	A comparative study	116
5.5	Conclusion	118
6	Singularity-free non-exotic compact star in $f(R, T)$ gravity	121
6.1	Introduction	121
6.2	The $f(R, T) = f(R) + 2\zeta T$ Formalism	123
6.3	The KB Metric and Field Equations	124
6.3.1	Solution of Field Equations & Physical Parameters	125
6.4	Boundary Conditions	127
6.5	Physical Consequences of Model Under $f(R, T)$ Gravity	129
6.5.1	Validity of energy conditions	129
6.5.2	Stability	131
6.5.3	Adiabatic index	132
6.5.4	Mass-radius relation	133
6.5.5	Compactness and red-shift	133
6.6	Physical Validity of Model	134
6.7	Result and Discussion	135
7	A new model for dark matter fluid sphere	137
7.1	Introduction	137
7.2	Einstein field equations	141
7.3	Generalized Tolman-Oppenheimer-Volkoff equation	142
7.4	The interior Solutions	143
7.4.1	Solution in the core region, $0 \leq r \leq b$	144
7.4.2	Solution in the outer region, $b \leq r \leq R$	146
7.5	Boundary conditions	148
7.6	Physical features of the model	149
7.6.1	Energy condition	149
7.6.2	Equilibrium condition	150
7.6.3	stability analysis	151
7.6.3.1	Causality condition	152
7.6.3.2	Adiabatic index	154
7.6.3.3	Harrison-Zeldovich-Novikov criterion	154

Contents

7.7	Discussions and conclusion	155
8	Lyapunov exponent, ISCO and Kolmogorov-Senai entropy for Kerr-Kiselev black hole	161
8.1	Introduction	161
8.2	Proper time Lyapunov exponents and Radial potential	164
8.3	Lyapunov exponent and Kolmogorov-Senai entropy:	166
8.4	Rotating Black hole:	167
8.4.1	Circular geodesics in the equatorial plane:	168
8.4.1.1	Circular null geodesic:	170
8.4.1.2	Circular time-like geodesics	172
8.4.2	Lyapunov Exponent:	177
8.4.2.1	Time-like circular geodesics (Equation of ISCO):	177
8.4.2.2	Null circular geodesics:	180
8.4.3	Angular velocity of time-like circular geodesic:	181
8.4.4	Critical Exponent:	183
8.4.4.1	Time-like circular geodesics:	183
8.4.4.2	Null circular geodesics:	184
8.5	Marginally bound circular orbit:	186
8.6	Ratio of Angular velocity between null-circular geodesics and time-circular geodesics:	188
8.7	Ratio of Time period between null-circular geodesics and time-circular geodesics :	190
8.8	Conclusions	192
9	Coccluding Remarks and Future Prospectus	195
9.1	Conclusion	195
9.2	Future research	198
	References	201

List of Figures

1.1	Gravity (Collected from internet).	3
1.2	Rotating Black hole (Collected from internet).	17
1.3	Shadow of the Black hole (Collected from internet).	21
2.1	$f(r)$ versus r with $\nu = 1$ for New class BH (upper panel), $\nu = 2$ for Bardeen BH (middle panel) and $\nu = 3$ for Hayward BH (lower panel). Here, we set $M = 0$, $q = 1$, $\mu = 3$ and $\alpha = 0.5$. The right panels are plotted for values of ν in the range $0 \leq \nu \leq 40$	29
2.2	$f(r)$ versus r for various values of ν ; the other parameters fixed to $M = 0$, $q = 1$, $\mu = 3$ and $\alpha = 0.5$	30
2.3	The figure describes the variation of V_{null} with r (first panel), M (second panel), q (third panel), α (fourth panel) and L (fifth panel). We have set $\mu = 3$	35
2.4	Black hole shadow in the Celestial plane $\beta - \gamma$ for varying α with $\mu = 1$, $\nu = 1$ and $q = 1$ (up- left panel), varying μ with $\alpha = 1$, $\nu = 1$ and $q = 1$ (up- right panel), varying q with $\alpha = 1$, $\mu = 1$ and $\nu = 1$ (down left panel), varying ν with $\alpha = 1$, $\mu = 1$ and $q = 1$ (down- left panel). We set $M = 1$	37
2.5	The figure shows R_s versus r (up-left panel) for varying α and varying μ (down-left panel). BH shadow in the Celestial plane $\beta - \gamma$ for varying α with $\mu = 1$, $\nu = 1$ and $q = 1$ (up- left panel), varying μ with $\alpha = 1$, $\nu = 1$ and $q = 1$ (down- right panel). We set $M = 1$	40

2.6	The figure shows R_s versus r (up-left Panel) for varying q and varying ν (down-left Panel). Black hole shadow in the Celestial plane $\beta - \gamma$ for varying q with $\alpha = 1, \mu = 1$ and ν (up- right panel), varying ν with $\alpha = 1, \mu = 1$ and $q = 1$ (down- right panel). We set the parameter $M = 1$	41
2.7	The figure shows the V_{null}^m versus r for varying values of the mass m . Here, $M = 1, q = 0.5, \mu = 3, \nu = 1, l = 1$ and $\alpha = 0.5$	45
2.8	The figure shows the V_{eff} versus r for varying ν (left Panel) and M (right panel); the other parameters fixed to $l = 1, \mu = 3$ and $\alpha = 0.5$	45
2.9	The figure shows the V_{eff} versus r for varying l (left Panel) and q (right panel); the other parameters fixed to $M = 1, \mu = 3$ and $\alpha = 0.5$	46
2.10	The figure shows the V_{null}^m versus r for varying values of the mass m . Here, $M = 1, q = 0.5, \mu = 3, \nu = 1, l = 1$ and $\alpha = 0.5$	47
2.11	The figure shows QNMs frequency $Re(w)$ versus r (left Panel) and $Im(w)$ versus r (right panel). Here $q = 0.5, \mu = 3, \alpha = 0.5$ and $\nu = 2$	49
2.12	The figure shows QNMs frequency $Re(w)$ versus q (left Panel) and $Im(w)$ versus r (right panel); the other parameter fixed to $M = 1, \mu = 3, \alpha = 0.5$ and $\nu = 2$	49
2.13	The figure shows QNMs frequency $Re(w)$ versus M (left Panel) and $Im(w)$ versus M (right panel). Here $q = 0.5, \mu = 3, \alpha = 0.5$ and $\nu = 2$	50
2.14	Plot of V_{time} versus r (first panel), M (second panel), L (third panel) and q (fourth panel) respectively. We have set $\mu = 3$	52
2.15	Plot of E_c^2 versus r_c for $M = 2, q = 0.05, \mu = 3$ and $\alpha = 0.5$. The left panel is plotted for $\nu = 1$ and right panel is plotted for values of ν in the range $0 \leq \nu \leq 4$	53
2.16	Plot of L_c^2 versus r_c for $M = 2, q = 0.05, \mu = 3$ and $\alpha = 0.5$. The left panel is graphed for $\nu = 1$ and right panel is graphed for values of ν in the range $0 \leq \nu \leq 100$	54
2.17	The figure depicts the variation of $Y = 2r_c^{2\mu}q^6s + r_c^\mu q^3\alpha(r_c^\nu + q^\nu)^{\frac{\mu}{\nu}}(t + w) - M(r_c - 6M)(r_c^\nu + q^\nu)^{2(\frac{\mu+\nu}{\nu})}\alpha^2$ versus r_c (first panel), M (second panel), q (third panel) and α (fourth panel) respectively. We have set $\mu = 3$	58
2.18	Plot of λ_0 versus r_0 for $M = 2, q = 0.05, \mu = 3$ and $\alpha = 0.5$. The left panel is graphed for $\nu = 1$ and right panel is graphed for values of ν in the range $0 \leq \nu \leq 100$	59

List of Figures

3.1	The figure shows the $f(r)$ versus r . Here, $l = 0.5$ for Hayward BH . .	69
3.2	The effective potential V_{ef} , for null-circular geodesics in Hayward BH and in Schwarzschild BH is compared. The constants are with $m = 1, L = 1, E = 1$ and for HBH $l = 0.5$	71
3.3	The variation of $\frac{\lambda_p}{\lambda_c}$ with $\frac{r_g}{m}$ for Hayward BH.	76
3.4	The figure shows QNMs frequency $Re(w)$ versus r (left Panel) and $Im(w)$ versus r (right panel) of HBH and Sch BH ; the other parameters fixed to $m = 1$ and $l = 0.7$ (solid), $l = 1$ (dashed) and $l = 1.2$ (dotted) for HBH.	79
3.5	The figure shows QNMs frequency $Re(w)$ versus m (left Panel) and $Im(w)$ versus m (right panel) of HBH and Sch BH ; the other parameter fixed to $l = 0.5$ for HBH.	80
3.6	The figure shows QNMs frequency $Re(w)$ versus l (left Panel) and $Im(w)$ versus l (right panel) of Hayward BH; the other parameter fixed to $m = 1$	80
4.1	Behavior of the “energy density” with respect to the radial coordinate “ r ” for the compact star PSR J1614-2230 (left panel), Vela X-1 (middle panel) and 4U 1538-52 (right panel) corresponding to the numerical value of constants A and B from the table 4.2 and for different values of β	90
4.2	Behavior of the “pressure” with respect to the radial coordinate “ r ” for the compact star PSR J1614-2230 (left panel), Vela X-1 (middle panel) and 4U 1538-52 (right panel) corresponding to the numerical value of constants A and B from the table 4.2 and for different values of β	90
4.3	Behavior of the “Speed sound” with respect to the radial coordinate “ r ” for the compact star PSR J1614-2230 (left panel), Vela X-1 (middle panel) and 4U 1538-52 (right panel) corresponding to the numerical value of constants A and B from the table 4.2 and for different values of β	92

4.4	Variation of “adiabatic index” with respect to the radial coordinate “ r ” for the compact star PSR J1614-2230 (left panel), Vela X-1 (middle panel) and 4U 1538-52 (right panel) corresponding to the numerical value of constants A and B from the table 4.2 and for different values of β	92
4.5	Behavior of the “week energy condition” with respect to the radial coordinate “ r ” for the compact star PSR J1614-2230 (left panel), Vela X-1 (middle panel) and 4U 1538-52 (right panel) corresponding to the numerical value of constants A and B from the table 4.2 and for different values of β	92
4.6	Behavior of the “Strong energy condition” with respect to the radial coordinate “ r ” for the compact star PSR J1614-2230 (left panel), Vela X-1 (middle panel) and 4U 1538-52 (right panel) corresponding to the numerical value of constants A and B from the table 4.2 and for different values of β	93
4.7	Behavior of the “Dominant energy condition” with respect to the radial coordinate “ r ” for the compact star PSR J1614-2230 (left panel), Vela X-1 (middle panel) and 4U 1538-52 (right panel) corresponding to the numerical value of constants A and B from the table 4.2 and for different values of β	93
4.8	Behavior of the “EoS parameter” with respect to the radial coordinate “ r ” for the compact star PSR J1614-2230 (left panel), Vela X-1 (middle panel) and 4U 1538-52 (right panel) corresponding to the numerical value of constants A and B from the table 4.2 and for different values of β	95
4.9	Behavior of the “mass profile” with respect to the radial coordinate “ r ” for the compact star PSR J1614-2230 (left panel), Vela X-1 (middle panel) and 4U 1538-52 (right panel) corresponding to the numerical value of constants A and B from the table 4.2 and for different values of β	99
4.10	Behavior of the “EoS parameter” with respect to the radial coordinate “ r ” for the compact star PSR J1614-2230 (left panel), Vela X-1 (middle panel) and 4U 1538-52 (right panel) corresponding to the numerical value of constants A and B from the table 4.2 and for different values of β	99

List of Figures

6.1	Plot of λ versus r	126
6.2	Plots of $\rho(r)$ vs r (upper panel), $p_r(r)$ vs r (middle panel) and $p_t(r)$ vs r (lower panel).	126
6.3	The variation of the force Δ due to the local anisotropy against r . . .	127
6.4	Validation of energy conditions of singularity-free compact star. . . .	130
6.5	Profile of Mass versus Radius.	132
6.6	Profile of Γ versus r	133
6.7	Profile of $u(r)$ versus r	134
6.8	Profile of $Z(r)$ versus r	134
7.1	Behavior of the density with respect to the radial coordinate r for the compact star EXO 1785-248 corresponding to the numerical value of constants given in Table-7.1	142
7.2	Behaviors of the radial and transverse pressures with respect to the radial coordinate r for the compact star EXO 1785-248 corresponding to the numerical value of constants given in Table-7.1	143
7.3	Behaviors of the mass and compactness parameter with respect to the radial coordinate r for the compact star EXO 1785-248 corresponding to the numerical value of constants given in Table-7.1	144
7.4	Behavior of the anisotropic factor with respect to the radial coordinate r for the compact star EXO 1785-248 corresponding to the numerical value of constants given in Table-7.1	147
7.5	Behaviors of the equation of state parameters with respect to the radial coordinate r for the compact star EXO 1785-248 corresponding to the numerical value of constants given in Table-7.1	150
7.6	Behaviors of the energy conditions with respect to the radial coordinate r for the compact star EXO 1785-248 corresponding to the numerical value of constants given in Table-7.1	151
7.7	Behaviors of the forces with respect to the radial coordinate r for the compact star EXO 1785-248 corresponding to the numerical value of constants given in Table-7.1	152
7.8	Behaviors of the radial and transverse velocities of sound with respect to the radial coordinate r for the compact star EXO 1785-248 corresponding to the numerical value of constants given in Table-7.1 . . .	153

7.9	Behavior of the stability factor with respect to the radial coordinate r for the compact star EXO 1785-248 corresponding to the numerical value of constants given in Table-7.1	153
7.10	Behavior of the adiabatic index with respect to the radial coordinate r for the compact star EXO 1785-248 corresponding to the numerical value of constants given in Table-7.1	154
7.11	Behavior of the mass with respect to the core density ρ_c for the compact star EXO 1785-248 corresponding to the numerical value of constants given in Table-7.1	155
8.1	Dimensionless instability exponent $\frac{\lambda_\sigma}{\Omega_\sigma}$ as a function of rotation a for real value of Lyapunov eponent. We use units such that $M = 1, c = 2$. Solid lines refer to corotating orbits and dashed lines refer to counter-rotating orbits.	179
8.2	The plots shows the time-like orbital frequency Ω_σ to the radial coordinate r_σ of corotating orbits (left panel) and counterrotating orbits (right panel) for different values of w . We use units $M = 1, a = 0.9$ and $c = 2$	182
8.3	The plot shows the orbital time period of time-like circular geodesic T_σ to the radius r_σ . We use units such that $M = 1, a = 0.9$ and $c = 2$. Solid lines refer to corotating orbits and dashed lines refer to counterrotating orbits.	182
8.4	The plot shows the orbital angular frequency Ω Versus a for different values of radius r in the range $r_o \leq r \leq r_\sigma$, where r_σ and r_o are the radius of time-like geodesic and null-circular geodesic, respectively. Green (solid) color indicates for the value where the radius of time-like and null-circular geodesics are coincide, Red(Dashed) color indicates for the value of radius of null-circular geodesic and blue (Dot-Dashed) color indicates the value of radius of time-like geodesic. We use units such that $M = 1, c = 2$	190

List of Figures

- 8.5 The plot shows the orbital time period T versus a for different values of radius r in the range $r_o \leq r \leq r_\sigma$, where r_σ and r_o are the radius of time-like geodesic and null-circular geodesic, respectively. Blue color indicates for the value where the radius of time-like and null-circular geodesics are coincide, green color indicates for the value of radius of time-like geodesic and red color indicates the value of radius of null-circular geodesic. We use units such that $M = 1, c = 2$ 191

List of Tables

1.1	Mass, radius, mean density, surface potential and Schwarzschild radius for some celestial objects.	11
2.1	Photon sphere radius for variation of massive parameters with $M = 1$.	38
2.2	Radius of photon sphere r_{ps} of the BH, shadow radius R_s for variation of massive parameters with $M = 1$	44
4.1	Numerical values of three well-known celestial compact stars.	98
4.2	The numerical values of A , B , surface density, surface redshift, central values of adiabatic index and surface compactness factor for three well-known celestial compact stars for different values of coupling constant β	98
5.1	Measurement of Advance of Perihelion ($\delta\phi$ in arcsecs. per century.) for different values of σ , taking $L = 2.23 \times 10^{14}$ and $E = 1$	111
5.2	Measurement of Angle of Deflection (in arcsecs.) for different values of σ , taking distance of closest approach as $1M_o$. Only for the first row, we have taken $R=3.5 \times 10^{17}$ m.	115
5.3	Measurement of Time Delay (in secs.) for different values of σ . The distance of closest approach have been taken as $1M_o$ for all values of σ . We have taken $l_1 = 149.6 \times 10^9$ m and $l_2 = 227.9 \times 10^9$ m which are the distances of our Sun from Earth and Mars respectively.	116
6.1	Determination of model parameters A & B for different star candidates.	129
6.2	Comparison of estimated value of model parameters with observed data sets.	132

7.1	Numerical values of constants for three well-known celestial compact stars.	156
7.2	Numerical values of the physical parameters for three well-known celestial compact stars corresponding to the values of constant given in Table-7.1.	156

Chapter 1

Introduction

The thesis entitled “**Some theoretical aspects of black holes and compact stars**” comprises nine chapters and deals with the study of black hole solution with topological defects, some physically viable models for celestial compact stars in Einstein’s gravity and modified gravity. We are providing a brief overview of the relevant topics and theories in order to make the thesis self-explanatory.

1.1 Einstein’s Theory of Relativity

The theory of gravitation proposed by Newton was accepted without question and remained so until the beginning of 20th century. Famous physicist Albert Einstein presented the Special theory of Relativity in 1905 and a geometric explanation of gravitation known as General Relativity (1915) that generalizes both special relativity and Newton’s law of universal gravitation. Newton’s laws of motion and gravitation were shown by Einstein in the General Theory of Relativity to be only approximately accurate, failing to hold when velocities approached the speed of light or when extremely strong gravitational fields existed. Gravity is geometry, which is the fundamental idea of general relativity, the theory of space, time and gravity. When we contrast Einstein’s General Theory of Relativity with Newton’s theory of gravity, we can observe

1. The applicability of Einstein’s theory is wider than that of Newton’s theory, making it more general.
2. The predictions of Einstein’s theory and Newton’s theory are nearly equivalent at the limit of very small fields and low velocities.

1.1.1 Postulates of General Relativity

- **Principle of covariance:** The coordinate system shouldn't affect the application of the law of gravitation. This indicates that the form of the field equation of gravity should be invariant under any arbitrary coordinate transformation. In other words, tensorial form is required for the field equation.
- **Principle of equivalence:** In all inertial systems, the laws of physics remain unchanged. There is no ideal inertial system. The phrase "the Law of Physics" in the aforementioned statement refers to the strong equivalency principle; on the other hand, when the Law of Physics is substituted with the Law of Motion of freely falling particles, the principle refers to the weak principle of equivalent.
- **Principle of correspondence:** According to the equivalent principle, in situations where the previous theory is known to be valid, a new scientific theory must precisely replicate the predictions of the prior theory. This occurrence is sometimes referred to as the "limit of correspondence". The correspondence principle is a fundamental concept in both relativistic and quantum mechanics. Einstein's Special Theory of Relativity specifically satisfies the correspondence principle because, at moderate velocities compared to the speed of light, it reduces to classical physics. In order to meet the correspondence principle, the General Theory of Relativity should approximate Newton's Theory of Gravitation in weak fields and at slow speeds, and it should reduce to the Special Theory of Relativity for the inertial frames.
- **Mach's Principle:** Large-scale structure in the universe determines local physical principles. General theory of relativity was developed by Einstein with this idea serving as a driving force. Einstein realized that the entire distribution of matter determined the metric tensor, which indicates which frame is rotationally stationary. Therefore the Mach principle can therefore be expressed as follows: The geometry is determined by the distribution of matter; geometry cannot exist without matter.
- **Principle of minimum gravitational coupling:** The theory of minimum gravitational coupling states that the free gravitational Lagrangian and external source fields in curved spacetime should be the two additive components that make up the total Lagrangian for the field equation of general relativity.

1.1. Einstein's Theory of Relativity

1.1.2 Einstein's Field Equations

Einstein presented his general relativity field equations to the Prussian Academy of Science in Berlin in November 1915. All matter and energy are equivalent according to the weak principle of equivalence. Also, it is known that all energy acts as a source for the gravitational field. Therefore, the Einstein field equations can be formulated using the energy momentum tensor $T^{\alpha\beta}$ as a source term.

According to the minimal gravitational coupling concept, we have

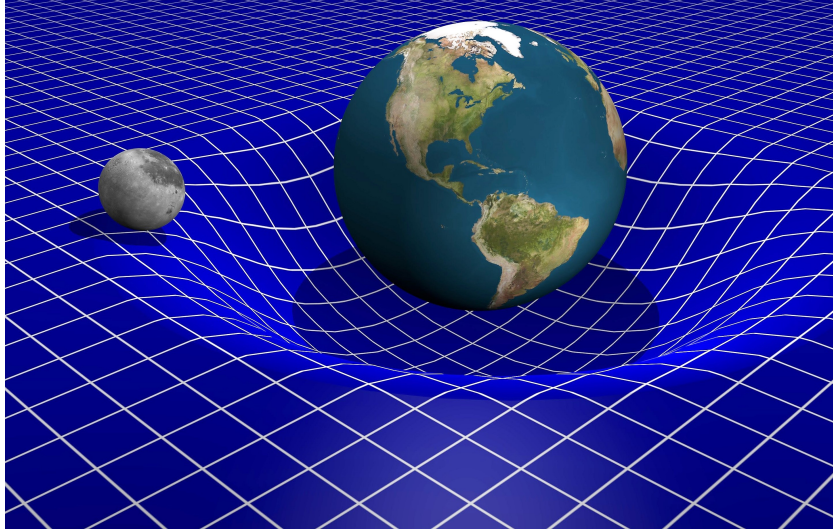


Figure 1.1: Gravity (Collected from internet).

$$\nabla_b T^{\alpha\beta} = 0. \quad (1.1)$$

The covariant derivative of the Einstein tensor vanishes, as well, according to the contracted Bianchi's identities.

$$\nabla_b G^{\alpha\beta} = 0. \quad (1.2)$$

These above two significant equations, together with Mach's principle, allowed Einstein to develop his gravitational field equations as

$$G^{\alpha\beta} \propto T^{\alpha\beta} \Rightarrow G^{\alpha\beta} = \kappa T^{\alpha\beta}, \quad (1.3)$$

where, $\kappa = \frac{8\pi G}{c^4}$ is Einstein gravitational constant, c is speed of light and G is gravitational constant. Therefore, the Einstein field equation is

$$G^{\alpha\beta} = \frac{8\pi G}{c^4} T^{\alpha\beta}, \quad (1.4)$$

Which is equivalent to

$$R_{\alpha\beta} - \frac{1}{2} R g_{\alpha\beta} = -\kappa T_{\alpha\beta}. \quad (1.5)$$

where, R , $R_{\alpha\beta}$ and $g_{\alpha\beta}$, are represents Ricci scalar, Ricci tensor and metric tensor, respectively. Developed from pure idea and physical intuition, these field equations are regarded as the greatest scientific and intellectual achievement of all time. The distribution of energy, pressure mass and momentum throughout the cosmos is represented by the R.H.S. of Eqn. (1.5), while the bending of spacetime is represented by the L.H.S. All varieties of spacetime, including cosmic spacetimes, Minkowski spacetime, and the outside and inside spacetimes of massive objects, may be described by these equations. Later, a variety of techniques were used to derive the Einstein field equations, including (i) a heuristic approach and (ii) the variational principle.

1.1.3 Consequences of Einstein's General Relativity

The gravitational force can be satisfactorily explained by Einstein's General Theory of Relativity (GTR), which postulates a direct relationship between momentum and energy and the structure of space time. The Einstein GTR has consistently resolved several unresolved issues after its discovery. The following are few physical consequences of the GTR:

1. Gravitational time dilation and Frequency shift ([Rindler \[2012\]](#), [Ohanian and Ruffini \[2013\]](#), [Greenstein et al. \[1971\]](#)).
2. Gravitational time dilation and Light deflections ([Ohanian and Ruffini \[2013\]](#), [Shapiro et al. \[2004\]](#)).
3. Gravitational waves ([Abbott et al. \[2016a\]](#)).
4. Orbital effects and the relativity of direction ([Stairs \[2003\]](#), [Krauss \[2001\]](#)).
5. Explained the experimental results like Lense-Thirring gravito-magnetic advancement ([Lense and Thirring \[1918\]](#), [Pfister \[2007\]](#)).
6. The gravitational deflection of light by sun and Precession of Mercury ([Eisberg \[1990\]](#)).

1.2. Modified Theories of Gravity

1.1.4 Limitation of Einstein's General Relativity

The basic theory behind the gravitational interaction is Einstein's general theory of relativity. But within the past few decades, a number of problems have been raised that seem to indicate its limitations. The uniqueness of the theory's formalism was questioned by a number of physicists ([Wheeler \[2014\]](#), [Eddington \[1923\]](#)). Though Einstein's general theory of relativity has so far proven to be reliable in all observational and experimental tests, there are theoretical arguments that suggest a more consistent explanation of gravity may need to take its place. Einstein's GTR does not account for theoretical obstacles such as the horizon and flatness problem ([Dodelson \[2003\]](#)). The cosmos' accelerating expansion ([Riess et al. \[1998\]](#), [Knop et al. \[2003\]](#), [Riess et al. \[2004\]](#)) is beyond the scope of Einstein's General Theory of Relativity. It should be noted that the field equations will not hold true for extremely high densities of both matter and field. As a result, one should not presume that the equations are valid for these extreme cases. Consequently, it is not possible to draw the conclusion that the universe's expansion's beginning must represent a mathematical singularity, and as a result, the equations might not continue over such places.

1.2 Modified Theories of Gravity

The most recent database from the Cosmic Microwave Background Radiation (CMBR) and supernovae studies shows that dark matter (20%), dark energy (76%), and ordinary baryonic matter (4%), make up the distribution of matter in our univers. The combined inspiration from astrophysics, high energy physics, and cosmology has led to a recent acknowledgement of the increased attention towards modified gravity theories. As an extension of Einstein's theory of gravity, modified gravity theories have been put out to explain the most recent astrophysical and cosmological findings on dark energy and dark matter.

The modified gravity theory is quite interesting in applications for dark energy and the late time acceleration of the universe. The following are the methods used in modified gravity theories:

1. The early-time inflation and late-time acceleration for the various gravitational factors that are significant at different curvatures present a natural unification in modified gravity.
2. Dark energy has an extremely natural gravitational substitute in modified gravity.

- 3 **3.** Acceleration to deceleration throughout the evolution of the cosmos is entirely composed of modified gravity.
4. Modified gravity theory might naturally compose the universe's transition from non-phantom phase to phantom phase without adding any exotic materials.
5. One possible Unified explanation for dark energy and dark matter is the modified gravity theory. Different cosmic effects could explain it.

There are various modified gravity theories that could compete with General Relativity in the modern period. However, they must be supported by a number of observational data points and relevant Solar System tests. Some well-known modified theories of gravity that can be found in the literature include the following:

1. $f(R)$ gravity ([Buchdahl \[1970\]](#)).
2. $f(R, T)$ gravity ([Harko et al. \[2011\]](#)).
3. Massive gravity ([Fierz and Pauli \[1939\]](#)).
4. Gause-Bonnet gravity ([Lanczos \[1938\]](#)).
5. $f(T)$ gravity ([Fiorini and Ferraro \[2009\]](#), [Harko et al. \[2014\]](#))
6. Bigravity ([Rosen \[1973, 1974, 1975, 1978\]](#)).

Here, we discuss first two mentioned modified theories of gravity, respectively.

1.2.1 $f(R)$ Theories of Gravity

Einstein's general relativity is generalized into $f(R)$ gravity, which is an intriguing and comparatively straightforward substitute for GR. $f(R)$ theory was first developed by Buchdahl in 1970 ([Buchdahl \[1970\]](#)). Since Starobinsky ([Starobinsky \[1980\]](#)) discovered cosmic inflation, the field has seen significant research. There are primarily two types of $f(R)$ gravity, which vary depending on whether variational principle is selected.

- (i) Metric $f(R)$ gravity.
- (ii) Palatini $f(R)$ gravity ([Buchdahl \[1970\]](#)).

Another $f(R)$ gravity was proposed in 2007 by Sotiriou and Liberati ([Sotiriou and Liberati \[2007\]](#)): namely, Metric-affine $f(R)$ gravity. They use the independence of matter action with the connection and employ only the Palatini version. Undoubtedly among these theories, metric affine $f(R)$ gravity is the most general.

1.2.1.1 Einstein's Field Equations in metric $f(R)$ Gravity

1.2. Modified Theories of Gravity

The Lagrangian for the Einstein-Hilbert action in the background of metric $f(R)$ is as follows:

$$S = \frac{1}{2k} \int d^4x \sqrt{-g} f(R), \quad (1.6)$$

where $k = 8\pi G c^{-4}$ ($G = c = 1$). Here, G , R , $f(R)$ and $g = |g_{\mu\nu}|$ are represents the gravitational constant, Ricci scalar, general function of R , and the determinant of the metric tensor $g_{\mu\nu}$, respectively. When a matter term is added to the action (1.6), the entire action for $f(R)$ gravity has the following form

$$S_{met} = \frac{1}{2k} \int d^4x \sqrt{-g} f(R) + \int d^4x \sqrt{-g} L_M, \quad (1.7)$$

where, L_M represents the matter Lagrangian density.

Varying the above action (1.7) with respect to $g_{\mu\nu}$, we get the field equation as

$$f'(R) R_{\mu\nu} - \frac{1}{2} f(R) g_{\mu\nu} + [g_{\mu\nu} \square - \nabla_\mu \nabla_\nu] f(R) = k T_{\mu\nu}, \quad (1.8)$$

where, $R_{\mu\nu}$ and $T_{\mu\nu}$ are Ricci tensor and energy momentum tensor, respectively. ∇_μ is covariant derivative connected with the Levi-Civita connection of the metric, $\square \equiv \nabla^\mu \nabla_\mu$ and prime ($'$) denotes the differentiation with respect to R . Einstein general relativity is given by the metric $f(R)$ gravity in the case $f(R)=R$.

1.2.1.2 Einstein's Field Equations in Palatini $f(R)$ Gravity

Using the independent variation with regard to the metric and an independent connection (Palatini formalism), one can deduce the Einstein equations. Within the context of Palatini $f(R)$ gravity, the action has the following form

$$S_{pal} = \frac{1}{2k} \int d^4x \sqrt{-g} f(R) + L_M(g_{\mu\nu}, \psi), \quad (1.9)$$

where, the matter action L_M depends on the matter fields and the metric, not on the independent connection.

After varying the action (1.10) independently with respect to the metric and the connection we get the Einstein field equations as

$$f'(R) R_{\mu\nu} - \frac{1}{2} f(R) g_{\mu\nu} = \kappa T_{\mu\nu}, \quad (1.10)$$

where, $(\mu\nu)$ represents symmetrization over the indices μ and ν . Einstein general relativity is also given by the metric $f(R)$ gravity in this case $f(R)=R$.

1.2.1.3 Some Consequences of $f(R)$ Theories of Gravity

Starobinsky (Starobinsky [1980]) created cosmic inflation within the context of $f(R)$ gravity and since then both theoretical and observational researchers have actively pursued research in $f(R)$ gravity. There are numerous implications of the $f(R)$ gravity, some of them:

1. The existence of a late-time cosmic acceleration of the cosmos (Carroll et al. [2004]) can be explained by the $f(R)$ gravity.
2. The gravity models with $f(R)$ satisfying the solar system test and integrating dark energy (Nojiri and Odintsov [2007, 2008]) and inflation.
3. In the context of $f(R)$ gravity (Capozziello et al. [2006], Martins and Salucci [2007]), the galactic dynamic of massive test particles can be interpreted without dark matter.

1.2.2 $f(R, T)$ Theories of Gravity

$f(R, T)$ gravity is a another type of modified theories of gravity in which the trace T of the energy momentum tensor $T_{\mu\nu}$ is considered as an arbitrary function of the gravitational Lagrangian and the Ricci scalar R . By expanding the $f(R)$ theories of gravity, Harko and his associates (Harko et al. [2011]) initially developed the $f(R, T)$ gravity. They developed a number of theoretical models that matched particular functions (R, T) .

Recently, there has been a great enthusiasm among researchers to study various consignments in cosmology with late-time acceleration in $f(R, T)$ gravity. Different features of $f(R, T)$ gravity have been studied separately and several researchers have produced different cosmological models, such as the Bianchi type I cosmological model (Adhav [2012]), the Bianchi type III dark energy model (Reddy et al. [2013]), and the Bianchi type V string model (Ahmed and Pradhan [2014]).

The action for the modified theories of gravity takes the following form

1.2. Modified Theories of Gravity

$$S = \frac{1}{2k} \int d^4x \sqrt{-g} f(R, T) + \int d^4x \sqrt{-g} L_M, \quad (1.11)$$

where $k = 8\pi G c^{-4}$ ($G=c=1$). $f(R, T)$ and L_M are arbitrary function of R and the trace T of the energy momentum tensor $T_{\mu\nu}$ and matter Lagrangian density, respectively.

Varying the action S of the gravitational field with respect to the metric tensor $g^{\mu\nu}$ and after some manipulation we get the following relationship

$$\begin{aligned} \delta S &= \frac{1}{2k} \int [f_R(R, T) R_{\mu\nu} \delta g^{\mu\nu} + f_R(R, T) g_{\mu\nu} \square \delta g^{\mu\nu} \\ &\quad - f_R(R, T) \nabla_\mu \nabla_\nu \delta g^{\mu\nu} + f_T(R, T) \frac{\delta(g^{\alpha\beta} T_{\alpha\beta})}{\delta g^{\mu\nu}} \delta g^{\mu\nu} \\ &\quad - \frac{1}{2} g_{\mu\nu} f(R, T) \delta g^{\mu\nu} + 2k \frac{1}{\sqrt{-g}} \frac{\delta(\sqrt{-g} L_M)}{\delta g^{\mu\nu}}] \sqrt{-g} d^4x. \end{aligned} \quad (1.12)$$

Integrating second and third terms of the above equation partially, we get the field equations of $f(R, T)$ gravity as following

$$\begin{aligned} f_R(R, T) R_{\mu\nu} &- \frac{1}{2} g_{\mu\nu} f(R, T) + (g_{\mu\nu} \square - \nabla_\mu \nabla_\nu) f_R(R, T) \\ &= 8\pi T_{\mu\nu} - f_T(R, T) T_{\mu\nu} - f_T(R, T) g^{\alpha\beta} \frac{\delta T_{\alpha\beta}}{\delta g^{\mu\nu}}. \end{aligned} \quad (1.13)$$

If one consider $f(R, T) \equiv f(R)$, then field equations of $f(R)$ gravity can be derived from the equation (1.6).

1.2.2.1 Einstein' field equation corresponding to $f(R, T) = R + 2f(T)$

The Einstein field equation (1.13) becomes with the choice of $f(R, T) = R + 2f(T)$

$$R_{\mu\nu} - \frac{1}{2} R g_{\mu\nu} = 8\pi T_{\mu\nu} - f'(T) T_{\mu\nu} - 2f'(T) T_{\mu\nu} - 2f'(T) \Phi_{\mu\nu} + f(T) g_{\mu\nu}, \quad (1.14)$$

where, $f(T)$ represents arbitrary function of the strass - energy tensor of matter. $(')$ represents the derivative with respect to the argument.

1.2.2.2 Einstein' field equation corresponding to $f(R, T) = f_1(R) + f_2(T)$

The Einstein field equation (1.13) becomes with the choice of $f(R, T) = f_1(R) + f_2(T)$

$$R_{\mu\nu} - \frac{1}{2}Rg_{\mu\nu} = 8\pi T_{\mu\nu} - 2f'(T)T_{\mu\nu} - 2f'(T)\Phi_{\mu\nu} + f(T)g_{\mu\nu}, \quad (1.15)$$

where, $f_1(R)$ and $f_2(T)$ represents arbitrary functions of the R and T of the stress - energy tensor of matter, respectively.

1.2.2.3 Einstein' field equation corresponding to $f(R, T) = f_1(R) + f_2(R)f_3(T)$

For the choice of $f(R, T) = f_1(R) + f_2(R)f_3(T)$, the Einstein field equation (1.13) becomes

$$R_{\mu\nu} - \frac{1}{2}Rg_{\mu\nu} = 8\pi T_{\mu\nu} - 2f'(T)T_{\mu\nu} - 2f'(T)\Phi_{\mu\nu} + f(T)g_{\mu\nu}, \quad (1.16)$$

where, $f_1(R)$, $f_2(R)$ and $f_3(T)$ represents arbitrary functions of the R and T of the stress - energy tensor of matter, respectively. $(')$ represents the derivative with respect to the argument.

1.2.2.4 Some consequence of $f(R, T)$ Theories of Gravity

Nowadays, many scientists are working continuously to discover several important outcomes in cosmology with late-time acceleration in $f(R, T)$ gravity. Numerous results have already been discovered in the $f(R, T)$ gravity, including

1. Several cosmological models were created by researchers, including the Bianchi type I cosmological model ([Adhav \[2012\]](#)).
2. In $f(R, T)$ gravity, a Bianchi type III dark energy model is developed ([Reddy et al. \[2013\]](#)).
3. A string model of Bianchi type V is obtained $f(R, T)$ gravity ([Ahmed and Pradhan \[2014\]](#)).
4. Furthermore, several facets of $f(R, T)$ gravity have been studied separately.

1.3 Compact stars

Star remnants generated during the course of stellar evolution are known as compact stars. Since so much mass is contained in a small radius, compact stars are in

1.3. Compact stars

Table 1.1: Mass, radius, mean density, surface potential and Schwarzschild radius for some celestial objects.

Objects	Mass M_{\odot}	Radius R_{\odot}	Sch radius km	Mean density gm/cm^3	Surface Potential GM/Rc^2
Earth	3×10^{-6}	8×10^{-3}	9×10^{-6}	5	10^{-16}
Jupiter	10^{-3}	10^{-3}	3×10^{-3}	1	10^{-12}
Sun	1	1	3	1	10^{-6}
Newton star	$1 \sim 3$	10^{-5}	6	$\leq 10^{15}$	10^{-1}
White dwarf	≤ 1	10^{-2}	3	$\leq 10^7$	10^{-4}
Black hole	arbitray	$2GM/c^2$	$2GM/c^2$	M/R^3	1

fact incredibly dense things.

- **Formation:** When a celestial compact object reaches the end of its evolutionary cycle, its thermonuclear fuel runs out and it is unable to resist the pull of gravity. As a result, the object collapses and becomes a compact star. The Big Bang theory has revealed that the formation of compact stars can also be attributed to the phase separations that occurred in the early universe. Following the collapse, the remnant matter configuration shrinks significantly from its initial size, increasing the density in the range. Furthermore, all four of nature's fundamental forces interact with the compact stars.

For many years, one of the main areas of study in modern astronomy has been the realistic model of a stellar configuration of compact object and the composition of its internal matter. They are always working to offer compact stellar models that are consistent with observational evidence and are physically valid.

1.3.1 White dwarfs

White dwarfs are thought to represent the last stage of star evolution for stars whose masses are insufficient to make them neutron stars. Its mass is similar to that of the Sun and its volume is comparable to that of the Earth. In a white dwarf, mass is transformed into energy without any fusion occurring.

A white dwarf is a remnant of a star's core made primarily of extremely dense electron degenerate materials. These indicate the culmination of stars whose starting masses varied from about 0.07 to approximately $8M_{\odot}$. The Milky Way galaxy has around 97

stars, including the Sun, which are predicted to eventually become white dwarfs due to their wide range. Among the hundred stars closest to the Sun, eight are thought to be white dwarfs.

In the triple star system of 40 Eridani, the first white dwarf was found. The smaller part of the Sirius binary star, Sirius B, is the closest known white dwarf. Sirius B is located 8.6 light years away from Earth.

1.3.2 Neutron stars

The smallest and densest stars, known as neutron stars, are the collapsing cores of enormous (1030 solar mass) stars during a supernova explosion, sustained by pressure from neutron degeneracy. The constituents of a neutron star's interior include charge-neutral neutrons, protons, electrons and muons. The mass of a neutron star on the order of $2M$ and its radius is about 10 km on the order. Four regions characterize the interior structure of a neutron star.

(i) **The outer crust:** This portion is about 0.3-0.5 kilometers long. This section is composed of electrons and ions.

(ii) **Inner crust:** This segment is 1-2 kilometers long. Atoms, neutrons and nuclei are included in this section.

(iii) **Outer core:** This core is almost 9 km across. It is composed of protons, neutrons, Fermi liquid and a little amount of DD electron Fermi gas.

(iv) **inner core:** This core has a width of between 0 and 3 kilometres. The inner core's composition is still unknown to scientists.

The pulsar PSR B1919+21 was discovered in 1967 by A. Hewish and his associates; it was subsequently determined to be a rotating neutron star. Neutron stars are categorized as follows based on the discovery of thousands of pulsars and our understanding of particle interactions at the extreme densities.

(i) Neutron stars are made up of leptons and neutrons.

(ii) Hybrid stars in which nuclear matter covers the quark matter core.

(iii) Quark matter composes quark/stranger stars.

1.3.3 Black Hole

A black hole is an area of space where light cannot escape due to the intense gravitational pull of the black hole.

1.3. Compact stars

The regions of a black hole is as follows: **(i)** Singularity, **(ii)** Event horizon, **(iii)** Ergosphere, **(iv)** Photons sphere.

1.3.3.1 Black Holes in General Relativity

The existence of black holes is one of the more intriguing predictions of Einstein's general relativity. The regions of spacetime with extreme gravity, from which nothing can escape, are described by black holes, which are the solutions of the gravitational field equations. Thus, the black hole's boundary functions like a one-way membrane. Nothing can come out of a black hole but things can go into them.

1.3.3.2 Different Black Hole

(i) Super-massive black holes: Super-massive black hole is the largest one. This kind of black hole has a mass that is more than 1 million times that of the Sun and a size comparable to a solar system. Recent investigations indicate that a super-massive black hole is present at the center of every large galaxy. In the center of the Milky Way galaxy is a super-massive black hole called Sagittarius. Its size is the same as the sun's and its mass is almost 4 million times that of the solar. The super-massive black hole of mass $2.9 \times 10^9 M_{\odot}$ at the center of our Milky Way galaxy is powered by jet emissions from the galaxy M87.

(ii) Intermediate black holes: The globular cluster's center contained intermediate black holes. These black holes are the end result of a series of stellar collisions. One of the intermediate black holes identified in the spiral galaxy's arm. A similar-sized intermediate black hole, weighing 50,000 times the mass of the sun, was recently reported by NASA.

(iii) Stellar black holes: The medium-sized black hole is called the stellar. A stellar black hole can have a mass up to 20 times that of the sun, which is equivalent to a ball with a radius of 5 miles. Numerous stellar mass black holes can be found in the Milky Way galaxy.

(iv) Primordial black holes: The smallest of the several kinds of black holes are called primordial black holes. This kind of black hole has a mass comparable to a big mountain yet a size comparable to a single atom.

1.3.3.3 Black Hole solutions

In the context of General Relativity, we briefly explore well-known four-dimensional black hole solutions. A four-dimensional black hole solution of general relativity is either a vacuum or connected with an electromagnetic field, based on the black hole uniqueness theorem and No-hair theorem ([Hawking and Ellis \[2023\]](#)). Specifically, these black holes are either rotating and axisymmetric or non-rotating and spherically symmetric. We classify black holes according to these features in the following manner.

- **Non-rotating black holes:**
 - (i) Schwarzschild Black Hole (M)
 - (ii) Reissner- Nordstrom Black Hole (M, Q)

- **Rotating black holes:**
 - (i) Kerr Black Hole (M,a)
 - (ii) Kerr-Newman Black Hole (M, a, Q)

1.3.3.4 Non-rotating black holes:

The two main characteristics of non-rotating black holes are their mass and charge. Astrophysical black holes rotate, but they are classified as static, or non-spinning, black holes when their spin stops. Now, we discussed about a few non-rotating black hole.

- **Schwarzschild Black Hole:**

The solutions of Einstein field equations that arise in regions of spacetime devoid of any matter or radiation are called vacuum solutions. Hence in the absence of any source these solutions must have $T_{\mu\nu} = 0$. The Schwarzschild metric is the first and most important non-trivial solution of Einstein field equations. The Schwarzschild coordinates are a system of spherical coordinates originating at the centre of a massive body having mass M and are defined as : $x^0 = ct$, $x^1 = r$, $x^2 = \theta$, $x^3 = \phi$.

1.3. Compact stars

The Schwarzschild metric is as follows:

$$ds^2 = \left(1 - \frac{2GM}{c^2 r}\right) c^2 dt^2 - \left(1 - \frac{2GM}{c^2 r}\right)^{-1} dr^2 - r^2(d\theta^2 + \sin^2 \theta d\phi^2). \quad (1.17)$$

The Schwarzschild metric has the following characteristics:

1. **Spherical Symmetry:** On the surface of a sphere of radius R , the Schwarzschild metric reduces to the two-dimensional geometry for every given fixed value of the coordinates $r = R$ and $t = T$,

$$ds^2 = -R^2(d\theta^2 + \sin^2 \theta d\phi^2). \quad (1.18)$$

2. **Asymptotic Flatness:** The Minkowski metric is approached by the Schwarzschild metric as the coordinate $r \rightarrow \infty$

$$ds^2 = c^2 dt^2 - dr^2 - r^2(d\theta^2 + \sin^2 \theta d\phi^2). \quad (1.19)$$

3. **Stationary and Static :** To be stationary means that all of the metric coefficients $g_{\mu\nu}$ are independent of t and Static spacetime refers to a metric that remains invariant by time-reversing transformations, $t \rightarrow -t$. Additionally, there are no form terms in the line element $drdt$, $d\theta dt$, $d\phi dt$.
4. **Singularity :** The metric coefficients $g_{00} \rightarrow 0$ and $g_{11} \rightarrow \infty$ increase as the coordinate r approaches to the Schwarzschild radius, $R_S = 2GM/c^2$. Due to the coordinate system being employed, this singularity is known as the coordinate singularity. A physical or gravitational singularity, however, exists at $r = 0$. The Schwarzschild radius of our Sun is only 3 km, meaning it is located inside the body. However, as is the case with black holes, R_S could possibly be greater than the body's radius.

- **Reissner- Nordstrom Black Hole**

The Reissner-Nordstrom(R-N) black hole is another well-known non-rotating black hole solution. The Einstein-Maxwell field equations that represent the gravitational field of a static, spherically symmetric body with mass M and electric charge Q are the source of this equation. The following metric ($G = c$

= 1) provides the solution

$$ds^2 = -\left(1 - \frac{2M}{r} + \frac{Q^2}{r^2}\right)dt^2 + \left(1 - \frac{2M}{r} + \frac{Q^2}{r^2}\right)^{-1}dr^2 + r^2(d\theta^2 + \sin^2\theta d\phi^2), \quad (1.20)$$

The R-N black hole solution's event horizons are derived from $(1 - \frac{2M}{r} + \frac{Q^2}{r^2}) = 0$ as

$$r_{\pm} = M \left[1 \pm \sqrt{1 - \frac{Q^2}{M^2}} \right]. \quad (1.21)$$

Here, r_+ and r_- denote the R-N black hole's outer and inner horizons, respectively. We may observe from Eq. (1.21) that the relationship between mass M and charge Q determines the characteristics of the Reissner-Nordstrom black hole.

1.3.3.5 Rotating Black Hole:

Since most stars have some angular momentum, rotating black holes are the astrophysical black hole candidates, according to various astrophysical observations. Characteristics of the rotating black holes includes mass, charge and angular momentum. Since the angular momentum of an ancestor massive star is often non-vanishing, the newly formed black hole would remain rotating. A black hole will always gain angular momentum as a result of its interactions with the surrounding material, whether it is generated with small value or no angular momentum. Now, we will discuss two well-known rotating black hole.

- **Kerr Black Hole:**

The complete solution to the Einstein field equations describing an axially symmetric, revolving, stationary and chargeless black hole was given by New Zealand mathematician Roy Kerr in 1963 (Kerr [1963]). In Boyer-Lindquist coordinates, the Kerr black hole metric is as follows (Chandrasekhar [1998])

$$\begin{aligned} ds^2 = & -\left(1 - \frac{2Mr}{\rho^2}\right)dt^2 - \frac{4Mra \sin^2\theta}{\rho^2}d\phi dt + \frac{\rho^2}{\Delta}dr^2 + \rho^2 d\theta^2 \\ & + \left(r^2 + a^2 + \frac{2Mra^2 \sin^2\theta}{\rho^2}\right)\sin^2\theta d\phi^2, \end{aligned} \quad (1.22)$$

1.3. Compact stars

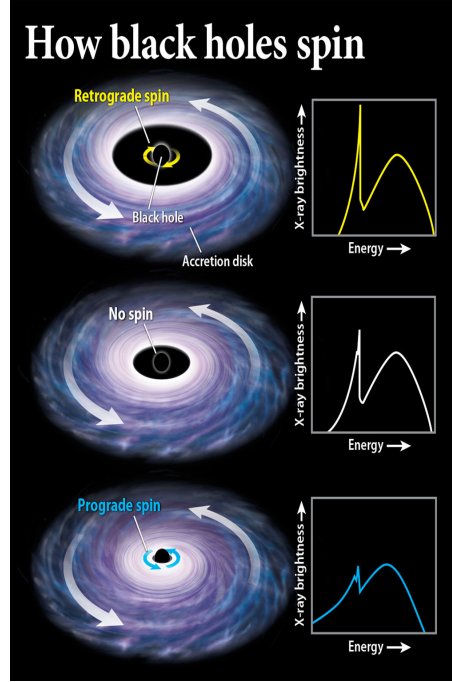


Figure 1.2: Rotating Black hole (Collected from internet).

where, $\rho^2 = r^2 + a^2 \cos^2 \theta$, $\Delta \equiv r^2 - 2Mr + a^2$ and the spin parameter, $a = J/M$, denotes the direction of rotation (M is mass and J is angular momentum). The rotation will be clockwise or anticlockwise according to $a > 0$ or $a < 0$, respectively. In the case of a rotating Kerr black hole, the event horizon must exist if $|a| \leq M$; otherwise, spacetime will create a naked singularity.

We can see some properties of Kerr black hole solution as:

- (i) If $a \rightarrow 0$, the spinning Kerr black hole solution transforms into the Schwarzschild black hole solution.
- (ii) For $r \gg M$ and $r \gg a$, the Kerr solution will be asymptotically flat.
- (iii) The location of the event horizon is $r_{\pm} = M \pm \sqrt{M^2 - a^2}$.
- (iv) The rotation of the Kerr black hole appears to be independent of time, meaning that it is not static but rather stationary.
- (v) Under the transformations $t \rightarrow -t$ and $\phi \rightarrow -\phi$, the Kerr black hole remains invariant.

- [Kerr-Newman Black Hole:](#)

A stationary spinning black hole solution with charge Q and angular momentum $J \equiv Ma$ is found in the Kerr-Newman solution of the Einstein-Maxwell field equations in GTR.

In Boyer-Lindquist coordinates, the Kerr-Newman black hole metric is given as

$$\begin{aligned}
 ds^2 = & -\left(\frac{\Delta - a^2 \sin^2 \theta}{\rho^2}\right) dt^2 - \frac{a \sin^2 \theta}{\rho^2} (r^2 + a^2 - \Delta) d\phi dt + \frac{\rho^2}{\Delta} dr^2 \\
 & + \rho^2 d\theta^2 + \left(\frac{(r^2 + a^2)^2 - \Delta a^2 \sin^2 \theta}{\rho^2}\right) \sin^2 \theta d\phi^2,
 \end{aligned} \tag{1.23}$$

where, $\rho^2 = r^2 + a^2 \cos^2 \theta$, $\Delta \equiv r^2 + a^2 + Q^2 - 2Mr$.

Additionally, the Kerr-Newman black hole solution has a few intriguing characteristics, such as:

- (i) When $a = Q = 0$, the Kerr-Newman metric reduces to the Schwarzschild black hole solution.
- (ii) For $a = 0$, the Kerr-Newman solution with a charged electric field becomes the Reissner-Nordstrom solution.

1.3.3.6 Black Hole in modified gravity

The study of black holes is a popular topic for both theoretical and observational researchers. Researchers have been examining black hole solutions in various modified theories of gravity over the past few decades. The importance of studying black hole solutions in modified theories of gravity is highlighted because the results can be compared to general relativity. Two methods exist for studying black holes in modified gravity:

- (i) **approximation method:** In dynamical Chern-Simons (CS) gravity, the slowly rotating black hole solution has been studied using the approximation approach ([Yunes and Pretorius \[2009\]](#), [Alexander and Yunes \[2009\]](#)).
- (ii) **numerical approach:** Numerical methods have been used to solve the black hole solutions in Einstein-Dilaton-Gauss-Bonnet (EDGB) gravity ([Kanti et al. \[1996\]](#), [Torii et al. \[1997\]](#), [Kanti et al. \[1998\]](#), [Pani and Cardoso \[2009\]](#)).

1.3. Compact stars

Nowadays, the various black hole solutions can be found in various modified theories of gravity, including:

1. Black hole in dilaton gravity ([Gibbons and Maeda \[1988\]](#)).
2. Black hole in extended Chern-Simons modified gravity ([Konno et al. \[2009\]](#)).
3. Black hole in dRGT massive gravity ([Cai et al. \[2013\]](#), [Hendi et al. \[2018\]](#)).
4. Black holes in Rastall gravity ([Kumar and Ghosh \[2018\]](#)).
5. Black holes in a type-II minimally modified gravity ([De Felice et al. \[2021\]](#)).

Many other black hole solutions can be found in various modified theories of gravity.

1.3.3.7 Regular Black Hole

Regular black holes have invariant scalars throughout spacetime and are black hole solutions without curvature singularity. A number of scholars have published many regular black hole models in the literature during the past few decades. Bardeen ([Bardeen \[1968a\]](#)) initially proposed a nonsingular, spherically symmetric, static black hole solution. He solved the Einstein field equation coupled with nonlinear electrodynamics and eliminated the central singularity by substituting a de-Sitter core.

The Bardeen black hole metric can be expressed as

$$ds^2 = -f(r)dt^2 + \frac{dr^2}{f(r)} + r^2(d\theta^2 + \sin^2\theta d\phi^2), \quad (1.24)$$

where

$$f(r) = \left(1 - \frac{2Mr^2}{(r^2 + q^2)^{3/2}}\right). \quad (1.25)$$

Here M and q are the black hole mass and the monopole charge, respectively. When $r = 0$, Bardeen black hole reduces to Schwarzschild black hole. It's interesting to note that in the limit of $r \rightarrow 0$, the Bardeen metric function behaves like de-Sitter spacetime as

$$f(r) = \left(1 - \frac{2Mr^2}{q^3}\right). \quad (1.26)$$

Eventually, the physical source of the nonsingularity of the Bardeen black hole ([Bardeen \[1968a\]](#)) solution is discovered. Numerous scientists were inspired to investigate self-

consistent nonsingular black hole (Toshmatov et al. [2014], Ghosh and Maharaj [2015]) solutions by this intriguing work. Bambi et al. (Bambi and Modesto [2013]) also investigated the rotating counter portion of the Bradeen spacetime metric using the Newman-Janis algorithm and the result was a spinning Bradeen black hole solution that was Kerr-like.

1.4 Lyapunov Exponent

The rate at which two infinitesimally close trajectories separate is defined by the Lyapunov exponent (λ), also known as the Lyapunov characteristic exponent, of a dynamic system. Two trajectories with initial separation vectors of δZ_0 in phase space quantitatively diverge at a rate defined by

$$|\delta Z(t)| \approx e^{\lambda t} |\delta Z_0|$$

For various initial separation vector orientations, the separation rate can vary. As a result, there is a spectrum of λ that has dimensions equal to the phase space's dimensions. The greatest one, which establishes a concept of predictability for a dynamical system, is frequently referred to as the maximal Lyapunov exponent (MLE). A positive MLE is generally seen as evidence of chaos in the system.

1.4.1 The maximal Lyapunov exponent(MLE)

The maximal Lyapunov exponent (λ) can be defined as

$$\lambda = \lim_{t \rightarrow \infty} \lim_{|\delta Z_0| \rightarrow 0} \frac{1}{t} \log \left(\frac{|\delta Z(t)|}{|\delta Z_0|} \right).$$

The linear approximation is always valid by the limit $\lim_{|\delta Z_0| \rightarrow 0}$ at all times.

For a discrete time system where $x_{n+1} = f(x_n)$ is used, the following is the equivalent for an orbit with the number x_0

$$\lambda(x_0) = \lim_{n \rightarrow \infty} \frac{1}{n} \sum_{i=0}^{n-1} \ln |f'(x_i)|.$$

1.4.2 Lyapunov spectrumt

1.5. Shadow of the black hole

The spectrum of Lyapunov exponents $\{\lambda_1, \lambda_2, \dots, \lambda_n\}$ depends generally on the initial point x_0 for a dynamical system with evolution equation $\dot{x}_i = f_i(x)$ in an n -dimensional phase space. If there are multiple attractors, the system's end point may depend on the choice of starting point. The Jacobian matrix is used to define the Lyapunov exponents, which describes how vectors behave in the phase space.

$$J_{ij}(t) = \left. \frac{df_i(x)}{dx_j} \right|_{x(t)}$$

This Jacobian determines the expansion of the tangent vectors, which are provided by the matrix Y through the equation

$$\dot{Y} = JY$$

using $J_{ij}(0) = \delta_{ij}$ as the initial condition. The limit

$$\Lambda = \lim_{t \rightarrow \infty} \frac{1}{2t} \log(Y(t)Y^T(t))$$

determines a matrix Λ . The eigenvalues of Λ are used to define the Lyapunov exponents λ_i .

1.5 Shadow of the black hole

The shadow of the black hole is directly related to the impact parameter of the photon circular orbit.

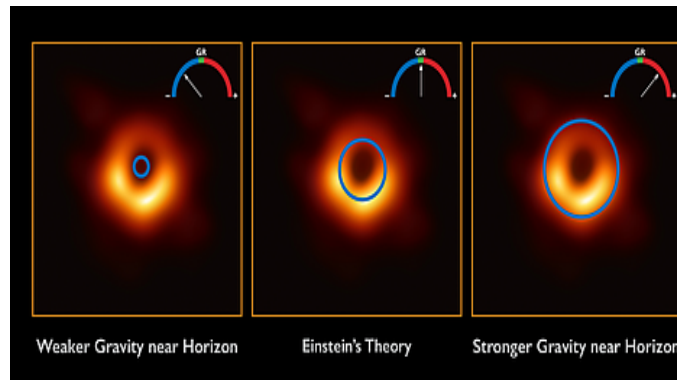


Figure 1.3: Shadow of the Black hole (Collected from internet).

The unstable photon region of a black hole is projected as a shadow into the sky by an observer. A step-like decrease in brightness will be seen that coincides with the shadow if the black hole is surrounded by an geometrically thick emission, optically thin area. The two major changes that GR suggests namely, (i) Gravitational lensing causes the shadow to grow in size. (ii) The path-lengthening effect causes the cloud outside the shadow to get brighter. Even if the size of the shadow and the brightness of the source close to the black hole's boundary are both greatly altered by these two processes, still the blocking effect is still the main cause of the shadow.

1.5.1 Radius of shadow

The black hole's mass determines the shadow's radius, and given the favorable circumstances, the black hole's spin can be inferred from the shadow's shape. Due to these factors, the Event Horizon Telescope's key driver and one of its most accurate predictions was to observe the black hole shadow.

1.6 Photon sphere

A photon circle or photon sphere is a region of space in which gravity is so much strong that photons are compelled to move in orbits, also known as the last photon orbit. Also, The photon sphere is a spherical border with zero thickness where photons traveling on its tangents would be caught, creating a ring-shaped orbit around the black hole. For a Schwarzschild black hole, the radius of the photon sphere, which also serves as the lower constraint for any stable orbit, is

$$r = \frac{3GM}{c^2} = \frac{3r_s}{2}, \quad (1.27)$$

where, G , M , c and r_s represents Gravitational constant, mass of the black hole, speed of light (in vacuum) and the Schwarzschild radius, respectively.

The photon sphere is further away from a black hole's center than the event horizon. Imagine a photon being emitted from one's back of the head, orbiting the black hole, and then being caught by one's eyes and allow to see the back of the head within a photon sphere.

1.6.1 Photon sphere for non-rotating black hole:

1.7. Equating of ISCO

The photon sphere for non-rotating black holes is a sphere with a radius of $\frac{3r_s}{2}$. The photon sphere does not include any stable free-fall orbits, nor does it intersect. Any free-fall orbit that enters the black hole from outside spirals into it. Any orbit that enters from the inside crosses it, either falls back in and spirals towards the black hole or escapes to infinity.

1.6.2 Photon sphere for rotating black hole:

There are two photon spheres for rotating black hole. The closer photon sphere of the black hole rotates in the same direction as it does, whereas the photon sphere that is farther away rotates in the opposite direction. The distance between two photon spheres increases with a black hole's rotational angular velocity. There is one photon sphere in a polar orbit.

1.7 Equating of ISCO

Test particles can maintain a stable orbit around a central object at any distance with Newtonian gravity. However, according to general relativity, there is an innermost stable circular orbit (ISCO) for which any small deviations from a circular orbit will cause them to spiral towards the black hole and any large deviations will cause them to either escape to infinity or spiral inward to the black hole, depending on the amount of energy involved. The ISCO's location depends on the black hole's spin and for a Schwarzschild black hole (zero spin), it is as follows:

$$r = \frac{6GM}{c^2} = 3r_s \quad (1.28)$$

and increasing for particles orbiting a black hole with decreasing spin when they are traveling in the equal direction as the spin.

Chapter 2

Null geodesics and QNMs in the field of regular black holes ¹

2.1 Introduction

Geodesics motion describes the key features of black hole (BH) space-time. In the background spacetime, the geodesics shows a very rich structure and convey some important information related to the BH space-time. There are various kinds of geodesics motions but among these, the circular geodesics motions are more interesting due to its connection to the gravitational binding energy. In Ref. ([Zhang et al. \[1997\]](#)), it was shown that the binding energy of the stable circular time-like geodesics could be used to estimate the spin of astrophysical BHs through the observations of accretion disks. In Refs. ([Kokkotas and Schmidt \[1999\]](#), [Nollert \[1999\]](#), [Mondal et al. \[2021a\]](#)), the effectiveness of null geodesics to explaining the characteristic modes of a BH quasinormal modes are described. It is important to note that general relativity (GR) predicts precessing elliptical orbits around a central star. In the extreme case of a Schwarzschild black hole, there are also a simple set of unstable circular orbits which are referred as the outcome of the non-linearity of general relativity. Cornish and Levin have investigated that all unstable orbits, whether regular or chaotic, can be quantified by their Lyapunov exponents ([Cornish and Levin \[2003\]](#)).

¹A considerable part of this chapter has been published in **International Journal of Modern Physics D**, Vol. **30**, No. **12**, 2150095 (2021).

2. Null geodesics and QNMs in the field of regular black holes

Some important reviews on QNMs of astrophysical BHs and stars are given in Refs. (Nollert [1999], Kokkotas and Schmidt [1999], Berti et al. [2009], Konoplya and Zhidenko [2011]). In particular, it has been explained in Refs. (Nollert [1999], Kokkotas and Schmidt [1999]) that null geodesics play an important role in describing the characteristic modes of a BH while in Refs. Berti et al. [2009], the authors have described the various aspects of QNMs of BHs and branes. Konoplya (Konoplya and Zhidenko [2011]) has considered the possible perturbations of BHs in the context of astrophysical observations. In 1985, Mashhoon (Mashhoon [1985]) has interpreted the free modes of vibrations as null particles which are trapped at the unstable circular orbits. Later on, Berti et al. (Berti and Kokkotas [2005]) have investigated that the null particles trapped at the unstable circular orbits are leaking out slowly. Pretorius and Khurana (Pretorius and Khurana [2007]) have investigated that unstable circular orbits might be useful to obtaining information on phenomena occurring at the threshold of BH formation in the high-energy scattering of BHs. Later on Steklain and Letelier (Steklain and Letelier [2009]) have studied Lyapunov exponents in the context of the stability of circular orbits for different spins of the central body. It is well known that the unstable orbits come out with positive Lyapunov exponents (Schnittman and Rasio [2001]). Some useful applications of Lyapunov exponents have been described in Refs. (Barrow [1981], Hobill et al. [2013], Manna et al. [2020], Semerák and Karas [1999], Das et al. [2020b]). It is important to note that the Lyapunov exponent has been known to erroneously lead to zero Lyapunov exponents for chaotic systems therefore topological measures of chaos are not provoked by the relativism of space and time (Dettmann et al. [1994], Cornish and Levin [1997]).

Very recent past, Prasobha and Kuriakose (Prasobh and Kuriakose [2014]) have studied QNMs frequency of Lovelock BHs and investigated that the real part of the modes decreases as with increase of space-time dimension. This predicts the the presence of lower frequency modes in higher dimensions. In Ref. (Motl and Neitzke [2003]), the authors have investigated QNMs of Schwarzschild BHs in four and higher dimension in the boundary of infinite damping. Note that the asymptotic real part of the BH QNMs holds the same frequency as emitted by a BH whose area falls by an amount which is natural from the point of view of distinct preludes to quantization of gravity such as loop quantum gravity (Dreyer [2003]). Fernando and Clark (Fernando and Clark [2014]) have studied QNMs of scalar perturbations in four dimensional

2.1. Introduction

space-time and compare their result with Schwarzschild BH. Recently Hendi and Nemati ([Hendi and Nemati \[2019\]](#)) have investigated QNMs of scalar perturbations in five dimensional massive gravity by using WKB method.

It is argued that the spacetime singularities are made due to gravitational collapse that are always buried inside black holes. Till now, this signature is a major open question in general relativity. Still we are yet to have any healthy and consistent quantum theory of gravity that resolves the singularities in the interior of black holes. Therefore, there is remarkable consideration towards the models of regular black hole i.e. black hole solutions without the central singularity. S G Ghosh and his collaborators ([Ghosh et al. \[2014\]](#)) established that the regular black holes could be contemplated as the particle accelerator. Toshmatov et al ([Toshmatov et al. \[2015\]](#)) have discussed explicitly the quasinormal modes of test fields around the regular black holes. The above investigations motivate us to study the regular black holes. The main focus of the work is to investigate the geodesics structure of regular black holes. We have studied both null geodesics as well as time-like geodesics. As an application of null geodesics, we have derived the radius of photon sphere and study the shadow of the BH visually. Also we find the relation between radius of photon sphere (r_{ps}) and the shadow as observed by a distance observer. Furthermore, we discuss the implication of various parameters on the radius of shadow R_s . Also we derive the angle of deflection for the photons. By computing the Lyapunov exponent we find the relation between null geodesics and QNMs frequency in the eikonal approximation. Also we study the massless scalar perturbations and analyze the effective potential graphically. Moreover we compute the ISCO and MBCO of the said which are closely related to the BH accretion disk theory.

The chapter is organized as follows. In the next section [2.2](#), we briefly discuss the regular BHs. In Section [2.3](#), we investigate thoroughly the null geodesics of the said BH in AdS space. In Section [2.4](#), we study the Klien-Gordon equations for massless perturbations and derived the effective potential. We plotted it graphically and compared the result with Hayward class and Bardeen class of BHs. Section [2.5](#), is described to study the massive scalar perturbations and computed the effective potential. In Section [2.6](#), we study the relation between QNMs frequency and null circular geodesics through massless scalar perturbations in the eikonal limit. In Section [2.7](#), we investigated the time-like geodesics in the said BH. We also compute the ISCO

2. Null geodesics and QNMs in the field of regular black holes

and MBCO. In Section 2.8, we have given the conclusions and future outlook.

2.2 Introduction of Regular BHs

In this section, we will consider a static, spherically symmetric and asymptotically flat solutions of regular BH (Fan and Wang [2016]) as follows:

$$ds^2 = -f(r)dt^2 + \frac{dr^2}{f(r)} + r^2(d\theta^2 + \sin^2\theta d\phi^2), \quad (2.1)$$

where

$$f(r) = \left(1 - \frac{2M}{r} - \frac{2\alpha^{-1}q^3r^{\mu-1}}{(r^\nu + q^\nu)^{\frac{\mu}{\nu}}}\right) \quad (2.2)$$

Here, $\mu > 0$ is a dimensionless constant, $\alpha > 0$ has the dimension of length squared and q is a free integrating constant.

Special case:

(A) Bardeen class:

If $\nu = 2$, then the function (2.2) is reduced to

$$f = \left(1 - \frac{2M}{r} - \frac{2\alpha^{-1}q^3r^{\mu-1}}{(r^2 + q^2)^{\frac{\mu}{2}}}\right). \quad (2.3)$$

For $M = 0, \mu = 3$, the solution is the Bardeen BH (Bardeen [1968b]).

(B) Hayward class:

If $\nu = \mu$, then the function (2.2) is reduced to

$$f = \left(1 - \frac{2M}{r} - \frac{2\alpha^{-1}q^3r^{\mu-1}}{(r^\mu + q^\mu)}\right). \quad (2.4)$$

For $M = 0, \mu = 3$, the solution is the Hayward BH (Hayward [2006]).

(C) A new class:

If $\nu = 1$, then the function (2.2) is reduced to

$$f = \left(1 - \frac{2M}{r} - \frac{2\alpha^{-1}q^3r^{\mu-1}}{(r + q)^\mu}\right). \quad (2.5)$$

2.2. Introduction of Regular BHs

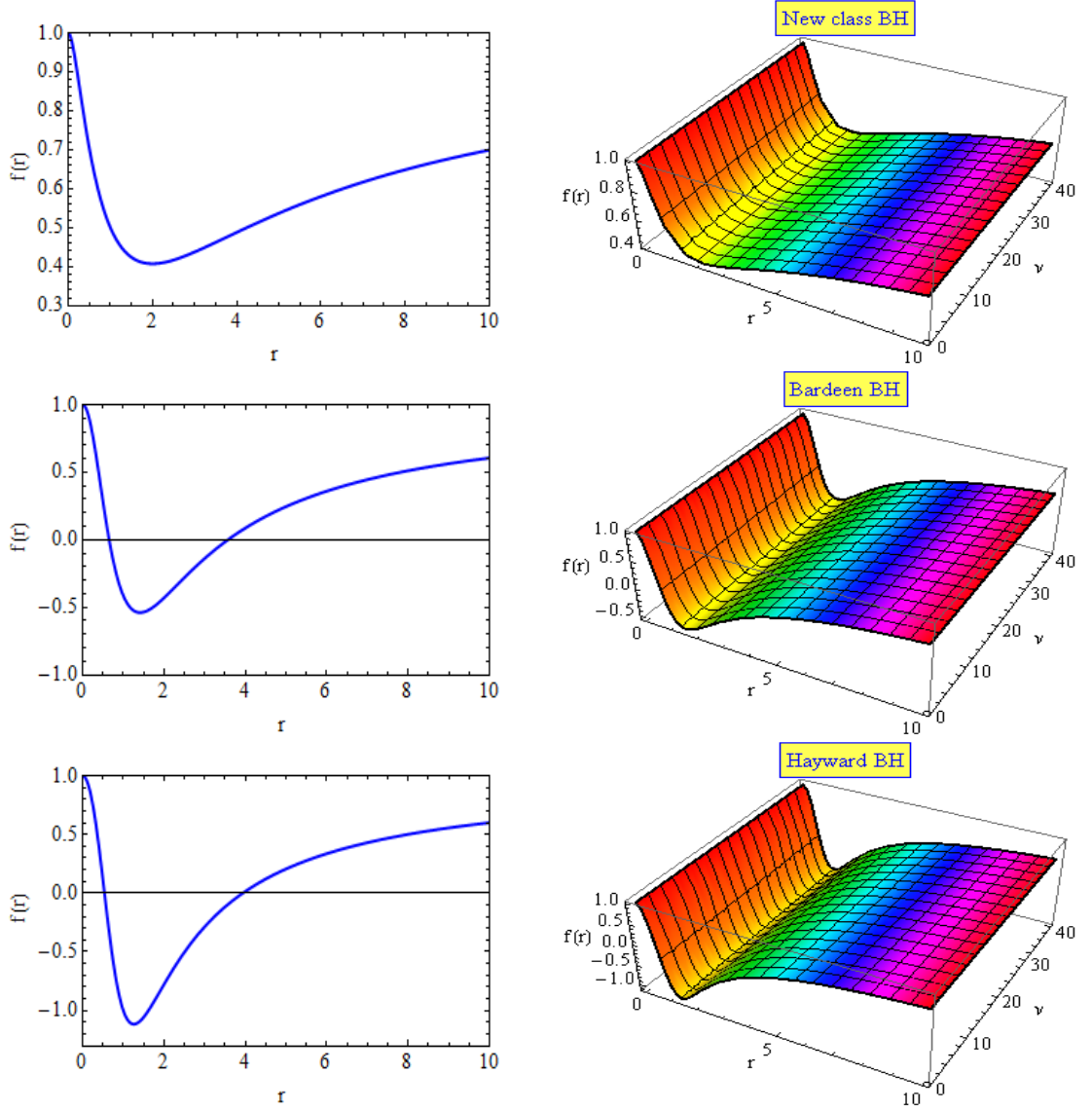


Figure 2.1: $f(r)$ versus r with $\nu = 1$ for New class BH (upper panel), $\nu = 2$ for Bardeen BH (middle panel) and $\nu = 3$ for Hayward BH (lower panel). Here, we set $M = 0$, $q = 1$, $\mu = 3$ and $\alpha = 0.5$. The right panels are plotted for values of ν in the range $0 \leq \nu \leq 40$.

For $M = 0$, the solution can be treated as a new class solution. Also, regular BH has a solution for $\mu \geq 3$.

The variation of $f(r)$ versus r could be seen from Fig. 2.1 and Fig. 2.2. From the figures we can see that, when $\nu = 1$ the solution New class BH has no zero, when $\nu = 2, 3$ the solution BBH and HBH both has two horizon, respectively.

2. Null geodesics and QNMs in the field of regular black holes

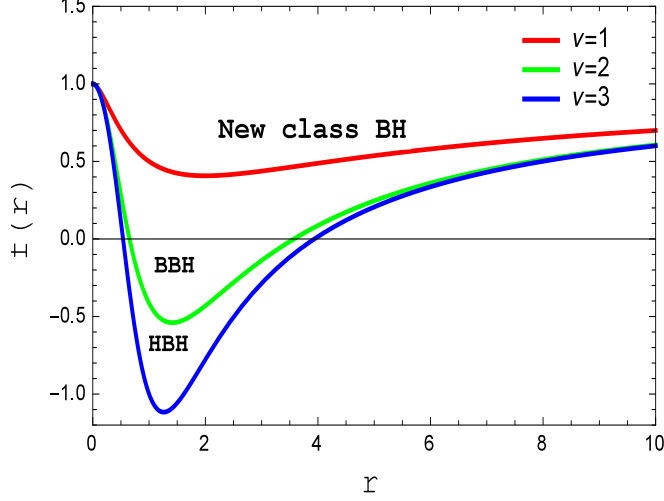


Figure 2.2: $f(r)$ versus r for various values of ν ; the other parameters fixed to $M = 0$, $q = 1$, $\mu = 3$ and $\alpha = 0.5$.

2.3 Action and field equations

The action for Einstein gravity coupled to a non-linear electromagnetic field is read as

$$I = \frac{1}{16\pi} \int \sqrt{-g} (R - \mathcal{L}(\mathcal{F})) d^4x \quad (2.6)$$

where, $\mathcal{F} \equiv F_{ij}F^{ij}$ with $F = dA$ as field strength of the vector field and Lagrangian density \mathcal{L} is a function of \mathcal{F} .

Also, the co-variant equation of motions are given by

$$G_{ij} = T_{ij}, \quad \nabla_i (\mathcal{L}_{\mathcal{F}} F^{ij}) = 0 \quad (2.7)$$

where, $\mathcal{L}_{\mathcal{F}} = \frac{\partial \mathcal{L}}{\partial \mathcal{F}}$ and $G_{ij} = R_{ij} - \frac{1}{2} R g_{ij}$. R and g have their usual meaning as in Einstein tensor.

The energy momentum tensor T_{ij} in this case is defined as

$$T_{ij} = 2 \left(\mathcal{L}_{\mathcal{F}} F_{ij}^2 - \frac{1}{4} g_{ij} \mathcal{L} \right) \quad (2.8)$$

In this paper, we have considered a static, spherically symmetric and asymptotically

2.3. Action and field equations

flat solutions of regular BH.

$$ds^2 = -f(r)dt^2 + \frac{dr^2}{f(r)} + r^2(d\theta^2 + \sin^2\theta d\phi^2), \quad (2.9)$$

Thus, the independent field equations are read as

$$0 = \frac{f'}{r} + \frac{f-1}{r^2} + \frac{1}{2}\mathcal{L} \quad (2.10)$$

$$0 = f'' + \frac{2f'}{r} + \mathcal{L} - \frac{q^8}{\alpha^2 r^4} \mathcal{L}_{\mathcal{F}} \quad (2.11)$$

A detail description of action and field equations of regular BH are found in Ref. (Fan and Wang [2016]).

Here, we have assumed three special class

(A) Bardeen class with Lagrangian density $\mathcal{L} = \frac{4\mu}{\alpha} \frac{(\alpha\mathcal{F})^{\frac{5}{4}}}{(1+\sqrt{\alpha\mathcal{F}})^{1+\frac{\mu}{2}}}$

(B) Hayward class with Lagrangian density $\mathcal{L} = \frac{4\mu}{\alpha} \frac{(\alpha\mathcal{F})^{\frac{\mu+3}{4}}}{(1+(\alpha\mathcal{F})^{\frac{\mu}{4}})^2}$

(C) New class with Lagrangian density $\mathcal{L} = \frac{4\mu}{\alpha} \frac{\alpha\mathcal{F}}{(1+(\alpha\mathcal{F})^{\frac{1}{4}})^{\mu+1}}$

2.3.1 Circular orbits in the Equatorial Plane

In an equatorial plane, we compute the geodesic for the space-time (2.1) by using the method of Chandrasekhar et al. (Chandrasekhar [1998]). In order to do that, we consider $\dot{\theta} = 0$ and $\theta = \text{constant} = \frac{\pi}{2}$. Now, the Lagrangian equation of motion becomes

$$2\mathcal{L} = \left[- \left(1 - \frac{2M}{r} - \frac{2\alpha^{-1}q^3 r^{\mu-1}}{(r^\nu + q^\nu)^{\frac{\mu}{\nu}}} \right) \dot{t}^2 + \frac{\dot{r}^2}{\left(1 - \frac{2M}{r} - \frac{2\alpha^{-1}q^3 r^{\mu-1}}{(r^\nu + q^\nu)^{\frac{\mu}{\nu}}} \right)} + r^2 \dot{\phi}^2 \right], \quad (2.12)$$

where ϕ denotes the angular momentum. Now the canonical momentum is defined as

$$P_q = \frac{\partial \mathcal{L}}{\partial \dot{q}}. \quad (2.13)$$

By using the Eqn. (2.13), the generalized momenta can be derived from the lagrangian

2. Null geodesics and QNMs in the field of regular black holes

are as follows

$$p_t = -\left(1 - \frac{2M}{r} - \frac{2\alpha^{-1}q^3r^{\mu-1}}{(r^\nu + q^\nu)^{\frac{\mu}{\nu}}}\right)\dot{t} = -E = \text{const.} \quad (2.14)$$

$$p_\phi = r^2\dot{\phi} = L = \text{const.} \quad (2.15)$$

$$p_r = \frac{\dot{r}}{\left(1 - \frac{2M}{r} - \frac{2\alpha^{-1}q^3r^{\mu-1}}{(r^\nu + q^\nu)^{\frac{\mu}{\nu}}}\right)}. \quad (2.16)$$

Here, the Lagrangian equation of motion is not depends on ‘ t ’ and ‘ ϕ ’ both, thus p_t and p_ϕ are conserved quantities. After solving Eqns. (2.14) and (2.15) for \dot{t} and $\dot{\phi}$, we get

$$\dot{t} = \frac{E}{\left(1 - \frac{2M}{r} - \frac{2\alpha^{-1}q^3r^{\mu-1}}{(r^\nu + q^\nu)^{\frac{\mu}{\nu}}}\right)} \quad \text{and} \quad \dot{\phi} = \frac{L}{r^2}. \quad (2.17)$$

Integral equation of the geodesic motion is obtained by normalizing the four velocity (u^a) as follows

$$g_{ab}u^au^b = \delta, \quad (2.18)$$

which is similar to

$$-E\dot{t} + L\dot{\phi} + \frac{\dot{r}^2}{\left(1 - \frac{2M}{r} - \frac{2\alpha^{-1}q^3r^{\mu-1}}{(r^\nu + q^\nu)^{\frac{\mu}{\nu}}}\right)} = \delta. \quad (2.19)$$

Here, $\delta = -1$ determines the time-like geodesic, $\delta = 0$ determines the null geodesic and $\delta = 1$ determines the space-like geodesic. Putting the value of \dot{t} and $\dot{\phi}$ from (2.17) into (2.19), we find the radial equation for space-time as

$$\dot{r}^2 = E^2 - \left(\frac{L^2}{r^2} - \delta\right)\left(1 - \frac{2M}{r} - \frac{2\alpha^{-1}q^3r^{\mu-1}}{(r^\nu + q^\nu)^{\frac{\mu}{\nu}}}\right). \quad (2.20)$$

2.4 Null Geodesics of Regular BHs

The radial equation of the test particle for null circular geodesic as using the

2.4. Null Geodesics of Regular BHs

equation (2.20) by setting $\delta = 0$ is given by

$$\dot{r}^2 = E^2 - V_{null} = E^2 - \frac{L^2}{r^2} \left(1 - \frac{2M}{r} - \frac{2\alpha^{-1}q^3 r^{\mu-1}}{(r^\nu + q^\nu)^{\frac{\mu}{\nu}}} \right). \quad (2.21)$$

where V_{null} is the effective potential of null-circular geodesics is given by

$$V_{null} = \frac{L^2}{r^2} \left(1 - \frac{2M}{r} - \frac{2\alpha^{-1}q^3 r^{\mu-1}}{(r^\nu + q^\nu)^{\frac{\mu}{\nu}}} \right). \quad (2.22)$$

2.4.1 Radial null geodesics:

The radial geodesics is corresponding to zero angular momentum ($L=0$). Hence the effective potential for radial null geodesics is

$$V_{null} = 0 \quad (2.23)$$

The equation for \dot{t} and \dot{r} are simplified to

$$\dot{r} = \pm E \quad \text{and} \quad \dot{t} = \frac{E}{f(r)}. \quad (2.24)$$

The above equation gives

$$\frac{dt}{dr} = \pm \frac{1}{f(r)} = \pm \frac{1}{\left(1 - \frac{2M}{r} - \frac{2\alpha^{-1}q^3 r^{\mu-1}}{(r^\nu + q^\nu)^{\frac{\mu}{\nu}}} \right)}. \quad (2.25)$$

The above equation can be integrated to find the coordinate time t as

$$t = \pm \int \frac{1}{\left(1 - \frac{2M}{r} - \frac{2\alpha^{-1}q^3 r^{\mu-1}}{(r^\nu + q^\nu)^{\frac{\mu}{\nu}}} \right)} + \text{constant}. \quad (2.26)$$

When $r \rightarrow 2M$ and $q \rightarrow 0$, $t \rightarrow \infty$. Hence we can obtain the proper time by integrating

$$\frac{d\tau}{dr} = \pm \frac{1}{E}, \quad (2.27)$$

2. Null geodesics and QNMs in the field of regular black holes

which gives

$$\tau = \pm \frac{r}{E} + \text{constant}. \quad (2.28)$$

When $r \rightarrow 2M$ and $q \rightarrow 0$, $\tau \rightarrow \pm \frac{2M}{E}$ is finite. Hence the coordinate time is infinite while the proper time is finite. This is the same with the result for the Schwarzschild BH.

2.4.2 Geodesics with angular momentum ($L \neq 0$):

In this case, the effective potential is

$$V_{null} = \frac{L^2}{r^2} \left(1 - \frac{2M}{r} - \frac{2\alpha^{-1}q^3 r^{\mu-1}}{(r^\nu + q^\nu)^{\frac{\mu}{\nu}}} \right). \quad (2.29)$$

We have plotted the graph V_{null} against r (first panel) in the Fig. 2.3. Initially, V_{null} reaches a peak value then it decreases for larger value of r as evident from Fig. 2.3. In the same figure one can see that V_{null} is linearly decreasing with M (second panel), then it decreases with decreasing value of q (third panel) while V_{null} increases with increasing value of α (fourth panel) and L (fifth panel) respectively.

In case of circular geodesics (Chandrasekhar [1998])

$$\dot{r}^2 = (\dot{r}^2)' = 0, \quad (2.30)$$

Now, the angular momentum and energy at $r = r_o$ for the null geodesics are as follows:

$$\left(r_o^\mu q^3 ((\mu - 3)q^\nu - 3r_o^\nu) + (r_o - 3M)(r_o^\nu + q^\nu)^{\frac{\mu+\nu}{\nu}} \alpha \right) = 0 \quad \text{and}$$

$$\frac{E_o}{L_o} = \pm \sqrt{\frac{\left((r - 2M)(r_o^\nu + q^\nu)^{\frac{\mu}{\nu}} - 2\alpha^{-1}q^3 r_o^\mu \right)}{r_o^2 (r_o^\nu + q^\nu)^{\frac{\mu}{\nu}}}}. \quad (2.31)$$

Let us consider $D_o = \frac{L_o}{E_o}$ be the impact parameter, then the equation (2.31) reduces to

$$\frac{1}{D_o} = \frac{E_o}{L_o} = \sqrt{\frac{M + q^3 r_o^\mu q^3 \alpha^{-1} (r_o^\nu + (1 - \mu)q^\nu) (r_o^\nu + q^\nu)^{(-\frac{\mu+\nu}{\nu})}}{r_o^3}}. \quad (2.32)$$

2.4. Null Geodesics of Regular BHs

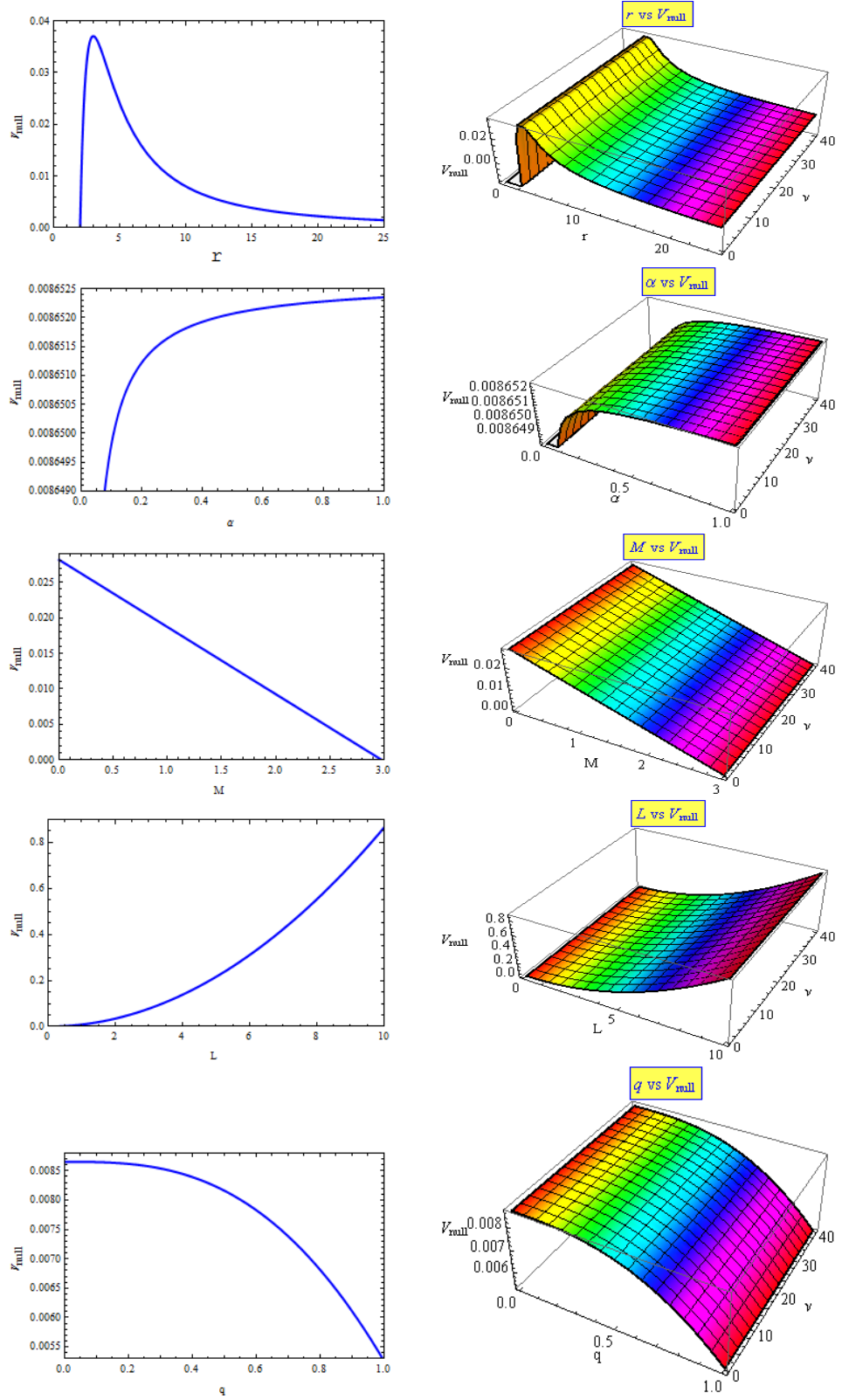


Figure 2.3: The figure describes the variation of V_{null} with r (first panel), M (second panel), q (third panel), α (fourth panel) and L (fifth panel). We have set $\mu = 3$.

2.4.3 Radius of photon sphere :

A photon sphere is a area where the gravitational field of BH is so strong that light can travel in circles. At the photon sphere, no light released outside can reach observer from below- the observer watch into the vast wide emptiness of the BH. For spherical geodesics of a circular light orbits, we use two conditions

$$V_{null}(r)|_{r_o=r_{ps}} = 0 \quad \text{and} \quad \frac{\partial V_{null}(r)}{\partial r}|_{r_o=r_{ps}} = 0,$$

where, r_{ps} is the radius of the photon orbit. The first condition gives

$$\frac{L^2}{E^2} = \frac{r_{ps}^2}{f(r_{ps})}, \quad (2.33)$$

and the second condition implies

$$r_{ps}f'(r_{ps}) - 2f(r_{ps}) = 0. \quad (2.34)$$

Substituting the equation (2.2) into the above equation, we have

$$r_{ps}^\mu q^3((\mu - 3)q^\nu - 3r_{ps}^\nu) + (r_{ps} - 3M)(r_{ps}^\nu + q^\nu)^{\frac{\mu+\nu}{\nu}}\alpha = 0. \quad (2.35)$$

The analytical solution r_{ps} of the above equation is not a trivial task. But for some special cases, we can find a relation for the radius of the photon sphere, as

- when $\alpha = 0$, the radius of photon sphere is follows

$$r_{ph} = 3^{-\frac{1}{\nu}} q^{-\frac{3}{\nu}} \left(q^{3+\nu} (-3 - \mu) \right)^{\frac{1}{\nu}}. \quad (2.36)$$

- when $q = 0$, the radius of the photon sphere is

$$r_{ps} = 3M. \quad (2.37)$$

- when $\mu = 0$, the radius of the photon sphere is as follows

$$r_{ps} = 3(-q^\nu)^{\frac{1}{\nu}} \left(M + \frac{q^3}{\alpha} \right). \quad (2.38)$$

2.4. Null Geodesics of Regular BHs

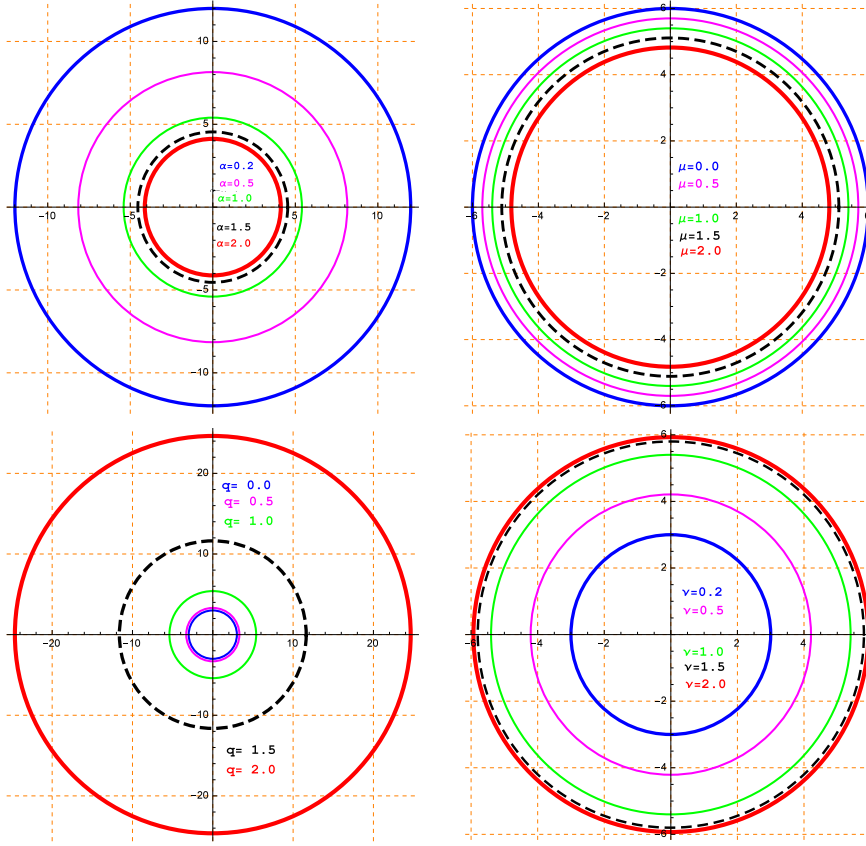


Figure 2.4: Black hole shadow in the Celestial plane $\beta - \gamma$ for varying α with $\mu = 1, \nu = 1$ and $q = 1$ (up- left panel), varying μ with $\alpha = 1, \nu = 1$ and $q = 1$ (up-right panel), varying q with $\alpha = 1, \mu = 1$ and $\nu = 1$ (down left panel), varying ν with $\alpha = 1, \mu = 1$ and $q = 1$ (down- left panel). We set $M = 1$.

2. Null geodesics and QNMs in the field of regular black holes

Table 2.1: Photon sphere radius for variation of massive parameters with $M = 1$.

α	0.2	0.5	1.0	1.5	2.0
$r_{ps}(\mu = \nu = q = 1)$	16.99	8.15	5.4	4.54	4.12
μ	0.0	0.5	1.0	1.5	2.0
$r_{ps}(\alpha = \nu = q = 1)$	6.0	5.7	5.4	5.11	4.82
ν	0.2	0.5	1.0	1.5	2.0
$r_{ps}(\mu = \alpha = q = 1)$	3.14	4.21	5.4	5.8	5.93
q	0.0	0.5	1.0	1.5	2.0
$r_{ps}(\mu = \nu = \alpha = 1)$	3.0	3.31	5.4	11.63	24.64

•••• when $\nu = 1(\nu \neq 0)$, the relation for the radius of the photon sphere is as follows

$$r_{ps}^\mu q^3((\mu - 3)q - 3r_{ps}) + (r_{ps} - 3M)(r_{ps} + q)^\mu \alpha = 0. \quad (2.39)$$

In general, it is possible to numerical that there are many roots (real, complex according to the value of the parameter α, μ, ν and q) of the Eqn. (2.35), which are bigger than the event horizon radius and then we have many small and larger spherical light orbits. To understand which one is stable with respect to radial perturbation, we should examine the sign of V''_{null} , when $V''_{null} < 0$ it indicates unstable orbit and $V''_{null} > 0$ indicates the stable one. In the following Table 2.1, the radius of the unstable photon sphere (the larger photon sphere) is listed for some parameters, thereby we conclude the nature of r_{ps} under variation of the massive parameters.

We plot the BH shadow in Fig. 2.4 for different values of parameters. We observe that in both cases α and μ when the values increase the radius decrease while keeping other parameter fixed. We observe that the shadow size shrinks with increasing “ α ” and “ μ ”, respectively. Further, we notice that with increase in “ q ”, the shadow size increase with fixed other parameters. The shadow size also increase with increase in “ ν ”. One can observed from Fig. 2.4 that μ has weaker effect whereas q has stronger effect on the BH shadow.

2.4.4 Shadow of the BH:

Now, we study the shadow Ref. Jusufi [2020] of the BH. We assume that a bright object released photons and after releasing from the bright object, photons comes towards the BH which is situated between a bright object and an observer. Around

2.4. Null Geodesics of Regular BHs

the BH there are three possible trajectories of the photon geodesics: (i) falling into the BH, (ii) scattered away from BH to infinity, (iii) first two sets are separated by critical geodesics. The observer can see only the scattered photons which fall from a dark region into the BH. This dark region is called BH shadow.

Now, to study the shadow of the BH we are going to introduce a new celestial coordinate (β, γ) , where β is the perpendicular distance of the shadow from symmetry axis and γ is the apparent perpendicular distance of the shadow from its projection on the equatorial plane. Following the calculation of Ref. [Das et al. \[2020a\]](#) we can obtain an equation representing a circle of radius in celestial plane $\beta - \gamma$, as follows

$$\beta^2 + \gamma^2 = R_s^2 = \frac{\frac{r_{ps}^2}{f(r_{ps})}}{1 - \frac{r_{ps}}{f(r_{ps})} \cdot \frac{f(r_{ob})}{r_{ob}^2}}, \quad (2.40)$$

where subscripts “ ps ” and “ ob ” represents the photon sphere and observer, respectively. Considering the equation (2.2), for distant observer when $r \rightarrow \infty$, we can find that $\frac{f(r_{ob})}{r_{ob}^2} \rightarrow 0$. So the radius of the shadow(R_s) reduces to

$$R_s = \frac{r_{ps}}{\sqrt{f(r_{ps})}} \quad (2.41)$$

2.4.5 Dependence of shadow radius R_s on various parameters:

From Eqn. (2.41) we can write the expression of the shadow radius R_s as follows

$$R_s = \frac{r_{ps}}{\sqrt{\left(1 - \frac{2M}{r_{ps}} - \frac{2\alpha^{-1}q^3 r_{ps}^{\mu-1}}{(r_{ps}^\nu + q^\nu)^\frac{\mu}{\nu}}\right)}} \quad (2.42)$$

The above expression of R_s shows the effects of the parameter α, μ, ν and q on the silhouette of the shadow. The variation in the silhouette of the BH shadow are shown graphically in Fig. 2.5 and Fig. 2.6 for different values of parameters.

In Table 2.2, we represent the computed the values of radius of photon sphere (r_{ps}) and the BH shadow radius (R_s) for different values of the parameters.

In Fig. 2.5, R_s is plotted against r upper and lower left panel for varying α and

2. Null geodesics and QNMs in the field of regular black holes

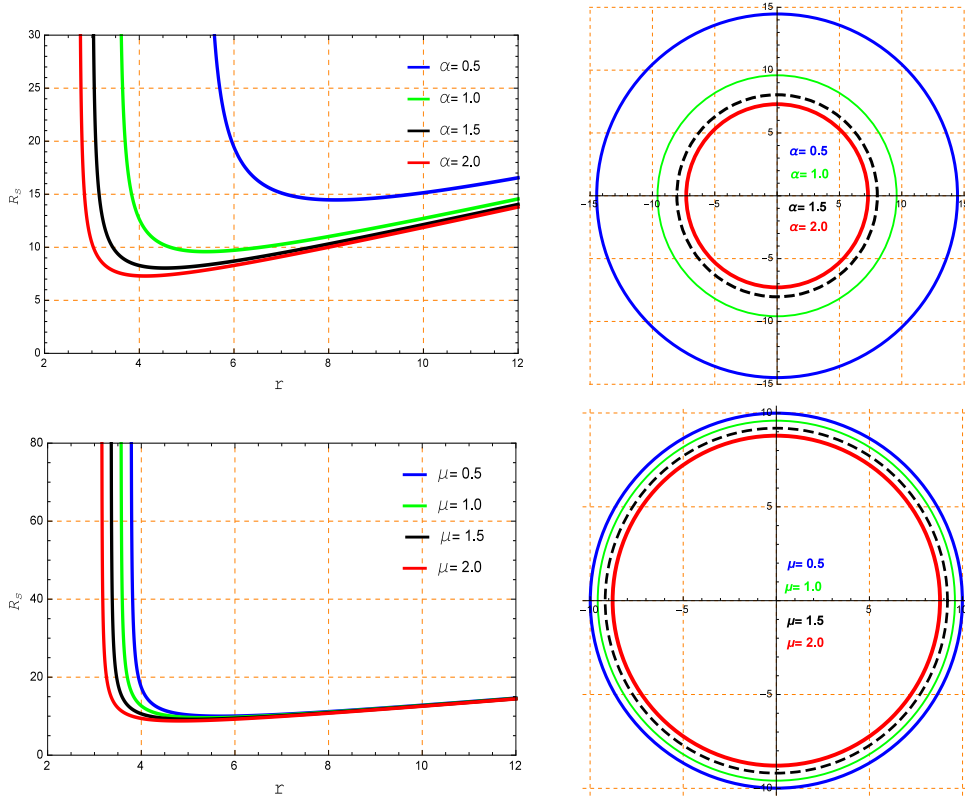


Figure 2.5: The figure shows R_s versus r (up-left panel) for varying α and varying μ (down-left panel). BH shadow in the Celestial plane $\beta-\gamma$ for varying α with $\mu = 1, \nu = 1$ and $q = 1$ (up-left panel), varying μ with $\alpha = 1, \nu = 1$ and $q = 1$ (down-right panel). We set $M = 1$.

2.4. Null Geodesics of Regular BHs

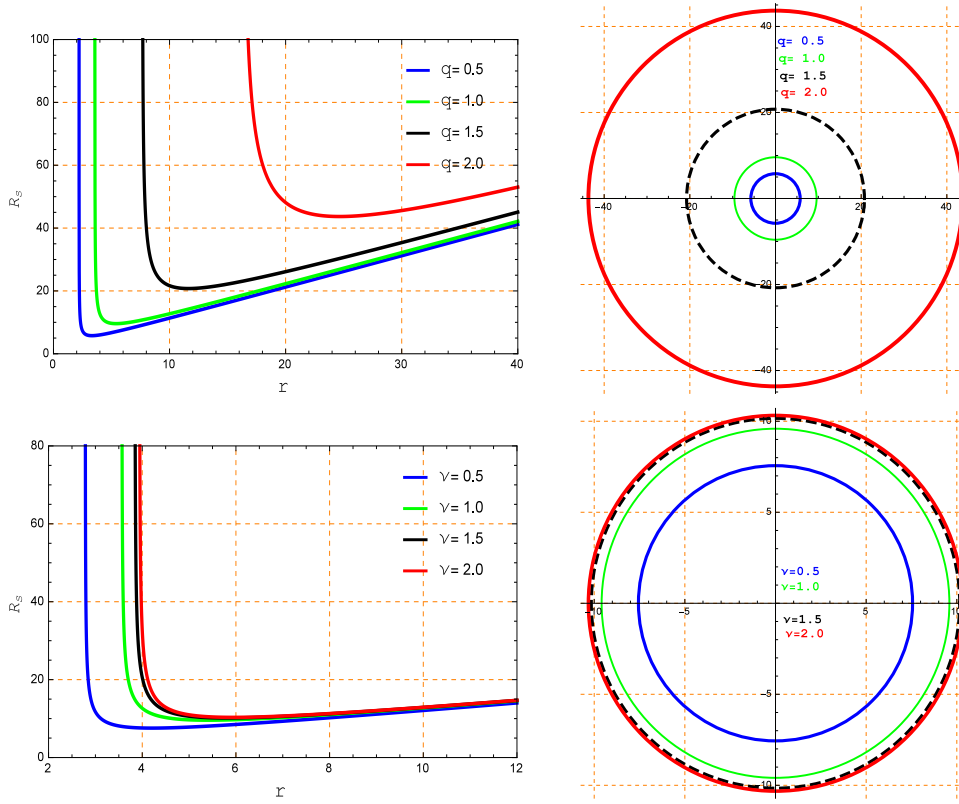


Figure 2.6: The figure shows R_s versus r (up-left Panel) for varying q and varying ν (down-left Panel). Black hole shadow in the Celestial plane $\beta - \gamma$ for varying q with $\alpha = 1, \mu = 1$ and ν (up- right panel), varying ν with $\alpha = 1, \mu = 1$ and $q = 1$ (down- right panel). We set the parameter $M = 1$.

2. Null geodesics and QNMs in the field of regular black holes

μ , respectively and the BH shadow against R_s is plotted upper and lower right panel for varying α and ν , respectively. From Fig. (2.5) we observe that the shadow size shrinks with increasing “ α ” and “ μ ” when the value of the other parameters is fixed.

In Fig. 2.6, R_s is plotted against r upper and lower left panel for varying q and ν , respectively. The BH shadow against R_s is plotted upper and lower right panel for varying q and μ , respectively. One can see from Fig. (2.6) that the shadow size increase with increasing “ q ” and “ ν ”, the shadow radius R_s increase, while other parameters is fixed.

Also one can find that variation of μ has weaker effect on the shadow size than the other parameter and q has more significant effect on the BH shadow.

2.4.6 Gravitional Bending of light

A non-stable circular photon orbit is called “Photon Sphere”. This non-stable photon sphere represents the shadow of the BH. From Eqn. (2.15) and Eqn. (2.16) we have

$$\frac{dr}{d\phi} = \frac{\dot{r}}{\dot{\phi}} = \frac{p_r \left(1 - \frac{2M}{r} - \frac{2\alpha^{-1}q^3 r^{\mu-1}}{(r^\nu + q^\nu)^{\frac{\mu}{\nu}}} \right) r^2}{L}. \quad (2.43)$$

Again the Eqn. (2.21) can be rewritten as

$$p_r^2 \left(1 - \frac{2M}{r} - \frac{2\alpha^{-1}q^3 r^{\mu-1}}{(r^\nu + q^\nu)^{\frac{\mu}{\nu}}} \right) = \frac{E^2}{\left(1 - \frac{2M}{r} - \frac{2\alpha^{-1}q^3 r^{\mu-1}}{(r^\nu + q^\nu)^{\frac{\mu}{\nu}}} \right)} - \frac{L^2}{r^2}. \quad (2.44)$$

We can get p_r from the Eqn. (2.44) as

$$p_r = \pm \sqrt{\frac{1}{\left(1 - \frac{2M}{r} - \frac{2\alpha^{-1}q^3 r^{\mu-1}}{(r^\nu + q^\nu)^{\frac{\mu}{\nu}}} \right)}} \sqrt{\frac{E^2}{\left(1 - \frac{2M}{r} - \frac{2\alpha^{-1}q^3 r^{\mu-1}}{(r^\nu + q^\nu)^{\frac{\mu}{\nu}}} \right)} - \frac{L^2}{r^2}}. \quad (2.45)$$

Using p_r from the above equation, we can write the Eqn. (2.43) as follows

$$\frac{dr}{d\phi} = \pm \sqrt{\left(1 - \frac{2M}{r} - \frac{2\alpha^{-1}q^3 r^{\mu-1}}{(r^\nu + q^\nu)^{\frac{\mu}{\nu}}} \right)} \sqrt{\frac{E^2}{L^2} \chi^2(r) - 1}, \quad (2.46)$$

2.5. Basic equation for the perturbation of the regular BH :

where,

$$\chi^2(r) = \frac{r^2}{\left(1 - \frac{2M}{r} - \frac{2\alpha^{-1}q^3r^{\mu-1}}{(r^\nu+q^\nu)^{\frac{\mu}{\nu}}}\right)}. \quad (2.47)$$

Now, a light ray coming from infinity, reaches at minimum radius (R) and again returns back to infinity, the bending angle ($\beta_{bending}$) is read by the formula

$$\beta_{bending} = -\pi + 2 \int_R^\infty \frac{dr}{\sqrt{r^2 \left(1 - \frac{2M}{r} - \frac{2\alpha^{-1}q^3r^{\mu-1}}{(r^\nu+q^\nu)^{\frac{\mu}{\nu}}}\right) \left(\frac{E^2}{L^2} \chi^2(r) - 1\right)}}. \quad (2.48)$$

As R is the turning point of the trajectory, the necessary condition $\frac{dr}{d\phi}|_{R=0}$ must be satisfied.

This leads to the equation

$$\chi^2(R) = \frac{L^2}{E^2}. \quad (2.49)$$

Then the deflection angle as a function of R can be written as

$$\beta_{bending} = -\pi + 2 \int_R^\infty \frac{dr}{\sqrt{r^2 \left(1 - \frac{2M}{r} - \frac{2\alpha^{-1}q^3r^{\mu-1}}{(r^\nu+q^\nu)^{\frac{\mu}{\nu}}}\right) \left(\frac{\chi^2(r)}{\chi^2(R)} - 1\right)}}. \quad (2.50)$$

Substituting the value of $\chi^2(r)$ and $\chi^2(R)$, the equation of bending angle of regular BH is

$$\beta_{bending} = -\pi + 2 \int_R^\infty \frac{dr}{\sqrt{r^2 \left(1 - \frac{2M}{r} - \frac{2\alpha^{-1}q^3r^{\mu-1}}{(r^\nu+q^\nu)^{\frac{\mu}{\nu}}}\right) \left(\frac{r^2}{D^2 \left(1 - \frac{2mr^2}{r^3+2l^2m}\right)} - 1\right)}}, \quad (2.51)$$

where, $D = \frac{L}{E}$ is the impact parameter of the regular BH. The formula of bending angle is derived in [Chiba and Kimura \[2017\]](#).

2.5 Basic equation for the perturbation of the regular BH :

2. Null geodesics and QNMs in the field of regular black holes

Table 2.2: Radius of photon sphere r_{ps} of the BH, shadow radius R_s for variation of massive parameters with $M = 1$.

S. N.	α	$r_{ps}(\mu = \nu = q = 1)$	$R_s(\mu = \nu = q = 1)$
1.	0.5	8.15	14.47
2.	1.0	5.4	9.59
3.	1.5	4.54	8.04
4.	2.0	4.12	7.29

S. N.	μ	$r_{ps}(\alpha = \nu = q = 1)$	$R_s(\mu = \nu = q = 1)$
1.	0.5	5.7	9.99
2.	1.0	5.4	9.59
3.	1.5	5.11	9.19
4.	2.0	4.82	8.79

S. N.	ν	$r_{ps}(\alpha = \mu = q = 1)$	$R_s(\mu = \nu = q = 1)$
1.	0.5	4.21	7.56
2.	1.0	5.4	9.59
3.	1.5	5.8	10.16
4.	2.0	5.93	10.32

S. N.	q	$r_{ps}(\alpha = \mu = \nu = 1)$	$R_s(\mu = \nu = q = 1)$
1.	0.5	3.31	5.76
2.	1.0	5.4	9.59
3.	1.5	11.63	20.76
4.	2.0	24.64	43.68

2.5. Basic equation for the perturbation of the regular BH :

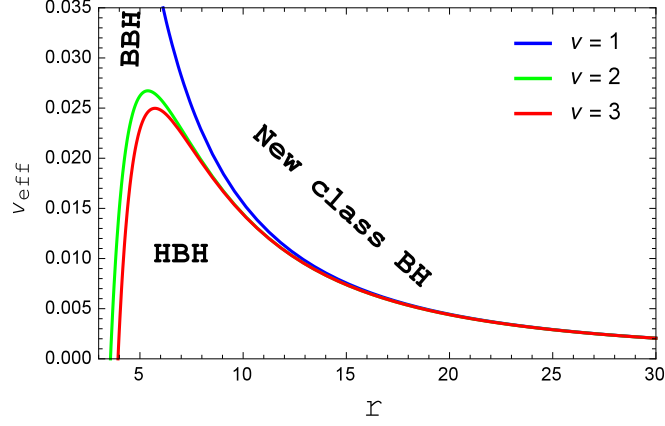


Figure 2.7: The figure shows the V_{null}^m versus r for varying values of the mass m . Here, $M = 1, q = 0.5, \mu = 3, \nu = 1, l = 1$ and $\alpha = 0.5$.

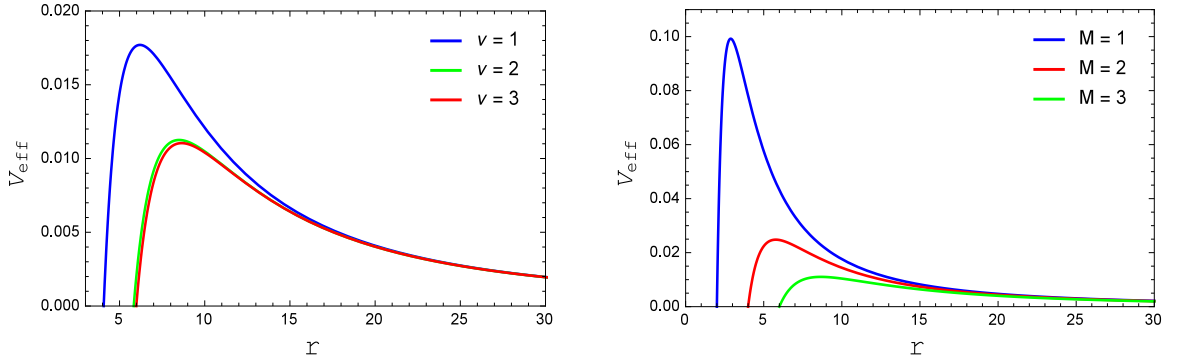


Figure 2.8: The figure shows the V_{eff} versus r for varying ν (left Panel) and M (right panel); the other parameters fixed to $l = 1, \mu = 3$ and $\alpha = 0.5$.

The Klein-Gordon equation around the regular BH of the massless scalar field is given by

$$\nabla^2 \xi = 0. \quad (2.52)$$

By separation of the variable we have

$$\xi = e^{-i\omega t} X_{l,m}(\theta, \phi) \frac{\eta(r)}{r}. \quad (2.53)$$

After simplifying equation (2.52) we obtain a Schrödinger-type equation which is

2. Null geodesics and QNMs in the field of regular black holes

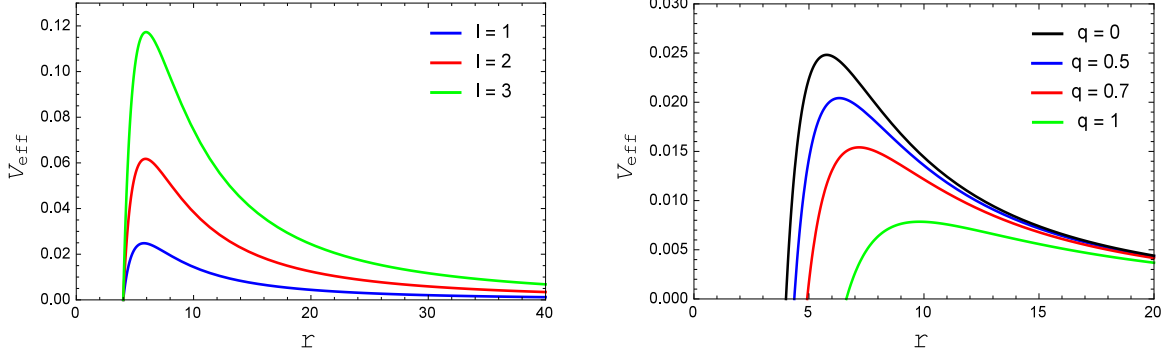


Figure 2.9: The figure shows the V_{eff} versus r for varying l (left Panel) and q (right panel); the other parameters fixed to $M = 1, \mu = 3$ and $\alpha = 0.5$.

given by

$$\frac{d^2\eta(r_*)}{dr_*^2} + \left(w^2 - V_{eff}(r_*)\right)\eta(r_*) = 0, \quad (2.54)$$

where, $V_{eff}(r_*)$ is given by

$$V_{eff}(r_*) = \left[\frac{l(l+1)}{r^2} + \frac{2}{r^3} \left(M + \frac{q^3 r^\mu q^3 (r^\nu + (1-\mu)q^\nu)}{\alpha(r^\nu + q^\nu)^{\frac{\mu+\nu}{\nu}}} \right) \right] \left[1 - \frac{2M}{r} - \frac{2\alpha^{-1} q^3 r^{\mu-1}}{(r^\nu + q^\nu)^{\frac{\mu}{\nu}}} \right].$$

Here, $w, X_{l,m}(\theta, \phi)$ and r_* represents the frequency of the wave mode, the spherical harmonic and the tortoise coordinate, respectively. The effective potential $V_{eff}(r)$ depends on the parameters l, M, α, q, μ and ν .

The comparison of effective potentials among the Hayward BH (HBH), Bardeen BH (BBH) and new class BH are shown in Fig. 2.7. One can see from Fig. 2.7 that the effective potential of new class BH is greatest compared to Bardeen BH and Hayward BH.

In Fig. 2.8, V_{eff} is plotted against r (left panel) by varying ν and V_{eff} is plotted against r (right panel) by varying M . One can see that for both cases height of V_{eff} is decreasing for increasing of ν and M , respectively.

Fig. 2.9 represents the plot of V_{eff} versus r (left panel) by varying l and V_{eff} versus r (right panel) by varying q . The height of V_{eff} increases as l increases and when q increases the height of the V_{eff} decreases.

2.6. Massive scalar perturbations:

2.6 Massive scalar perturbations:

In this section, we will see how the massive scalar field decay. It has been observed for Schwarzschild BH that the massless modes decays faster than massive scalar field (Konoplya and Zhidenko [2005]). Hence it is quite interesting to see that if such characteristics is possible for the above metric (2.1).

Let us take the equation of motion for massive scalar field as

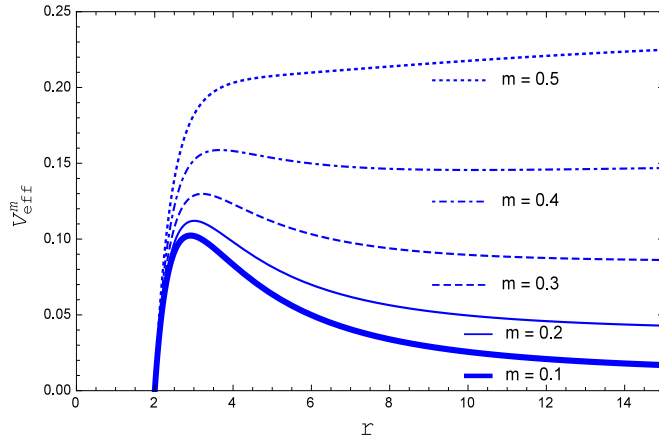


Figure 2.10: The figure shows the V_{null}^m versus r for varying values of the mass m . Here, $M = 1, q = 0.5, \mu = 3, \nu = 1, l = 1$ and $\alpha = 0.5$.

$$\nabla^2 \xi - m^2 \xi = 0. \quad (2.55)$$

After using the separation of variable similar to the Eqn. (2.53), we obtain the following equation for radial component as

$$\frac{d^2 \eta(r_*)}{dr_*^2} + \left(w^2 - V_{eff}^m(r_*) \right) \eta(r_*) = 0, \quad (2.56)$$

and the modified potential $V_{eff}^m(r_*)$ is given by

$$V_{eff}^m(r_*) = \left[\frac{l(l+1)}{r^2} + \frac{2}{r^3} \left(M + \frac{q^3 r^\mu q^3 (r^\nu + (1-\mu)q^\nu)}{\alpha (r^\nu + q^\nu)^{(\frac{\mu+\nu}{\nu})}} \right) + m^2 \right] \left[1 - \frac{2M}{r} - \frac{2\alpha^{-1} q^3 r^{\mu-1}}{(r^\nu + q^\nu)^{\frac{\mu}{\nu}}} \right].$$

The effective potential $V_{eff}^m(r_*)$ is plotted in the Fig. 2.10 for different values of the

2. Null geodesics and QNMs in the field of regular black holes

mass parameter m . The Fig. 2.10 shows that when mass increases the height of the effective potential also increases. Also the potential terminates to have maximum at the critical values of m .

2.7 Unstable null geodesics and quasinormal modes of massless scalar field in the eikonal limit

A quasinormal mode is a solution to the differential equation which has a complex frequency. It satisfies the boundary condition of purely “Outgoing” waves, which propagating away from the boundary, from $-\infty$ to $+\infty$. WKB method gives the correct approximation of QNMs at an eikonal limit.

Here, the central equation (wave Eqn.) can be taken in the following form

$$\frac{d^2\psi}{dx^2} + Q(x)\psi = 0, \quad (2.57)$$

where,

$$Q = w^2 - V_{eff}(r)$$

and

$$V_{eff}(r) = \left[\frac{l(l+1)}{r^2} + \frac{2}{r^3} \left(M + \frac{q^3 r^\mu q^3 (r^\nu + (1-\mu)q^\nu)}{\alpha(r^\nu + q^\nu)^{\left(\frac{\mu+\nu}{\nu}\right)}} \right) \right] \left[1 - \frac{2M}{r} - \frac{2\alpha^{-1}q^3 r^{\mu-1}}{(r^\nu + q^\nu)^{\frac{\mu}{\nu}}} \right].$$

In case of BH, ψ represents the radial part of perturbation variable, which assumed to be time dependent. The coordinate x is linearly connected to the “tortoise” coordinate r_* , which ranges from $-\infty$ (at the horizon) to $+\infty$ (at the spatial infinity). The tortoise coordinate r_* and the radial coordinate r are related by the following relation

$$\frac{dr}{dr_*} = \left(1 - \frac{2M}{r} - \frac{2\alpha^{-1}q^3 r^{\mu-1}}{(r^\nu + q^\nu)^{\frac{\mu}{\nu}}} \right). \quad (2.58)$$

The function $Q(x)$, which depends on the angular momentum and the mass of the BH, is constant at $x = \pm\infty$. At $l \rightarrow \infty$ (i.e., in case of eikonal limit), we get

$$Q_0 \simeq \omega^2 - \frac{l^2}{r^2} \left(1 - \frac{2M}{r} - \frac{2\alpha^{-1}q^3 r^{\nu-1}}{(r^\nu + q^\nu)^{\frac{\mu}{\nu}}} \right), \quad (2.59)$$

2.7. Unstable null geodesics and quasinormal modes of massless scalar field in the eikonal limit

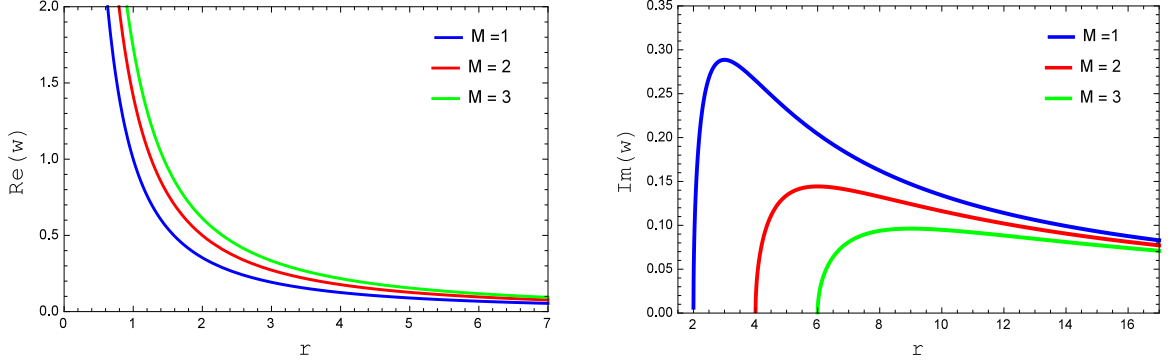


Figure 2.11: The figure shows QNMs frequency $\text{Re}(w)$ versus r (left Panel) and $\text{Im}(w)$ versus r (right panel). Here $q = 0.5, \mu = 3, \alpha = 0.5$ and $\nu = 2$.

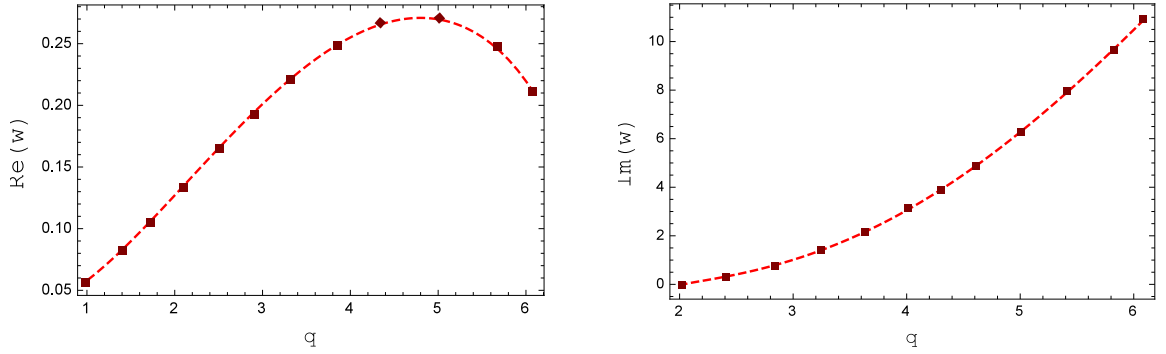


Figure 2.12: The figure shows QNMs frequency $\text{Re}(w)$ versus q (left Panel) and $\text{Im}(w)$ versus r (right panel); the other parameter fixed to $M = 1, \mu = 3, \alpha = 0.5$ and $\nu = 2$.

where l represents the angular harmonic index.

From the eqn. (2.59), the maximum value of Q_0 at $r = r_\sigma$, is given by

$$\left(r_\sigma^\mu q^3 ((\mu - 3)q^\nu - 3r_\sigma^\nu) + (r_\sigma - 3M)(r_\sigma^\nu + q^\nu)^{\frac{\mu+\nu}{\nu}} \alpha \right) = 0. \quad (2.60)$$

At $r = r_o$, the unstable null circular geodesic can be calculated by using $\dot{r}^2 = (\dot{r}^2)' = 0$, we have

$$\left(r_o^\mu q^3 ((\mu - 3)q^\nu - 3r_o^\nu) + (r_o - 3M)(r_o^\nu + q^\nu)^{\frac{\mu+\nu}{\nu}} \alpha \right) = 0. \quad (2.61)$$

At the point $r_\sigma = r_o$, the maximum value of Q_0 and the null circular geodesics are

2. Null geodesics and QNMs in the field of regular black holes

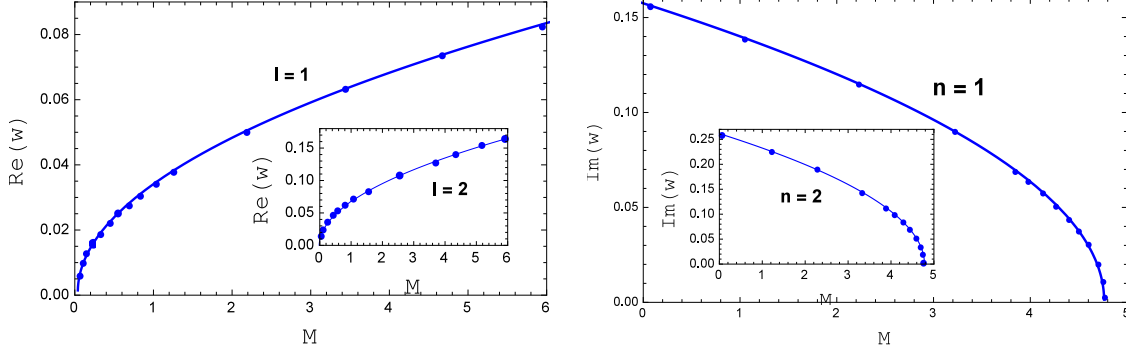


Figure 2.13: The figure shows QNMs frequency $\text{Re}(w)$ versus M (left Panel) and $\text{Im}(w)$ versus M (right panel). Here $q = 0.5, \mu = 3, \alpha = 0.5$ and $\nu = 2$.

coincident, then the QNM leads to the following form

$$\frac{Q_0(r_\sigma)}{\sqrt{2Q_0''(r_\sigma)}} = i(n + 1/2), \quad (2.62)$$

where $Q_0'' \equiv \frac{d^2 Q_0}{dr_*^2}$ and the Eqn. (2.62) is calculated at an extremum of Q_0 (that is, $\frac{dQ_0}{dr_*} = 0$ at r_0).

Following the formula that has been derived by Cardoso et al. (Cardoso et al. [2009]) as

$$\omega_{QNM} = l\Omega_o - i(n + 1/2)\lambda_o, \quad (2.63)$$

where n represents the overtone number, Ω_o is the angular frequency measured by the asymptotic observers and λ_o is the coordinate Lyapunov exponent of null-circular geodesics. Angular frequency (Ω_o) and Lyapunov exponent (λ_o) for null-circular geodesics are studied in Appendix. In case of eikonal approximation (i.e., in the large- l limit) the QNM frequency for BH (Mondal et al. [2020]) can be represented by the following two parameters:

$$\omega_{QNM} = l\sqrt{\frac{M + q^3 r_o^\mu q^3 \alpha^{-1} (r_o^\mu + (1 - \mu)q^\nu)(r_o^\nu + q^\nu)^{-\left(\frac{\mu+\nu}{\nu}\right)}}{r_o^3}} - i(n + 1/2) \times \sqrt{\frac{((r_o - 2M)(r_o^\nu + q^\nu)^{\frac{\mu}{\nu}} \alpha - 2q^3 r_o^\mu)(r_o \alpha (r_o^\nu + q^\nu)^{2+\frac{\mu}{\nu}} + \mu q^{(3+\nu)} r_o^\mu (3q^\nu(\nu - 3) - r_o^\nu(\nu + 3)))}{r_o^2 \alpha (r_o^\nu + q^\nu)^{\frac{\mu+\nu}{\nu}}}} \quad (2.64)$$

2.8. Time-like Geodesics of Regular BHs

Which is the key results of our manuscript and the importance of the equation (2.64) is that in case of eikonal limit, the real and complex parts of the QNMs for the spherically symmetric, asymptotically flat space-time are stated by the frequency and instability time scale for the case of unstable null circular geodesics.

Fig. 2.11 represents the plot of $Re(w)$ versus q (left panel) and $Im(w)$ versus q (right panel) by varying M . $Re(w)$ decreases as r increases and when M increases, the height of the $Im(w)$ decreases.

In Fig. 2.12, $Re(w)$ is graphed versus q (left panel) and $Im(w)$ is graphed versus q (right panel). One can see that $Re(w)$ is increased for the initial value of q . However, it seems $Re(w)$ decrease for large value of q as evident from Fig. 2.12. But the $Im(w)$ is always increasing with increasing the value of q .

In Fig. 2.13, $Re(w)$ is graphed versus M (left panel) for both $l = 1$ and $l = 2$. $Im(w)$ is graphed versus M (right panel) for both $n = 1$ and $n = 2$. $Re(w)$ increases with M and $Im(w)$ is decreased when M increased. Interestingly, when M increases, there is a critical point where $Im(w)$ approaches to zero leading to purely real modes.

2.8 Time-like Geodesics of Regular BHs

2.8.1 The Effective Potential

For time-like circular geodesics ($\delta = -1$) the radial Eqn.(2.20) reduces to

$$\dot{r}^2 = E^2 - V_{time} = E^2 - \left(1 + \frac{L^2}{r^2}\right) \left(1 - \frac{2M}{r} - \frac{2\alpha^{-1}q^3 r^{\mu-1}}{(r^\nu + q^\nu)^{\frac{\mu}{\nu}}}\right), \quad (2.65)$$

V_{time} denoted the effective potential for time-like geodesics which is given by

$$V_{time} = \left(1 + \frac{L^2}{r^2}\right) \left(1 - \frac{2M}{r} - \frac{2\alpha^{-1}q^3 r^{\mu-1}}{(r^\nu + q^\nu)^{\frac{\mu}{\nu}}}\right). \quad (2.66)$$

The geodesic motion of neutral test particles can be analyzed by using the effective potential diagram which is graphically shown in Fig. 2.14.

Analogously, the effective potential with zero angular momentum geodesics is

$$V_{time} = \left(1 - \frac{2M}{r} - \frac{2\alpha^{-1}q^3 r^{\mu-1}}{(r^\nu + q^\nu)^{\frac{\mu}{\nu}}}\right), \quad (2.67)$$

2. Null geodesics and QNMs in the field of regular black holes

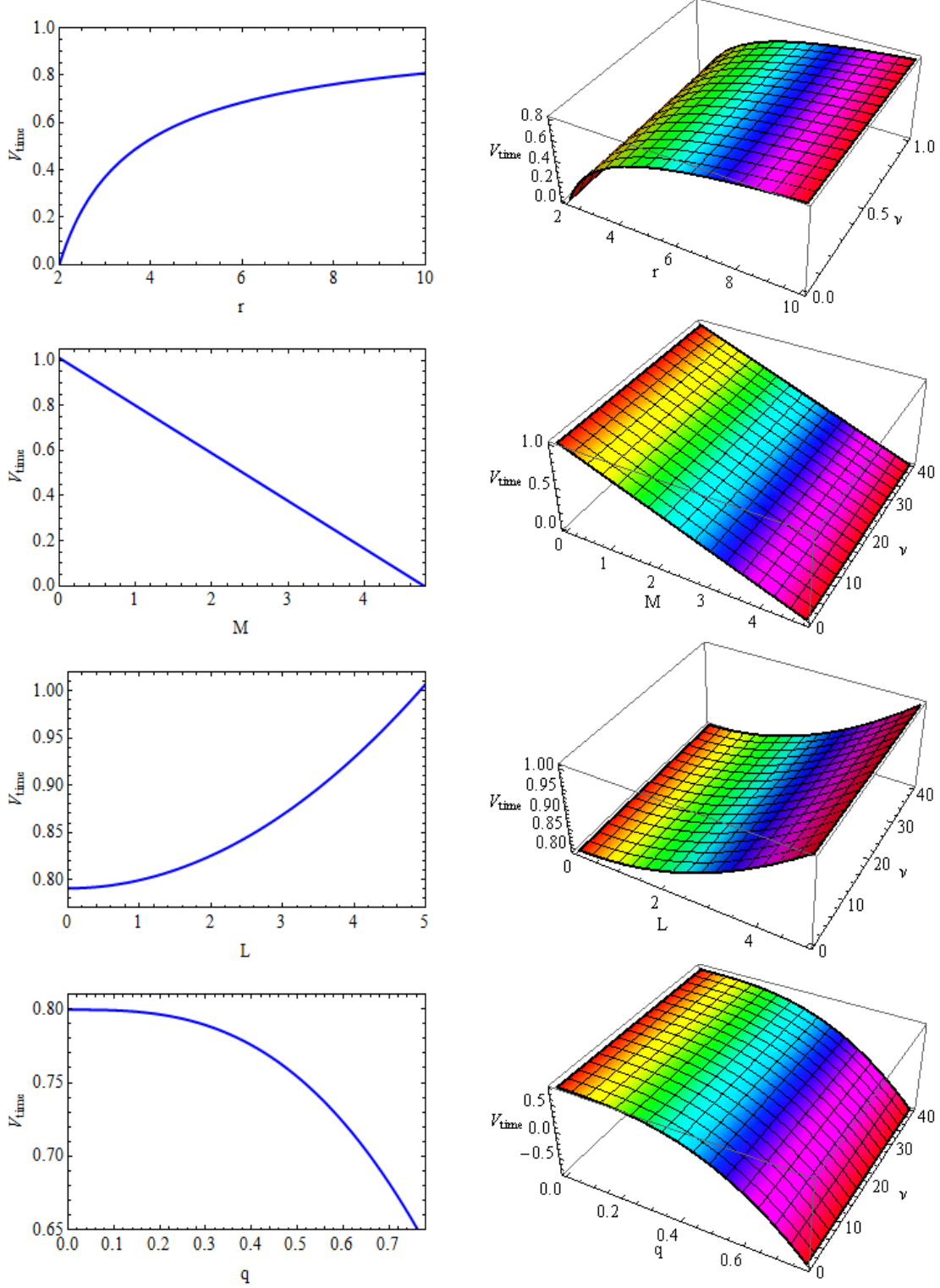


Figure 2.14: Plot of V_{time} versus r (first panel), M (second panel), L (third panel) and q (fourth panel) respectively. We have set $\mu = 3$.

2.8. Time-like Geodesics of Regular BHs

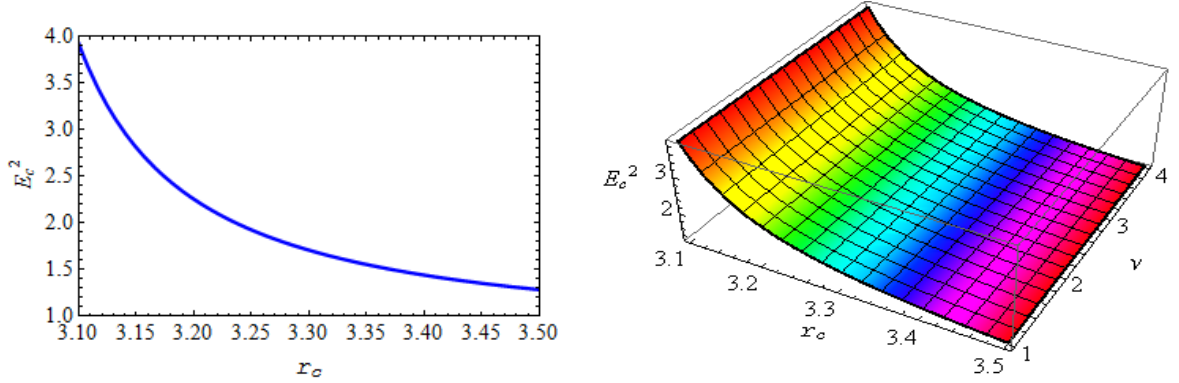


Figure 2.15: Plot of E_c^2 versus r_c for $M = 2$, $q = 0.05$, $\mu = 3$ and $\alpha = 0.5$. The left panel is plotted for $\nu = 1$ and right panel is plotted for values of ν in the range $0 \leq \nu \leq 4$.

To calculate the circular geodesics motion of the test particle, we will use the condition $\dot{r} = 0$ and $\dot{r}' = 0$ at $r = r_c$. From the Eqn. (2.65) we get

$$V_{time} = 0, \quad (2.68)$$

and

$$\frac{dV_{time}}{dr} = 0. \quad (2.69)$$

Hence the energy and angular momenta per unit mass of the test particle are as follows:

$$E_c^2 = \frac{(r_c^\nu + q^\nu)^{1-\frac{\mu}{\nu}} \left((r - 2M)(r_c^\nu + q^\nu)^{\frac{\mu}{\nu}} \alpha - 2q^3 r_c^\mu \right)^2}{r_c \alpha \left(r_c^\mu q^3 ((\mu - 3)q^\nu - 3r_c^\nu) + (r_c - 3M)(r_c^\nu + q^\nu)^{\frac{\mu+\nu}{\nu}} \alpha \right)}, \quad (2.70)$$

and

$$L_c^2 = \frac{r_c^2 \left(q^3 r_c^\mu (r_c^\nu - (\mu - 1)q^\nu) + M(r_c^\nu + q^\nu)^{\frac{\mu+\nu}{\nu}} \alpha \right)}{\left(r_c^\mu q^3 ((\mu - 3)q^\nu - 3r_c^\nu) + (r_c - 3M)(r_c^\nu + q^\nu)^{\frac{\mu+\nu}{\nu}} \alpha \right)}. \quad (2.71)$$

The 2D and 3D diagram of variation of energy (E_c) and angular momentum (L_c) along time-like circular geodesics could be seen from Fig. 2.15 and Fig. 2.16, respectively.

2. Null geodesics and QNMs in the field of regular black holes

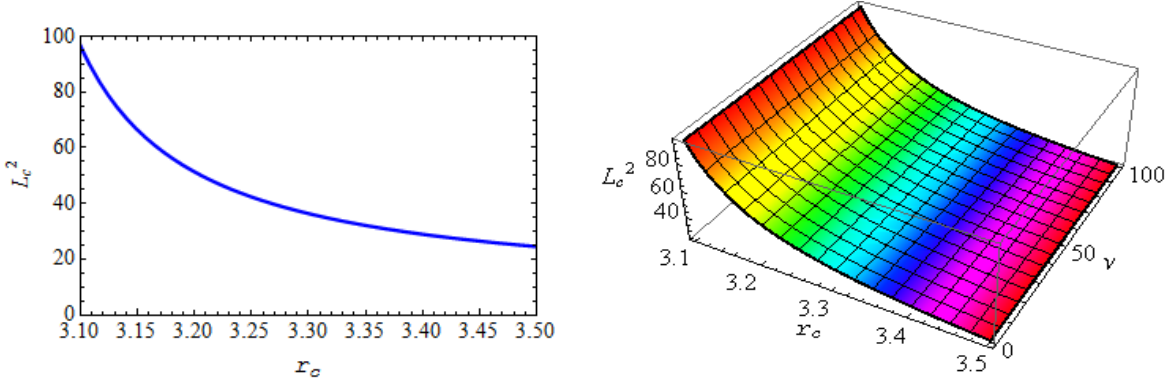


Figure 2.16: Plot of L_c^2 versus r_c for $M = 2$, $q = 0.05$, $\mu = 3$ and $\alpha = 0.5$. The left panel is graphed for $\nu = 1$ and right panel is graphed for values of ν in the range $0 \leq \nu \leq 100$.

To exist the circular motion of test particle, the energy and angular momentum must be real and finite.

Therefore we require,

$$\left(r^\mu q^3 ((\mu - 3)q^\nu - 3r^\nu) + (r - 3M)(r^\nu + q^\nu)^{\frac{\mu+\nu}{\nu}} \alpha \right) > 0,$$

and

$$\left(q^3 r^\mu (r^\nu - (\mu - 1)q^\nu) + M(r^\nu + q^\nu)^{\frac{\mu+\nu}{\nu}} \alpha \right) > 0.$$

The equality with limit indicates a circular orbit with diverging energy per unit rest mass, that is, a photon orbit. This photon orbit is the inner most boundary of the time-like circular orbits for particles.

The orbital velocity is given by

$$\Omega_c = \frac{\dot{\phi}}{\dot{t}} = \sqrt{\frac{M + q^3 r_c^\mu q^3 \alpha^{-1} (r_c^\nu + (1 - \mu)q^\nu)(r_c^\nu + q^\nu)^{(-\frac{\mu+\nu}{\nu})}}{r_c^3}}. \quad (2.72)$$

2.8.2 Marginally bound circular orbit (MBCO):

2.9. Conclusion and future work:

The equation of MBCO looks like

$$4M\alpha^2 r_c (r_c - M)(r_c^\nu + q^\nu)^{\frac{(\mu+\nu)}{\nu}} + 4\alpha(r_c - 2M)r_c^\mu q^3(r_c^\nu + q^\nu)^{\frac{\mu}{\nu}} - 4q^6 r_c^{2\mu}(r_c^\nu + q^\nu)^{\frac{(\nu-\mu)}{\nu}} + r_c^{\mu+1} q^3 \alpha((\mu - 3)q^\nu - 3r_c^\nu) = 0 \quad (2.73)$$

Let $r_c = r_{mb}$ be the solution of the above equation which gives the radius of MBCO close to the Regular BH.

2.8.3 Equation of ISCO:

The equation of innermost stable circular orbit (ISCO) can be obtained from the second derivative of the effective potential (V_{time}) of the time like geodesics, that is,

$$\frac{d^2 V_{time}}{dr^2} = 0. \quad (2.74)$$

Thus the equation of ISCO is

$$2r_c^{2\mu} q^6 s + r_c^\mu q^3 \alpha(r_c^\nu + q^\nu)^{\frac{\mu}{\nu}} (t + w) - M(r_c - 6M)(r_c^\nu + q^\nu)^{2\frac{(\mu+\nu)}{\nu}} \alpha^2 = 0, \quad (2.75)$$

where

$$\begin{aligned} s &= (\mu - 3)(\mu - 1)q^{2\nu} + (\mu(\nu - 4) + 6)r_c^\nu q^\nu + 3r_c^{2\nu}, \\ t &= r_c^{2\nu}(12M - r_c) - q^{2\nu}((\mu^2 + 4\mu - 6)2M + (1 - \mu^2)r_c), \\ w &= r_c^\nu q^\nu((\mu\nu - 4\mu + 12)2M - (2 + \mu\nu)r_c). \end{aligned} \quad (2.76)$$

Let $r_c = r_{ISCO}$ be the smallest real root of the Eq. (2.75) which gives the radius of the ISCO of the regular BH. When $q \rightarrow 0$, we obtain the radius of ISCO for Schwarzschild BH which occurs at $r_{ISCO} = 6M$. The 2D and 3D diagrams of variation of ISCO could be seen from Fig. 2.17.

2.9 Conclusion and future work:

We investigated the null geodesics of regular BHs. A complete geodesic study has been made both for time-like geodesics and null geodesics. Studies of test particle both for photon and massive particles as an interesting approach to understand the strong gravity around the BH spacetime. As an application of null geodesics, we derived the radius of photon sphere and gravitational bending of light. We also studied

2. Null geodesics and QNMs in the field of regular black holes

the shadow of the BH spacetime. Moreover, we showed the relation between radius of photon sphere (r_{ps}) and the shadow observed by a distance observer.

Using null-circular geodesics, we evaluated the celestial coordinates (β, γ) and the radius R_s of the regular BH shadow and presented it graphically. The effect of dimensionless constant μ of the BH, the free integration constant q and the other parameter (like α and ν) on the radius of shadow are studied in detail. In particular, the radius of BH shadow is increased with increasing value of ν and q while the radius is decreased with increasing value of the parameters α and μ respectively.

Moreover, we discussed the effect of various parameters on the radius of shadow R_s . Also we computed the angle of deflection for the photons as a physical application of null-circular geodesics. We determined the relation between null geodesics and quasinormal modes frequency in the eikonal approximation by computing the Lyapunov exponent. It was also shown that (in the eikonal limit) the quasinormal modes (QNMs) of BHs are governed by the parameter of null-circular geodesics. The real part of QNMs frequency determined the angular frequency whereas the imaginary part determined the instability time scale of the circular orbit.

Quite apart from the circular geodesics analogy, we determined the relation between unstable null-circular geodesics and QNMs, which is quite general and being valid for large limit for any spherically symmetric, static and asymptotically flat space-time. We showed that the QNMs in the eikonal limit of the BH are defined by the parameter of the null-circular geodesics. The real part of the complex QNMs frequencies is related to the angular velocity in the unstable null-circular geodesics and the imaginary part is determined by the instability timescale of the orbit. More specifically, we showed that the Lyapunov exponent and the angular velocity (Ω_o) at the unstable null circular geodesics, governing the instability timescale for the orbit admit with an analytic WKB approximation of QNMs.

Furthermore, we examined the massless scalar perturbations and analyzed the effective potential graphically. We also studied the massive scalar perturbations around the BH spacetime. As an application of time-like geodesics we computed the ISCO and MBCO of the regular BHs which was closely related to the BH accretion disk theory. In the appendix, we showed the relation between angular frequency and

2.9. Conclusion and future work:

Lyapunov exponent for null-circular geodesics.

Appendix : Angular frequency and Lyapunov exponent for null-circular geodesics

Angular frequency of regular BH is given by

$$\Omega_o = \frac{\dot{\phi}}{\dot{t}} = \sqrt{\frac{f'_o}{2r_o}} = \frac{f_o^{\frac{1}{2}}}{r_o}. \quad (2.77)$$

Using the equation (2.2), we obtain the angular frequency as follows

$$\Omega_o = \sqrt{\frac{M + q^3 r_o^\mu q^3 \alpha^{-1} (r_o^\nu + (1 - \mu)q^\nu)(r_o^\nu + q^\nu)^{(-\frac{\mu+\nu}{\nu})}}{r_o^3}}. \quad (2.78)$$

The Lyapunov exponent can be defined in terms of the second derivative of the effective potential for radial motion V_{null} of null-circular geodesics as

$$\lambda_o = \sqrt{\frac{(V_{null})''}{2\dot{t}^2}}. \quad (2.79)$$

Using the equation (2.79) the Lyapunov exponent for null circular geodesics is given by

$$\lambda_o = \frac{\sqrt{\left((r_o - 2M)(r_o^\nu + q^\nu)^{\frac{\mu}{\nu}} \alpha - 2q^3 r_o^\mu \right) \left(r_o \alpha (r_o^\nu + q^\nu)^{2+\frac{\mu}{\nu}} + \mu q^{(3+\nu)} r_o^\mu (3q^\nu (\nu - 3) - r_o^\nu (\nu + 3)) \right)}}{r_o^2 \alpha (r_o^\nu + q^\nu)^{\frac{\mu+\nu}{\nu}}}.$$

We have plotted the graph λ_o against r_o in the Fig. 2.18. From the Fig. 2.18 it is clear that λ_o increases for the initial.

2. Null geodesics and QNMs in the field of regular black holes

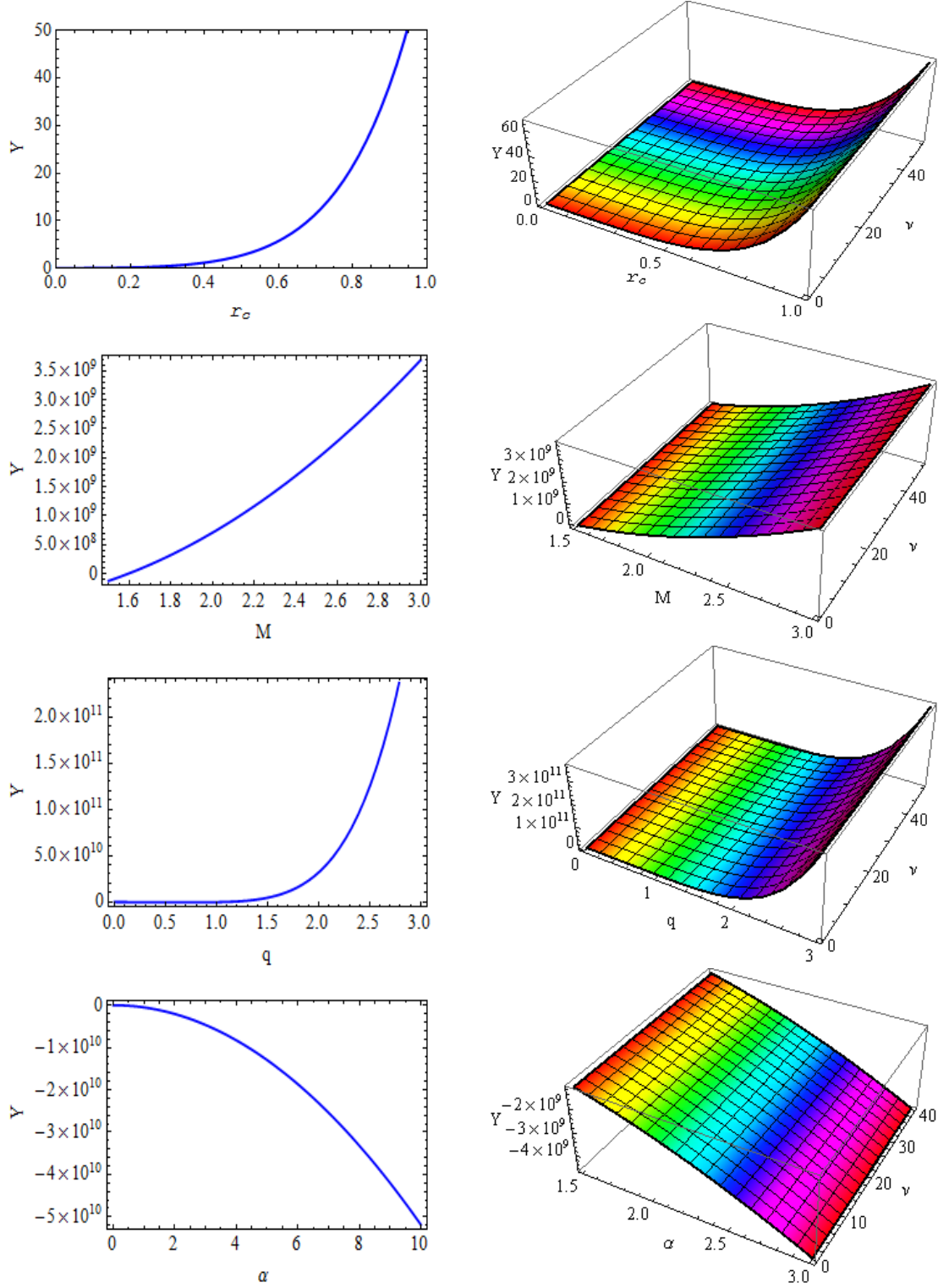


Figure 2.17: The figure depicts the variation of $Y = 2r_c^{2\mu}q^6s + r_c^\mu q^3\alpha(r_c^\nu + q^\nu)^\frac{\mu}{\nu}(t + w) - M(r_c - 6M)(r_c^\nu + q^\nu)^{2(\frac{\mu+\nu}{\nu})}\alpha^2$ versus r_c (first panel), M (second panel), q (third panel) and α (fourth panel) respectively. We have set $\mu = 3$.

2.9. Conclusion and future work:

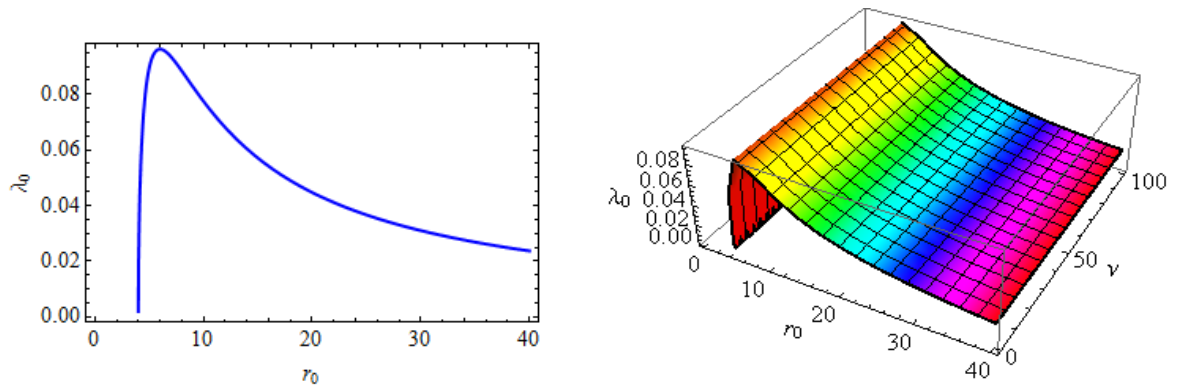


Figure 2.18: Plot of λ_0 versus r_0 for $M = 2$, $q = 0.05$, $\mu = 3$ and $\alpha = 0.5$. The left panel is graphed for $\nu = 1$ and right panel is graphed for values of ν in the range $0 \leq \nu \leq 100$.

Chapter 3

Geodesic stability and quasi normal modes via Lyapunov exponent for Hayward black hole ¹

3.1 Introduction

An elementary set of unstable circular orbits about a Schwarzschild black hole (BH) are consequences of the non-linearity of general theory of relativity. Their instability could be measured by a positive Lyapunov exponent ([Cornish \[2001\]](#)). Albeit the Lyapunov exponent are often related with chaotic dynamics ([Motter \[2003\]](#), [Dorfman \[1999\]](#)), the geodesics about a Schwarzschild BH are not chaotic; the orbits are completely solvable and hence integrable. The unstable geodesic orbits should have positive Lyapunov exponent ([Lyapunov \[1992\]](#)), which has the invariant properties first established in ([Karas and Vokrouhlický \[1992\]](#)). Lyapunov exponent has a great impact on general relativity for its numerous applications: they are relative and depend on the coordinate system used, they vary from orbit to orbit. In this work, we are interested to focus on analytical formulation of Lyapunov exponent and QNMs in terms of the expressions of the radial equation of circular geodesics about a BH space-time. In this regard an equatorial circular geodesics about a BH may play

¹A considerable part of this chapter has been published in **Modern Physics Letters A** **2050249** (2020).

3. Geodesic stability and quasi normal modes via Lyapunov exponent for Hayward black hole

crucial role in general theory of relativity for classification of the orbits.

Black holes and singularities are approached to be unavoidable predictions of the theory of general relativity (GR). In order to solve the black hole singularity, several phenomenological propositions have been studied in the existing literatures. Bardeen Black hole was the first model that has proposed as a spherically symmetric compact object with an event horizon and satisfying the weak energy condition. In the year 2006, Hayward ([Hayward \[2006\]](#)) proposed the formation and evaporation of a new kind of regular solution in space-time. The static region of a Hayward space-time is similar to Bardeen black hole. In the article ([Lin et al. \[2013\]](#)), the authors discussed the massive scalar quasinormal modes of the Hayward black hole. In this study, variations of the Hayward solutions have also been studied as Hayward with charge ([Frolov \[2016\]](#)) and Rotating Hayward ([Amir and Ghosh \[2015\]](#)).

The authors in ([Cardoso et al. \[2009\]](#), [Cardoso and Lemos \[2003\]](#), [Sperhake et al. \[2008\]](#)) derived the Lyapunov exponent to study the instability for the circular null geodesics in terms of the expressions for QNM of spherically symmetric space-time. Here, the main focus is on the null circular geodesics, which play an important role for the Lyapunov exponent. The null circular geodesics is described by the shortest possible orbital period as estimated by the asymptotic observers ([Hod \[2011\]](#)). The time circular geodesics provide the slowest way to circle the BH, among all the possible circular geodesics.

The QNMs spectrum for stable BH represents an infinite set of complex frequencies, which designates damped oscillations for the amplitude. It is clear that the oscillations with lower level of damping rate is controlled with slow time, whereas oscillations with higher level of damping rate are exponentially terminated ([Konoplya and Zhidenko \[2011\]](#)). In 1971, Press ([Press \[1971\]](#)), first introduced the term ‘quasi-normal frequency’. He showed that when a Schwarzschild BH is perturbed it vibrates with an angular frequency $\omega = \frac{\ell}{\sqrt{27}M}$. Where M is BH mass and ℓ is spherically symmetric index. He then interpreted it as vibration frequency of BHs. In the same year the lowest QNMs were computed by investigating test particle falling about Schwarzschild BH. So far the QNMs has been explored substantially in diverse field. The WKB method gives an exact estimation of QNM frequency in the eikonal limit. Also WKB method was first introduced by Schutz and Will ([Schutz and Will \[1985\]](#)) to analyze the problem of scattering about BH.

The plan of the chapter is as follows: in section 3.2, we derive a formula for the proper

3.1. Introduction

time Lyapunov ¹ exponent λ_p and coordinate time Lyapunov exponent λ_c in terms of second order derivative of the effective potential for the radial motion \dot{r}^2 :

$$\lambda_p = \pm \sqrt{\frac{(\dot{r}^2)''}{2}}, \quad (3.1)$$

$$\lambda_c = \pm \sqrt{\frac{(\dot{r}^2)''}{2\dot{t}^2}}. \quad (3.2)$$

In section 3.3, we describe the equatorial circular geodesics of spherically symmetric regular Hayward BH. Then we calculate the Lyapunov exponent in terms of the timelike circular geodesics and null circular geodesics. We also discuss the gravitational bending of light and photon sphere for this BH.

In section 3.4, we derive the relation between QNMs in the eikonal limit and Lyapunov exponent of a static, spherically symmetric regular Hayward BH. In the limit $l = 0$, one obtains the QNMs frequency of spherically-symmetric Schwarzschild BH which was first calculated in Pradhan and Majumdar [2011].

Moreover we compute the angular velocity Ω_c of the unstable null geodesics. Also, we compute the Lyapunov exponent, which investigates the instability of the time-scale of circular orbit (Cornish and Levin [2003], Bombelli and Calzetta [1992], Manna et al. [2020]) also which is in agreement with analytic WKB approximations of QNMs of the Hayward BH in the eikonal limit. Thus the QNMs frequency in the eikonal limit is found to be

$$\omega_{QNM} = j \left(\frac{\sqrt{m(r_c^3 - 4ml^2)}}{(r_c^3 + 2ml^2)} \right) - i \left(n + \frac{1}{2} \right) \sqrt{\frac{3m^2[r_c^5 - 6l^2(r_c^3 - 2ml^2)]}{(r_c^3 + 2ml^2)^3}}, \quad (3.3)$$

where, n represents the overtone number and j represents the angular momentum of the perturbation.

For schwarzschild BH, the QNMs frequency becomes

$$\omega_{QNM} = j \sqrt{\frac{m}{r_c^3}} - i \left(n + \frac{1}{2} \right) \frac{\sqrt{3}m}{r_c^2}. \quad (3.4)$$

The real part of the complex QNM frequency can be determined by the angular veloc-

¹Since the Lyapunov exponent is explicitly coordinate dependent and therefore have a degree of un-physicality. That's why we define two types of Lyapunov exponent. One is coordinate type Lyapunov exponent and the other one is proper time Lyapunov exponent. This is strictly for timelike geodesics.

3. Geodesic stability and quasi normal modes via Lyapunov exponent for Hayward black hole

ity of the unstable null geodesics and the imaginary part is related to the instability time scale of the orbit. Finally, we briefly discuss about the outcome of this chapter in section 3.5.

3.2 Proper time Lyapunov exponent, Coordinate time Lyapunov exponent and Geodesic stability

The Lyapunov exponent or Lyapunov characteristic exponent of a dynamical system is a measure of the average rate of expansion and contraction of adjacent trajectories in the phase space. A negative Lyapunov exponent designates the convergence between nearby trajectories. A positive Lyapunov exponent determines the divergence between nearby geodesics in which the path of such a system are the most active to change the starting circumstances. The vanishing Lyapunov exponent designates the existence of marginal stability. The equation of motion in terms of Lyapunov exponents for geodesic stability analysis should be written as

$$\frac{dZ_i}{dt} = F_i(Z_j), \quad (3.5)$$

and its linearized form around a certain orbit is

$$\frac{d\delta Z_i(t)}{dt} = A_{ij}(t)\delta Z_j(t). \quad (3.6)$$

Here,

$$A_{ij}(t) = \left. \frac{\partial F_i}{\partial Z_j} \right|_{Z_i(t)}, \quad (3.7)$$

represents the linear stability matrix ([Cornish and Levin \[2003\]](#)). Now, the solution of the Eqn. (2) can be written as

$$\delta Z_i(t) = X_{ij}(t)\delta Z_j(0), \quad (3.8)$$

3.2. Proper time Lyapunov exponent, Coordinate time Lyapunov exponent and Geodesic stability

where, $X_{ij}(t)$ represents the evolution matrix, which leads to

$$\dot{X}_{ij}(t) = A_{im}X_{mj}(t), \quad (3.9)$$

with $X_{ij}(0) = \delta_{ij}$. The principal Lyapunov exponent λ can be expressed in terms of the eigenvalues X_{ij} as follows:

$$\lambda = \lim_{t \rightarrow \infty} \frac{1}{t} \log \left(\frac{X_{ij}(t)}{X_{mj}(0)} \right). \quad (3.10)$$

If there exists a set of n Lyapunov exponents connected with an n -dimensional independent system, then they can be arranged by the size as

$$\lambda_1 \geq \lambda_2 \geq \lambda_3 \geq \dots, \geq \lambda_n. \quad (3.11)$$

The set of n numbers of λ_i are known as Lyapunov spectrum.

In an equatorial plane, for any static spherically symmetric space-time, the Lagrangian of a test particle can be written as

$$\mathcal{L} = \frac{1}{2} \left[g_{tt} \dot{t}^2 + g_{rr} \dot{r}^2 + g_{\phi\phi} \dot{\phi}^2 \right]. \quad (3.12)$$

From the above expression, the canonical momenta can be derived as

$$p_q = \frac{\partial \mathcal{L}}{\partial \dot{q}}. \quad (3.13)$$

The generalized momenta derived from the above Lagrangian are

$$p_t = g_{tt} \dot{t} = -E = \text{Const}, \quad (3.14)$$

$$p_\phi = g_{\phi\phi} \dot{\phi} = L = \text{Const}, \quad (3.15)$$

$$p_r = g_{rr} \dot{r}. \quad (3.16)$$

Here, ‘dot’ represents the differentiation with respect to proper time (τ). E and L are the energy and angular momentum per unit rest mass of the test particle, respectively.

3. Geodesic stability and quasi normal modes via Lyapunov exponent for Hayward black hole

Now, from Euler-Lagrange's equation of motion, we can write

$$\frac{dp_q}{d\tau} = \frac{\delta\mathcal{L}}{\delta q}. \quad (3.17)$$

Linearizing the above equation of motion in two-dimensional phase space with respect to $Z_i(t) = (p_r, r)$, around the circular orbit (taking r as a constant), we get

$$\frac{dp_r}{d\tau} = \frac{\partial\mathcal{L}}{\partial q} \quad \text{and} \quad \frac{dr}{d\tau} = \frac{p_r}{g_{rr}}, \quad (3.18)$$

and an infinitesimal evolutionary matrix can be expressed as

$$A_{ij} = \begin{pmatrix} 0 & A_1 \\ A_2 & 0 \end{pmatrix}, \quad (3.19)$$

where

$$A_1 = \frac{d}{dr} \left(\dot{t}^{-1} \frac{\delta\mathcal{L}}{\delta r} \right), \quad (3.20)$$

$$A_2 = -(\dot{t}g_{rr})^{-1}. \quad (3.21)$$

For the case of circular orbit, the eigenvalues of the matrix are called principal Lyapunov exponent which can be written as

$$\lambda^2 = A_1 A_2. \quad (3.22)$$

Then the Lagrange's equation of motion leads to

$$\frac{d}{d\tau} \left(\frac{\partial\mathcal{L}}{\partial\dot{r}} \right) - \frac{\partial\mathcal{L}}{\partial r} = 0, \quad (3.23)$$

and

$$\frac{d}{d\tau} \left(\frac{\partial\mathcal{L}}{\partial\dot{r}} \right) = \frac{d}{d\tau} (-g_{rr}\dot{r}) = -\dot{r} \frac{d}{dr} (-g_{rr}\dot{r}). \quad (3.24)$$

Thus, the Lyapunov exponent in terms of square of radial velocity \dot{r}^2 , can be expressed

3.2. Proper time Lyapunov exponent, Coordinate time Lyapunov exponent and Geodesic stability

as

$$\begin{aligned}\frac{\partial \mathcal{L}}{\partial r} &= \frac{d}{dr}(-\dot{r}g_{rr})^2 \\ &= -\frac{1}{2g_{rr}}\frac{d}{dr}(\dot{r}^2 g_{rr}^2).\end{aligned}\tag{3.25}$$

Finally, from (3.22) and (3.25), the principal Lyapunov exponent can be written as

$$\lambda^2 = \frac{1}{2} \frac{1}{g_{rr}} \frac{d}{dr} \left[\frac{1}{g_{rr}} \frac{d}{dr} (\dot{r} g_{rr})^2 \right].\tag{3.26}$$

For the case of circular geodesics (Chandrasekhar [1998]), we have

$$\dot{r}^2 = (\dot{r}^2)' = 0,\tag{3.27}$$

where, \dot{r}^2 is the square of radial potential or effective radial potential. From (3.26), we can obtain the proper time Lyapunov exponent as

$$\lambda_p = \pm \sqrt{\frac{(\dot{r}^2)''}{2}},\tag{3.28}$$

and the coordinate time Lyapunov (Cardoso et al. [2009]) can be derived from (3.26) as follows

$$\lambda_c = \pm \sqrt{\frac{(\dot{r}^2)''}{2\dot{t}^2}}.\tag{3.29}$$

The above Eqns. (3.28) and (3.29) for λ_p and λ_c are respectively satisfied for any spherically symmetric BH space-times (Pradhan and Majumdar [2011], Pugliese et al. [2011], Setare and Momeni [2011]). Now, we shall drop the \pm sign and consider only positive Lyapunov exponent. The circular orbit is stable when λ is imaginary, the circular orbit is unstable when λ is real and for $\lambda = 0$, the circular orbit becomes marginally stable or saddle point.

Due to Pretorius and Khurana (Pretorius and Khurana [2007]), we can define the critical exponent as

$$\gamma = \frac{\Omega}{2\pi\lambda} = \frac{T_\lambda}{T_\Omega},\tag{3.30}$$

3. Geodesic stability and quasi normal modes via Lyapunov exponent for Hayward black hole

where T_λ represents the Lyapunov time scale, T_Ω represents the orbital time scale and Ω represent the angular velocity, where $T_\lambda = \frac{1}{\lambda}$ and $T_\Omega = \frac{2\pi}{\Omega}$. Now, the critical exponent can be written in terms of second order derivative of the square of radial velocity (\dot{r}^2), as

$$\gamma_p = \frac{1}{2\pi} \sqrt{\frac{2\Omega^2}{(\dot{r}^2)''}}, \quad (3.31)$$

$$\gamma_c = \frac{1}{2\pi} \sqrt{\frac{2\dot{\phi}^2}{(\dot{r}^2)''}}. \quad (3.32)$$

Here, ϕ is an angular coordinate. For circular geodesics $(\dot{r}^2)'' > 0$, which implies instability. Now, we shall determine the equatorial circular geodesics of Hayward space-time.

3.3 Equatorial Circular Geodesics in Spherically Symmetric metric Hayward Space-time

In this paper, the metric ([Hayward \[2006\]](#)) for a static, spherically symmetric space-time can be taken as follows

$$ds^2 = -f(r)dt^2 + \frac{dr^2}{f(r)} + r^2(d\theta^2 + \sin^2\theta d\phi^2), \quad (3.33)$$

where

$$f(r) = \left(1 - \frac{2mr^2}{r^3 + 2l^2m}\right). \quad (3.34)$$

Here, the parameters l and m are positive constants. This is similar to the Bardeen BH, which can be reduced to the Schwarzschild solution for $l = 0$, and become flat space-time for $m = 0$.

The function $f(r)$ is plotted in Fig. [3.1](#). One can observe that the geometry is similar to the Schwarzschild BH with a single horizon. Also there could be a single, double or no horizon which depends on the relation between the parameters.

3.3. Equatorial Circular Geodesics in Spherically Symmetric metric Hayward Space-time

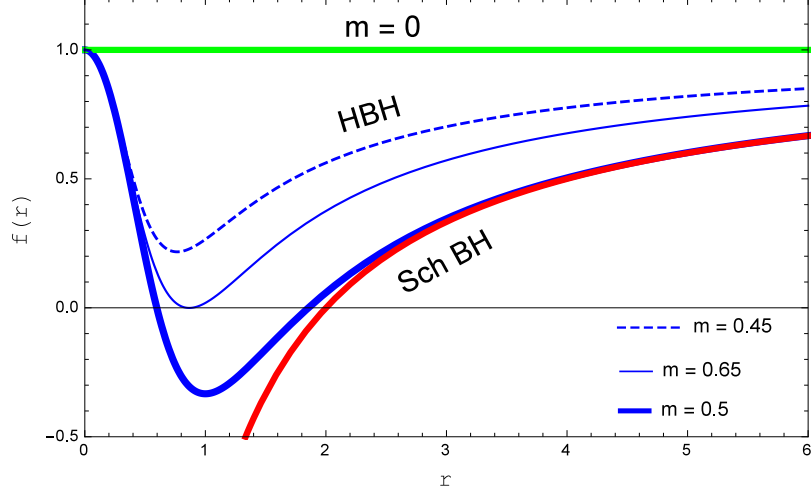


Figure 3.1: The figure shows the $f(r)$ versus r . Here, $l = 0.5$ for Hayward BH

3.3.1 Circular orbits

To calculate the geodesics in an equatorial plane for space-time of (3.33), we follow the work of Chandrasekhar (Chandrasekhar [1998]). In an equatorial plane, we set $\dot{\theta} = 0$ and $\theta = \frac{\pi}{2} = \text{constant}$. Here, we restrict our attention to the equatorial orbits, for which the Lagrangian is given by

$$2\mathcal{L} = \left[- \left(1 - \frac{2mr^2}{r^3 + 2l^2m} \right) \dot{t}^2 + \frac{\dot{r}^2}{\left(1 - \frac{2mr^2}{r^3 + 2l^2m} \right)} + r^2 \dot{\phi}^2 \right], \quad (3.35)$$

where, ϕ represents an angular coordinate. By using (3.13), the generalized momenta can be represented as

$$p_t = - \left(1 - \frac{2mr^2}{r^3 + 2l^2m} \right) \dot{t} = -E = \text{const}, \quad (3.36)$$

$$p_\phi = r^2 \dot{\phi} = L = \text{const}, \quad (3.37)$$

$$p_r = \frac{\dot{r}}{\left(1 - \frac{2mr^2}{r^3 + 2l^2m} \right)}. \quad (3.38)$$

The Lagrangian is independent on both t and ϕ , so p_t and p_ϕ are the conserved

3. Geodesic stability and quasi normal modes via Lyapunov exponent for Hayward black hole

quantities. Solving Eqns. (3.36) and (3.37) for \dot{t} and $\dot{\phi}$, we get

$$\dot{t} = \frac{E}{\left(1 - \frac{2mr^2}{r^3 + 2l^2m}\right)} \quad \text{and} \quad \dot{\phi} = \frac{L}{r^2}. \quad (3.39)$$

The normalization of the four velocity vector (u^α) can be represented as an integral equation for the geodesic motion

$$g_{\alpha\beta}u^\alpha u^\beta = \xi, \quad (3.40)$$

which is equivalent to

$$-E\dot{t} + L\dot{\phi} + \frac{\dot{r}^2}{\left(1 - \frac{2mr^2}{r^3 + 2l^2m}\right)} = \xi. \quad (3.41)$$

Here, $\xi = -1, 0, 1$, represents the time-like geodesics, null geodesics and space-like geodesics, respectively. Replacing the values of \dot{t} and $\dot{\phi}$ from (3.39) in (3.41), we obtain the radial equation for spherically symmetric space-time:

$$\dot{r}^2 = E^2 - \left(\frac{L^2}{r^2} - \xi\right) \left(1 - \frac{2mr^2}{r^3 + 2l^2m}\right). \quad (3.42)$$

3.3.1.1 Time-like geodesics

The radial equation of test particle for time-like circular geodesics (Pradhan [2016], Pretorius and Khurana [2007]) is given by

$$\dot{r}^2 = E^2 - \left(1 + \frac{L^2}{r^2}\right) \left(1 - \frac{2mr^2}{r^3 + 2l^2m}\right). \quad (3.43)$$

For circular orbit with constant $r = r_\sigma$ and using the condition (3.27), we get the energy and angular momentum per unit mass of the test particle are

$$E_\sigma^2 = \frac{(r_\sigma^3 + 2l^2m - 2mr_\sigma^2)^2}{(r_\sigma^3 + 2l^2m)^2 - 3mr_\sigma^5}, \quad (3.44)$$

$$L_\sigma^2 = \frac{mr_\sigma^4(r_\sigma^3 - 4l^2m)}{(r_\sigma^3 + 2l^2m)^2 - 3mr_\sigma^5}. \quad (3.45)$$

3.3. Equatorial Circular Geodesics in Spherically Symmetric metric Hayward Space-time

In order to obtain the energy and angular momentum real and finite, the conditions $(r_\sigma^3 + 2l^2m)^2 > 3mr_\sigma^5$ and $mr_\sigma^4(r_\sigma^3 - 4l^2m) > 0$ must be satisfied. Thus the orbital velocity becomes

$$\Omega_\sigma = \frac{\dot{\phi}}{\dot{t}} = \frac{\sqrt{m(r_\sigma^3 - 4l^2m)}}{r_\sigma^3 + 2l^2m}. \quad (3.46)$$

3.3.1.2 Null geodesics

In case of null geodesics, there is no proper time for photons. Thus, we have to calculate only the coordinate time Lyapunov exponent. The radial equation of the test particle for null circular geodesics is

$$\dot{r}^2 = V_{ef} = E^2 - \frac{L^2}{r^2} \left(1 - \frac{2mr^2}{r^3 + 2l^2m} \right). \quad (3.47)$$

The comparison between the Hayward BH and Schwarzschild BH effective potentials are shown in Fig. 3.2 for null-circular geodesics. Fig. 3.2 shows that the effective potential of Hayward BH is smallest compared to Schwarzschild BH.

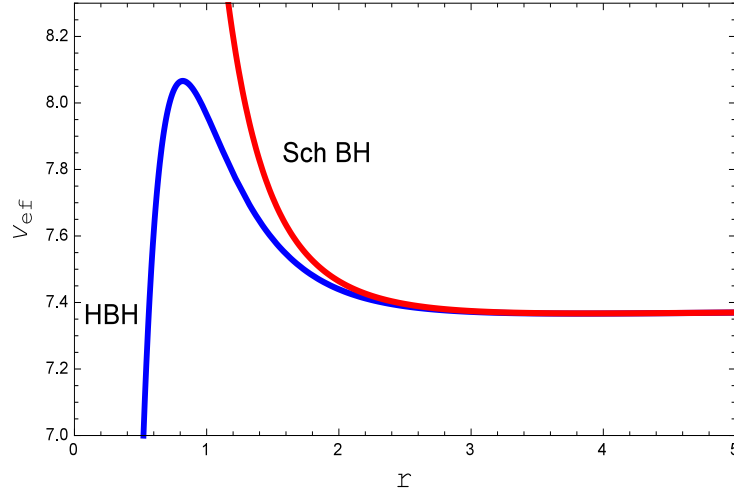


Figure 3.2: The effective potential V_{ef} , for null-circular geodesics in Hayward BH and in Schwarzschild BH is compared. The constants are with $m = 1, L = 1, E = 1$ and for HBH $l = 0.5$.

3. Geodesic stability and quasi normal modes via Lyapunov exponent for Hayward black hole

Now, the energy and angular momentum at $r = r_c$, for the null geodesics is

$$\frac{E_c}{L_c} = \pm \sqrt{\frac{(r_c^3 + 2l^2m - 2mr_c^2)}{r_c^2(r_c^3 + 2l^2m)}} \quad \text{and} \quad (r_c^3 + 2l^2m)^2 - 3mr_c^5 = 0. \quad (3.48)$$

Let $D_c = \frac{L_c}{E_c}$ be the impact parameter, then the equation (3.48) reduces to

$$\frac{1}{D_c} = \frac{E_c}{L_c} = \frac{\sqrt{m(r_c^3 - 4l^2m)}}{(r_c^3 + 2l^2m)} = \Omega_c = \frac{\dot{\phi}}{\dot{t}}. \quad (3.49)$$

3.3.2 Bending of light

A unstable circular photon orbit is called ‘‘Photon Sphere’’. The unstable photon sphere constitutes the shadow of the BH. From Eqn. (3.37) and Eqn. (3.38) we find

$$\frac{dr}{d\phi} = \frac{\dot{r}}{\dot{\phi}} = \frac{p_r \left(1 - \frac{2mr^2}{r^3 + 2l^2m}\right) r^2}{L}. \quad (3.50)$$

Again the Eqn. (3.47) can be written as

$$p_r^2 \left(1 - \frac{2mr^2}{r^3 + 2l^2m}\right) = \frac{E^2}{\left(1 - \frac{2mr^2}{r^3 + 2l^2m}\right)} - \frac{L^2}{r^2}. \quad (3.51)$$

We can obtain p_r from above equation as

$$p_r = \pm \sqrt{\frac{1}{\left(1 - \frac{2mr^2}{r^3 + 2l^2m}\right)}} \sqrt{\frac{E^2}{\left(1 - \frac{2mr^2}{r^3 + 2l^2m}\right)} - \frac{L^2}{r^2}}. \quad (3.52)$$

Using p_r from Eqn. (3.52), we can write the Eqn. (3.50) as follows

$$\frac{dr}{d\phi} = \pm \sqrt{r^2 \left(1 - \frac{2mr^2}{r^3 + 2l^2m}\right)} \sqrt{\frac{E^2}{L^2} \chi^2(r) - 1}, \quad (3.53)$$

where,

$$\chi^2(r) = \frac{r^2}{\left(1 - \frac{2mr^2}{r^3 + 2l^2m}\right)}. \quad (3.54)$$

3.3. Equatorial Circular Geodesics in Spherically Symmetric metric Hayward Space-time

A light ray which comes in from infinity, reaches at minimum radius R and again goes back to infinity, the bending angle ($\beta_{bending}$) is given by the formula

$$\beta_{bending} = -\pi + 2 \int_R^\infty \frac{dr}{\sqrt{r^2 \left(1 - \frac{2mr^2}{r^3 + 2l^2 m}\right) \left(\frac{E^2}{L^2} \chi^2(r) - 1\right)}}. \quad (3.55)$$

Since R is the turning point of the trajectory, the condition $\frac{dr}{d\phi}|_{R=0}$ must be hold. Which implies the following equation

$$\chi^2(R) = \frac{L^2}{E^2}. \quad (3.56)$$

Then the deflection angle can be written in terms of R as

$$\beta_{bending} = -\pi + 2 \int_R^\infty \frac{dr}{\sqrt{r^2 \left(1 - \frac{2mr^2}{r^3 + 2l^2 m}\right) \left(\frac{\chi^2(r)}{\chi^2(R)} - 1\right)}}. \quad (3.57)$$

After putting the value of $\chi^2(r)$ and $\chi^2(R)$, the equation of bending angle of Hayward BH is

$$\beta_{bending} = -\pi + 2 \int_R^\infty \frac{dr}{\sqrt{r^2 \left(1 - \frac{2mr^2}{r^3 + 2l^2 m}\right) \left(\frac{r^2}{D^2 \left(1 - \frac{2mr^2}{r^3 + 2l^2 m}\right)} - 1\right)}}, \quad (3.58)$$

where, $D = \frac{L}{E}$ is the impact parameter of the Hayward BH. The exact formula of bending angle is derived in [Chiba and Kimura \[2017\]](#).

3.3.2.1 Radius of the Shadow

A circular light orbits corresponds to zero velocity and acceleration, so that $\dot{r} = 0$ and $\ddot{r} = 0$, implies that $p_r = 0$ and $\dot{p}_r = 0$. From Eqn. (3.51) we obtain

$$\frac{E^2}{\left(1 - \frac{2mr^2}{r^3 + 2l^2 m}\right)} - \frac{L^2}{r^2} = 0. \quad (3.59)$$

Now differentiating Eqn. (3.51) with respect to affine parameter and putting the

3. Geodesic stability and quasi normal modes via Lyapunov exponent for Hayward black hole

value of $p_r = 0$ and $\dot{p}_r = 0$ we have

$$\frac{E^2(8m^2l^2r - 2mr^4)}{(r^3 + 2l^2m - 2mr^2)^2} + \frac{2L^2}{r^3} = 0. \quad (3.60)$$

From equations (3.59) and (3.60) we have

$$L^2 = \frac{r^2 E^2(r^3 + 2l^2m)}{(r^3 + 2l^2m - 2mr^2)^2} = \frac{r^3 E^2(2mr^4 - 8m^2l^2r)}{2(r^3 + 2l^2m - 2mr^2)^2}. \quad (3.61)$$

Subtracting these two equations and after some simplification we can obtain an equation for radius of the circular light orbit in the following form

$$\frac{d}{dr}\chi^2(r) = 0 \quad (3.62)$$

Hence, from Eqn. (3.62), the equation of photon sphere is at $r = r_c$

$$r_c^6 - 3mr_c^5 + 4ml^2r_c^3 + 4m^2l^4 = 0. \quad (3.63)$$

Let $r_{ps} = r_c$ be the real root of the equation then r_{ps} is the radius of circular photon sphere. Let R be the critical value of the minimum radius. Then we can write R in terms of r_{ps} as follows

$$R = \frac{r_{ps}^2(r_{ps}^3 + 2l^2m)}{(r_{ps}^3 + 2l^2m - 2mr_{ps}^2)}. \quad (3.64)$$

Here, we consider a light ray which is send from the observer's position at r_c into the past under an angle β with respect to the radial direction. Therefore, we have

$$\cot \beta = \frac{1}{\sqrt{r^2 \left(1 - \frac{2mr^2}{r^3 + 2l^2m}\right)}} \frac{dr}{d\phi} \Big|_{R=0}. \quad (3.65)$$

Again from Eqn. (3.53) we have

$$\frac{dr}{d\phi} = \pm \sqrt{r^2 \left(1 - \frac{2mr^2}{r^3 + 2l^2m}\right)} \sqrt{\frac{\chi^2(r)}{\chi^2(R)} - 1}. \quad (3.66)$$

3.3. Equatorial Circular Geodesics in Spherically Symmetric metric Hayward Space-time

For the angle β we have

$$\cot^2 \beta = \frac{\chi^2(r_c)}{\chi^2(R)} - 1, \quad (3.67)$$

and

$$\sin^2 \beta = \frac{\chi^2(R)}{\chi^2(r_c)} = \frac{D_c^2(r_c^3 + 2l^2m - 2mr_c^2)}{r_c^2(r_c^3 + 2l^2m)}. \quad (3.68)$$

The boundary of Shadow β_{shadow} is described by light rays which spiral asymptotically towards a circular light orbit at radius r_{ps} . Then the angular radius of the shadow is given by

$$\sin^2 \beta_{shadow} = \frac{\chi^2(r_{ps})}{\chi^2(r_c)} = \frac{r_{ps}^2(r_{ps}^3 + 2l^2m - 2mr_{ps}^2)(r_c^3 + 2l^2m)}{r_c^2(r_c^3 + 2l^2m - 2mr_c^2)(r_{ps}^3 + 2l^2m)}, \quad (3.69)$$

where, r_{ps} has to be determined from the equation (3.63).

3.3.3 Lyapunov exponent

3.3.3.1 Time-like case

Using Eqns. (3.28) and (3.29), the proper time Lyapunov exponent and coordinate time Lyapunov exponent becomes

$$\lambda_p = \sqrt{\frac{-m[r_\sigma^5(r_\sigma - 6m) + 22ml^2r_\sigma^3 - 32l^4m^2]}{(r_\sigma^3 + 2l^2m)[(r_\sigma^3 + 2ml^2)^2 - 3mr_\sigma^5]}}, \quad (3.70)$$

$$\lambda_c = \sqrt{\frac{-m(r_\sigma^5(r_\sigma - 6m) + 22ml^2r_\sigma^3 - 32l^4m^2)}{(r_\sigma^3 + 2ml^2)^3}}. \quad (3.71)$$

The time-like circular geodesics is stable when $r_\sigma^5(r_\sigma - 6m) + 22l^2mr_\sigma^3 - 32l^4m^2 > 0$, that is, λ_p and λ_c become imaginary. The time-like circular geodesics is unstable when $r_\sigma^5(r_\sigma - 6m) + 22l^2mr_\sigma^3 - 32l^4m^2 < 0$, that is, λ_p and λ_c become real and the time-like circular geodesics is marginally stable when $r_\sigma^5(r_\sigma - 6m) + 22ml^2r_\sigma^3 - 32l^4m^2 = 0$, that is, λ_p and λ_c becomes zero.

Now one can analyze the equation $r_\sigma^6 - 6mr_\sigma^5 + 22ml^2r_\sigma^3 - 32l^4m^2 = 0$ which gives us the radii of innermost stable circular orbit. Since it is a non-trivial equation. One can determine its root numerically for various values of l . For example if we choose

3. Geodesic stability and quasi normal modes via Lyapunov exponent for Hayward black hole

the value of $l = 1$ then one obtains the ISCO radius at $r_{isco} = 5.19m$. For $l = 2$, we find ISCO radius is at $r_{isco} = 1.91m$.

The ratio of proper time and coordinate time Lyapunov exponent is

$$\frac{\lambda_p}{\lambda_c} = \frac{(r_\sigma^3 + 2l^2m)}{\sqrt{(r_\sigma^3 + 2l^2m)^2 - 3mr_\sigma^5}}. \quad (3.72)$$

One could see the variation of $\frac{\lambda_p}{\lambda_c}$ in graphically (See Fig. 3.3) for Hayward BH.

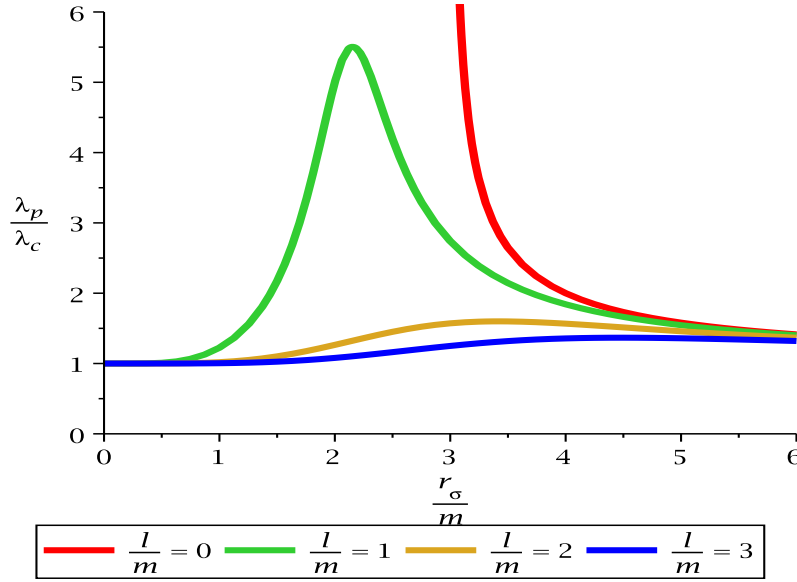


Figure 3.3: The variation of $\frac{\lambda_p}{\lambda_c}$ with $\frac{r_\sigma}{m}$ for Hayward BH.

It can be easily seen from above Fig. 3.3 that, the ratio of λ_p and λ_c varies from orbit to orbit for various values of $\frac{l}{m}$. Also, Fig. 3.3 shows that the ratio $\frac{\lambda_p}{\lambda_c}$ of Hayward BH is smallest compared to Schwarzschild ($\frac{l}{m} = 0$) BH.

Therefore, the reciprocal of critical exponent is given by

$$\frac{1}{\gamma_p} = \frac{T_\Omega}{T_\lambda} = 2\pi \sqrt{\frac{-[r_\sigma^5(r_\sigma - 6m) + 22ml^2r_\sigma^3 - 32l^4m^2](r_\sigma^3 + 2l^2m)}{(r_\sigma^3 - 4l^2m)[(r_\sigma^3 + 2l^2m)^2 - 3mr_\sigma^5]}}. \quad (3.73)$$

Special case:

For Schwarzschild BH $l = 0$, the proper time Lyapunov exponent and coordinate time

3.3. Equatorial Circular Geodesics in Spherically Symmetric metric Hayward Space-time

Lyapunov exponent are given by

$$\lambda_p^{Sch} = \sqrt{\frac{-m(r_\sigma - 6m)}{r_\sigma^3(r_\sigma - 3m)}}, \quad (3.74)$$

$$\lambda_c^{Sch} = \sqrt{\frac{-m(r_\sigma - 6m)}{r_\sigma^4}}. \quad (3.75)$$

The ratio of $\frac{\lambda_p}{\lambda_c}$ reduces to

$$\frac{\lambda_p}{\lambda_c} = \sqrt{\frac{r_\sigma}{(r_\sigma - 3m)}}. \quad (3.76)$$

The reciprocal of critical exponent for schwarzschild BH is given by

$$\frac{1}{\gamma_p} = \frac{T_\Omega}{T_\lambda} = 2\pi \sqrt{\frac{-(r_\sigma - 6m)}{(r_\sigma - 3m)}}. \quad (3.77)$$

When $r_\sigma = 4m$, the circular orbit become unstable and critical exponent (γ_p) become $\frac{1}{2\sqrt{2}\pi}$. In this case, Lyapunov time scale $T_\lambda = \frac{1}{\lambda}$ will be less than the orbital time scale $T_\Omega = \frac{2\pi}{\Omega}$, that is, $T_\lambda < T_\Omega$ in the approximation of a test particle around a Schwarzschild BH.

3.3.3.2 Null geodesics

By using Eqn. (3.29) the Lyapunov exponent for null geodesics is given by

$$\lambda_c = \sqrt{\frac{3m^2 [r_c^5 - 6l^2(r_c^3 - 2l^2m)]}{(r_c^3 + 2l^2m)^3}}. \quad (3.78)$$

Here we can see that the circular geodesics is unstable as λ_c is real.

Special case:

For Schwarzschild BH $l = 0$, the Lyapunov exponent becomes

$$\lambda_c^{Sch} = \frac{\sqrt{3}m}{r_c^2}. \quad (3.79)$$

3. Geodesic stability and quasi normal modes via Lyapunov exponent for Hayward black hole

It can be easily seen that for $r_c = 3m$; λ_c^{Sch} is real which implies that Schwarzschild photon sphere is unstable.

3.4 Null Circular Geodesic and QNMs for Hayward BH in the Eikonal limit

We consider the usual wave like equation, with an effective potential which was first derived by Iyer and Will (Iyer and Will [1987]),

$$\frac{d^2 Y}{dr_*^2} + \Psi_0 Y = 0, \quad (3.80)$$

where,

$$\Psi_0 = w^2 - V_s(r), \quad (3.81)$$

and

$$V_s(r) = \left[\frac{j(j+1)}{r^2} + \frac{2m(r^3 - 4l^2 m)}{(r^3 + 2l^2 m)^2} \right] \left(1 - \frac{2mr^2}{r^3 + 2l^2 m} \right). \quad (3.82)$$

Here, where j being the angular harmonic index, Y represents the radial part of the perturbation variable and r_* is a convenient “tortoise” coordinate, ranging from $-\infty$ to $+\infty$.

The radial coordinate r and the tortoise coordinate r_* are related by the equation

$$\frac{dr}{dr_*} = 1 - \frac{2mr^2}{r^3 + 2l^2 m}. \quad (3.83)$$

In case of the eikonal limit ($j \rightarrow \infty$), we get

$$\Psi_0 \simeq \omega^2 - \frac{j^2}{r^2} \left(1 - \frac{2mr^2}{r^3 + 2l^2 m} \right). \quad (3.84)$$

With the help of Eqn. (3.84), we can find the maximum value of Ψ_0 which occurs at $r = r_o$

$$(r_o^3 + 2l^2 m)^2 - 3mr_o^5 = 0. \quad (3.85)$$

3.4. Null Circular Geodesic and QNMs for Hayward BH in the Eikonal limit

Also from the null circular geodesic at $r = r_c$, we obtain

$$(r_c^3 + 2l^2m)^2 - 3mr_c^5 = 0. \quad (3.86)$$

Since the location of the null circular geodesics and the maximum value of Ψ_0 are coincident at $r_c = r_o$, then we get the following

QNM condition (Iyer and Will [1987], Berti et al. [2007])

$$\frac{\Psi_0(r_o)}{\sqrt{-2\Psi_0''(r_o)}} = i(n + 1/2), \quad (3.87)$$

where, $\Psi_0'' \equiv \frac{d^2\Psi_0}{dr_*^2}$ and Eqn. (3.87) is evaluated at an extremum of Ψ_0 (the point r_o at which $\frac{d\Psi_0}{dr_*} = 0$).

Now, the formula (3.87) allows us to conclude that, in case of the large- j limit

$$\omega_{QNM} = j \left(\frac{\sqrt{m(r_c^3 - 4l^2m)}}{(r_c^3 + 2l^2m)} \right) - i \left(n + \frac{1}{2} \right) \sqrt{\frac{3m^2 [r_c^5 - 6l^2(r_c^3 - 2l^2m)]}{(r_c^3 + 2l^2m)^3}}. \quad (3.88)$$

Cardoso et al. (Cardoso et al. [2009]) showed in general sense that this is one

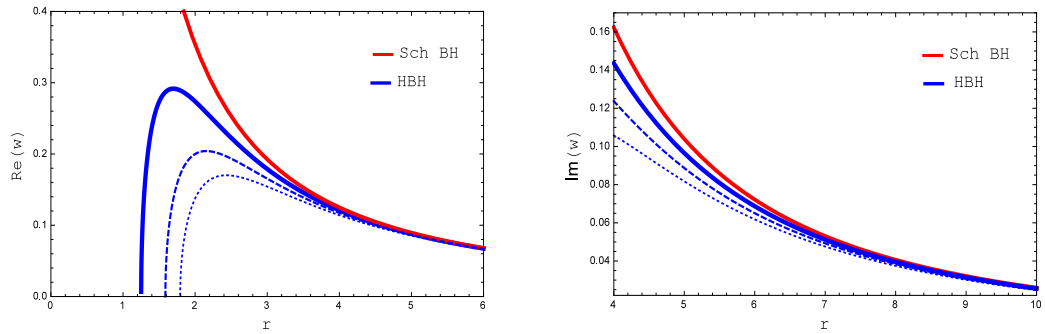


Figure 3.4: The figure shows QNMs frequency $Re(w)$ versus r (left Panel) and $Im(w)$ versus r (right panel) of HBH and Sch BH ; the other parameters fixed to $m = 1$ and $l = 0.7$ (solid), $l = 1$ (dashed) and $l = 1.2$ (dotted) for HBH.

of the most important results of QNMs and the significance of the Eqn. (3.88) is that in case of eikonal limit (Baker et al. [2008]), the real and imaginary parts of the QNMs (Nollert [1999], Kokkotas and Schmidt [1999], Yadav et al. [2020]) of the spherically symmetric, asymptotically flat Hayward regular BH space-time are given by the frequency and instability time scale of the unstable null circular geodesics.

3. Geodesic stability and quasi normal modes via Lyapunov exponent for Hayward black hole

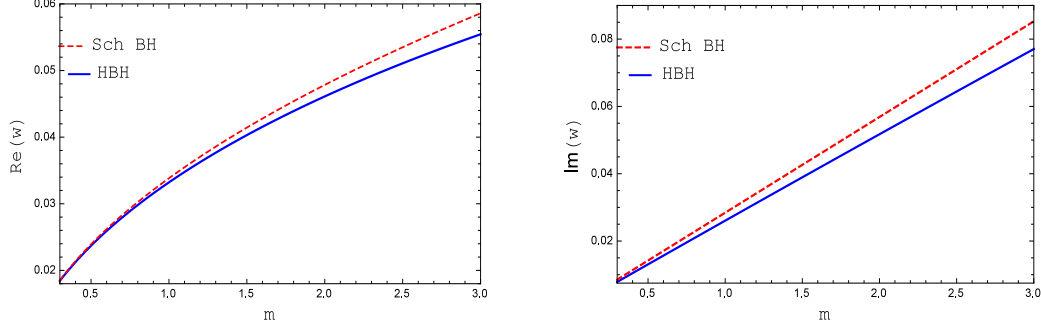


Figure 3.5: The figure shows QNMs frequency $Re(w)$ versus m (left Panel) and $Im(w)$ versus m (right panel) of HBH and Sch BH ; the other parameter fixed to $l = 0.5$ for HBH.

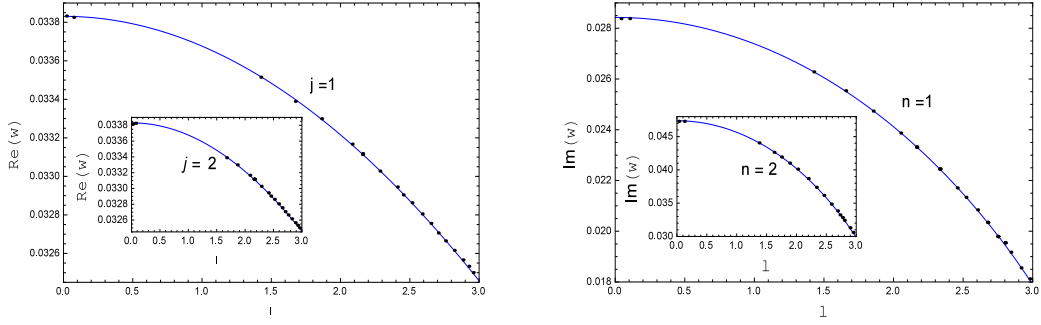


Figure 3.6: The figure shows QNMs frequency $Re(w)$ versus l (left Panel) and $Im(w)$ versus l (right panel) of Hayward BH; the other parameter fixed to $m = 1$.

Special case:

For Schwarzschild BH $l = 0$, in case of eikonal limit the frequency of QNM is

$$\omega_{QNM} = j \sqrt{\frac{m}{r_c^3}} - i \left(n + \frac{1}{2} \right) \frac{\sqrt{3}m}{r_c^2}. \quad (3.89)$$

Hence, by determining the Lyapunov exponent, we established that in case of eikonal limit, the frequency of quasi-normal modes of Schwarzschild BH might be determined by the parameters of the null circular geodesics.

In Fig. 3.4, $Re(w)$ is plotted as a function of r (left panel) by varying l . When l increase, the height of the $Re(w)$ decrease. Also $Im(w)$ is plotted as a function of r (right panel) by varying l . One can observe that $Im(w)$ decreases when r increases

3.5. Conclusions

and $Im(w)$ of Hayward BH is the smallest compared to Schwarzschild BH.

The Fig. 3.5, shows that the behavior is similar for Hayward BH and Schwarzschild BH in both cases $Re(w)$ and $Im(w)$ increase when m is increase, respectively. In fact $Im(w)$ is linearly dependent on m . Also, the angular velocity and instability time scale of null-circular geodesics of Hayward BH is the smallest compared to Schwarzschild BH regardless of the value of mass, respectively.

In Fig. 3.6, $Re(w)$ is plotted against l (left panel) and $Im(w)$ is plotted against l (right panel). Both of $Re(w)$ and $Im(w)$ are decrease when l increases, that is, the modes decays faster for large l . Compared to the Schwarzschild BH ($l = 0$) the modes decays faster.

3.5 Conclusions

We investigated the geodesic stability via Lyapunov exponent for a static, spherically symmetric regular Hayward BH. We have considered both time-like case and null case. Using Lyapunov exponent one can easily determined whether the geodesics is stable or unstable or marginally stable. Also, we computed the QNMs frequency in the geometric-optics approximation (eikonal) limit. We have showed that the real part of QNMs frequency are evaluated by the angular velocity in terms of the unstable circular photon orbit. While the imaginary part is related to the instability time scale of photon orbit.

Moreover, we examined the Lyapunov exponent that could be used to established the instability of equatorial circular geodesics both for time-like and null cases. When the parameter $l = 0$, one gets the result of Schwarzschild BH. We derived both the proper time Lyapunov exponent and coordinate time Lyapunov exponent. We have calculated their ratio. We have also calculated the reciprocal of critical exponent. Moreover, we have showed that for any unstable circular orbit, $T_\Omega > T_\lambda$, that is, orbital time scale is greater than the Lyapunov time scale.

The most important result that we derived is the relation between unstable null circular geodesics and QNMs frequency in the eikonal limit. Moreover we discussed the gravitational bending of light and radius of shadow for this regular BH.

Chapter 4

Tolman VI Fluid Sphere in $f(R, T)$ Gravity ¹

4.1 Introduction

The analysis of the interior of the stars is fascinating to astrophysicists, mainly to the General theory of relativity (GR). For the fact that, about the late phase of stellar evolution, general relativistic effects much more important. In this direction, one of the incredible works was that of the Tolman solution (1939) ([Tolman \[1939\]](#)). Tolman extensively deliberated the stellar interior and gave us a explicit solutions for the static, spherically symmetric equilibrium fluid distribution ([Gupta and Maurya \[2011\]](#)). In different dimension, it has been tested in which include cosmology, gravitational waves, astrophysics and thermodynamics ([Alves et al. \[2016\]](#)) of the stellar system and it has present important contributions to the different astrophysics and cosmological issues. Many of them present collapsing of wormhole solution with static spherically symmetric geometry ([Moraes and Sahoo \[2018\]](#)) and non static spherically symmetric object with anisotropic fluid profile. Moraes and his co-authors studied modified Tolman-Oppenheimer-Volkoff (TOV) equation in which they illustrates the equilibrium conditions of the compact structures.

In the modifying form of gravitational action asks for lots of fundamental challenges. These models can show ghost-like behavior, instabilities, while on the other

¹A considerable part of this chapter has been published in **Universe** **2023**, **9**, **122**.

4. Tolman VI Fluid Sphere in $f(R, T)$ Gravity

side, it has to match with experiments and observations in the low energy limit. Also in the framework of $f(R, T)$ gravity some interesting results have been found at solar system ([Manna et al. \[2020\]](#)), galactic and cosmological scales.

Several models exist which attempt to explain the early acceleration of the universe. The most accepted models contain a slowly varying potential and a scalar field. There are another class of models where the gravity is modified under the general relativity. One of the procedure of the modifications depended upon phenomenological considerations is provided by $f(R, T)$ theory of gravity. Indeed, $f(R, T)$ theories are conformally identical to Einstein's theory plus a scalar degree of freedom classified the scalar in which potential is uniquely established from Ricci scalar. There are various model, in the literature, where the authors ([Rej and Bhar \[2021\]](#)) considered Einstein equation with corrections. The consistent theory of gravity, modified or classified, should be equally suitable to the strong gravity regime.

Here $f(R, T)$ is an analytic (general) function of R (Ricci scalar). As an example, cosmological solutions gives the accelerated expansion of the universe at late times. Also it have been found that many stability conditions may lead to avoid tachyon and ghost solution. In addition, there exist viable $f(R, T)$ models satisfying both stability conditions ([Li and Barrow \[2007\]](#)) and background cosmological constraints and results have been obtained to place constants on $f(R, T)$ cosmological model by cosmic microwave background radiation (CMBR) galaxy and anisotropic power spectrum ([Bean et al. \[2007\]](#), [Mondal et al. \[2021a\]](#)). To consider $f(R, T)$ gravity in low energy limit, it is viable to obtain accurate gravitational potentials capable of describing the flat rotational curves of the dynamics of galaxy or spiral galaxies clusters without considering large amount of dark matter ([Das et al. \[2020b\]](#)).

Numerous investigations ([De la Cruz-Dombriz and Dobado \[2006\]](#), [Bergliaffa \[2006\]](#), [Mondal et al. \[2020\]](#), [Rahaman et al. \[2021\]](#), [Mondal et al. \[2021b\]](#)) have used different method to examined the stability as well as consistency of $f(R)$ gravity theory. There are definite form of $f(R)$ algebraic function which eliminated the existence of stable astrophysical form and reported unrealistic. In recent years, more research has been performed on the steadiness, dynamical unsteadiness, existence of celestial stellar system of this theory ([Ganguly et al. \[2014\]](#), [Goswami et al. \[2014\]](#), [Yadav et al. \[2020\]](#)). Harko et.al ([Harko et al. \[2011\]](#)) proposed the concept of matter and curvature couplings to represent a new version of altered theory of gravity, namely $f(R, T)$ gravity. They also represented the relating field equation with the help of gravitational potential mechanism and showed the important of alternative gravity

4.1. Introduction

theory. Also the same authors have initiated various model for $f(R, T)$ algebraic functional for detachable compose viz. $f(R, T) = f_1(R) + f_2(T)$. Houndjo (Houndjo [2012]) investigated matter instructed age of accelerating cosmic by $f(R, T)$ gravity. Also, Baffou and his teammates (Baffou et al. [2015]) examined spatially uniform cosmic in the field of $f(R, T)$ gravity.

Modified and extended models are always popular due to the potential of representation of gravitational field nature near curvature singularities accurately and as well to overcome the cosmological constant problems. Convincing confirmation for the extension of the universe has been provided by the many independent observations, some of these are supernovas Ia data (Riess et al. [1998], Tonry et al. [2003], Knop et al. [2003], Riess et al. [2004], Hinshaw et al. [2003]), cosmic microwave background radiation and baryon acoustic oscillation (Percival et al. [2010]) according to the study by the WMAP. For addressing this phenomenon, several assumption have been suggested from dark energy model to modified theories of gravity. Nowadays, dark energy model have no sufficient observational support. In particular, the dark energy idea requires an eqn. of state (EoS) $\omega = \frac{p}{\rho}$, where p, ρ represents spatially homogeneous pressure, energy density, respectively and the value of the parameter ω is -1 . Several results have initiated for interior exact solutions of the Einstein field equation and Schwarzschild found the first interior solution. Tolman proposed an inventive method for treatment of the Einstein field equation which are known as Tolman I, II, III, IV, V, VI, VII and VIII (Hansraj and Banerjee [2018]).

In this chapter, we consider Tolman VI model (Ray and Das [2004]) in the class of modified gravity in which the gravitational action carries a general function $f(R, T)$. For this model, the study of the background cosmological evolution can be simplified by performing transformation on metric. Such type of transformation maps from a frame where the resulting field equations and gravitational action are modified from general relativity (GR), called the Jordan frame, to a frame where the gravitational action for the new obtain metric is the Einstein-Hilbert one, called the Einstein frame. The $f(R, T)$ gravity theory has been related to stellar astrophysics (Deb et al. [2018]) and cosmology (Singha et al. [2020]), among other areas, giving testable and interesting results.

The present chapter deals with isotropic Tolman VI in modified $f(R, T)$ gravity. The physical characteristics of our obtained model are studied for three compact stars PSR J1614-2230, Vela X-1 and 4U 1538-52. The chapter is organized in following

order of sections. section 4.2, we explain about the general formalism of $f(R, T)$ gravity and in section 4.3, the proposed model is obtained for different values of coupling parameter β . At the boundary, we matched our interior space-time to the exterior space-time in section 4.4. Section 4.5 explains the physical properties between Einstein theory and $f(R, T)$ gravity. Finally in section 4.6, we discuss and concludes the whole work by pointing on major findings.

4.2 Mathematics behind $f(R, T)$ gravity

In this section we devote how the $f(R, T)$ was introduced. The Ricci scalar is integrated over a four dimensional volume element d^4x when Einstein's field equation is derived from Einstein-Hilbert action as

$$S_{EH} = \frac{1}{16\pi} \int R \sqrt{-g} d^4x \quad (4.1)$$

If we replace the Ricci scalar R by $f(R, T)$, we can get the $f(R, T)$ field equations. Therefore, the complete action in $f(R, T)$ formalism is

$$S = \int \mathcal{L}_m \sqrt{-g} d^4x + \frac{1}{16\pi} \int f(R, T) \sqrt{-g} d^4x \quad (4.2)$$

where, T is the trace of the energy momentum tensor $T_{\mu\nu}$. Also, \mathcal{L}_m represents the Lagrangian matter dencity and $g = \det(g_{\mu\nu})$.

The energy momentum tensor is defined as

$$T_{\mu\nu} = -\frac{2}{\sqrt{-g}} \frac{\partial(\sqrt{-g} \mathcal{L}_m)}{\partial g^{\mu\nu}} \quad (4.3)$$

along with the trace $T = g^{\mu\nu} T_{\mu\nu}$. Also the Lagrangian density \mathcal{L}_m depends only the metric tensor component $g_{\mu\nu}$, not its derivatives. Here, we have

$$T_{\mu\nu} = g_{\mu\nu} \mathcal{L}_m - 2 \frac{\partial \mathcal{L}_m}{\partial g^{\mu\nu}} \quad (4.4)$$

4.3. Interior space-time and the realistic viable $f(R, T)$ gravity models:

By variation principle w.r.t $g_{\mu\nu}$, eqn. (4.2) gives the field equation

$$\begin{aligned} (R_{\mu\nu} - \nabla_\mu \nabla_\nu) f_R(R, T) + g^{\mu\nu} \square f_R(R, T) - \frac{1}{2} f(R, T) g_{\mu\nu} \\ = 8\pi T_{\mu\nu} - T_{\mu\nu} f_T(R, T) - \Theta_{\mu\nu} f_T(R, T) \end{aligned} \quad (4.5)$$

where, $f_R(R, T) = \frac{\partial f(R, T)}{\partial R}$ and $f_T(R, T) = \frac{\partial f(R, T)}{\partial T}$. Here, covariant derivative ∇_μ is associated with Levi-Civita connection of the metric tensor $g_{\mu\nu}$ and the box operation \square is defined as $\square \equiv \frac{1}{\sqrt{-g}} \frac{\partial}{\partial x^\mu} (\sqrt{-g} g^{\mu\nu} \frac{\partial}{\partial x^\nu})$ with $\Theta_{\mu\nu} = g^{\alpha\beta} \frac{\delta T_{\alpha\beta}}{\delta g^{\mu\nu}}$.

The covariant derivative of the equation (4.5) gives

$$\nabla^\mu T_{\mu\nu} = \frac{f_T(R, T)}{8\pi - f_T(R, T)} \left[(T_{\mu\nu} + \Theta_{\mu\nu}) \nabla^\mu \ln f_T(R, T) + \nabla^\mu T_{\mu\nu} - \frac{1}{2} g_{\mu\nu} \nabla^\mu T \right], \quad (4.6)$$

In $f(R, T)$ gravity, the stress-energy tensor of the matter field do not obey the conservation law due to interaction between the curvature and matter as in general relativity.

With the help of the equation (4.3), we get the tensor $\Theta_{\mu\nu}$ as follows

$$\Theta_{\mu\nu} = g_{\mu\nu} \nabla^\mu - 2T_{\mu\nu} - 2g^{\alpha\beta} \frac{\partial^2 \mathcal{L}_m}{\partial g^{\mu\nu} \partial g^{\alpha\beta}}, \quad (4.7)$$

for the field equation, we assume the energy-momentum tensor as

$$T_{\mu\nu} = (\rho + p)u_\mu u_\nu - p g_{\mu\nu}, \quad (4.8)$$

provided, the μ^μ four velocity, such that $\mu_\mu \mu^\mu = 1$ and $\mu_\mu \nabla^\mu \mu_\mu = 0$ with ρ, p_r and p_t are matter density, radial pressure and transverse pressure, respectively. If we specify pressure as $-\mathcal{P} = \mathcal{L}_m$, the equation (4.7) reduces to

$$\Theta_{\mu\nu} = -\mathcal{P} g_{\mu\nu} - 2T_{\mu\nu} \quad (4.9)$$

4.3 Interior space-time and the realistic viable $f(R, T)$ gravity models:

We will represent the model with the help of realistic $f(R, T)$ gravity model. Here,

4. Tolman VI Fluid Sphere in $f(R, T)$ Gravity

we consider a separable functional form of $f(R, T)$ given by,

$$f(R, T) = f_1(R) + f_2(T) \quad (4.10)$$

in the relativistic structures to study the coupling effects of matter and curvature components in $f(R, T)$ gravity, where $f_1(R)$ and $f_2(T)$ representing arbitrary functions of R and T , respectively. Several viable model in $f(R, T)$ gravity can be generated in linear combining of different forms of $f_1(R)$ and $f_2(T)$. In the present model, we assume $f_1(R) = R$ and $f_2(T) = 2\beta T$. Then the expression for $f(R, T)$ becomes

$$f(R, T) = R + 2\beta T \quad (4.11)$$

where, β is arbitrary constant to be evaluated depending on many physical requirements.

In curvature coordinate, we consider the static and spherically symmetric line element describing a wormhole region by the following metric:

$$ds^2 = -e^\nu dt^2 + e^\lambda dr^2 + r^2 d\Omega^2, \quad (4.12)$$

where, both ν, λ depends on r , *i.e* both are purely radial and $d\Omega^2 = \sin^2 \theta d\phi^2 + d\theta^2$. In modified gravity, the field equation along the line element (4.12) can be written as

$$8\pi\rho + \beta(3\rho - p) = \frac{1 - e^{-\lambda}}{r^2} + \frac{e^{-\lambda}\lambda'}{r}, \quad (4.13)$$

$$8\pi p - \beta(\rho - 3p) = \frac{e^{-\lambda} - 1}{r^2} + \frac{e^{-\lambda}\nu'}{r}, \quad (4.14)$$

$$8\pi p - \beta(\rho - 3p) = e^{-\lambda} \left[\frac{\nu''}{2} + \frac{\nu'^2}{4} - \frac{\nu'\lambda'}{4} + \frac{\nu' - \lambda'}{2r} \right]. \quad (4.15)$$

where, prime (') denotes differentiation with respect to the radial coordinates 'r'.

We denote ρ_E and p_E by,

$$\rho_E = \rho + \frac{\beta}{8\pi}(3\rho - p), \quad (4.16)$$

$$p_E = p - \frac{\beta}{8\pi}(\rho - 3p). \quad (4.17)$$

where, ρ_E represents the density and p_E represents the pressure in Einstein gravity. To solve the equations (4.13)–(4.15), we use the metric potential by Tolman (Tolman

4.3. Interior space-time and the realistic viable $f(R, T)$ gravity models:

[1939]) in which the expression

$$e^\lambda = 2 - n^2, \quad (4.18)$$

$$e^\nu = (Ar^{1-n} - Br^{1+n})^2. \quad (4.19)$$

where, A, B are arbitrary constant. The restriction of λ is $0 < \lambda < \sqrt{2}$, but this is not most general choice. Using the expression of the equation (4.18) and the equation (4.13), we obtain the Einstein density as

$$\rho_E = \frac{1 - n^2}{8\pi r^2(2 - n^2)} \quad (4.20)$$

Similarly, using the expression of the equations (4.18), (4.19) and the equation (4.14), we obtain the Einstein pressure as follows

$$p_E = \frac{A(n-1)^2 - B(n+1)^2 r^{2n}}{8\pi r^2(2 - n^2)(A - Br^{2n})}. \quad (4.21)$$

If we eliminate radius r from equations (4.20) and (4.21), we obtain the relation between Einstein density and pressure. Also, the positivity of density profile demands the range for n are $n < -\sqrt{2}$ or $n > \sqrt{2}$ or $-1 < n < 1$. So the interval of validity is $0 < n < 1$. Now, using the expression ρ_E and p_E from equations (4.16) and (4.21), we get the expression for matter density(ρ) and pressure(p) in modified $f(R, T)$ gravity as follows

$$\rho = \frac{A(n-1)\chi_1 - B(n+1)\chi_2 r^{2n}}{4r^2(n^2 - 2)(2\pi + \beta)(4\pi + \beta)(A - Br^{2n})}, \quad (4.22)$$

$$p = \frac{-A(n-1)\chi_2 + B(n+1)\chi_1 r^{2n}}{4r^2(n^2 - 2)(2\pi + \beta)(4\pi + \beta)(A - Br^{2n})}, \quad (4.23)$$

where,

$$\begin{aligned} \chi_1 &= 4(n+1)\pi + (n+2)\beta, \\ \chi_2 &= 4(n-1)\pi + (n-2)\beta. \end{aligned} \quad (4.24)$$

The square of the sound velocity for Einstein and our present model are obtained as

4. Tolman VI Fluid Sphere in $f(R, T)$ Gravity

follows

$$V_E^2 = \left(\frac{dp}{d\rho} \right)_E = - \frac{(A(n-1) + B(n+1)r^{2n})^2}{(n^2-1)(A - Br^{2n})^2}, \quad (4.25)$$

$$V^2 = \frac{dp}{d\rho} = - \frac{A^2(n-1)\chi_2 + 4AB(n^2-1)(2\pi + \beta)r^{2n} + B^2(n+1)\chi_1 r^{4n}}{A^2(n-1)\chi_1 - 4AB(n^2-1)(2\pi + \beta)r^{2n} + B^2(n+1)\chi_2 r^{4n}}. \quad (4.26)$$

Negative sign in the sound speed index can be removed in the interval $0 < n < 1$.

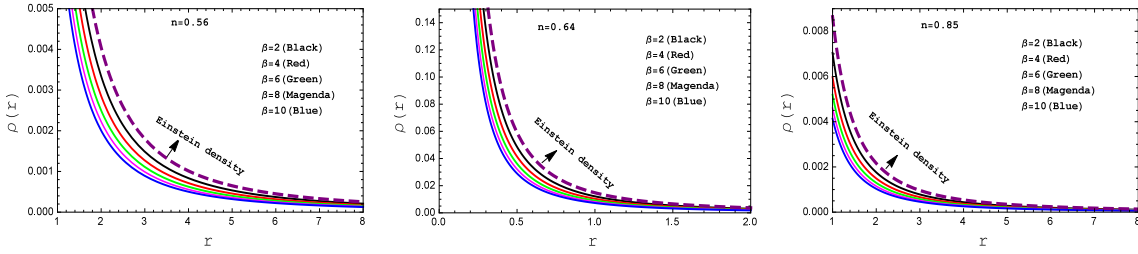


Figure 4.1: Behavior of the “energy density” with respect to the radial coordinate “ r ” for the compact star PSR J1614-2230 (left panel), Vela X-1 (middle panel) and 4U 1538-52 (right panel) corresponding to the numerical value of constants A and B from the table 4.2 and for different values of β .

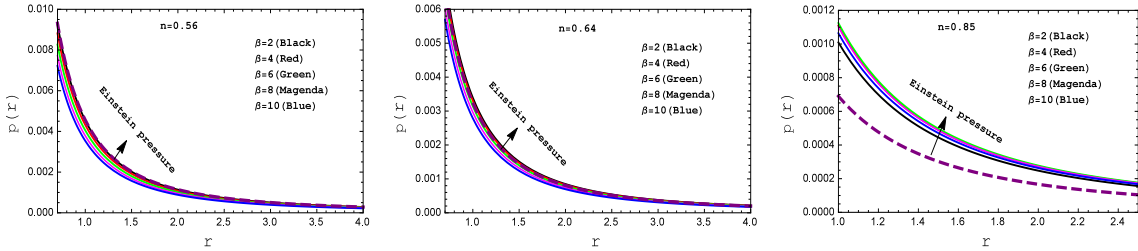


Figure 4.2: Behavior of the “pressure” with respect to the radial coordinate “ r ” for the compact star PSR J1614-2230 (left panel), Vela X-1 (middle panel) and 4U 1538-52 (right panel) corresponding to the numerical value of constants A and B from the table 4.2 and for different values of β .

The profile of density and pressure are shown in Fig. 4.1 and Fig. 4.2, respectively. One can see that the density and pressure are both positive definite but at the stellar center both are infinite. Also, from Fig. 4.2 we can see that Einstein pressure are gradually decreasing with increasing value of ‘ n ’ i.e Einstein pressure at the point

4.4. Exterior space-time and boundary condition:

$n = 0.56 >$ Einstein pressure at the point $n = 0.64 >$ Einstein pressure at the point $n = 0.85$.

In the literature, it is well-known that the mass distributions must obey all the energy conditions in its interiors. These energy conditions are named as null, strong, week and dominant energy conditions and symbolized by NEC, SEC, WEC and DEC. All the energy conditions are satisfied for our present model if the following inequality are hold.

NEC: $\rho + p \geq 0$, SEC: $\rho + p \geq 0$, $\rho + 3p \geq 0$, WEC: $\rho + p \geq 0$, $p \geq 0$, DEC: $\rho - p \geq 0$, $p \geq 0$.

$$(\rho + p)_E = \frac{A(n-1) + B(n+1)r^{2n}}{4\pi r^2(n^2-2)(A - Br^{2n})}, \quad (4.27)$$

$$\rho + p = \frac{A(n-1) + B(n+1)r^{2n}}{r^2(n^2-2)(4\pi + \beta)(A - Br^{2n})}, \quad (4.28)$$

$$(\rho + 3p)_E = \frac{-A(n-1)(n-2) + B(n+1)(n+2)r^{2n}}{4r^2\beta(n^2-2)(A - Br^{2n})}, \quad (4.29)$$

$$\rho + 3p = \frac{A(n-1)(t - 2(2\pi + \beta))B(n+1)r^{2n}(S + 2(2\pi + \beta))}{2r^2(n^2-2)(2\pi + \beta)(4\pi + \beta)(A - Br^{2n})}, \quad (4.30)$$

$$(\rho - p)_E = \frac{n(A(n-1) + B(n+1)r^{2n})}{4\pi r^2(n^2-2)(A - Br^{2n})}, \quad (4.31)$$

$$\rho - p = \frac{n(A(n-1) - B(n+1)r^{2n})}{4r^2\beta(n^2-2)(A - Br^{2n})}. \quad (4.32)$$

$$(4.33)$$

It is clear from Fig. 4.3 that $\rho + p \geq 0$, in the Fig. 4.4, $\rho + 3p \geq 0$ and $\rho - p \geq 0$ is non negative shown in the Fig. 4.5. So all the necessary energy conditions have been fulfilled for our $f(R, T)$ gravity model.

4.4 Exterior space-time and boundary condition:

Now, we have matched our interior space-time to exterior Schwarzschild line ele-

4. Tolman VI Fluid Sphere in $f(R, T)$ Gravity

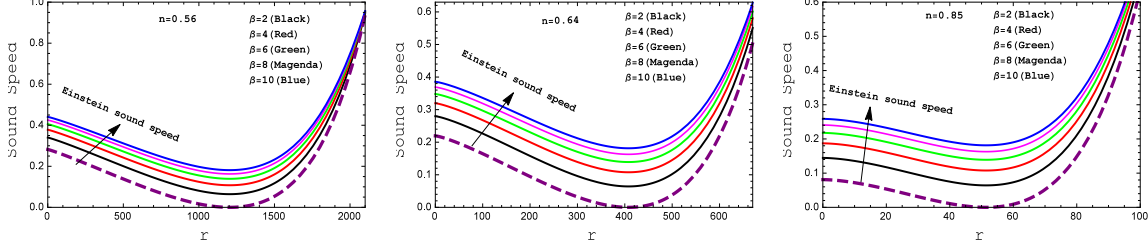


Figure 4.3: Behavior of the “Speed sound” with respect to the radial coordinate “ r ” for the compact star PSR J1614-2230 (left panel), Vela X-1 (middle panel) and 4U 1538-52 (right panel) corresponding to the numerical value of constants A and B from the table 4.2 and for different values of β .

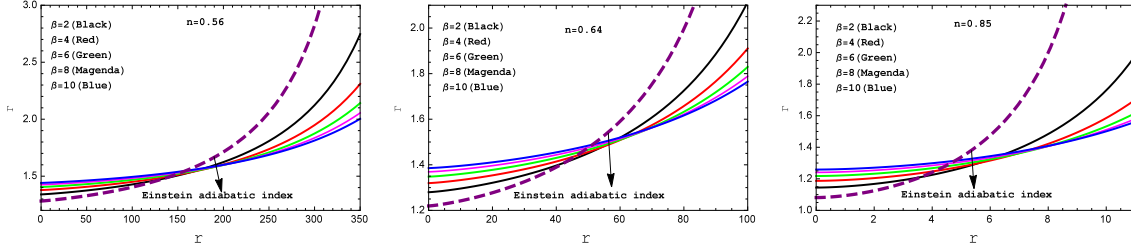


Figure 4.4: Variation of “adiabatic index” with respect to the radial coordinate “ r ” for the compact star PSR J1614-2230 (left panel), Vela X-1 (middle panel) and 4U 1538-52 (right panel) corresponding to the numerical value of constants A and B from the table 4.2 and for different values of β .

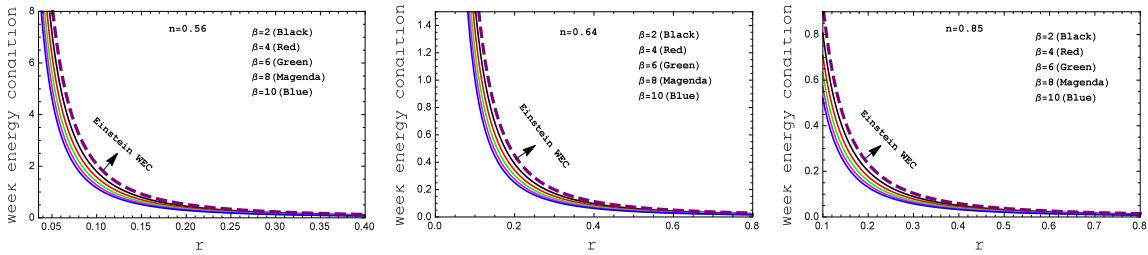


Figure 4.5: Behavior of the “week energy condition” with respect to the radial coordinate “ r ” for the compact star PSR J1614-2230 (left panel), Vela X-1 (middle panel) and 4U 1538-52 (right panel) corresponding to the numerical value of constants A and B from the table 4.2 and for different values of β .

ment at the $r = R$. The Exterior line element is

$$ds_+^2 = -\left(1 - \frac{2M}{r}\right)dt^2 + \left(1 - \frac{2M}{r}\right)^{-1}dr^2 + r^2(\sin^2\theta d\phi^2 + d\theta^2). \quad (4.34)$$

4.4. Exterior space-time and boundary condition:

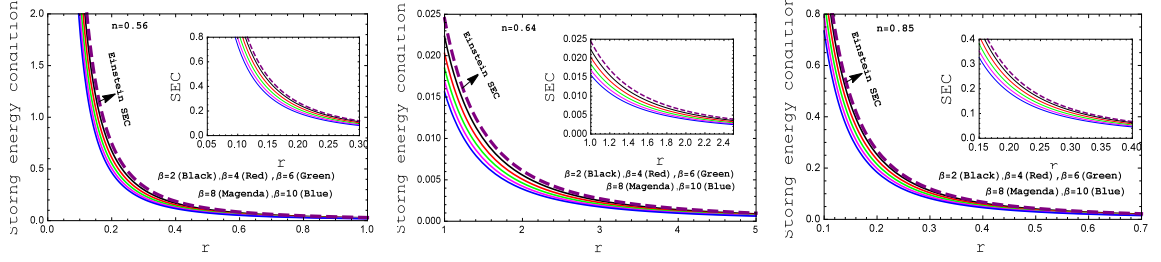


Figure 4.6: Behavior of the “Strong energy condition” with respect to the radial coordinate “ r ” for the compact star PSR J1614-2230 (left panel), Vela X-1 (middle panel) and 4U 1538-52 (right panel) corresponding to the numerical value of constants A and B from the table 4.2 and for different values of β .

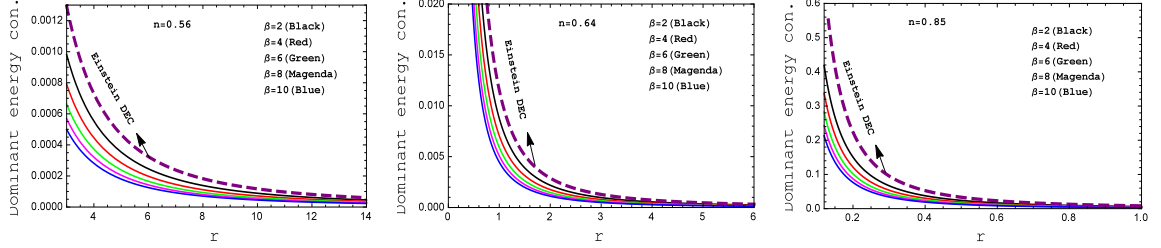


Figure 4.7: Behavior of the “Dominant energy condition” with respect to the radial coordinate “ r ” for the compact star PSR J1614-2230 (left panel), Vela X-1 (middle panel) and 4U 1538-52 (right panel) corresponding to the numerical value of constants A and B from the table 4.2 and for different values of β .

and the interior line element is

$$ds_-^2 = -(Ar^{1-n} - Br^{1+n})^2 dt^2 + (2 - n^2) dr^2 + r^2 (\sin^2 \theta d\phi^2 + d\theta^2). \quad (4.35)$$

The continuity of the metric

$$\left(1 - \frac{2M}{R}\right)^{-1} = (2 - n^2), \quad (4.36)$$

$$\left(1 - \frac{2M}{R}\right) = (AR^{1-n} - BR^{1+n})^2. \quad (4.37)$$

The pressure vanishes at the boundary $r = R$ i.e $p(r = R) = 0$ which gives the

4. Tolman VI Fluid Sphere in $f(R, T)$ Gravity

following equation in modified gravity as follows

$$\frac{-A(n-1)\chi_2 - B(n+1)\chi_2 R^{2n}}{4R^2(n^2-2)(2\pi+\beta)(4\pi+\beta)(A-BR^{2n})} = 0 \quad (4.38)$$

- **Determination of n and the constants A and B :** Solving the equations (4.36)-(4.38), we get the expression for n and the constants A and B as follows:

$$\begin{aligned} n &= \pm \sqrt{\frac{R-4M}{R-2M}}, \\ A &= -\frac{(n+1)\chi_2 R^{n-2} \sqrt{R(R-2M)}}{2n\beta}, \\ B &= \frac{(1-n)\chi_1 R^{n-2} \sqrt{R(R-2M)}}{2n\beta}. \end{aligned}$$

For numeric values of the constants A and B , we chosen Mass M , radius R accordingly different compact stars. Also, for well-behaved solution, we use different values of the parameter β

4.5 Physical properties of the present model:

- **Nature of equation of state:** It is very important to describe a relationship between energy density and the pressure which is called the equation of state (EoS). The relation between the pressure and matter density can be find out by dimensionless quantity which is known as the equation of state parameter.

$$p = \omega \times \rho. \quad (4.39)$$

Hence, the equation of state parameter (w) for Einstein and our model are obtained as follows

$$\omega_E = \frac{p_E}{\rho_E} = \frac{A(n-1)^2 - B(n+1)^2 r^{2n}}{(1-n^2)(A-Br^{2n})}, \quad (4.40)$$

$$\omega = \frac{p}{\rho} = \frac{-A(n-1)\chi_2 + B(n+1)\chi_1 r^{2n}}{A(n-1)\chi_1 - B(n+1)\chi_2 r^{2n}} \quad (4.41)$$

The behavior of equation of state parameter is shown in the Fig. 4.8. We can see that equation of state parameter is monotonic decreasing function of radius

4.5. Physical properties of the present model:

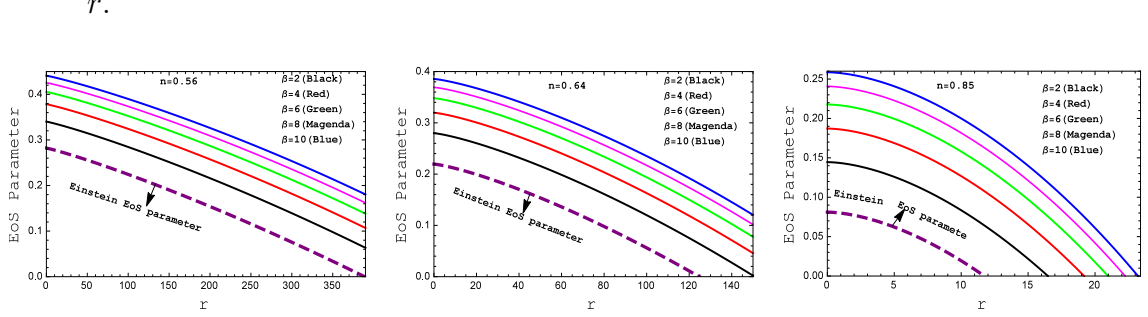


Figure 4.8: Behavior of the “EoS parameter” with respect to the radial coordinate “ r ” for the compact star PSR J1614-2230 (left panel), Vela X-1 (middle panel) and 4U 1538-52 (right panel) corresponding to the numerical value of constants A and B from the table 4.2 and for different values of β .

- Relativistic adiabatic index:** For a compact star, stability is one of the most crucial requirement. For this reason we have discussed stability along with the variation of adiabatic index (Γ) inside the compact star. The adiabatic index can be displays the stability for both non-relativistic and relativistic compact stars. The stability condition for a Newtonian sphere is $\Gamma > \frac{4}{3}$ and $\Gamma = \frac{4}{3}$ is the condition for a neutral equilibrium according to (Bondi [1964]). The expression relativistic adiabatic index for Einstein and our present model are

$$\Gamma_E = \left(\frac{\rho + p}{p} \frac{dp}{d\rho} \right)_E = \frac{2(A(n-1) + B(n+1)r^{2n})}{B(n+1)^2 r^{2n} - A(n-1)^2} V^2, \quad (4.42)$$

$$\Gamma = \frac{4(A(n-1) + B(n+1)r^{2n})(2\pi + \beta)}{A(n-1)\chi_2 - B(n+1)^2\chi_2 r^{2n}} V^2. \quad (4.43)$$

- TOV Equation:** The hydrostatic equilibrium (F_h) equation is an important feature of the physical realistic compact objects. The fluid sphere remains at equilibrium under three forces namely, gravitational force (F_g), hydrostatic force (F_h) and the additional force due to modified gravity (F_m) and this situation represents by an equation, which is known as Tolman-Oppenheimer-Volkov (TOV) equation. With the help of generalized TOV equation, we can analyze the equilibrium equation for our three compact stars. The generalized TOV Eqn. for the isotropic fluid (Bhar et al. [2022]) distribution in $f(R, T)$ modified gravity

4. Tolman VI Fluid Sphere in $f(R, T)$ Gravity

can be written as

$$-\frac{\nu'}{2}(\rho + p) - \frac{dp}{d\rho} - \frac{\beta}{2(4\pi + \beta)}(p' - \rho') = 0 \quad (4.44)$$

The equation (4.44) can be written as follows,

$$F_g + F_h + F_m = 0, \quad (4.45)$$

where,

$$F_g = \frac{(A(n-1) + B(n+1)r^{2n})^2}{r^3(n^2-2)(4\pi + \beta)(A - Br^{2n})^2}, \quad (4.46)$$

$$F_h = \frac{A^2(n-1)\chi_2 + 4AB(n^2-1)(2\pi + \beta)r^{2n} + B^2(n+1)\chi_1 r^{4n}}{2r^3(2-n^2)(2\pi + \beta)(4\pi + \beta)(A - Br^{2n})^2}, \quad (4.47)$$

$$F_m = \frac{n\beta(A^2(n-1) + B^2(n+1)r^{4n})}{2r^3(2-n^2)(2\pi + \beta)(4\pi + \beta)(A - Br^{2n})^2}. \quad (4.48)$$

Since, $\beta = 0$ corresponds to GR. Hence $F_m = 0$, the TOV Eqn. for Einstein reduces to

$$-\frac{\nu'}{2}(\rho + p)_E - \left(\frac{dp}{d\rho}\right)_E = 0 \quad (4.49)$$

The equation (4.49) can be written as follows,

$$(F_g)_E + (F_h)_E = 0, \quad (4.50)$$

where,

$$(F_g)_E = \frac{(A(n-1) + B(n+1)r^{2n})^2}{4\pi r^3(n^2-2)(A - Br^{2n})^2}, \quad (4.51)$$

$$(F_h)_E = \frac{(A(n-1) + B(n+1)r^{2n})^2}{4\pi r^3(2-n^2)(A - Br^{2n})^2}. \quad (4.52)$$

- **Mass radius relationship and compactness parameter :** let \mathcal{U} be the compactification factor and M be the mass function. Then we can get following

4.5. Physical properties of the present model:

relation between them,

$$\mathcal{U}_E = \frac{\mathcal{M}_E}{R} = \frac{(1 - n^2)}{2(2 - n^2)}, \quad (4.53)$$

$$\mathcal{U} = \frac{\mathcal{M}}{R} = \frac{\pi((n+1)\chi_2) + 2n\beta_2 F_1(1, \frac{1}{2n}, 1 + \frac{1}{2n}, \frac{BR^{2n}}{A})}{(2\pi + \beta)(4\pi + \beta)(A - BR^{2n})}. \quad (4.54)$$

where, $\mathcal{M} = m(r)|_{r=R}$ and ${}_2F_1$ represents the hypergeometric function. The expression for mass function for Einstein and our present model are

$$m_E = 4\pi \int_0^r \rho_E r^2 dr = \frac{(1 - n^2)r}{2(2 - n^2)}, \quad (4.55)$$

$$m = 4\pi \int_0^r \rho r^2 dr = \frac{\pi r((n+1)\chi_2) + 2n\beta_2 F_1(1, \frac{1}{2n}, 1 + \frac{1}{2n}, \frac{Br^{2n}}{A})}{(2\pi + \beta)(4\pi + \beta)(A - Br^{2n})} \quad (4.56)$$

- **Gravitational red-shift($z(r)$) function and surface red-shift(z_s) :** The gravitational redshift can be determined by the formula

$$z(r) = e^{-\nu/2} - 1 = \frac{1}{(Ar^{1-n} - Br^{1+n})} - 1, \quad (4.57)$$

Furthermore, the following formula can be used to calculate surface redshift (z_s) for Einstein and our present model are

$$(z_s)_E = \frac{1}{\sqrt{1 - 2\mathcal{U}_E}} - 1 = \sqrt{2 - n^2} - 1, \quad (4.58)$$

$$z_s = \frac{1}{\sqrt{1 - 2\mathcal{U}}} - 1 \quad (4.59)$$

$$= \frac{1}{\sqrt{1 - \frac{2\pi((n+1)\chi_2) + 2n\beta_2 F_1(1, \frac{1}{2n}, 1 + \frac{1}{2n}, \frac{BR^{2n}}{A})}{(2\pi + \beta)(4\pi + \beta)(A - BR^{2n})}}} - 1. \quad (4.60)$$

Fig. 4.10 shows the nature of redshift function with respect to the radial coordinate function r . For our model, $z(r)$ is monotonically decreasing function. The value of surface redshift (z_s) for three compact stars are shown in Table 4.2. One can see from the table that the value of redshift (z_s) lies within the range $z_s < 1$.

4. Tolman VI Fluid Sphere in $f(R, T)$ Gravity

Table 4.1: Numerical values of three well-known celestial compact stars.

Compact Star	M_{obs}/M_{\odot}	$R_{obs} (km)$	$M (M_{\odot})$	$R (km)$	$n = \sqrt{\frac{R-4M}{R-2M}}$
PSR J1614-2230	1.97 ± 0.4	9.69 ± 0.02	1.97	9.69	0.56
Vela X-1	1.77 ± 0.08	9.56 ± 0.08	1.77	9.56	0.64
4U 1538-52	9.69	1.97	9.69	1.97	0.85

Table 4.2: The numerical values of A , B , surface density, surface redshift, central values of adiabatic index and surface compactness factor for three well-known celestial compact stars for different values of coupling constant β

$n = 0.56$							
Compact Star	β	A	B	$\rho_s (gm/cm^3)$	z_s	$\Gamma(r=0)$	\mathcal{U}_s
PSR J1614-2230	2	0.31368	0.00236	1.88338×10^{14}	0.22404	1.80526	0.33257
	4	0.31746	0.00266	1.57940×10^{14}	0.18006	3.42727	0.28188
	6	0.32019	0.00288	1.35301×10^{14}	0.15082	5.59965	0.24493
	8	0.32225	0.00304	1.19365×10^{14}	0.12990	8.32942	0.21671
	10	0.32386	0.00316	1.06375×10^{14}	0.11415	11.6206	0.19441
$n = 0.64$							
Compact Star	β	A	B	$\rho_s (gm/cm^3)$	z_s	$\Gamma(r=0)$	\mathcal{U}_s
Vela X-1	2	0.37509	0.00128	1.76517×10^{14}	0.19764	1.22451	0.30282
	4	0.37862	0.00148	1.47994×10^{14}	0.15965	2.43408	0.25640
	6	0.38117	0.00162	1.27408×10^{14}	0.13419	4.08345	0.22263
	8	0.38309	0.00173	1.11849×10^{14}	0.11585	6.17906	0.19687
	10	0.38460	0.00181	0.99677×10^{14}	0.10200	8.72458	0.17655
$n = 0.85$							
Compact Star	β	A	B	$\rho_s (gm/cm^3)$	z_s	$\Gamma(r=0)$	\mathcal{U}_s
4U 1538-52	2	0.65534	0.00230	1.52410×10^{14}	0.10190	0.19370	0.17640
	4	0.65764	0.00299	1.27783×10^{14}	0.83973	0.48583	0.14893
	6	0.65930	0.00349	1.10008×10^{14}	0.07154	0.91913	0.12907
	8	0.66055	0.00387	0.96574×10^{14}	0.06237	1.49672	0.11398
	10	0.66153	0.00416	0.860641×10^{14}	0.05532	2.22038	0.10211

4.6. Discussion and concluding remarks

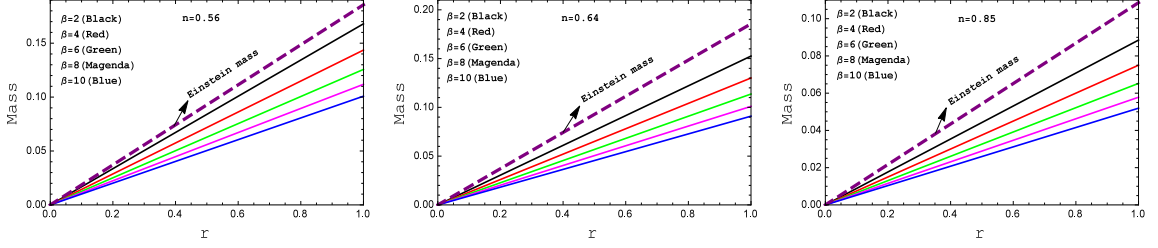


Figure 4.9: Behavior of the “mass profile” with respect to the radial coordinate “ r ” for the compact star PSR J1614-2230 (left panel), Vela X-1 (middle panel) and 4U 1538-52 (right panel) corresponding to the numerical value of constants A and B from the table 4.2 and for different values of β .

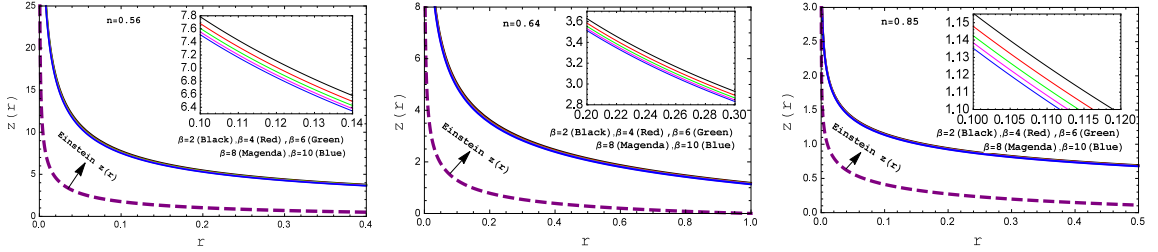


Figure 4.10: Behavior of the “EoS parameter” with respect to the radial coordinate “ r ” for the compact star PSR J1614-2230 (left panel), Vela X-1 (middle panel) and 4U 1538-52 (right panel) corresponding to the numerical value of constants A and B from the table 4.2 and for different values of β .

4.6 Discussion and concluding remarks

In this present work, we have investigated the behavior of Tolman VI spacetime in modified gravity. We endeavored to solve the modified field equations and investigated the physical viability according to the standard theory. We contrasted the behavior of the matter energy density, isotropic pressure, the sound speed energy, the all energy conditions (namely, weak, strong and dominated energy condition), EoS parameter, mass profile as well as gravitational redshift between the modified $f(R, T)$ theory and standard Einstein theory.

For the arbitrary constant $\beta = 2, 4, 6, 8$ and 10 the graphical picture have been presented in the Fig. 4.1 - 4.10 for the compact stars *PSRJ1614 – 2230*, *VelaX – 1* and *4U1538 – 52* while, $\beta = 0$ gives the General relativity case.

4. Tolman VI Fluid Sphere in $f(R, T)$ Gravity

- A clear picture of energy progression has been obtained in Fig. 4.1. The figure shows declining nature about the surface and promises the real origination of stellar body with positive behavior at the stellar interior.
- We have plotted pressure p versus radius r in Fig. 4.2 for the three compact stars PSR J1614-2230(left panel), Vela X-1(middle panel) and 4U 1538-52(right panel) for various values of β . One can see that $p > 0$ i.e positive, continuous and monotonically decreasing. Also, at some radial value, the pressure does vanish for both the cases.
- Square of the sound speed and relativistic adiabatic index have been plotted in Fig. 4.3 and Fig. 4.4, respectively. From the Fig. 4.3, one can see that the square of the sound speed lies in the predicted range i.e. $0 < V^2 < 1$ throughout the fluid sphere. The Fig. 4.4 confirms the stability of under the adiabatic index $\Gamma > \frac{4}{3}$ for our present model.
- In our $f(R, T)$ gravity model, the weak energy condition (WEC) in Fig. 4.5, the strong energy condition (SEC) in Fig. 4.6 and dominant energy condition (DEC) in Fig. 4.7 are also met . For the complication in the expressions of density and pressure we have shown graphical presentation which certifies about the well behaved nature of the energy conditions.
- We have plotted equation of state parameter profile ω in Fig. 4.8 for different values of β . It is clear from the figure that at the center of the star these parameter take maximum values while it decreases towards the boundary. Moreover, ω lies between 0 to 1 i.e $0 < \omega < 1$ which indicates the non-exotic behavior of matter distribution. Also, we can see that there are linear relation between isotropic pressure (p) and matter density (ρ).
- The mass function is plotted against radius in Fig. 4.9. This figure shows that mass function is monotonic increasing function of radius and having no central singularity. The mass functional values are in agreement with required physical conditions as one can investigate from the figure.
- We have plotted the Gravitational redshift in Fig. 4.10 for different values of β . One can see that Gravitational redshift is monotonic decreasing function of radius. Also, gravitational redshift is lower with higher values of coupling parameter β

4.6. Discussion and concluding remarks

From all graphical illustrations and obtained results, we can conclude that our present model is regular and potentially stable. Also, detailed numerical features can be found from Table 4.1 and Table 4.2. The numerical values of A and B increases with increasing values of β . The surface density ρ_s , and surface red-shift z_s all takes lower values when coupling parameter β increases. Moreover, the central values of adiabatic index(Γ at $r = 0$) increase with increasing values of β , which concludes that for higher values of β our model becomes more stable. Through analytical, numerical and graphical analysis, all the features of our present model are well described. Finally, we summarize our discussion that we are convinced by the calculated outcomes which shows that the system is physically reasonable and viably stable. Also, our outcomes could be useable in modeling relativistic compact objects as a real astrophysical phenomena. In the future, we will study a perceptible magnetic pressure influence to the equilibrium of forces for the core of the highly compact stars as the magnetic effects calculation can give some idea of the dynamical distortion in nuclear impacts.

Chapter 5

Solar system Tests in Rastall gravity¹

5.1 Introduction

The sole reason behind the universal acceptance and creditibility of the theory of general relativity has been the absolute perfection with which this theory has successfully explained all astronomical observations, for over a hundred years. The classical tests have been heralded as a proof of the experimental verification of general relativity. It has solved the mystery behind the long standing discrepancy between Newtonian calculation and observation of the precession of perihelia of Mercury, which had intrigued the scientific community throughout the nineteenth century. In spite of the various hypothesis placed by many able scientists, including the famous one by Le Verrier ([Le Verrier \[1859\]](#)), claiming the presence of an undiscovered planet called “Vulcan” in 1860, none could give a proper mathematical derivation of the unexplained 43 arcsecs per century. In 1913, Besso and Einstein ([Klein et al. \[1995\]](#)), worked out a Mercury perihelion advance formula in the “Einstein-Grossmann Entwurf” theory but there was an error. In 1915, Einstein corrected their error and derived the correct value of precession of the perihelion of Mercury as 43.03 arcsecs per century which is in close agreement with the observation and this played a significant role in popu-

¹A considerable part of this chapter has been published in **Modern Physics Letters A**, 2050034 (2019).

5. Solar system Tests in Rastall gravity

larising general relativity. The fact that other solar system planets have a significant gravitational effect on Mercury, albeit tiny, meant Mercury did not move in precisely a $1/r$ orbit, being the Newtonian potential (Hartle, 2003). In the solar system, Mercury has the largest solar system gravitational potential among all planets and satellites and hence the largest general relativistic solar system gravitational correction.

In the year of 1907, Einstein predicted the angle of light deflection in the solar gravitational field (Einstein [1911]). This is the most popular test of general relativity. The observation of gravitational deflection of light was performed by noting the change in position of stars as they passed near the Sun during a solar eclipse in 1919. This observation was the result of a painstaking expedition proposed by Lord Eddington, whose report, when submitted to the Royal Society and Royal Astronomical Society, made general relativity worldwide famous. With the improvement of modern technology and advent of space era, Shapiro (Shapiro [1964]) proposed another test; the time delay of light in a gravitational field. We have derived all these three tests with respect to a neutral regular black hole under the effect of the modified Rastall gravity. Here we would like to mention that there are a good number of papers based on the classical tests in general relativity like a very recent one by Farook et. al. (Rahaman et al. [2014c], Bhar et al. [2016]) and many others (Manna et al. [2018], Rahaman et al. [2018]) using strong field limit. Other notable works in modified gravity include Horava-Lipshitz gravity (Zhou and Liu [2012]), Kaluza-Klein gravity (Kalligas et al. [1995]), Weyl gravity Ederly and Paranjape [1998], to name a few. Braneworld models also form the subject in many papers on the classical tests, as by Böhmer et.al. (Böhmer et al. [2010]), among many others like in references (Jalalzadeh et al. [2009], Cuzinatto et al. [2014], Dahia and de Albuquerque Silva [2015], Casadio et al. [2015]). It is almost impossible to present an exhaustive list in this area since there are numerous papers like those in multidimensional gravity (Eingorn and Zhuk [2010]) and (Frye and Efthimiou [2013]) also. Further, the effect of cosmological constant has been investigated in many works like (Islam [1983], Freire et al. [2001]) and in (Miraghaei and Nouri-Zonoz [2010]).

A possible modification of general theory of relativity was introduced by Peter Rastall in 1972 (Rastall [1972]). Here, the conservation of energy momentum tensor is invalid in general, *i.e.*, we assume $T_{\mu;\nu}^\nu \neq 0$, in curved spacetime. However, the Bianchi's identities on Einstein tensor are unaltered. Also, an important requirement is that, in flat spacetime, we get the trivial geometry of $T_\mu^\nu = 0$. In his original work, Rastall simply assumed that the energy momentum tensor is proportional to

5.1. Introduction

the gradient of Ricci scalar, *i.e.*,

$$T_{\mu;\nu}^{\nu} = \lambda R_{;\mu} \quad (5.1)$$

where λ is a constant, called the Rastall parameter and R the usual Ricci scalar. Thus the field equations in original Rastall gravity is written as,

$$R_{\mu\nu} - \frac{1}{2}Rg_{\mu\nu} = \kappa (T_{\mu\nu} - \lambda g_{\mu\nu}R),$$

where $\kappa = 8\pi G/c^4$. Note that though the relation given in Eqn. (5.1) was originally proposed by Rastall, yet this is not the only form. Any alternative form may be adopted, as long as T_{μ}^{ν} vanishes in flat spacetime (Rastall [1976]). Thus one can propose any general form like:

$$T_{\mu;\nu}^{\nu} = A_{\mu;\nu}^{\nu}, \quad (5.2)$$

where $A_{\mu\nu} = A_{\nu\mu}$ and $A_{\mu\nu}$ and its derivatives are sufficiently small in flat spacetimes, and hence may be neglected. Apart from major work done on Rastall gravity by Rastall himself, many other pioneering papers have been developed over the years. In a recent interesting paper by Visser (Visser [2018]), Rastall gravity has been shown to be equivalent to Einstein gravity. Motivated by this in our work we have tried to further investigate this claim by working out the classical test of general relativity. Since these test form an integral part of comparing any modified theory of gravity with Einstein gravity, we wish to see how the observational data of Einstein gravity agrees or disagrees with Rastall gravity. We believe this work might further encourage researchers to understand the link between the two theories. In this paper, motivated by Lin et.al. (Lin and Qian [2019]), we have proposed the following form :

$$A_{\mu\nu} = g_{\mu\nu} H(R), \quad (5.3)$$

where, $H = H(R)$ is any function of Ricci scalar R , satisfying the condition that, $H(R) = 0$ when $R = 0$, leading to the conservation of energy momentum in flat spacetime. A lot of motivating work has been done using Rastall gravity in recent years like in the following references: (Heydarzade and Darabi [2017], Graca and Lobo [2018], Bronnikov et al. [2016], Heydarzade and Darabi [2017], Spallucci and Smailagic [2018], Moradpour et al. [2017b], Kumar and Ghosh [2018], Ma and Zhao [2017]) and (Oliveira et al. [2015]). Also worth mentioning are the following works: (Santos and

5. Solar system Tests in Rastall gravity

Ulhoa [2015], de Mello et al. [2015], Lobo et al. [2018], Licata et al. [2017], Darabi et al. [2018], Caramês et al. [2014]) to name a few. Note that, Batista et. al. claimed, Rastall gravity can be interpreted as a implementation of specific quantum effects in a curved background (Salako et al. [2016]). In the field of cosmology, Rastall gravity has gained a lot of attention owing to various papers like in references: (Al-Rawaf and Taha [1996a], Fabris et al. [2012b], Bronnikov et al. [2017], Darabi et al. [2018], Yuan and Huang [2017], Fabris et al. [2012a], Batista et al. [2013]) and (Moradpour et al. [2017a]).

The outline of the present chapter is as follows: In Section 5.2, we give a brief outline of the a neutral regular black hole geometry in Rastall gravity, while in Section 5.3, we present the Classical Tests of General Relativity of the a neutral regular black hole solution using the method of null geodesics. This section is further subdivided into three parts : subsection (A) comprises of the test of precession of perihelion, in subsection (B) deflection of light has been extensively studied and subsection (C) deals with the phenomenon of time delay. Next in Section 5.4, we have compared our results with some previous known results of classical tests under different modified theories of gravity. Finally, in Section 5.5 we discuss some concluding comments regarding the results obtained in the study.

5.2 Neutral regular black hole solution in Rastall gravity

In this section, we start by considering the following static, spherically symmetric metric in four-dimensional spacetime (Lin and Qian [2019]),

$$ds^2 = -f(r)dt^2 + \frac{dr^2}{f(r)} + r^2(d\theta^2 + \sin^2\theta d\phi^2), \quad (5.4)$$

where

$$f(r) = 1 - \frac{2M(r)}{r} = 1 - \frac{2M_0}{r}C_M(r) \quad (5.5)$$

Here, M_0 is the mass of the black hole which can be measured by an inertial observer at infinity and C_M is incorporated as a parameter which satisfies $C_M \rightarrow 1$ as $r \rightarrow \infty$.

The radial distance of the event horizon is denoted by r_p . Then from metric (5.4)

5.3. Classical Tests of General Relativity

we must have, $f(r_p) = 0$. This leads us to $2M_0 = r_p/C_M(r_p)$. Thus we may write from Eqn.(5.5),

$$f(r) = 1 - \frac{r_p C_M(r)}{r C_M(r_p)}. \quad (5.6)$$

Note that, the condition $r_p > 0$ implies $C_M(r_p) > 0$. Now, avoiding the details of the various requirements of obtaining a regular black hole solution, which have been discussed in (Lin and Qian [2019]), we assume a simple form of $C_M(r)$, as given below,

$$C_M(r) = \frac{r^3}{r^3 + 2\sigma^2}, \quad (5.7)$$

where σ is a constant. Note that, the value $\sigma = 0$ is of special interest, since then, we get $C_M(r) = 1$ and hence Eqn.(5.5) reduces to the Schwarzschild solution. Further an interesting consequence of taking the form (5.7) of $C_M(r)$ is that it actually coincides with the Hayward regular black hole solution, which was proposed by Hayward in 2006 to describe a Planck star (Hayward [2006]). It has been studied in further details in references (Abbas and Sabiullah [2014], Halilsoy et al. [2014], Lin et al. [2013]). Recently Zhao et. al. (Zhao and Xie [2017]) have studied the gravitational lensing of a modified Hayward black hole in strong field regime.

In the next section, using Eqn. (5.6) and (5.7) we thus proceed with the following black hole solution,

$$f(r) = 1 - \frac{r^2 (r_p^3 + 2\sigma^2)}{r_p^2 (r^3 + 2\sigma^2)}. \quad (5.8)$$

5.3 Classical Tests of General Relativity

In this section, following (Böhmer et al. [2010]), we have investigated the three classical tests of general relativity with respect to our neutral black hole solution (5.8). In particular, we have derived all results for $\sigma = 0$ and we have found that this correspond to $C_M(r) = 1$ by Eqn. (5.7), which in turn gives $f(r) = 1 - \frac{2M_0}{r}$ from Eqn. (5.5). This is the well known Schwarzschild black hole solution. We have tabulated our results for some appropriate values of σ and compared them with the Schwarzschild case of $\sigma = 0$.

5.3.1 Precession of Perihelion

5. Solar system Tests in Rastall gravity

In the current chapter, we have investigated the behavior of a test particle in the vicinity of the neutral regular black hole under Rastall gravity through this classical test and tabulated our results at the end.

Considering a static spherically symmetric metric of the form

$$ds^2 = -e^{\nu(r)} dt^2 + e^{\lambda(r)} dr^2 + r^2(d\theta^2 + \sin^2\theta d\phi^2), \quad (5.9)$$

where the functions ν and λ are functions of radial coordinate r only, the coordinate θ is taken as $\theta = \pi/2$, since we consider a planar orbit and ϕ is the angular coordinate. For a test particle in the spacetime metric specified by (5.9), the variation principle states,

$$\delta \int \sqrt{e^{\nu} c^2 \dot{t}^2 - e^{\lambda} \dot{r}^2 - r^2 (\dot{\theta}^2 + \sin^2\theta \dot{\phi}^2)} ds = 0. \quad (5.10)$$

Now, since neither t nor ϕ are explicitly present in the variation principle, their conjugate momenta yield the following constants of motion :

$$\begin{aligned} e^{\nu} c^2 \dot{t} = E &= \text{constant}, \\ r^2 \dot{\phi} = L &= \text{constant}, \end{aligned} \quad (5.11)$$

where E and L are related with the conservation of energy and angular momentum, respectively.

Now, Eqn. (5.9) gives the following equation of motion

$$\dot{r}^2 + e^{-\lambda} r^2 \dot{\phi}^2 = e^{-\lambda} (e^{\nu} c^2 \dot{t}^2 - 1), \quad (5.12)$$

which using (5.11) transforms to

$$\dot{r}^2 + e^{-\lambda} \frac{L^2}{r^2} = e^{-\lambda} \left(e^{-\nu} \frac{E^2}{c^2} - 1 \right). \quad (5.13)$$

Let $u = 1/r$ and since $d/ds = Lu^2 d/d\phi$, the equation (5.13) gives us

$$\left(\frac{du}{d\phi} \right)^2 + e^{-\lambda} u^2 = \frac{e^{-\lambda}}{L^2} \left(e^{-\nu} \frac{E^2}{c^2} - 1 \right). \quad (5.14)$$

5.3. Classical Tests of General Relativity

Now comparing our metric Eqn. (5.4) with the metric (5.9) we have ,

$$\begin{aligned} e^{-\lambda} &= f(r) \\ e^{\nu} &= f(r) \end{aligned} \quad (5.15)$$

where $f(r)$ is the function of radial coordinate r as given in Eqn. (5.8).

Writing,

$$f(r) = 1 - g(r), \quad (5.16)$$

where we define using Eqn.(5.8),

$$g(r) = \frac{r_p C_M(r)}{r C_M(r_p)}, \quad (5.17)$$

we can then obtain from Eqn.(5.14),

$$\left(\frac{du}{d\phi}\right)^2 + u^2 = \left(u^2 + \frac{1}{L^2}\right) g(u) + \frac{E^2}{c^2 L^2} - \frac{1}{L^2} \equiv G(u). \quad (5.18)$$

Differentiating the above equation w.r.t ϕ we get,

$$\frac{d^2 u}{d\phi^2} + u = F(u), \quad (5.19)$$

where,

$$F(u) = \frac{(2\sigma^2 u_p^3 + 1)(-4\sigma^2 u^3 + 3u^2 L^2 + 1)}{2u_p L^2 (2\sigma^2 u^3 + 1)^2}. \quad (5.20)$$

Now in the trivial case, when the test particle follows a circular orbit, let the solution of Eqn. (5.19) be $u = u_*$. Then this solution actually corresponds to a root of the equation $u_* = F(u_*)$. We have calculated the root u_* analytically and tabulated in Table 5.1. Now in the actual scenario, the test particle follows a trajectory which is slightly deviated from the circular orbit, because of the curvature of spacetime under Rastall gravity of the black hole. Let, $\delta = u - u_*$ denote this slight deviation from circular orbit, which can then be obtained by solving the differential equation (5.19) in terms of δ by substituting $u = \delta + u_*$, as given below:

$$\frac{d^2 \delta}{d\phi^2} + \left[1 - \left(\frac{dF}{du}\right)_{u=u_*}\right] \delta = O(\delta^2). \quad (5.21)$$

5. Solar system Tests in Rastall gravity

Thus the trajectory of the deviated test particle to first order in δ is given by:

$$\delta = \delta_1 \cos \left[\left(1 - \left(\frac{dF}{du} \right)_{u=u_*} \right)^{1/2} \phi + \delta_2 \right], \quad (5.22)$$

or,

$$\begin{aligned} \delta = \delta_1 \cos \left[\left(1 - \frac{3u(2\sigma^2 u_p^3 + 1)}{u_p L^2 (2\sigma^2 u^3 + 1)^3} (4\sigma^4 u^4 \right. \right. \\ \left. \left. - 4\sigma^2 L^2 u^3 - 4\sigma^2 u + L^2) \right)^{1/2} \phi + \delta_2 \right], \end{aligned} \quad (5.23)$$

where δ_1 and δ_2 are constants of integration.

At the position of perihelia, the angles which the radial distance r of the test particle makes with the black hole is minimum, or in other words, u and δ is maximum. As the orbit of the test particle advances through successive precession of perihelion the corresponding variation of angle of the orbit is given by

$$\phi = \frac{2\pi}{\sqrt{1 - \left(\frac{dF}{du} \right)_{u=u_*}}} = \frac{2\pi}{1 - \sigma}, \quad (5.24)$$

where σ denotes the rate of advance of perihelion and is defined as,

$$\sigma = 1 - \sqrt{1 - \left(\frac{dF}{du} \right)_{u=u_*}}. \quad (5.25)$$

Approximating for small values of $\left(\frac{dF}{du} \right)_{u=u_*}$ we get,

$$\sigma = \frac{1}{2} \left(\frac{dF}{du} \right)_{u=u_*}. \quad (5.26)$$

Now, if a test particle advances through ϕ radians then its perihelion will advance through $\sigma\phi$ radians. For a complete rotation $\phi \approx 2\pi(1 + \sigma)$ and the advance of perihelion is given as $\delta\phi = \phi - 2\pi \approx 2\pi\sigma$.

We have tabulated the different values of root u_* and advance of perihelion $\delta\phi$ corresponding to different values of σ . We have taken the constants of motion as $L = 2.23 \times 10^{14}$ and $E = 1$, to get promising values of precision of perihelia. Note that, for $\sigma = 0$ we have the advance of perihelion $\delta\phi = 43.13876287$ arcsecs/century,

5.3. Classical Tests of General Relativity

Table 5.1: Measurement of Advance of Perihelion ($\delta\phi$ in arcsecs. per century.) for different values of σ , taking $L = 2.23 \times 10^{14}$ and $E = 1$.

Advance of Perihelia		
σ	u_*	Advance of Perihelion($\delta\phi$) (in arcsecs/century)
0	$1.493736921 \times 10^{-17}$	43.13876287
10^{-6}	$1.480420864 \times 10^{-17}$	42.75482095
10^{-5}	$1.534745603 \times 10^{-17}$	44.32388966
0.7187×10^{-4}	$1.523644028 \times 10^{-17}$	44.00247291
10^{-4}	$1.548794029 \times 10^{-17}$	44.729538046
10^{-3}	$1.563036235 \times 10^{-17}$	45.14088882
10^{-2}	$1.622015714 \times 10^{-17}$	46.84435283
0.1	$1.857055518 \times 10^{-17}$	53.63241839
0.2	$2.292683390 \times 10^{-17}$	66.21386860

which is quite close to the value calculated for Schwarzschild black hole in Einstein gravity.

5.3.2 Gravitational Lensing

Here we have calculated the angle of deflection of light, by considering the static spherically symmetric metric of the Eqn.(5.9), we know that a photon follows a null geodesic $ds^2 = 0$, when external forces are absent. Then the equation of motion of a photon can be written as :

$$\dot{r}^2 + e^{-\lambda} r^2 \dot{\phi}^2 = e^{\nu-\lambda} c^2 \dot{t}^2, \quad (5.27)$$

where the ‘dot’ represents derivative with respect to the arbitrary affine parameter. Using the two constants of motion from Eqn. (5.11) in Eqn. (5.27), we get

$$\dot{r}^2 + e^{-\lambda} \frac{L^2}{r^2} = \frac{E^2}{c^2} e^{-\nu-\lambda}. \quad (5.28)$$

Now, using $r = \frac{1}{u}$ and eliminating the derivatives with respect to the affine parameter by the help of the conservation equations, we obtain using (5.15),

$$\left(\frac{du}{d\phi} \right)^2 + u^2 f(u) = \frac{1}{c^2} \frac{E^2}{L^2}. \quad (5.29)$$

5. Solar system Tests in Rastall gravity

Now from Eqn. (5.16) and (5.8), the above equation gets transformed to the following

$$\left(\frac{du}{d\phi}\right)^2 + u^2 = P(u), \quad (5.30)$$

where we define

$$\begin{aligned} P(u) &= u^2 g(u) + \frac{1}{c^2} \frac{E^2}{L^2} \\ &= \frac{u^3 (1 + 2\sigma^2 u_p^3)}{u_p (1 + 2\sigma^2 u^3)} + \frac{1}{c^2} \frac{E^2}{L^2}. \end{aligned} \quad (5.31)$$

Differentiating Eqn. (5.30) with respect to ϕ , we get

$$\frac{d^2 u}{d\phi^2} + u = Q(u), \quad (5.32)$$

where we define

$$Q(u) = \frac{1}{2} \frac{dP(u)}{du},$$

Hence from equations (5.31) we have

$$Q(u) = \frac{3u^2 (1 + 2\sigma^2 u_p^3)}{2u_p (1 + 2\sigma^2 u^3)^2}. \quad (5.33)$$

Thus Eqn.(5.32) leads to the following second order non-linear differential equation,

$$\frac{d^2 u}{d\phi^2} + u = \frac{3u^2 (1 + 2\sigma^2 u_p^3)}{2u_p (1 + 2\sigma^2 u^3)^2}. \quad (5.34)$$

In order to solve the above differential equation we use a perturbative method as in (Böhmer et al. [2010]). First as a zeroth approximation, when the terms in the right hand side of differential equation (5.34) is neglected, the solution is given as

$$u = \frac{\cos\phi}{R}, \quad (5.35)$$

where R is the distance of closest approach to the black hole. This solution corresponds to the case, when the photon travel in a straight line path, without being deflected, in the absence of the gravitating black hole. Then in the next approximation, we replace u in the right hand side of Eqn. (5.34), with the zeroth solution in Eqn. (5.35), hence, the right hand function $Q(u)$ converts to a function $Q(\frac{\cos\phi}{R})$ in

5.3. Classical Tests of General Relativity

the independent variable ϕ . Thus Eqn. (5.34) gives,

$$\frac{d^2 u}{d\phi^2} + u = \frac{3R^4 (1 + 2\sigma^2 u_p^3) \cos^2 \phi}{2u_p (R^3 + 2\sigma^2 \cos^3 \phi)^2}. \quad (5.36)$$

Expanding the denominator of Eqn. (5.36) in the right hand side of the above equation and neglecting higher order terms, we get,

$$\frac{d^2 u}{d\phi^2} + u = \frac{3 (1 + 2\sigma^2 u_p^3)}{2u_p} \left[\left(\frac{\cos \phi}{R} \right)^2 - 4\sigma^2 \left(\frac{\cos \phi}{R} \right)^5 \right]. \quad (5.37)$$

The general solution of the differential equation (5.37) can then be obtained as a combination of the solutions of the two approximations, as,

$$u = \left(\frac{\cos \phi}{R} \right) + \frac{(1 + 2\sigma^2 u_p^3)}{8u_p R^5} (2\sigma^2 \cos^5 \phi + 5\sigma^2 \cos^3 \phi - 4R^3 \cos^2 \phi - 15\sigma^2 \cos \phi - 15\sigma^2 \phi \sin \phi + 8R^3). \quad (5.38)$$

Now, light approaches the black hole from a distant source, which can be assumed to be located at infinity, at an asymptotic angle $\phi = -(\frac{\pi}{2} + \epsilon)$, gets deflected near the black hole at a closest distance of approach R , and then reaches a distant observer on Earth, which can also be assumed to be located at infinity, at an asymptotic angle $\phi = (\frac{\pi}{2} + \epsilon)$. Thus, the solution of the equation $u(\frac{\pi}{2} + \epsilon) = 0$ yields the angle ϵ . The total deflection angle of the light ray can be obtained as $\delta = 2\epsilon$. Hence putting $\phi = \pi/2 + \epsilon$ and $u = 0$ in (5.38) and noting that $\cos(\frac{\pi}{2} + \epsilon) \approx -\sin \epsilon$ and $\sin(\frac{\pi}{2} + \epsilon) \approx \cos \epsilon$ we get,

$$-\left(\frac{\sin \epsilon}{R} \right) + \frac{(1 + 2\sigma^2 u_p^3)}{8u_p R^5} (-2\sigma^2 \sin^5 \epsilon - 5\sigma^2 \sin^3 \epsilon - 4R^3 \sin^2 \epsilon + 15\sigma^2 \sin \epsilon - 15\sigma^2 (\pi/2 + \epsilon) \cos \epsilon + 8R^3) = 0. \quad (5.39)$$

Writing $\sin \epsilon \approx \epsilon$ and $\cos \epsilon \approx 1$ since ϵ is small, Eqn.(5.39) becomes,

$$-\frac{\epsilon}{R} + \frac{(1 + 2\sigma^2 u_p^3)}{8u_p R^5} (-2\sigma^2 \epsilon^5 - 5\sigma^2 \epsilon^3 - 4R^3 \epsilon^2 + 15\sigma^2 \epsilon - 15\sigma^2 (\pi/2 + \epsilon) + 8R^3) = 0. \quad (5.40)$$

5. Solar system Tests in Rastall gravity

This reduces to the following fifth degree equation in ϵ ,

$$\begin{aligned} & (8u_p^3\sigma^4 + 4\sigma^2)\epsilon^5 + (20u_p^3\sigma^4 + 10\sigma^2)\epsilon^3 \\ & + (16R^3u_p^3\sigma^2 + 8R^3)\epsilon^2 + 16R^4u_p\epsilon + 30\pi u_p^3\sigma^4 \\ & - 32R^3u_p^3\sigma^2 + 15\pi\sigma^2 - 16R^3 = 0 \end{aligned} \quad (5.41)$$

Solving for ϵ we can obtain the total deflection angle as $\delta = 2\epsilon$.

For $\sigma = 0$, if we consider Eqn. (5.41) we get,

$$\epsilon^2 + 2Ru_p\epsilon - 2 = 0 \quad (5.42)$$

which yield the solution,

$$\delta = -2Ru_p + 2\sqrt{R^2u_p^2 + 2}. \quad (5.43)$$

When $\sigma = 0$, we have obtained the deflection angle as 1.750992937 arcsecs, taking distance of closest approach $R = 3.5 \times 10^{17}m$, but taking distance of closest approach $R = 1M_o$, we get the deflection angle as 583405.5203 arcsecs.

We have calculated the deflection angles for some other non zero values of σ and tabulated in Table 5.2, taking the distance of closest approach again as $1M_o$.

5.3.3 Time Delay

This phenomenon, by which the apparent travel time of light is altered by the gravity of a body, was originally discussed by L.I. Schiff and also by Shapiro, with reference to our Sun. The basic idea involves emission of a radar signal from earth and observing the time taken by the round trip after reflecting back from a distant planet or satellite. This observation is made under the following two conditions, one, when the signal passes close to the body under the influence of its gravity, and second when the signal does not travel close to it, *i.e.*, in the absence of the gravitational field. Now, the time of travel of light when the black hole is not in the vicinity can be given as:

$$T_0 = \int_{-l_1}^{l_2} \frac{dx}{c}, \quad (5.44)$$

where l_1 and l_2 are the distances of the Earth and the reflecting planet or satellite from

5.3. Classical Tests of General Relativity

Table 5.2: Measurement of Angle of Deflection (in arcsecs.) for different values of σ , taking distance of closest approach as $1M_o$. Only for the first row, we have taken $R=3.5 \times 10^{17}m$.

Angle of Deflection	
σ	Angle of Deflection (δ)(in arcsecs)
0 (when $R = 3.5 \times 10^{17}m$)	1.750992937
0	583405.5203
10^{-6}	125.8243863
10^{-5}	12.58243892
0.7187×10^{-4}	1.750721987
10^{-4}	1.258243892
10^{-3}	0.1258243892
10^{-2}	0.01258243892
0.1	0.001258243892
0.2	0.0006291219460
0.5	0.0002516487784
1	0.0001258243892

the black hole respectively; and dx is the differential distance in the radial direction. For the case when the light travels close to the black hole we have the time of travel as,

$$T_w = \int_{-l_1}^{l_2} \frac{dx}{v} = \frac{1}{c} \int_{-l_1}^{l_2} e^{(\lambda(r)-\nu(r))/2} dx, \quad (5.45)$$

where $v = ce^{(\nu-\lambda)/2}$ is the speed of light in the presence of gravitational field.

The time difference of the above two cases can then be calculated as,

$$\delta T = T_w - T_0 = \frac{1}{c} \int_{-l_1}^{l_2} [e^{(\lambda(r)-\nu(r))/2} - 1] dx. \quad (5.46)$$

Taking $r = \sqrt{x^2 + R^2}$ we can write in Eqn. (5.46) the functions λ and ν in terms of x as,

$$\delta T = \frac{1}{c} \int_{-l_1}^{l_2} [e^{(\lambda(\sqrt{x^2+R^2})-\nu(\sqrt{x^2+R^2}))/2} - 1] dx. \quad (5.47)$$

5. Solar system Tests in Rastall gravity

Table 5.3: Measurement of Time Delay (in secs.) for different values of σ . The distance of closest approach have been taken as $1M_o$ for all values of σ . We have taken $l_1 = 149.6 \times 10^9$ m and $l_2 = 227.9 \times 10^9$ m which are the distances of our Sun from Earth and Mars respectively.

Time Delay	
σ	Time Delay(δT)(in secs)
0	$5.615431364 \times 10^{-8}$
10^{-6}	$5.615431364 \times 10^{-8}$
10^{-5}	$5.615431364 \times 10^{-8}$
0.7187×10^{-4}	$5.615431380 \times 10^{-8}$
10^{-4}	$5.615431400 \times 10^{-8}$
10^{-3}	$5.615434790 \times 10^{-8}$
10^{-2}	$5.615773915 \times 10^{-8}$
0.1	$5.649686240 \times 10^{-8}$
0.5	$6.471803289 \times 10^{-8}$

Finally using Eqn. (5.15), Eqn. (5.17) and Eqn. (5.16); Eqn. (5.47) becomes,

$$\delta T = \frac{1}{c} \int_{-l_1}^{l_2} \frac{(r_p^3 + 2\sigma^2)(x^2 + R^2) dx}{r_p^2 \left[(x^2 + R^2)^{3/2} + 2\sigma^2 \right] - (r_p^3 + 2\sigma^2)(x^2 + R^2)}. \quad (5.48)$$

We have calculated the different values of time delay (δT) numerically corresponding to the different values of parameter σ and tabulated them in Table 5.3. The distance of closest approach have been taken as $1M_o$ for all values of σ . We have taken $l_1 = 149.6 \times 10^9$ m and $l_2 = 227.9 \times 10^9$ m which are the distances of our Sun from Earth and Mars respectively..

5.4 A comparative study

In this section we have briefly compared our results with some previously known results on the classical tests in modified gravity. Rahaman et. al. in ref. [Rahaman et al. \[2018\]](#) had studied the classical tests of general relativity with respect to static and spherically symmetric dyon black hole which carries both the electric and magnetic charge simultaneously, which are encoded in the parameters λ_0 and β_0 . The values of the two parameters have been constrained using the Solar system tests and the permissible ranges have been obtained from analysing the model with the available observational data. The values of classical tests for dyon black holes are close

5.4. A comparative study

to observational results when λ_0 and β_0 are closer to zero and they increase with increase in values of the parameters. In our current paper, though the parameter σ is in no way comparable to the parameters in ref. [Rahaman et al. \[2018\]](#), yet our model's precession of perihelia values are also closer to observational data when the value of our parameter is close to zero. For deflection of light however our model shows more fluctuations.

In ref. [Manna et al. \[2018\]](#), Manna et. al. had found the deflection angle of a regular black hole with electrodynamics source in the strong field regime and compared the angle of deflection as a function of distance of closest approach, graphically with Schwarzschild and Reissner-Norstrom case. The angle of deflection is infinitely large at the photon sphere since the light loops around the black hole, but as the distance of closest approach increases, its initially slightly higher than that of the Schwarzschild case but gradually decreases and becomes lesser than Schwarzschild angle. This phenomenon can also be observed in our model to the extent that initially the angle of deflection is enormously high but gradually decreases to negligible values. Refs. [Bhar et al. \[2016\]](#) and [Rahaman et al. \[2014c\]](#) investigate wormhole models. These papers provide an excellent background study for our paper but the results of these wormhole models with our black hole model is not directly comparable.

Zhou et. al. ([Zhou and Liu \[2012\]](#)) had investigated the three classical tests of general relativity, in the spherically asymptotically flat black hole solution of infrared modified Horava-Lifshitz gravity. The first order corrections from the standard general relativity have been used to limit the parameters in Horava-Lifshitz gravity. This leads to the conclusion that in Horava-Lifshitz gravity, the precession of perihelia is less while the angle of deflection is more, than that of traditional general theory of relativity. Note that it is possible to draw this conclusion from the concerned analytic expressions itself, but for our model no such conclusion could be drawn by studying the analytical expression and hence, we have obtained a plethora of diverse results, corresponding to a variety of values of our parameter. Then we have identified the value of our parameter which is matching with the observational data of traditional general relativity. Edery et. al. ([Edery and Paranjape \[1998\]](#)) had studied the deflection of light and time delay in the exterior of a static spherically symmetric source. Their expression of angle of deflection contains an extra term dependent on the Weyl parameter. Although the observational results have been used to constraint the magnitude of this parameter to the order of the inverse Hubble length, yet the signature cannot be ascertained. However, when this parameter is negative, it causes the angle

5. Solar system Tests in Rastall gravity

of deflection to increase and therefore imitate the effect of dark matter. Kalligas et. al. (Kalligas et al. [1995]) had investigated the classical tests in Kaluza-Klein gravity and found a variety of interesting results. Similar to our model, they too have found that for certain values of their parameters, they have the standard general relativity results, for other values they have obtained both positive and negative values of the classical tests. More elaborately for deflection of light they have shown certain values of parameters correspond to null deflection, and also some correspond to light repulsion, i.e., negative angle of deflection. Similarly there exists some values of the parameters for which radar ranging they have obtained negative results and geodetic regression instead of geodetic advance in case of precession of perihelia.

In the braneworld model of ref. (Jalalzadeh et al. [2009]) the observational results have been used to constraint the braneworld parameter but overall for positive value of the parameter the angle of deflection, precession of perihelia and time delay increases as compared to the Schwarzschild case. References (Cuzinatto et al. [2014], Dahia and de Albuquerque Silva [2015], Casadio et al. [2015]) have studied braneworld models and mainly constrained their parameters using the fact that the fifth dimensional causes a correction of 0.1 percent to the observational data obtained from the four dimensional case. All the papers on modified gravity discussed above have their individual parameters and these parameters are themselves neither comparable to each other nor to the parameter σ in our model, but the effect of these parameters in the results of the classical tests have been discussed above. In interesting common fact is that if we let these parameters vary by themselves we will get a variety of results, which may or may not be physically valid, but if we use the standard results of general relativity to constraint these parameters then we get more physically agreeable results. Also almost all the results of the modified theories can be reduced to the standard general relativity results for appropriate values of the parameters.

5.5 Conclusion

In this paper we have successfully conducted the tests of precession of perihelia, deflection of light and time delay with reference to a neutral regular black hole under Rastall gravity for various values of the parameter σ , and then compared them with $\sigma = 0$. The value $\sigma = 0$ is of special importance, since $\sigma = 0$ correspond to $C_M(r) = 1$ by Eqn. (5.7), which in turn gives $f(r) = 1 - \frac{2M_0}{r}$ from Eqn.(5.5). For this expression

5.5. Conclusion

of $f(r)$ the metric Eqn.(5.4) reduces to the Schwarzschild solution. Thus $\sigma = 0$ forms a basis to compare our results in modified Rastall gravity with the Einstein gravity.

From table 5.1, the value of precession of perihelia, for $\sigma = 0$, which correspond to the Schwarzschild solution, is given as 43.13876287 arcsecs per century, which is quite close to the actual value, with respect to solar system, in Einstein gravity. We have found the value of precession of perihelia for some other small values of σ , and found that the values of precession of perihelia oscillates when $\sigma < 10^{-3}$. But increases monotonically with increase in magnitude of $\sigma \geq 10^{-3}$. We have taken the constants of motion as $L = 2.23 \times 10^{14}$ and $E = 1$, to get promising values of precession of perihelia. Another interesting observation is that at the value of $\sigma = 0.7187 \times 10^{-4}$ we are arriving at the value of precession of perihelia as 44.00247291 arcsecs per century. The significance of taking this particular value will be more clear in the next paragraph.

We have tabulated the angle of deflection values in table 5.2. When $\sigma = 0$, we have obtained the deflection angle as $\delta = 583405.5203$, for $R = 1M_o$. The deflection angles for different non zero values of σ , taking the distance of closest approach as $1M_o$ are also tabulated. We have come to the conclusion that, for $R = 1M_o$, the angle of deflection decreases monotonically with increase in the magnitude of σ and becomes negligible for $\sigma > 1$. Note that as previously mentioned, very interesting feature of the tabulated values is that, corresponding to $\sigma = 0.7187 \times 10^{-4}$ and $R = 1M_o$, we get $\delta = 1.750721987$ arcsecs, which is close to the observed value of deflection of light with respect to our Sun. Also for $\sigma = 0$, the numerical value $R = 3.5 \times 10^{17}$ m, of the distance of closest approach, also yields the angle of $\delta = 1.749952260$ arcsecs. Thus, this value of $\sigma = 0.7187 \times 10^{-4}$ with $R = 1M_o$ in Rastall gravity corresponds to the observed value in Schwarzschild case.

We have calculated numerically the different values of time delay (δT) corresponding to the different values of parameter σ and tabulated them in table 5.3. The distance of closest approach have been taken as $1M_o$ for all values of σ . We have taken $l_1 = 149.6 \times 10^9$ m and $l_2 = 227.9 \times 10^9$ m which are the distances of our Sun from Earth and Mars respectively. we have found that the magnitude of time delay is of the order 10^{-8} and increases slightly with increase in value of σ . Thus we conclude that solar tests support Rastall gravity. However, to accept this theory, one will have to study the present state of the universe within the framework of Rastall gravity.

Chapter 6

Singularity-free non-exotic compact star in $f(R, T)$ gravity ¹

6.1 Introduction

Harko et al. (Harko et al. [2011]) have proposed the extended theory of gravity so called $f(R, T)$ by changing the geometrical part of the Einstein field equations instead of changing the source side by taking a generalized functional form of the argument to address galactic, extra-galactic, and cosmic dynamics. In this theory, the gravitational terms of total action is defined by the functional form of $f(R)$ and $f(T)$. The main aim of this theory is to address some observational phenomenons such as dark energy (Riess et al. [2004]), dark matter (Akerib et al. [2017]), massive pulsars (Antoniadis et al. [2013]) that were hardly explain by General Relativity (GR). Among the all extended/modified theories of gravity, the $f(R, T)$ theory attract more due to it's unique feature that is non-minimal coupling of matter and geometry (Yadav [2019]). In the recent past, several applications of $f(R, T)$ (Moraes and Sahoo [2017], Kumar Yadav [2014], Yadav and Ali [2018], Moraes [2015], Singh and Kumar [2014], Shabani and Farhoudi [2013, 2014], Reddy and Santhi Kumar [2013], Sharif and Zubair [2014]) have been reported in the literature.

In this paper, we focus ourselves to investigate a non-exotic compact star with

¹A considerable part of this chapter has been published in **Pramana J. Phys.** **94:90**, (2020).

6. Singularity-free non-exotic compact star in $f(R, T)$ gravity

in $f(R, T) = R + 2\zeta T$ formalism where ζ being the arbitrary constant. The compact star is a hypothetical dense body that may be black hole or degenerate star and the pressure inside it is not isotropic. In Astrophysics, the structure and properties of compact star had been studied by numerous authors in different physical context (Bowers and Liang [1974], Herrera et al. [2004], Sharma et al. [2001]). In 2006, the most significant compact star has been observed by Rosat Surveys due to their X-rays emission (Agüeros et al. [2006]). This means that the gravitational energy of compact star is radiated through X-rays. A long ago, Hewish et al (Hewish et al. [1979]) had investigated the some rapidly pulsating radio source which is in general the beam of electromagnetic radiation. This discovery inspire physicists to think about modeling of compact star like neutron star and quark star in framework of general relativity and its extended form (Maurya et al. [2015, 2016b, 2017], Das et al. [2016]). It is common understanding that one can not analyze the structure and properties of compact star by taking into account of equation of state which relate the pressure and energy density in proportion. In Refs. (Maurya et al. [2016a], Aziz et al. [2016], Rahaman et al. [2014b]), it has been found that the pressure of compact star is anisotropic in nature. In the recent past, Momeni et al (Momeni et al. [2017]) have constructed a model of compact star in Horndeski theory of gravity and analyzed it in modified theory of gravity. However, our model deals with the singularity-free compact star composed by non-exotic matter in $f(R, T)$ theory of gravity and its functional form $f(R, T) = R + 2\zeta T$. In Refs. Moraes and Sahoo [2017, 2018], some applications of $f(R, T)$ theory with respect to stellar objects are reported. Some other relevant investigations on different functional forms of extended $f(R, T)$ theory of gravitation can be observed in following studies (Zubair et al. [2016a]) under different physical context. In 2014, Rahaman et al (Rahaman et al. [2014a]) have studied the static Wormhole in $f(R)$ Gravity with Lorentzian distribution which generates two models - one is derived from power law form and second model is based on assumption of particular shape function which allows the reconstruction of the $f(R)$ theory. Zubair et al (Zubair et al. [2016b]) have investigated numerical solutions for different wormhole matter content in the realm of $f(R, T)$ gravity. Moraes et al (Moraes [2015]) have constructed the model of static Wormhole by applying $f(R, T)$ formalism.

In the present chapter, we are concerned with the singularity-free nonexotic model of compact star with the realm of functional form of $f(R, T) = R + 2\zeta T$. It is worth to mention that our model is derived from the well known barotropic equation of state

6.2. The $f(R, T) = f(R) + 2\zeta T$ Formalism

(EoS) in Krori and Barua (KB) space-time (Krori and Barua [1975]) that yield the singularity-free solution. In Ref. Das et al. [2016], the authors have investigated a model of stellar object in the static spherically symmetric space-time which is probably singular and generate a set of solutions describing the interior of a compact star under $f(R, T)$ theory of gravity which admits conformal motion whereas the present investigation is one with singularity-free solution. However a common feature of both the investigations is the non-exotic matter configuration in $f(R, T)$ gravity.

The chapter is structured as follows: The basics of $f(R, T) = f(R) + 2\zeta T$ formalism are presented in Section 6.2. Section 6.3 deals with the the KB metric, solution of field equations and physical behavior of the model. In section 6.4, we provide the boundary conditions, which are essential for finding the values of constants. In section 6.5, we demonstrate the validity of energy conditions, stability and mass -radius relation to show the physical acceptance of model. In Section 6.6, we match the model parameters with observation data sets. In section 6.7, we point out our results and discuss the future perspectives of the study.

6.2 The $f(R, T) = f(R) + 2\zeta T$ Formalism

The total action for the $f(R, T)$ theory of gravitation (Harko et al. [2011]) reads

$$S = \frac{1}{4\pi} \int d^4x f(R, T) \sqrt{-g} + \int d^4x L_m \sqrt{-g}, \quad (6.1)$$

where R is the Ricci scalar, T is the trace of energy-momentum tensor T_j^i , g is the metric determinant and L_m is the matter Lagrangian density.

By varying the total action S with respect to metric g_{ij} , we obtain

$$\begin{aligned} R_{ij} f'(R, T) - \frac{1}{2} f(R, T) g_{ij} + (g_{ij} \nabla^i \nabla_i - \nabla_i \nabla_j) f'(R, T) \\ = 8\pi T_{ij} - \dot{f}(R, T) \theta_{ij} - \dot{f}(R, T) T_{ij}. \end{aligned} \quad (6.2)$$

Here, $f'(R, T) = \frac{\partial f}{\partial R}$ and $\dot{f}(R, T) = \frac{\partial f}{\partial T}$ and θ_{ij} is read as

$$\theta_{ij} = g^{ij} \frac{\partial T_{ij}}{\partial g^{ij}}. \quad (6.3)$$

6. Singularity-free non-exotic compact star in $f(R, T)$ gravity

In this chapter, we take the more generic form matter Lagrangian as $L_m = -\rho$ (Moraes and Sahoo [2017]). Hence equation (6.3) leads to

$$\theta_{ij} = -2T_{ij} - \rho g_{ij} \quad (6.4)$$

Following the proposition of Refs. Harko et al. [2011], we assume the functional form of $f(R, T) = f(R) + 2\zeta T$ with ζ is constant. In the literature, this functional form is commonly used to obtain cosmological solution in $f(R, T)$ theory of gravitation (Kumar Yadav [2014], Yadav and Ali [2018], Moraes [2015]).

The equations (6.2) and (6.4) lead to

$$G_{ij} = (8\pi + 2\zeta)T_{ij} + \zeta(2\rho + T)g_{ij} \quad (6.5)$$

where G_{ij} is Einstein's tensor.

6.3 The KB Metric and Field Equations

The Krori and Barua space-time (Krori and Barua [1975], Rahaman et al. [2012]) is read as

$$ds^2 = -e^{\nu(r)}dt^2 + e^{\lambda(r)}dr^2 + r^2(d\theta^2 + \sin^2\theta d\phi^2), \quad (6.6)$$

with $\lambda(r) = Ar^2$ and $\nu(r) = Br^2 + C$ having A , B and C are constants.

In this chapter, we take an anisotropic fluid satisfying the matter content of stellar object as

$$T_{ij} = \text{diag}(-\rho, p_r, p_t, p_t), \quad (6.7)$$

where ρ , p_r and p_t are the energy density, radial pressure and tangential pressure respectively. Thus the trace of energy momentum tensor may be expressed as $T = -\rho + p_r + 2p_t$.

The metric (6.6) and field equation (6.5) along with equation (6.7) lead the following equations:

$$e^{-\lambda} \left(\frac{\lambda'}{r} - \frac{1}{r^2} \right) + \frac{1}{r^2} = (8\pi + \zeta)\rho - \zeta(p_r + 2p_t), \quad (6.8)$$

6.3. The KB Metric and Field Equations

$$e^{-\lambda} \left(\frac{\nu'}{r} + \frac{1}{r^2} \right) - \frac{1}{r^2} = \zeta \rho + (8\pi + 3\zeta)p_r + 2\zeta p_t, \quad (6.9)$$

$$\frac{e^{-\lambda}}{2} \left(\frac{\nu'^2 - \lambda' \nu'}{2} + \frac{\nu' - \lambda'}{r} + \nu'' \right) = \zeta \rho + \zeta p_r + (8\pi + 4\zeta)p_t. \quad (6.10)$$

6.3.1 Solution of Field Equations & Physical Parameters

To solve the above set of equations for the matter content of compact star, it is useful to invoke the equation of state (EoS) which gives the relation between energy density and pressure. The most common barotropic forms of EoS ([Azreg-Aïnou \[2015\]](#)) are

$$p_r = \alpha \rho, \quad (6.11)$$

$$p_t = \beta \rho, \quad (6.12)$$

where α and β are constants having values in the range (0,1).

Now, from metric (6.6), one may obtain $\lambda' = 2Ar$, $\nu' = 2Br$ and $e^{-\lambda} = e^{-Ar^2}$. Putting these values in equations (6.8)–(6.10) along with the barotropic EoS (6.11) and (6.12), we obtain

$$\rho = \frac{1}{[8\pi + \zeta - \zeta(\alpha + 2\beta)]} \left[\exp(-Ar^2) \left(2A - \frac{1}{r^2} \right) + \frac{1}{r^2} \right], \quad (6.13)$$

$$p_r = \frac{\alpha}{[8\pi + \zeta - \zeta(\alpha + 2\beta)]} \left[\exp(-Ar^2) \left(2A - \frac{1}{r^2} \right) + \frac{1}{r^2} \right], \quad (6.14)$$

$$p_t = \frac{\beta}{[8\pi + \zeta - \zeta(\alpha + 2\beta)]} \left[\exp(-Ar^2) \left(2A - \frac{1}{r^2} \right) + \frac{1}{r^2} \right]. \quad (6.15)$$

We observe that the barotropic EoS (6.11) and (6.12) are identically satisfied with solutions (6.13)–(6.15). Also we note that the energy density (ρ), radial pressure (p_r) and tangential pressure (p_t) decrease with r and finally approaches to a small positive values. The behavior of ρ , p_r and p_t is graphed in Fig. 6.2 for physically acceptable values of problem parameters. Fig. 6.1 depicts the variation of λ against r .

It is worth to note that $\frac{d\rho}{dt}$ and $\frac{dp_r}{dt}$ are negative which lead the following requirements for our model to be physically acceptable:

- (i) The energy density is positive and its first derivative is negative.

6. Singularity-free non-exotic compact star in $f(R, T)$ gravity

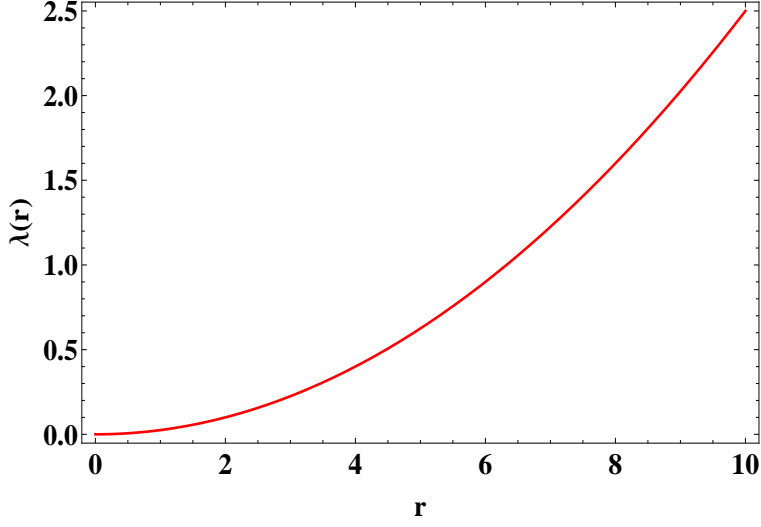


Figure 6.1: Plot of λ versus r .

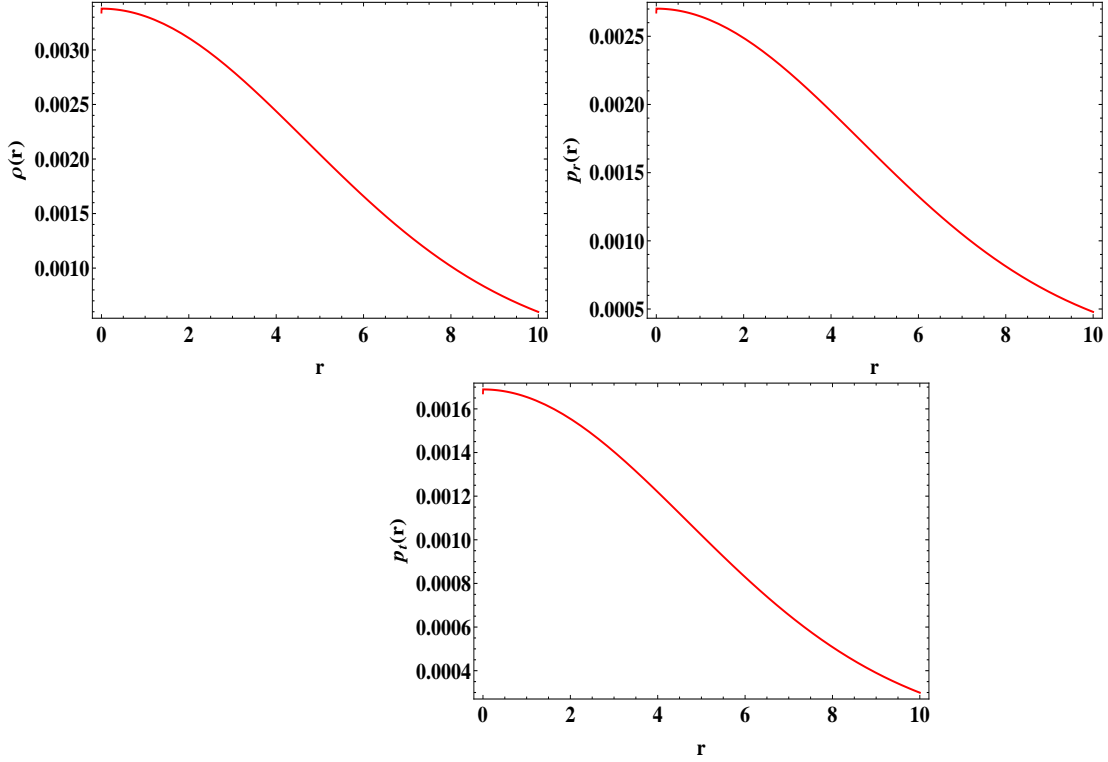


Figure 6.2: Plots of $\rho(r)$ vs r (upper panel), $p_r(r)$ vs r (middle panel) and $p_t(r)$ vs r (lower panel).

- (ii) The radial pressure is positive and radial pressure gradient is negative.

We also note that at $r = 0$, the second derivative of energy density as well as

6.4. Boundary Conditions

radial pressure are negative which shows that the energy density and radial pressure are maximum at the center of wormhole.

The anisotropic parameter (Δ) is computed as

$$\Delta = \frac{2(\beta - \alpha)}{r[8\pi + \zeta - \zeta(\alpha + 2\beta)]} \left[\exp(-Ar^2) \left(2A - \frac{1}{r^2} \right) + \frac{1}{r^2} \right]. \quad (6.16)$$

The anisotropic parameters is equivalent to a force due to the local anisotropy which is directed inward if radial pressure is greater than the tangential pressure and outward when radial pressure is less than tangential pressure. From equation (6.16), we observe that the nature of Δ depends on the free parameters α and β . These parameters are positive constant having values in between 0 and 1 but $(\beta - \alpha)$ may be positive or negative depending upon the choice of values of these parameters. Thus the repulsive anisotropic force ($\Delta > 0$) will appear when $\beta > \alpha$. Under this specification, the compact star allows the construction of more massive distribution ([Rahaman et al. \[2012\]](#)) that is why we have taken $\beta > \alpha$ throughout the all graphical analysis of the model. Fig. 6.3 shows the variation of Δ with respect to r for different choice of α and β .

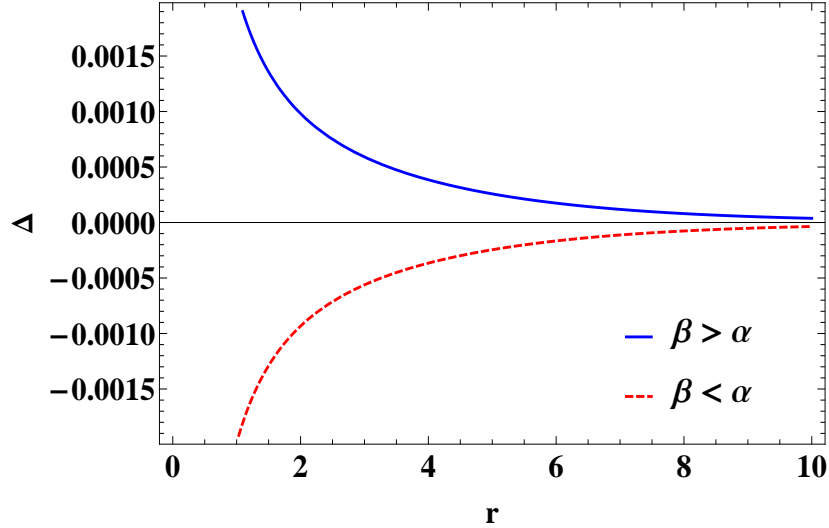


Figure 6.3: The variation of the force Δ due to the local anisotropy against r .

6.4 Boundary Conditions

6. Singularity-free non-exotic compact star in $f(R, T)$ gravity

The central density is obtained by putting $r = 0$ in equation (6.13) i.e.

$$\rho_c = \rho(r = 0) = \frac{3A}{8\pi + \zeta(1 - \alpha - 2\beta)}. \quad (6.17)$$

The radial pressure and tangential pressure at center are given by

$$p_{rc} = p_r(r = 0) = \frac{3A\alpha}{8\pi + \zeta(1 - \alpha - 2\beta)}, \quad (6.18)$$

$$p_{tc} = p_t(r = 0) = \frac{3A\beta}{8\pi + \zeta(1 - \alpha - 2\beta)}. \quad (6.19)$$

At center anisotropy is zero which leads $\alpha = \beta$. It is also required that the physical fluids must obey the Zeldovich's criterion i.e. $\frac{p_{rc}}{\rho_c} \leq 1$. This implies that $\alpha = \beta \leq 1$. This shows the physical constraints on α and β .

The surface density is obtained by putting $r = R$ in Eqn. (6.13) i.e.

$$\rho(r = R) = \frac{(1 - \frac{2M}{R})(2A - \frac{1}{R^2}) + \frac{1}{R^2}}{8\pi + \zeta(1 - \alpha - 2\beta)} \quad (6.20)$$

To obtain the boundary condition, we will compare the interior metric to the Schwarzschild exterior at the boundary $r = R$ which leads the following equations:

$$1 - \frac{2M}{R} = e^{BR^2+C}, \quad (6.21)$$

$$e^{AR^2} \left(1 - \frac{2M}{R}\right) = 1, \quad (6.22)$$

$$\frac{M}{R^3} = Be^{BR^2+C}. \quad (6.23)$$

The values of constants A and B are evaluated by choosing the boundary conditions such that $p_r = 0$ at $r = R$ and $\rho = a = \text{constant}$ at $r = 0$. Thus, solving equations (6.13), (6.14) and (6.21)–(6.23) along with boundary conditions, we obtain

$$A = \frac{[8\pi + \zeta(1 - \alpha - 2\beta)]a}{3} = \frac{1}{R^2} \ln \left[1 - \frac{2M}{R}\right]^{-1}, \quad (6.24)$$

$$B = \frac{1}{2R^2} \left[e^{\frac{[8\pi + \zeta(1 - \alpha - 2\beta)]aR^2}{3}} - 1 \right] = \frac{M}{R^3} \left(1 - \frac{2M}{R}\right)^{-1}. \quad (6.25)$$

From Equation (6.24), it is evident that A is a positive constant and its numerical

6.5. Physical Consequences of Model Under $f(R, T)$ Gravity

Table 6.1: Determination of model parameters A & B for different star candidates.

S.N.	Stars	A	B	$\rho(r=0)(gm/cm^3)$	$p(r=0)(dyne/cm^2)$
1.	PSRJ 1614-2230	0.00213	0.00128	0.361232×10^{15}	2.682920×10^{35}
2.	PSRJ 1903+327	0.00489	0.00306	0.815675×10^{15}	6.058156×10^{35}
3.	4U 1820-30	0.00515	0.00321	0.859045×10^{15}	6.380260×10^{35}
4.	VelaX-1	0.00506	0.00322	0.841611×10^{15}	6.250785×10^{35}
5.	4U 1608-51	0.00541	0.00345	0.899825×10^{15}	6.683146×10^{35}

value can be constraint by the specific choice of other free parameters namely ζ , α and β . In Refs. [Buchdahl \[1959\]](#), Buchdahl has obtained that the maximum allowable compactness for a fluid sphere is $\frac{2M}{R} < 8/9$. In table [6.1](#), we have presented the numerical values of model parameters A, B, central density and radial pressure for different strange star candidates. In this chapter, we have chosen $A = 0.00541$ for graphical analysis. Applying Buchdahl criteria for compactness in equation [\(6.24\)](#), the chosen value of A gives $R = 9.3749$ (see Table [6.2](#)) which is very close to observed value of R ([Güver et al. \[2010a\]](#)).

6.5 Physical Consequences of Model Under $f(R, T)$ Gravity

6.5.1 Validity of energy conditions

In this section, we check the validity of energy conditions namely, null energy condition (NEC), weak energy condition (WEC), dominant energy condition (DEC) and strong energy condition (SEC) for the proposed compact star. The violation of energy conditions lead the possible cause of existence of exotic matter in compact star. In Refs. [Hochberg and Visser \[1998\]](#), the EMT violates the NEC at the center ($r = 0$).

- (i) NEC: $\rho \geq 0$,
- (ii) WEC: $\rho + p_r \geq 0$ and $\rho + p_t \geq 0$,
- (iii) DEC: $\rho - p_r \geq 0$ and $\rho - p_t \geq 0$,
- (iv) SEC: $\rho + p_r \geq 0$ and $\rho + p_r + 2p_t \geq 0$.

From Fig. [6.4](#) below, we observe that the all energy conditions valid for radial pressure as well as tangential pressure with certain range of D. So the compact star presented

6. Singularity-free non-exotic compact star in $f(R, T)$ gravity

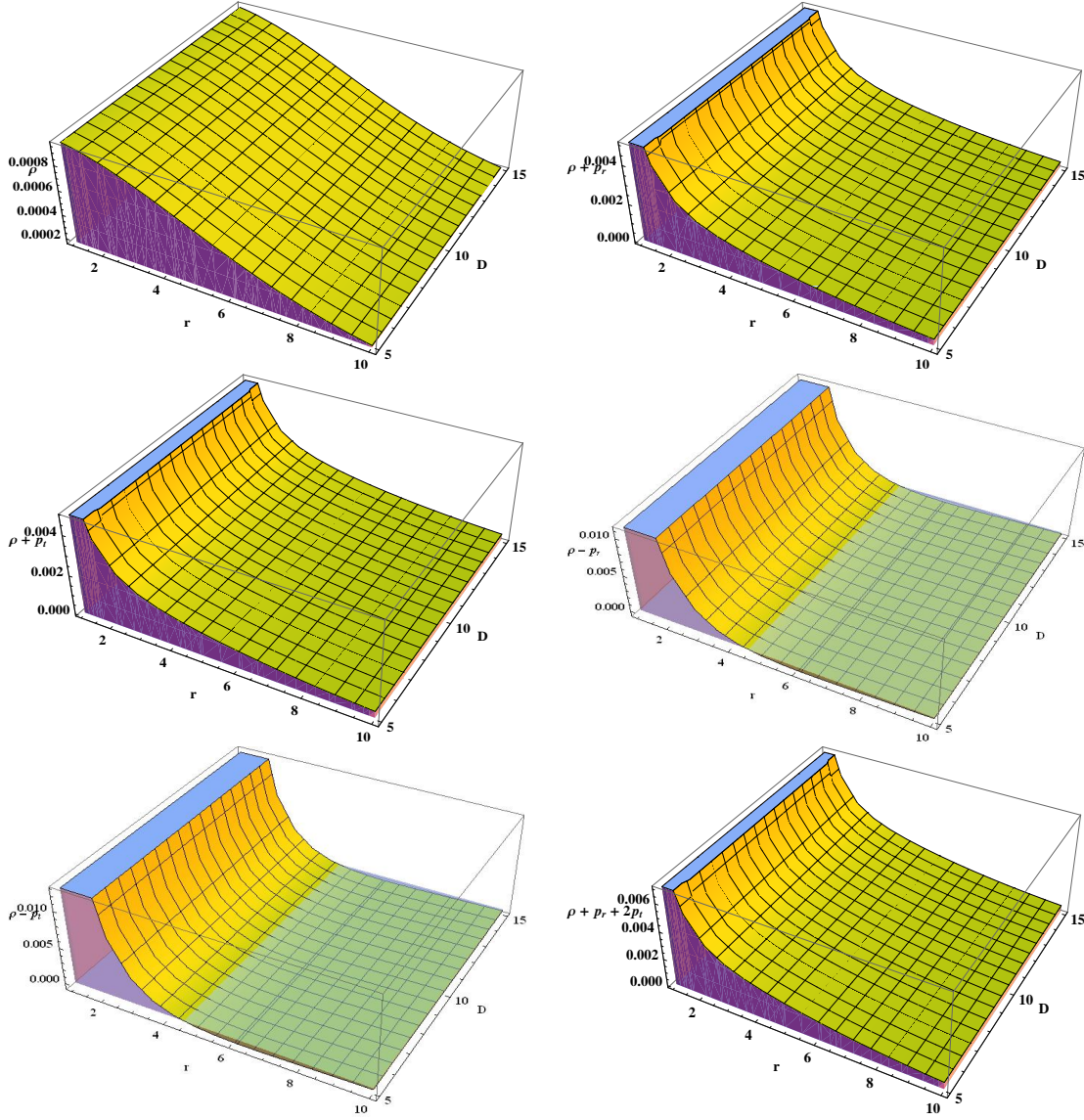


Figure 6.4: Validation of energy conditions of singularity-free compact star.

in this chapter is composed of non-exotic matter. Moraes and Sahoo ([Moraes and Sahoo \[2017\]](#)) have also constructed the model of wormholes composed by non-exotic matter in the trace of energy momentum-tensor squared gravity. Further it is interesting to note that we may avoid the presence of exotic matter in the framework of $f(R, T)$ gravity and hence no candidate of dark energy/matter is required to explain the accelerating feature of universe as reported in Refs. ([Yadav \[2019\]](#), [Moraes and Sahoo \[2017\]](#)).

6.5. Physical Consequences of Model Under $f(R, T)$ Gravity

- The value of A is constraint by employing the energy condition at the center. i.e.
- (i) NEC: $(\rho)_0 \geq 0 \Rightarrow A \geq 0$,
 - (ii) WEC: $(\rho)_0 + (p_r)_0 \geq 0$ and $(\rho)_0 + (p_t)_0 \geq 0 \Rightarrow A + \alpha A \geq 0$ & $A + \beta A \geq 0$,
 - (iii) DEC: $(\rho)_0 - (p_r)_0 \geq 0$ and $(\rho)_0 - (p_t)_0 \geq 0 \Rightarrow A - \alpha A \geq 0$ & $A - \beta A \geq 0$,
 - (iv) SEC: $(\rho)_0 + (p_r)_0 \geq 0$ and $(\rho)_0 + (p_r)_0 + 2(p_t)_0 \geq 0 \Rightarrow A + \alpha A \geq 0$ & $A + (\alpha + 2\beta)A \geq 0$.

In general theory of relativity, the stellar objects with violations of energy conditions are common. So, there are variety of toy models of stellar objects in which the matter source is in the form of Chaplygin gas (Rahaman et al. [2008]). But in this chapter, we have constructed the model of compact star with in the $f(R, T)$ formalism that validate all energy conditions and thus represents a viable model of compact star. The value of A is restricted by equation (6.24).

6.5.2 Stability

For Physically acceptable model, the velocity of sound should be less than the velocity of light i.e. $0 \leq v_s \leq 1$.

$$v_{sr}^2 = \frac{dp_r}{d\rho} = \alpha, \quad (6.26)$$

$$v_{st}^2 = \frac{dp_t}{d\rho} = \beta. \quad (6.27)$$

Since both α and β lie in between 0 and 1 ($0 \leq \alpha \leq 1$; $0 \leq \beta \leq 1$) which implies that velocity of sound is less than 1. Thus our solution validate the existence of physically viable compact star with in the specification of alternative theory of gravity.

Equations (6.26) and (6.27) lead to

$$|v_{st}^2 - v_{sr}^2| = |\beta - \alpha| \leq 1. \quad (6.28)$$

From Eqn. (6.28), the stability of compact star depends upon the free parameter α and β . According to Herrera (Herrera [1992]), the region of stellar object in which the radial speed of sound is greater than the transverse speed of sound, is a potentially stable region. Thus, by imposing restriction on the values of α and β , one may check the stability of derived model.

6. Singularity-free non-exotic compact star in $f(R, T)$ gravity

Table 6.2: Comparison of estimated value of model parameters with observed data sets.

S.N.	Compact star	M_{Obs} (M_{\odot})	Radii (r_{\odot})	ζ	M_{Esti}	Z_{Obs}	Z_{Esti}
1.	PSRJ 1614-2230	1.97 ± 0.04	13 ± 2	6	1.973	0.344793	0.345475
2.	PSRJ 1903+327	1.667 ± 0.02	9.438 ± 0.03	4	1.686	0.444945	0.407709
3.	4U 1820-30	1.58 ± 0.06	9.1 ± 0.4	4	1.592	0.431786	0.393753
4.	VelaX-1	1.77 ± 0.08	9.56 ± 0.08	3.65	1.814	0.484428	0.441777
5.	4U 1608-51	1.74 ± 0.14	9.3 ± 1.0	3.65	1.739	0.493929	0.489662

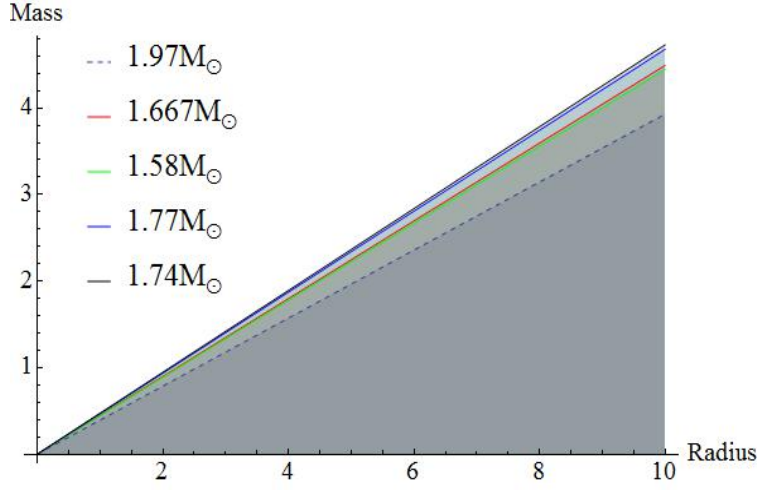


Figure 6.5: Profile of Mass versus Radius.

6.5.3 Adiabatic index

The adiabatic index is read as

$$\Gamma = \left(\frac{\rho + p_r}{p_r} \right) \frac{dp_r}{d\rho} = 1 + \alpha. \quad (6.29)$$

For stable configuration Γ should be greater than 1.33 with in the isotropic stellar system. Note that $\Gamma = 1.33$ is the critical value as reported in Refs. (Chandrasekhar [1965], Bondi [1964]). Equation (6.29) gives clue to choose the value of free parameter α . For stable configuration, we have to choose $\alpha \geq 0.33$ that is why in this paper, we have chosen $\alpha = 0.4$ for graphical (see Fig. 6.6) and numerical analysis of the model.

6.5. Physical Consequences of Model Under $f(R, T)$ Gravity

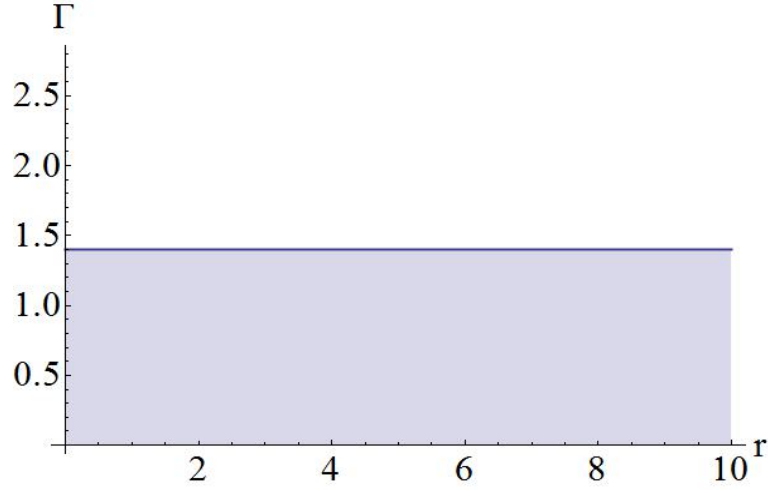


Figure 6.6: Profile of Γ versus r .

6.5.4 Mass-radius relation

In our model, the gravitational mass $m(r)$ in terms of radius r is expressed as

$$m(r) = \int_0^r 4\pi r^2 \rho dr = \frac{4\pi r [\exp(-Ar^2)(2Ar^2 - 1) + 1]}{8\pi + \zeta - \zeta(\alpha + 2\beta)}. \quad (6.30)$$

The profile of mass function $m(r)$ with respect to radius r for different values of ζ is shown in Fig. 6.5.

At $r = R$, the gravitational mass is read as

$$m(r)_{r=R} = \frac{4\pi r [(2AR^2 - 1) (1 - \frac{2M}{R}) + 1]}{8\pi + \zeta - \zeta(\alpha + 2\beta)}. \quad (6.31)$$

6.5.5 Compactness and red-shift

The compactness of star ($u(r)$) is read as

$$\begin{aligned} u(r) &= \frac{m(r)}{r} \\ &= \frac{4\pi [\exp(-Ar^2)(2Ar^2 - 1) + 1]}{8\pi + \zeta - \zeta(\alpha + 2\beta)}. \end{aligned} \quad (6.32)$$

The profile of compactness of star with respect to r is graphed in Fig. 6.7

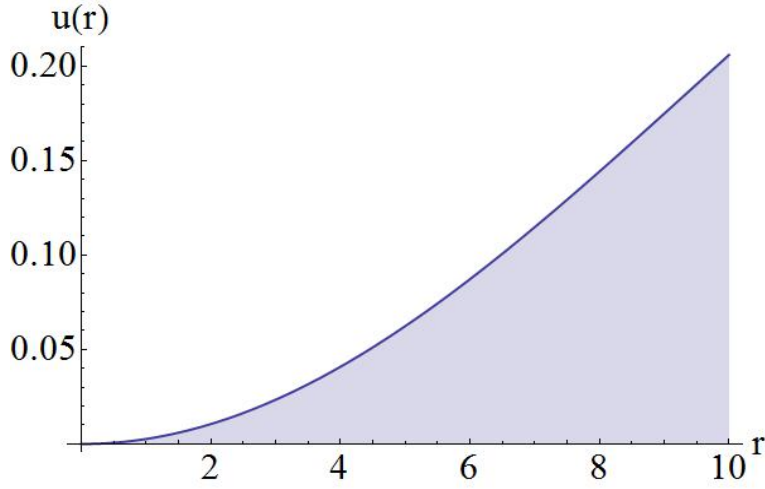


Figure 6.7: Profile of $u(r)$ versus r .

Therefore, the red-shift function $Z(r)$ is computed as

$$Z(r) = (1 - 2u)^{-\frac{1}{2}} - 1 = \left[1 - \frac{8\pi[\exp(-Ar^2)(2Ar^2 - 1) + 1]}{8\pi + \zeta - \zeta(\alpha + 2\beta)} \right]^{-\frac{1}{2}} - 1. \quad (6.33)$$

The profile of red-shift function with respect to r is depicted in Figure 8.

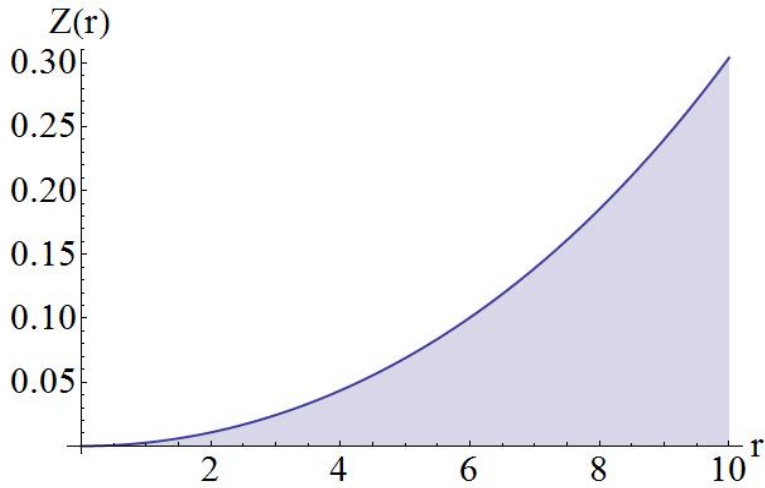


Figure 6.8: Profile of $Z(r)$ versus r .

6.6 Physical Validity of Model

6.7. Result and Discussion

In this subsection, we match the similarity of physical parameters of derived model with their observational values for certain choice of ζ . By using the observational data sets for mass (M_{\odot}) and radii (r_{\odot}), we carry out a comparative study of estimated mass (M_{Esti}), observed red-shift (Z_{Obs}) of derived model with observed mass and red-shift of different stars namely, PSRJ1614-2230, PSRJ1903+327, 4U1820-30, VelaX-1 and 4U1608-52 and the results are listed in Table 6.2. From Table 6.2, we observe that the derived model is very close to 4U 1608051 and PSRJ 1614-2230 for $\zeta = 3.65$ and $\zeta = 6$ respectively. Note that all the figures have been graphed for $\zeta = 3.65$.

6.7 Result and Discussion

We have constructed, in the present paper, a singularity-free anisotropic compact star in the framework of $f(R, T)$ gravity. The exact and singularity-free solution of gravitationally collapsing system is obtained by taking into account the well known equations of state which give the relation between energy density and pressure. The energy density, radial pressure and tangential pressure are decreasing function of r . At the center of compact star, ρ , p_r and p_t have certain fixed values which satisfy the relations $\sim (p_r)_0 = \alpha(\rho)_0$ and $(p_t)_0 = \beta(\rho)_0$. The behavior of anisotropic parameter has been graphed in Fig. 6.3 for the two different choice of α and β . Indeed, the anisotropy in stellar object representing a force which will directed outward when $p_t > p_r$ and inward if $p_t < p_r$ which allow the construction of more or less massive distribution respectively (Rahaman et al. [2012]). From Table 6.1, we observe that the estimated mass of derived compact star is good agreement with observed mass data sets (Demorest et al. [2010], Güver et al. [2010b], Gangopadhyay et al. [2013], Güver et al. [2010a]). In general, our solution validate all the energy conditions throughout the stellar region of compact star. The validation of energy conditions can be check by the Fig. 6.4 above, which is graphed by taking $A = 0.025$. Eqn. (6.28) exhibits the stability criteria of compact star which shows that the particular choice of α and β will generates the stable compact star. Let us now concentrate on the some other models of stellar objects with in $f(R, T)$ formalism, especially the work by Moraes and Sahoo (Moraes and Sahoo [2017]) and Das et al (Das et al. [2017]). In Refs. Das et al. [2017], authors have proposed unique model of stellar object in $f(R, T)$ theory of gravity and show that the gravastar is a viable alternative of black hole. It is worth to note that mechanism of obtaining solution is entirely different from the mechanism

6. Singularity-free non-exotic compact star in $f(R, T)$ gravity

adopted in Refs. [Das et al. \[2016\]](#).

As a final comment, we note that the present study represents the model of non-exotic compact star which validate the SEC as well as other energy conditions in the stellar region of compact star as a significance of extra-term of the $f(R, T)$ theory namely ζT . The T-dependence of the $f(R, T)$ theory may characterize in describing the physical facts, which is missing in general theory of relativity. In our previous work ([Rahaman et al. \[2012\]](#)), we have investigated a singularity free dark energy star which contains an anisotropic matter that is confined within the certain radius from center while in the present work, we propose a model of singularity free non exotic compact star with aid of $f(R, T)$ theory of gravitation. In future, one can check the viability of such solution under the specification of other valuable functional forms of $f(R, T)$ such as $f(R, T) = R + \zeta RT$ and $f(R, T) = R + \zeta R^2 + \lambda T$ where ζ and λ are arbitrary constants.

Chapter 7

A new model for dark matter fluid sphere ¹

7.1 Introduction

One of the most interesting facts is that the ordinary baryonic matter is not the dominant form of material in the universe as is against our common perception. It is accounted that the visible component of the total mass of the universe represents only a small fraction. On the large scale structure of the cosmos, the universe is composed of matter that is fundamentally different from our familiar matter composition. Based on the astronomical observations over the years, it is accepted that most of the mass appears to be in some as-yet-undiscovered strange new form which is non-luminous known as Dark Matter (DM). The most long-lasting challenges of modern astrophysics are understanding and unveiling the nature of dark matter. It is believed that the dark matter is the main component, responsible for the large-scale structure formation in the universe. Though the dark matter is not detected in the laboratory yet still a series of observations, find the existence of dark matter in strong footing. The nature of dark matter and the standard LCDM models can be tested on many scales, from the shape of the cosmic web to the properties of galaxies and galaxy clusters, down to particle physics experiments aiming at detecting the dark matter particles.

¹A considerable part of this chapter has been published in **Modern Physics Letters A**, 2050280 (2020).

7. A new model for dark matter fluid sphere

A complete understanding of the nature of dark matter component of the universe remains a mystery.

An undetected form of missing mass that emits no light, register its presence because we observe the effects of its gravity. It is found that more than 90 percent of the mass in the whole universe is dark. One can raise the question about the understanding of the gravity which gave birth of the mysterious dark matter, but it is needless to say that the gravity is so well tested that scientist prefers the existence of dark matter.

Dark matter at the core region of the galaxies is believed to exist since long ago from the observational pieces of evidence on the stellar motion. The first observational evidence indicating the existence of the dark matter came from the work of Oort ([Oort \[1970\]](#)) in 1932. He calculated the velocity scattered of stars in the galactic plane and found that it is greater than expected from gravitational potential from the stars. He naturally predicted more mass is needed to match the discrepancy in velocity which is apparently missing. Fritz Zwicky ([Zwicky \[1933\]](#)) in 1933 estimated the velocity dispersion of galaxies in the Coma cluster and inferred its total mass from the Virial theorem. He found that their velocities are much beyond the velocities that could be attributed to the luminous parts of galaxies. The dynamical mass inferred from relative motions of the galaxies which found much less of the accounted mass led Zwicky to concluded the galaxies were embedded in dark halos which do not radiate.

In 1970 Vera Rubin ([Rubin and Ford Jr \[1970\]](#)) discovered that the rotational curves of galaxies are almost flat at large distances, which should drop as $r^{-\frac{1}{2}}$ from the galactic centre if we consider only the star density in the galaxy. The constant rotational velocity can be accounted only if one considers each galaxy must be surrounded by a super-massive halo of matter and the growth of mass with distance as one move away from the central region. This large portion of the non-luminous form of the matter is due to dark matter. Milgrom ([Milgrom \[1983\]](#)) proposed Modified Newtonian dynamics (MOND) by modifying Newton's gravity that explained the flat nature of the observed velocity rotation curve of galaxies, thus eliminating the need for hidden mass hypothesis. Later on, several observational pieces of evidence suggest that MOND cannot eliminate the need for dark matter in all astrophysical systems thus dark matter to be ubiquitous in the universe.

The presence of an extensive dark matter halo turns out to be true for all types of galaxies in general: as for an example dwarf galaxies ([Bell and de Jong \[2001\]](#)), Stierwalt et al. ([Stierwalt et al. \[2017\]](#)), many other elliptical galaxies ([Fabian et al.](#)

7.1. Introduction

[1986]) is a kind of common feature of the existence of DM within galaxies. Later on, the observations Roberts and Whitehurst (Roberts and Whitehurst [1975]), Einasto et al. (Einasto et al. [1974]), Ostriker et al. (Ostriker et al. [1974]) on different galaxies gave similar results.

Gravitational lensing is an alternate method of measuring the mass of the cluster without considering the motion of the cluster has an important contribution to establishing the existence of unseen matter. It was Zwicky (Zwicky [1979]) who suggested that gravitational lens effects could also, be used to measure the total masses of extragalactic objects. It was confirmed that the dark matter component should be there to explain the gravitational lens effects (Fort and Mellier [1994]).

The best evidence to date in support of the existence of dark the matter is Bullet cluster ($1E0657 - 558$) (Markevitch et al. [2004]) that shows a separation of ordinary matter (gas) from dark matter. Cosmic microwave background radiation properties can be used to infer the total amount of matter created by dark-matter clustering. As a cosmological evidence, Big Bang Nucleosynthesis (BBN) or as Recent evidence hailed as the smoking-gun for dark matter.

Recent studies on the properties of a dark matter component declare that the dark matter particle could be Hot Dark Matter (HDM) as well as Cold Dark Matter (CDM) depending on whether the particle interaction at the initial stages of the Galaxy formation was relativistic or non-relativistic. Many exotic particles that are being proposed as a suitable candidate for dark matter including massive neutrinos, massive compact halo objects (MACHOs) which include brown dwarfs, old white dwarfs that have ceased glowing, neutron stars, black holes, weakly interacting massive particles (WIMPs)(Overduin and Wesson [2004]). MACHOs do not cause enough lensing events to explain all the dark matter. Matter consisting of undiscovered particles WIMPs are excellent dark matter candidates, consistent with astronomical observations. A massless invisible and intangible neutrino can be the candidate for dark matter, but if most of the dark matter were neutrinos, they would not stay put long enough to let those structures form. Even ordinary celestial bodies such as Jupiter like objects can be supposed as a dark matter candidate. Massless scalar field that may be Brans-Dicke type (Fay [2004]) or coupled to a potential (Matos et al. [2000]) have been proposed for the dark matter component. Several attempts have been made for primordial black holes to provide an explanation for the non-baryonic dark matter.

The dark matter candidate should obey at least the law of gravity and whose mass

7. A new model for dark matter fluid sphere

maybe 10^{11} eV (weak force scale) if thermally produced in the Big Bang. Maybe as low as 10^{-5} eV (axion) or as high as 10^{19} eV (WIMPZILLA) if not thermally produced. Other plausible candidates are axions, sterile neutrinos, Supersymmetric particles, high-resolution numerical simulation favored the standard cold dark matter (SCDM) as the candidate (Efstathiou et al. [1990], Pope et al. [2004]), Mirror matter, Λ -CDM (Tegmark et al. [2004b,a]) etc.

Dark matter is a property of gravitational effect in the aspect of the spatially geometrical structure. Earlier, it was found in the literature (Bharadwaj and Kar [2003], Su and Chen [2009]) that dark matter could be described by a fluid with non-zero effective pressure. Rahaman et al. (Rahaman et al. [2010a]) considered dark matter as perfect fluid in their work. Dark matter may be modeled as a mixture of two non-interacting perfect fluids as was shown by Harko and Lobo (Harko and Lobo [2011]). Interestingly they have shown that the two-fluid model can be described as an effective single anisotropic fluid having with non-vanishing radial and transverse components of pressures (Letelier [1980], Letelier and Alencar [1986]). The differences of pressures along radial and transverse directions are the anisotropy of a system. A review of the origins and effects of local anisotropy in astrophysical objects may also be found in Ref. (Herrera and Santos [1997], Chan [2003]).

In general, it is assumed that the galactic halo is mostly to be spherical in shape. Though the exact geometry of the galactic dark matter halo is not clear, but recent higher resolution simulations based on observational data predict the halos to be non-spherical. We shall examine the problem of modeling of dark matter in the spherically symmetric stellar configuration.

Very recent, R. P. Pant et al (Pant et al. [2019]) have studied a core-envelope model of compact star in which core is equipped with linear equation of state while the envelope is considered to be of quadratic equation of state and this work motivated us to generate a new model for stellar objects. In this work, we have proposed a new model by considering the stellar object consists of core and envelope regions. We also assume a particular EoS to describe isotropic fluid dark matter in the core region which provides constant density throughout the interior. The outer envelope region is considered as anisotropic in nature and satisfying a linear pressure-density relation. In the core boundary, we have assume de-sitter metric as the exterior while Schwarzschild solution is assumed to describe the exterior boundary of the stellar object. Accordingly, the matching conditions are used in addition to setting radial pressure zero at the exterior boundary. Energy conditions and stability has also been

7.2. Einstein field equations

discussed for the developed model.

Our chapter has been organized as follows: In Section 7.2, we have presented the basic equations governing the anisotropic system. In Section 7.3, we have presented the generalized Tolman-Oppenheimer-Volkoff (TOV) equation for anisotropic fluid distribution. By assuming a particular density profile, we have solved the relevant field equations to develop a model in Section 7.4. In Section 7.5 the exterior metric and the corresponding boundary conditions have been displayed. We have analyzed some physical features of our model in Section 7.6. Finally, we have discussed and concluded our results in Section 7.7.

7.2 Einstein field equations

We consider the line element in *Schwarzschild* co-ordinate system to describe the interior of a static and spherically symmetric stellar configuration as :

$$ds^2 = -e^{\nu(r)} dt^2 + e^{\lambda(r)} dr^2 + r^2 (d\theta^2 + \sin^2 \theta d\phi^2), \quad (7.1)$$

where $e^{\nu(r)}$ and $e^{\lambda(r)}$ are known as the metric potential functions, where $\nu(r)$ and $\lambda(r)$ are functions of the radial coordinate ‘ r ’ only.

The Einstein field equations can be written as:

$$T_{\mu\nu} = \frac{1}{8\pi} \left\{ R_{\mu\nu} - \frac{1}{2} R g_{\mu\nu} \right\}. \quad (7.2)$$

where, $T_{\mu\nu}$, $R_{\mu\nu}$, $g_{\mu\nu}$ and R are the stress energy tensor, Ricci tensor, metric tensor and Ricci scalar, respectively.

For an anisotropic matter distribution, the energy momentum tensor can be written as:

$$T_{\mu\nu} = \{\rho(r) + p_t(r)\} U_\mu U_\nu - p_t(r) g_{\mu\nu} + \{p_r(r) - p_t(r)\} \chi_\mu \chi_\nu, \quad (7.3)$$

where $\rho(r)$ is the energy density, $p_r(r)$ is the radial pressure and $p_t(r)$ is the tangential pressure of the fluid configuration. χ^μ is a unit 4-vector along the radial direction and U^μ is the 4-velocity. The quantities obey the following relation: $\chi_\mu \chi^\mu = 1$, $\chi_\mu U^\mu = 0$. Note that we have used system of units where $G = 1 = c$.

7. A new model for dark matter fluid sphere

The Einstein field equations (7.2) read as the following form for the metric (7.1) along with the energy tensor (7.3):

$$\rho(r) = \frac{1}{8\pi} \left\{ \frac{1 - e^{-\lambda}}{r^2} + \frac{e^{-\lambda}\lambda'}{r} \right\}, \quad (7.4)$$

$$p_r(r) = \frac{1}{8\pi} \left\{ \frac{e^{-\lambda} - 1}{r^2} + \frac{e^{-\lambda}\nu'}{r} \right\}, \quad (7.5)$$

$$p_t(r) = \frac{e^{-\lambda}}{8\pi} \left\{ \frac{\nu''}{2} + \frac{\nu'^2}{4} - \frac{\nu'\lambda'}{4} + \frac{\nu' - \lambda'}{2r} \right\}, \quad (7.6)$$

where, a prime (') denotes differentiation with respect to 'r'.

Also, the anisotropic factor is defined as $\Delta(r) = \{p_t(r) - p_r(r)\}$.

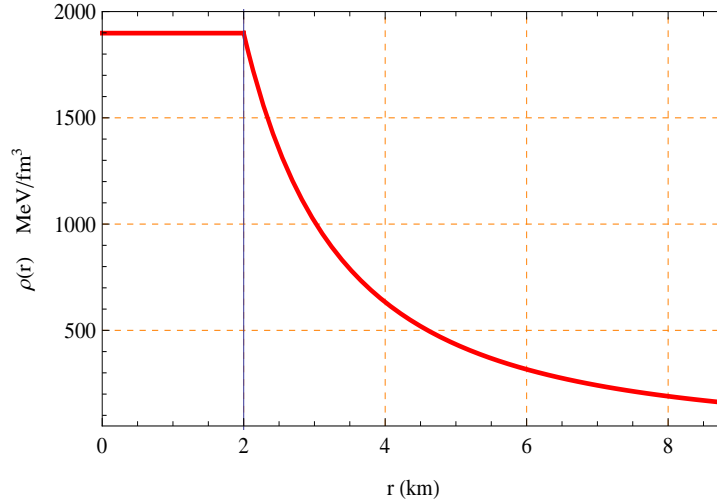


Figure 7.1: Behavior of the density with respect to the radial coordinate r for the compact star EXO 1785-248 corresponding to the numerical value of constants given in Table-7.1

7.3 Generalized Tolman-Oppenheimer-Volkoff equation

From Eqns. (7.4) and (7.5), we obtain

$$\rho(r) + p_r(r) = \frac{\lambda' + \nu'}{8\pi r} e^{-\lambda}. \quad (7.7)$$

7.4. The interior Solutions

Also, from Eqn. (7.5), we get

$$\frac{dp_r(r)}{dr} = \frac{1}{8\pi} \left[e^{-\lambda} \left\{ \frac{\nu''}{r} - \frac{\nu'\lambda'}{r} - \frac{\nu' + \lambda'}{r^2} \right\} + \frac{2(1 - e^{-\lambda})}{r^3} \right]. \quad (7.8)$$

Then, by using Eqns. (7.4)-(7.8), we can write

$$-\frac{\nu'\{\rho(r) + p_r(r)\}}{2} - \frac{dp_r(r)}{dr} - \frac{2\{p_t(r) - p_r(r)\}}{r} = 0. \quad (7.9)$$

The above Eqn. (7.9) represents generalized Tolman-Oppenheimer-Volkoff (TOV) equation for anisotropic fluid distribution.

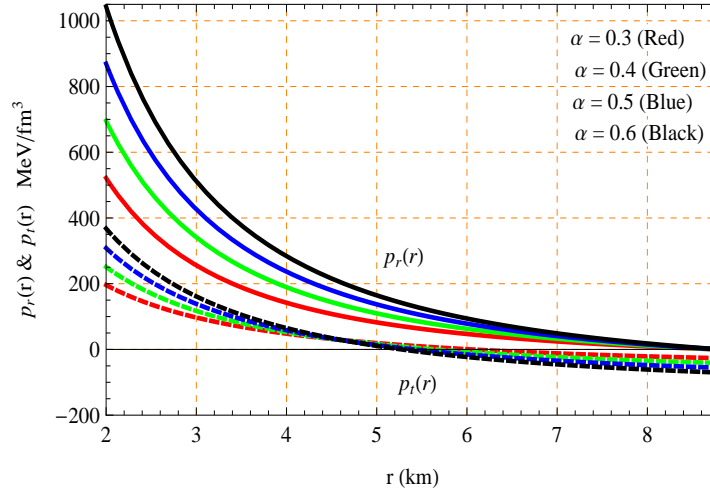


Figure 7.2: Behaviors of the radial and transverse pressures with respect to the radial coordinate r for the compact star EXO 1785-248 corresponding to the numerical value of constants given in Table-7.1

7.4 The interior Solutions

To solve the system of equations, we assume a density profile of the dark matter(DM) as:

$$\rho(r) = \frac{k}{r(1 + \frac{r}{b})}, \quad (7.10)$$

where, b is the scale radius and k is of dimension km^{-1} . We assume that the interior region of star is divided into two regions (i) The core, $0 \leq r \leq b$ and (ii) The outer region, $b < r \leq R$ to avoid the singularity at the center of stellar configuration.

7. A new model for dark matter fluid sphere

Any spherically symmetric anisotropic celestial compact star is a highly dense fluid configuration with comparatively very small radius. For that reason, researchers have the curiosity to find the exact details of the internal very dense matter compositions including its density profile. Consequently, we have motivated to find the new results which represent the highly dense fluid configuration with the above DM density profile (7.10) by dividing the interior of the star in two regions as follows from the core envelope compact star model of R.P.Pant et al (Pant et al. [2019]). Since the negative pressure is the cause of gravitational repulsion in a region which counters the inward gravitational pull and retains the region stable against the inward gravitational attraction. For this reason, we shall assume the negative pressure and positive energy density in the core region of the compact object which remains the core stable against the inward forces acted on the core boundary. This assumption makes sure to match our interior solution with the De Sitter space as the De Sitter space corresponds to vacuum solution of Einstein field equations with a positive energy density and negative pressure and hence with a non zero cosmological constant.

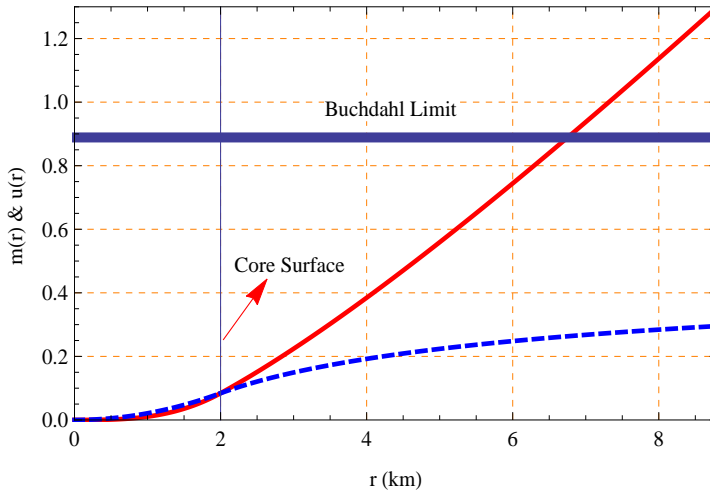


Figure 7.3: Behaviors of the mass and compactness parameter with respect to the radial coordinate r for the compact star EXO 1785-248 corresponding to the numerical value of constants given in Table-7.1

7.4.1 Solution in the core region, $0 \leq r \leq b$

We assume that the core of stellar object is isotropic in nature and satisfy the

7.4. The interior Solutions

following equation of state (EoS):

$$p(r) = p_r(r) = p_t(r) = -\rho(r). \quad (7.11)$$

Negative pressure in a fluid occurs when it pushes on its surroundings. The negative pressure is the cause of gravitational repulsion around the space. This gravitational repulsion created from pressure counters the inward gravitational pull and retain the smearing effect near the origin.

Therefore, from Eqns. (7.9) and (7.10), we obtain

$$\rho(r) = \text{constant} = \rho_c = \frac{k}{2b}. \quad (7.12)$$

Finally, the density profile (7.10) takes the following form

$$\begin{aligned} \rho(r) &= \frac{k}{2b}, \quad 0 \leq r \leq b, \\ \rho(r) &= \frac{k}{r(1 + \frac{r}{b})}, \quad b \leq r \leq R. \end{aligned} \quad (7.13)$$

The mass function is defined as

$$e^{-\lambda} = 1 - \frac{2m(r)}{r}. \quad (7.14)$$

Now, the mass of the core can obtain as:

$$m(r) = 4\pi \int_0^r r'^2 \rho_c dr' = \frac{2r^2 k \pi}{3}. \quad (7.15)$$

Therefore, the expressions of compactness parameter and surface redshift are obtained as

$$u(r) = \frac{2m(r)}{r} = \frac{4rk\pi}{3}, \quad (7.16)$$

$$z(r) = \{1 - u(r)\}^{-\frac{1}{2}} - 1 = \left(1 - \frac{4rk\pi}{3}\right)^{-\frac{1}{2}} - 1. \quad (7.17)$$

In Schwarzschild coordinate, we can write

$$e^{-\lambda} = 1 - \frac{2m(r)}{r} = 1 - \frac{4rk\pi}{3}. \quad (7.18)$$

7.4.2 Solution in the outer region, $b \leq r \leq R$

For the outer region, we assure the density profile (7.10) and an EoS in the following linear form:

$$p_r(r) = \alpha\rho - \beta, \quad (7.19)$$

where α (km^{-2}), β (km^{-2}) are constants.

Now, the mass of the stellar object can be obtained as:

$$m(r) = 4\pi \left\{ \int_0^b \xi^2 \rho_c d\xi + \int_b^r \xi^2 \rho(\xi) d\xi \right\} \quad (7.20)$$

$$= \frac{2bk\pi}{3} \{6r - 5b - 6bf_1\}, \quad (7.21)$$

where $f_1 = \log\left(\frac{r+b}{2b}\right)$.

Therefore, the compactness parameter and surface redshift are obtained as:

$$u(r) = \frac{2m(r)}{r} = \frac{4bk\pi}{3r} [6r - 5b - 6bf_1], \quad (7.22)$$

$$\begin{aligned} z(r) &= \{1 - u(r)\}^{-\frac{1}{2}} - 1 \\ &= \left(1 - \frac{4bk\pi}{3r} [6r - 5b - 6bf_1]\right)^{-\frac{1}{2}} - 1. \end{aligned} \quad (7.23)$$

In Schwarzschild coordinate, we can write

$$\begin{aligned} e^{-\lambda} &= 1 - \frac{2m(r)}{r}, \\ &= 1 - \frac{4bk\pi}{3r} [6r - 5b - 6bf_1]. \end{aligned} \quad (7.24)$$

On using Eqs. (7.10) and (7.19), we get the expression of radial pressure

$$p_r(r) = \frac{\alpha k}{r(1 + \frac{r}{b})} - \beta. \quad (7.25)$$

7.4. The interior Solutions

On imposing Eqns. (7.24)-(7.25) in Eqn. (7.5) we get

$$\begin{aligned} \nu'(r) = & \frac{4\pi}{r(r+b)f_2} \left[bk\{5b^2 - br - br^2(\alpha + 1)\} \right. \\ & \left. + 6r^3\beta(r+b) + 6b^2k(r+b)f_1 \right], \end{aligned} \quad (7.26)$$

whereas

$$f_2 = \left[4bk\pi(6r - 5b) - 24b^2k\pi f_1 - 3r \right]. \quad (7.27)$$

Therefore, the transverse pressure and anisotropic factor are obtained in the following

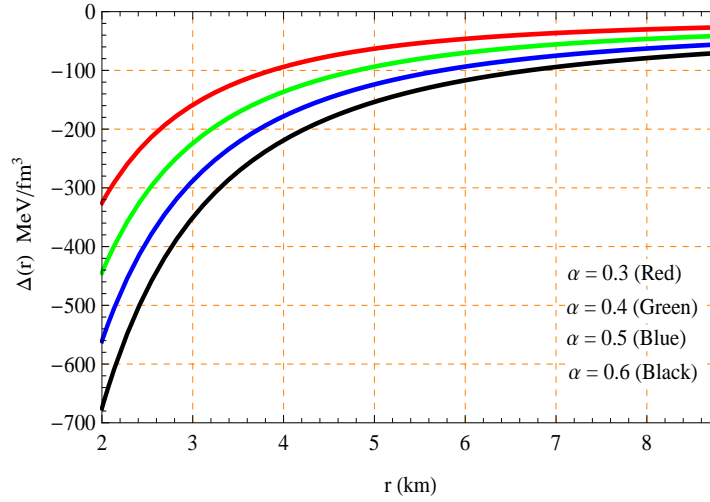


Figure 7.4: Behavior of the anisotropic factor with respect to the radial coordinate r for the compact star EXO 1785-248 corresponding to the numerical value of constants given in Table-7.1

exact forms:

$$\begin{aligned} p_t(r) = & \left[6r\beta(r+b)f_3 - 12\pi r^4\beta^2(r+b)^2 \right. \\ & \left. + 12\pi kb^2f_1f_4 - b^2kf_5 \right] \left[2r(r+b)^2f_2 \right]^{-1}, \end{aligned} \quad (7.28)$$

$$\begin{aligned} \Delta(r) = & \beta - \frac{\alpha k}{r(1 + \frac{r}{b})} + \left[2r(r+b)^2f_2 \right]^{-1} \times \\ & \left[6r\beta(r+b)f_3 - 24\pi r^4\beta^2(r+b)^2 - b^2kf_5 \right. \\ & \left. + 12\pi kb^2f_1f_4 \right], \end{aligned} \quad (7.29)$$

7. A new model for dark matter fluid sphere

whereas

$$\begin{aligned}
 f_3 &= 5\pi k b^3 - b^2 k \pi r + r^2 + b r \{1 + 4k\pi r(\alpha - 1)\}, \\
 f_4 &= b k \{b(\alpha - 1) - r(\alpha + 1)\} - 3r\beta(r + b)^2, \\
 f_5 &= 2b k \pi r(1 - 11\pi) + 10b^2 k \pi(\alpha - 1) + 3r\{\alpha + 4k\pi r(\alpha + 1)^2\}. \quad (7.30)
 \end{aligned}$$

For observing the actual behavior of our obtained solutions, we have displayed the graphical representations of solutions in Fig. 7.1- Fig. 7.5 for the well-known compact star EXO 1785-248 corresponding to $\alpha = 0.3, 0.4, 0.5$ and 0.6 . The exact behavior of the energy density is shown in Fig. 7.1. Fig. 7.2 and Fig. 7.3 show the variations of radial, transverse pressures and mass with compactness parameter, respectably. Further, Fig. 7.4 and Fig. 7.5 display the characteristics of anisotropic factor and equation of state (EoS) parameters, respectively, where the EoS parameters are defined as $\omega_r(r) = p_r(r)/\rho(r)$, $\omega_t(r) = p_t(r)/\rho(r)$.

7.5 Boundary conditions

To determine the values of involved constants within solutions, we have matched our solutions with the *de-sitter* metric at the core boundary $r = b$ and the exterior *Schwarzschild* solution at the surface boundary $r = R$ ($> 2M$). De Sitter space corresponds to vacuum solution of Einstein field equations with a positive energy density and negative pressure and hence with a non zero cosmological constant. In our model, the core region of the compact object we assume the pressure to be negative and energy density is positive. So it is justified to assume de Sitter metric at the core boundary. On the otherhand Schwarzschild metric is the solution Einstein field equations exterior of a spherical matter distribution with cosmological constant and charge to be zero. The compact object in our model is assumed to acquire no net charge and outer region is vacuum and hence described by Schwarzschild solution. The *de-sitter* and exterior *Schwarzschild* metric are given by

$$\begin{aligned}
 ds_d^2 &= \left(1 - \frac{r^2}{d^2}\right) dt^2 - \left(1 - \frac{r^2}{d^2}\right)^{-1} dr^2 \\
 &\quad - r^2(d\theta^2 + \sin^2\theta d\phi^2), \quad (7.31)
 \end{aligned}$$

7.6. Physical features of the model

$$ds_s^2 = \left(1 - \frac{2M}{r}\right) dt^2 - \left(1 - \frac{2M}{r}\right)^{-1} dr^2 - r^2(d\theta^2 + \sin^2\theta d\phi^2). \quad (7.32)$$

After matching, we have the following results:

$$e^{-\lambda}|_{r=b} = e^{\nu}|_{r=b} = \left(1 - \frac{b^2}{d^2}\right) = 1 - \frac{4\pi kb}{3}, \quad (7.33)$$

$$\begin{aligned} e^{-\lambda}|_{r=R} &= e^{\nu}|_{r=R} = \left(1 - \frac{2M}{R}\right) \\ &= 1 - \frac{4bk\pi}{3R} [6R - 5b - 6bf_1(R)]. \end{aligned} \quad (7.34)$$

Again, since the radial pressure $p_r(r)$ vanishes at the boundary $r = R$, which implies

$$p_r(R) = 0. \quad (7.35)$$

Using these boundary conditions (7.33)-(7.35), we arrived at

$$\begin{aligned} k &= \frac{3M}{2\pi b(6R - 5b - 6bf_1(R))}, \\ d &= \sqrt{\frac{3b}{4\pi k}}, \\ \beta &= \frac{\alpha bk}{R(R + b)}. \end{aligned} \quad (7.36)$$

where b is a free parameter, which will be the measurement of the core radius of the staler fluid configuration. For our model, we consider $b = 2 \text{ km}$.

7.6 Physical features of the model

Here, we are going to verify some well-established physical conditions regarding the compact star for our present solutions.

7.6.1 Energy condition

The energy conditions, which need to satisfy by the matter composition of stellar

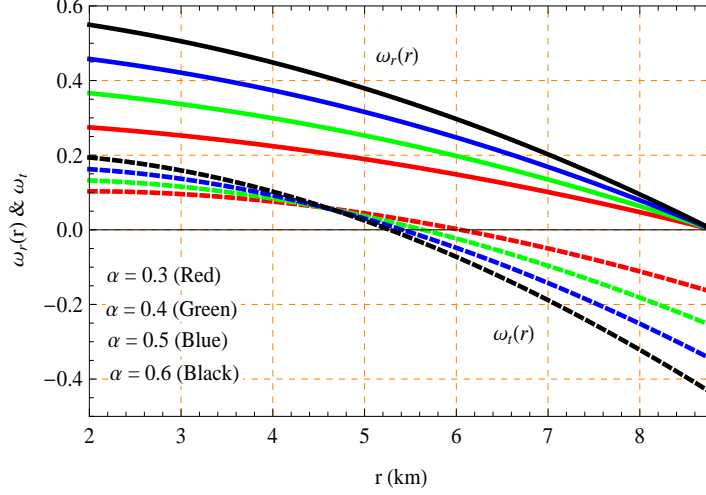


Figure 7.5: Behaviors of the equation of state parameters with respect to the radial coordinate r for the compact star EXO 1785-248 corresponding to the numerical value of constants given in Table-7.1

fluid for being physical matter (Hawking and Ellis [2023], Wald [1986], Maurya et al. [2016b]). The energy conditions are: Null energy condition (NEC), Weak energy condition (WEC) and Strong energy condition (SEC). All these energy conditions are defined in the following manner:

$$\begin{aligned}
 NEC_r & : \rho(r) + p_r(r) \geq 0, & NEC_t & : \rho(r) + p_t(r) \geq 0. \\
 WEC_r & : \rho(r) \geq 0, \quad \rho(r) + p_r(r) \geq 0. \\
 WEC_t & : \rho(r) \geq 0, \quad \rho(r) + p_t(r) \geq 0. \\
 SEC & : \rho(r) + p_r(r) + 2p_t(r) \geq 0.
 \end{aligned} \tag{7.37}$$

Our presented solutions have satisfied all these energy conditions within outer envelop of the compact star, shown in Figs. 7.1 and Fig. 7.6 by plotting the LHSs of all inequalities (7.37). Moreover, the energy density is positive and $\rho(r) + p(r) = 0$ within the core region *i.e.* NEC and WEC are satisfied there. Consequently, the solutions represent a physical matter distribution.

7.6.2 Equilibrium condition

The equilibrium position is a prime property of non-collapsing compact star. For this purpose, we are willing to verify the equilibrium condition for our solutions. Any anisotropic fluid sphere remains at equilibrium position under the action of

7.6. Physical features of the model

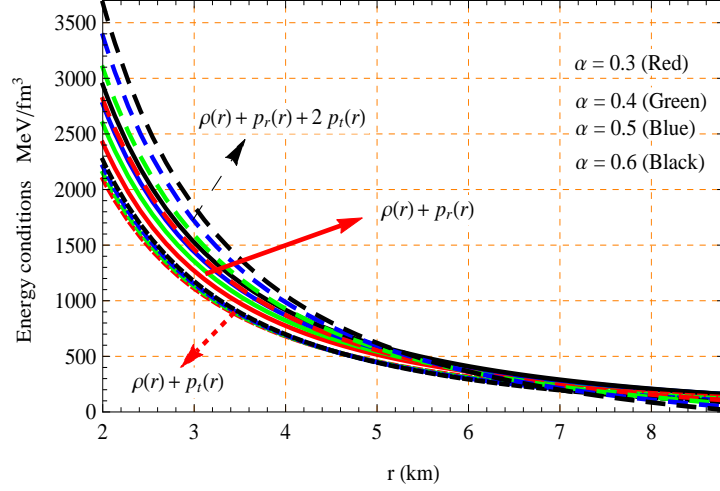


Figure 7.6: Behaviors of the energy conditions with respect to the radial coordinate r for the compact star EXO 1785-248 corresponding to the numerical value of constants given in Table-7.1

three different forces namely, gravitational, hydrostatic and anisotropic forces, respectively. The equilibrium situation represents by an equation, which is known as the Tolman-Oppenheimer-Volkoff (TOV) equation. The generalized TOV equation for the anisotropic fluid distribution (7.9) can be written as

$$F_g(r) + F_h(r) + F_a(r) = 0, \quad (7.38)$$

whereas

$$\begin{aligned} \text{Gravitational force, } F_g(r) &= -\frac{\nu' \{ \rho(r) + p_r(r) \}}{2}, \\ \text{Hydrostatic force, } F_h(r) &= -\frac{dp_r(r)}{dr}, \\ \text{Anisotropic force, } F_a(r) &= \frac{2\{p_t(r) - p_r(r)\}}{r}. \end{aligned} \quad (7.39)$$

The graphical demonstrations of these three forces for our solutions are shown in Fig. 7.7 and from there one can easily conclude that our model is in equilibrium state.

7.6.3 stability analysis

7. A new model for dark matter fluid sphere

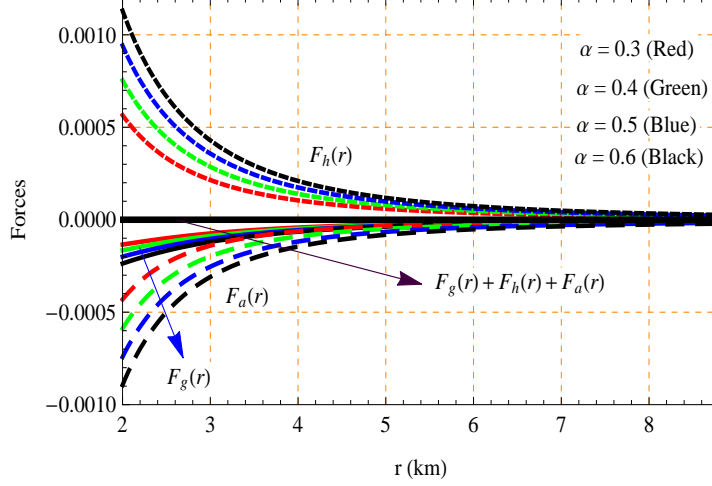


Figure 7.7: Behaviors of the forces with respect to the radial coordinate r for the compact star EXO 1785-248 corresponding to the numerical value of constants given in Table-7.1

7.6.3.1 Causality condition

I. Causality condition : Since the speed of light c is the cosmic speed limit, the speed of sound within a compact star must be less than c otherwise stellar fluid is non-physical. The sound velocity inside the compact star can be determined by using

$$v_r(r) = \sqrt{\frac{dp_r(r)}{d\rho(r)}}, \quad v_t(r) = \sqrt{\frac{dp_t(r)}{d\rho(r)}}. \quad (7.40)$$

In gravitational unit, velocity of light $c = 1$. Thus $0 \leq v_r(r), v_t(r) < 1$, this condition is known as the causality condition. Fig. 7.8 shows that our model satisfies the causality condition in outer region of the stellar object *i.e.* the model is of the physical stellar fluid.

II. Stability : To study the stability of an anisotropic fluid stellar, L. Herrera (Herrera [1992]) proposed the *cracking method* under the radial perturbations in the year 1992. Now using the concept of cracking, Abreu et al. (Abreu et al. [2007]) provided the stability conditions with respect to the stability factor $(= \{v_t(r)\}^2 - \{v_r(r)\}^2)$ for anisotropic fluid model. The conditions of Abreu et al. (Abreu et al. [2007]) state that : (i) The region is potentially stable if $-1 < \{v_t(r)\}^2 - \{v_r(r)\}^2 \leq 0$ and (ii) The region is potentially unstable if $0 < \{v_t(r)\}^2 - \{v_r(r)\}^2 < 1$.

7.6. Physical features of the model

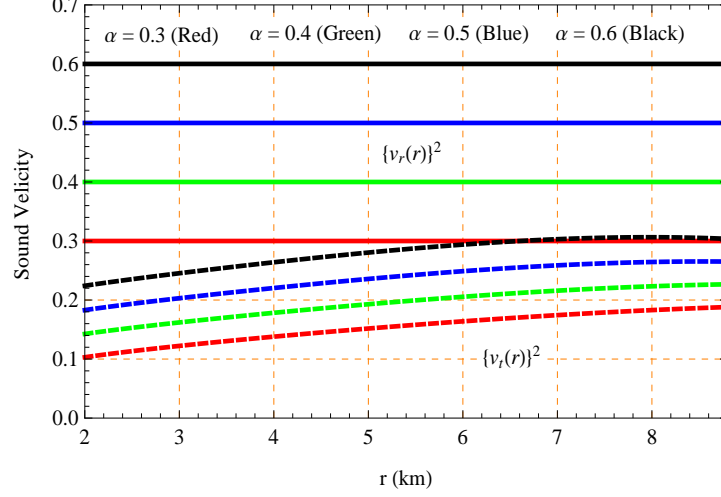


Figure 7.8: Behaviors of the radial and transverse velocities of sound with respect to the radial coordinate r for the compact star EXO 1785-248 corresponding to the numerical value of constants given in Table-7.1

Our solutions satisfy the condition $-1 < \{v_t(r)\}^2 - \{v_r(r)\}^2 < 0$ (see Fig. 7.9) within the outer region of fluid (anisotropic) configuration and therefore our model is potentially stable.

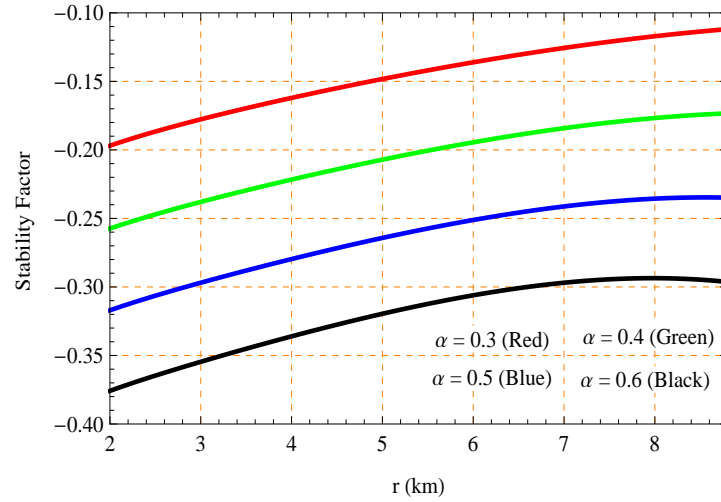


Figure 7.9: Behavior of the stability factor with respect to the radial coordinate r for the compact star EXO 1785-248 corresponding to the numerical value of constants given in Table-7.1

7. A new model for dark matter fluid sphere

7.6.3.2 Adiabatic index

The relativistic adiabatic index is also a considerable parameter that affect the stability of any stellar matter distribution. The relativistic adiabatic index is defined as:

$$\Gamma_r(r) = \frac{\rho(r) + p_r(r)}{p_r(r)} \frac{dp_r(r)}{d\rho(r)}. \quad (7.41)$$

For the Newtonian limit, any stable configuration will alter its stability by initiating an adiabatic gravitational collapse if $\Gamma_r(r) \leq 4/3$ and catastrophic if $< 4/3$ (Bondi [1964]). This condition changes for relativistic and/or anisotropic fluid which depends on the nature of anisotropy, provided by Chan et al. (Chan et al. [1993]). For our solutions, the value of adiabatic index $\Gamma_r(r)$ is more than $4/3$ throughout the outer region of compact star, clear from Fig. 7.10.

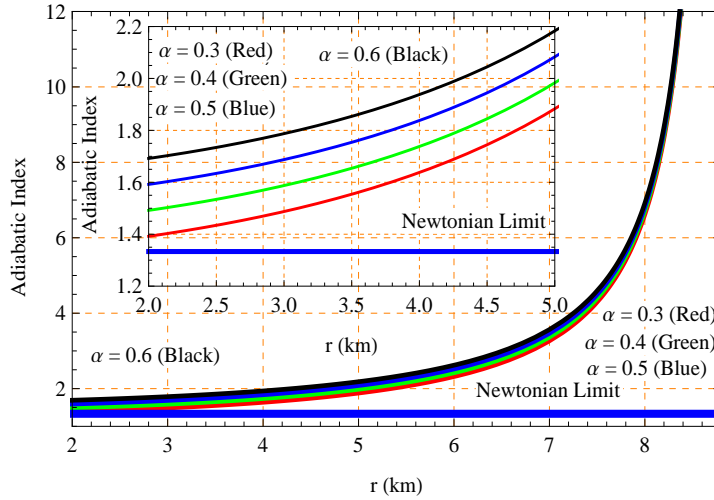


Figure 7.10: Behavior of the adiabatic index with respect to the radial coordinate r for the compact star EXO 1785-248 corresponding to the numerical value of constants given in Table-7.1

7.6.3.3 Harrison-Zeldovich-Novikov criterion

Harrison et al. (Harrison et al. [1965]) and Zeldovich & Novikov (Zeldovich and Novikov [1971]) proposed another important criterion for the stability of compact star. Their criterion states that the mass should increase with the increase in the

7.7. Discussions and conclusion

central density , i.e. $dM(\rho_c)/d\rho_c > 0$. For our solutions the mass as a function of the central density can be express as

$$M(\rho_c) = \frac{4\pi b^2 \rho_c}{3} [6R - 5b - 6bf_1(R)], \quad (7.42)$$

$$\frac{\partial M(\rho_c)}{\partial \rho_c} = \frac{4\pi b^2}{3} [6R - 5b - 6bf_1(R)] > 0. \quad (7.43)$$

In our model, the solutions hold static stability criterion and hence stable, obvious

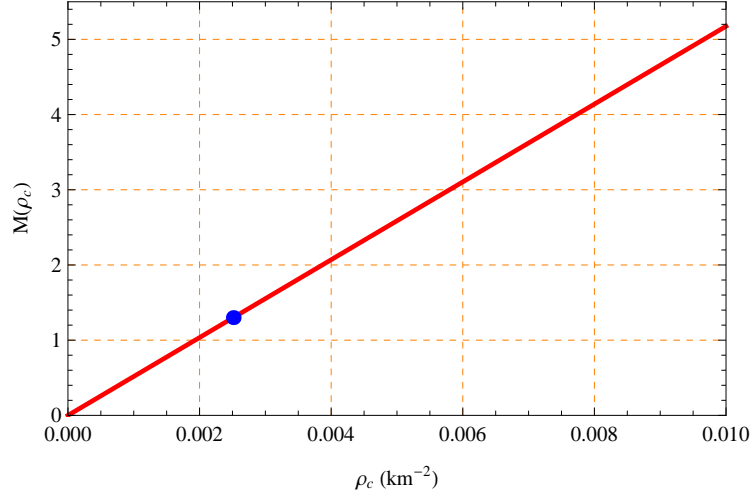


Figure 7.11: Behavior of the mass with respect to the core density ρ_c for the compact star EXO 1785-248 corresponding to the numerical value of constants given in Table-7.1

from Fig. 7.11. Also, the “dot” sing in Fig. 7.11 represents the corresponding mass of the compact star in solar mass unit.

7.7 Discussions and conclusion

In this paper, we have presented a model for spherically symmetric dark matter (DM) fluid (isotropic as well as anisotropic) sphere, where the DM is characterized by a density profile $\rho(r) = k/r(1 + \frac{r}{b})$. For having the singularity of the density profile at the centre of celestial compact star, we have assumed that the star is divided into two regions: **A.** The isotropic core region with equation of state(EoS) $p_r(r) = -\rho(r)$ and **B.** The anisotropic outer region along with EoS $p_r(r) = \alpha\rho(r) - \beta$. In the core region,

7. A new model for dark matter fluid sphere

Table 7.1: Numerical values of constants for three well-known celestial compact stars.

Compact Star	$M(M_\odot)$	$R(km)$	$\alpha(km^{-2})$	$\beta(km^{-2})$	$b(km)$	$k(km^{-1})$	$d(km)$
EXO 1785-248	1.3 ± 0.2	8.8 ± 0.4	0.3	0.00006	2	0.01005	6.8927
			0.4	0.00008	2	0.01005	6.892
			0.5	0.00011	2	0.01005	6.892
			0.6	0.00012	2	0.01005	6.892
Vela X-1	1.77 ± 0.08	9.56 ± 0.08	0.3	0.00007	2	0.01220	6.2549
			0.4	0.00009	2	0.01220	6.254
			0.5	0.00011	2	0.01220	6.254
			0.6	0.00013	2	0.01220	6.254
4U 1538-52	0.87	7.87	0.3	0.000061	2	0.00787	7.7876
			0.4	0.00008	2	0.00787	7.787
			0.5	0.00010	2	0.00787	7.787
			0.6	0.00012	2	0.00787	7.787

Table 7.2: Numerical values of the physical parameters for three well-known celestial compact stars corresponding to the values of constant given in Table-7.1.

Compact Star	$\rho_c (10^{15})$ (gm/cm^3)	$\rho_s (10^{14})$ (gm/cm^3)	$p_{nc} (10^{35})$ ($dyne/cm^2$)	z_s	u_s	Buchdahl Limit
EXO 1785-248	3.384	2.849	8.357	0.1914	0.2955	$< \frac{8}{9}$
	3.384	2.849	11.142	0.1914	0.2955	$< \frac{8}{9}$
	3.384	2.849	13.928	0.1914	0.2955	$< \frac{8}{9}$
	3.384	2.849	16.714	0.1914	0.2955	$< \frac{8}{9}$
Vela X-1	4.110	2.975	10.279	0.2602	0.3703	$< \frac{8}{9}$
	4.109	2.975	13.705	0.2602	0.3703	$< \frac{8}{9}$
	4.109	2.975	17.131	0.2602	0.3703	$< \frac{8}{9}$
	4.109	2.975	20.557	0.2602	0.3703	$< \frac{8}{9}$
4U 1538-52	2.651	2.731	6.412	0.1331	0.2211	$< \frac{8}{9}$
	2.651	2.731	8.549	0.1331	0.2211	$< \frac{8}{9}$
	2.651	2.731	10.687	0.1331	0.2211	$< \frac{8}{9}$
	2.651	2.731	12.824	0.1331	0.2211	$< \frac{8}{9}$

7.7. Discussions and conclusion

the density becomes constant depending upon the EoS, which we have assumed to avoid the singularity at the centre. To analyze our obtained solutions with the help of graphical representations, we have considered the well-known compact star EXO 1785-248. Moreover, we have calculated the numerical values of all physical parameters for the compact stars EXO 1785-248 along with more well-known compact stars Vela X-1 and 4U 1538-52 in tabular form to make our solutions more feasible.

The salient key features of our solutions are:

(i) Energy density and pressures: The energy density of a compact star should be positive inside the star. In our solutions, the energy density is positive with constant and monotonically decreasing in nature towards the surface within the inner region and outer region, respectively. Moreover, inner and outer values of the energy densities are coincided at the inner surface boundary $b = 2 \text{ km}$, clear from Fig. 7.1. The pressures (radial and transverse) are monotonically decreasing towards the surface in outer envelope. In the inner region, the pressure (radial = transverse) becomes negative depending on EoS and due to negative pressure, the inner part pushes back the surrounding matter to remain at the same size. However, the radial pressure is positive within the outer part of the compact star and vanishes at the outer surface but the transverse pressure has changed its phase from positive to negative around $r = 6 \text{ km}$ (see Fig. 7.2). Also, we have computed the numerical values of core energy density ρ_c and surface (outer region) energy density ρ_s for three well-known compact stars and all are of orders 10^{15} and 10^{14} , respectively. The numerical values of pressures p_{nc} very near to the core boundary from the side of outer region are of orders 10^{35} . Therefore, all these values are physically well-valued.

(ii) Anisotropy: For the isotropy, the anisotropic factor $\Delta(r) = 0$ in inner part. However, in the outer region, the radial pressure is always greater than the transverse pressure (see Fig. 7.2) in our solutions. Therefore, the anisotropy becomes negative in nature, also obvious from Fig. 7.4. This nature of anisotropy indicates that the force due to anisotropy is inward-directed *i.e.* compact star becomes less stable, that can be also seen from Fig. 7.7.

(iii) Equation of state parameters: The EoS $p_r(r) = -\rho(r)$ shows that the EoS parameter $\omega(r) = -1$. For the real feasible matter distribution, the radial EoS pa-

7. A new model for dark matter fluid sphere

parameter $\omega_r(r)$ should be lie in $0 < \omega_r(r) < 1$ (Rahaman et al. [2010b]). The obtained solution has satisfied the condition $0 < \omega_r(r) < 1$, provided in Fig. 7.5 in outer part of the fluid configuration and hence the DM becomes as real feasible matter within outer region. Thus, it is the beauty of our solutions regarding the celestial compact stars, which are formed by DM distributed in two parts: (i) Inner part, formed by unfeasible DM, (ii) Outer part, formed by real feasible DM.

(iv) Energy conditions: The satisfaction all energy conditions are necessary for physical matter distribution and evidently, we can see from Fig. 7.6 along with Fig. 7.1 that our solutions satisfied all the energy conditions within outer envelope of star. Moreover, inner part has maintained the NEC and WEC. Therefor, the matter distribution is physical one.

(v) Equilibrium: Under the action of gravitational, hydrostatic and anisotropic forces any celestial anisotropic fluid configuration remains at the equilibrium position. The matter distribution represented by our solutions is in the equilibrium position, clear from Fig. 7.7. In equilibrium position, hydrostatic is repulsive and gravitational, anisotropic forces are attractive in nature.

(vi) Mass function and compactness parameter: The exact behaviors of mass function $m(r)$ and compactness parameter $u(r)$ are demonstrated in Fig. 7.3. From that figure, we can see that $m(r)$ and $u(r)$ are finite, zero at the centre and then monotonically increasing toward the outer layer surface of the fluid configuration. Moreover, the value of compactness parameter is more than the mass in the region $0 < r < b$ and coincide at the core boundary $r = b = 2 \text{ km}$ (see Fig. 7.3). According to Buchdahl (Buchdahl [1959]), the value of the compactness parameter at the outer layer surface of compact star, $u_s = u(R) = \frac{2M}{R} < \frac{8}{9}$. We have calculated the numerical values u_s , provided in Table-7.2 and all these values ensure that our solutions satisfied the Buchdahl limit.

(vii) Stability: The stable situation is one of the essential characteristics of compact star. We have analyzed the stability situation with the help of causality condition, adiabatic index and Harrison-Zeldovich-Novikov criterion. The radial and transverse velocities of sound are positive and less than 1 (see Fig. 7.8) and hence our solutions satisfied the causality condition within the outer region of compact fluid

7.7. Discussions and conclusion

configuration. The stability factor $\{v_r(r)\}^2 - \{v_r(t)\}^2$ is negative, shown in Fig. 7.9, *i.e.* DM within outer region is physical matter, which are potentially stable. The profiles of adiabatic index and mass in terms of central density also indicate that our solutions represent stable matter configuration, clear from Fig. 7.10 and Fig. 7.10, respectively.

(viii) Surface redshift: The variation of obtained surface redshift $z(r)$ is shown in Fig. 7.11. From that figure, we can see that the $z(r) \rightarrow 0$ as $r \rightarrow 0$ and thereafter monotonically increasing unto the surface. Moreover, the inner and outer values of $z(r)$ have coincided at the inner boundary. Further, we have computed the maximum numerical values of surface redshift $z_s = z(R)$ at the outer boundary of the celestial fluid configuration, provided in Table-7.2 and all these values of z_s are within the range provided by the author of (Ivanov [2002]).

Finally, all the salient key features of our solutions ensure that our solutions are well-behaved and physically acceptable to represent the physical DM fluid configuration containing two parts: the isotropic inner part of unfeasible DM with constant density and anisotropic outer part filled with feasible DM.

Chapter 8

Lyapunov exponent, ISCO and Kolmogorov-Senai entropy for Kerr-Kiselev black hole ¹

8.1 Introduction

The first detection of black hole (BH) merger GW150914 strongly supports the existence of black holes ([Abbott et al. \[2016a,b\]](#)) by observing the gravitational waves generated during the process of coalescence. Further, the first observation of the shadow of a super massive black hole in the giant elliptical galaxy M87 strengthen this claim for the existence of BHs. BHs are usually surrounded by diffused matter in orbital motion named as “accretion disk”. An accretion disk can be influenced by cosmic repulsion and magnetic field. A detail analysis was presented by Stuchlk et al. ([Stuchlík \[2005\]](#)) by considering thin and thick disks. Stuchlk ([Stuchlík \[1983\]](#)) have also discussed the motion of test particle with non-zero cosmological constant, further he also presented equation of motions for electrically charge and magnetic monopoles. There exist many stable and unstable circular orbits. Another type of orbit also exist which lie between dynamically unstable and stable orbits known as “homoclinic orbits” ([Bombelli and Calzetta \[1992\]](#), [Levin et al. \[2000\]](#), [Manna et al. \[2020\]](#)). These orbits started asymptotically closed to unstable circular orbits and

¹A considerable part of this chapter has been published in **Eur. Phys. J. C, 81:84 (2021)**.

8. Lyapunov exponent, ISCO and Kolmogorov-Senai entropy for Kerr-Kiselev black hole

ends with spiraling in and out about the central BH. During the in-spiraling phase a significant amount of angular momentum is lost into gravitational waves thereby circularizing the orbit. In addition to these orbits, “chaotic orbits” have been discovered recently for fast spinning BHs (Suzuki and Maeda [1997], Levin et al. [2000], Das et al. [2020b]). The innermost stable circular orbits (ISCO) (Mondal et al. [2021b]) is of more interest as it will identify the onset of dynamical instability.

The instability of an orbit can be identified by a positive value of Lyapunov exponent (Mondal et al. [2020]). It is also well-known that maximal Lyapunov exponents (MLE) can distinguish a chaotic dynamics from others, which may initiate unstable/homoclinic orbits by a perturbation. For a spinning black hole the number of unstable orbits increase very rapidly and crowded into the corresponding phase (Levin [2003], Dettmann et al. [1994], Yadav et al. [2020]). However, determining LE in general relativistic regime is very difficult as each orbits has different LE and it is impractical to scan the overall nature of the orbits. Also, since LE determines the separation to neighboring orbits in time and time itself is relative which will eventually lead to relative LE (Cornish and Levin [2003]). Lyapunov coefficient delineates the measure of instability of the circular orbits and not a measure of chaos. On the other hand, if we consider magnetized black holes *i.e.* a black holes immersed in an external magnetic field, the equations of motion become chaotic (Kološ et al. [2015], Stuchlík and Kološ [2016], Tursunov et al. [2016]). Pánis et al. (Pánis et al. [2019]) discussed about Keplerian disk orbiting a Schwarzschild black hole embedded in an asymptotically uniform magnetic field where they have found three possible scenarios *i.e.* (i) regular oscillatory motion, (ii) destruction due to capture by the magnetized black hole and (iii) chaotic motion. They have used a time series of the solution of equations of motion for different conditions to analyzed the transition from regular to chaotic motion. Further, the authors Tursunov et al. (Tursunov et al. [2020]) describes the possible fate of magnetized Keplerian disk in case of particles escaping along the magnetic field lines that is another special case of regular motion. Extending this work, Kološ et al. (Kološ et al. [2017]) explained observational data for few microquasars using magnetized standard geodesic models of QPOs. Wu et al. (Wu et al. [2006]) developed a method of determining fast Lyapunov indicator (FLI) using two-nearby-orbits method without projection operations and with proper time as the independent variable, which can quickly identify chaos. Since LE is not invariant under coordinates transformations in GR, Wu and Huang (Wu and Huang [2003])

8.1. Introduction

proposed a new relativistic LE which is invariant in a curve manifold. In general relativity, chaos takes an important role in describing more realistic physical systems. The amplification of chaos restricted relativistic three-body systems (Kiselev [2003]). It has also been reported that chaos also exists in two relativistic systems like two fixed black holes (Contopoulos et al. [1999], Iyer and Will [1987]), Schwarzschild's black hole and a dipolar shell (Vieira and Letelier [1997], Konoplya and Zhidenko [2011]) etc. Chaotic behavior must be well understood in binary gravitational waves sources or otherwise its detection will highly uncertain. Levin et al. (Levin et al. [2000]) shown that in the absence of radiative back reaction a chaotic motion is developed in rapidly rotating compact stars where the relativistic precession of apastron is supplemented by chaotic precession of the orbital plane. Burd and Tavakol (Burd and Tavakol [1993]) used Bianchi type-IX cosmology to describe chaos as gauge invariant model by calculation spectrum of LEs. The invariant formulation of LE was developed by Motter (Motter [2003]) showing that chaos is represented by positive LE and coordinate invariant.

The organization of the chapter is as follows: In section 8.2, we begin with a basic definition of Lyapunov exponent and provide a simple formula for finding Lyapunov exponent (λ) in terms of the second derivative of the effective potential in radial motion \dot{r}^2 . In section 8.3, we encapsulate the relation between Lyapunov exponent and KS-entropy. In section 8.4, we analyze the rotating black hole and described completely the equatorial circular geodesics. We showed that Lyapunov exponent can be demonstrated in terms of ISCO equation and deliberated stability of time-like geodesics. We derived angular velocity and reciprocal of Critical exponent for both the cases of time-like and null-circular geodesics of the space-time. In section 8.5, we constructed the equation of marginally bound circular orbit for finding the radius of marginally bound circular orbit to the black holes. We calculated the ratio of angular velocity of null-circular geodesics to time-like geodesics in section 8.6. In section 8.7, we determined the ratio of time period of null-circular geodesics to time-like geodesics. In section 8.8, we summarize our work.

8.2 Proper time Lyapunov exponents and Radial potential

In a dynamical system the LE is a quantity that classified the rate of separation of extremely close trajectories. This rate of separation depends on orientations of initial separation vector. Among all LE, a positive Maximal Lyapunov exponent (MLE) is taken to indicate that the system is chaotic. If the system is conservative then the sum of all Lyapunov exponents must be zero and if negative then the system is dissipative. The Lyapunov spectrum can be utilized to give an evaluate of the rate of entropy production. According to Pesin's theorem ([Pesin \[1977\]](#)), the sum of all positive LEs provide an estimate of the KS entropy. Also, a positive LE and a negative LE designates a divergence and a convergence between to nearby trajectories, respectively.

In classical physics, the study of autonomous smooth dynamical system analyzes differential equations of the form

$$\frac{dx}{dt} = F(x), \quad (8.1)$$

where t represents the time parameter. If the following four conditions satisfied by chaos, we may quantify chaos in terms of LEs. The condition are as follows:

- i) the system is autonomous;
- ii) the relevant part of the phase space is bounded;
- iii) the invariant measure is normalizable;
- iv) the domain of the time parameter is infinite.

This types of characterization is advantageous for space-time because LE does not change under space diffeomorphisms of the form $z = \psi(x)$. That's why we may say that chaos is a property of the physical system and independent on the coordinate which is used to describe the system.

There is no absolute time in general relativity. Therefore, the time parameter in-force us to consider the equation (8.1) under the diffeomorphism: $z = \psi(x)$, $d\tau = \eta(x, t) dt$ in the space-time. Since the classical indicator of chaos *i.e.* LE and KS

8.2. Proper time Lyapunov exponents and Radial potential

entropy depends on the choice of the time parameter, there is a conceptual problem. This problem was first arise in the mix-master cosmological model (Misner [1969]), where the largest LE was positive or zero depends on different choice of the coordinate. In general relativity (GR), this non-invariance features implies that chaos is not a property of physical system, it is a property of the coordinate system.

Following the work by Motter (Motter [2003]), we find that the chaos can be characterized by positive LE and KS entropy. The Lyapunov exponent and KS entropy transform under the space-time according to

$$\lambda_j^\tau = \frac{\lambda_j^t}{\langle \xi \rangle_t} \quad (j = 1, 2, \dots, N), \quad (8.2)$$

and

$$h_{ks}^\tau = \frac{h_{ks}^t}{\langle \xi \rangle_t} \quad (8.3)$$

respectively. Where N is phase-space dimension and $0 < \langle \xi \rangle_t < \infty$ is time average of $\xi = d\tau/dt$ over typical trajectory. For natural measure of the equations (8.2) and (8.3) to be well defined, $0 < \langle \xi \rangle_t < \infty$ is the basic requirement condition. Finally we can say that, the coordinate transformation is always transformed into the time independent transformation which is given by

$$z = \psi(x), \quad d\tau = \xi(x, t)dt \quad (8.4)$$

where ξ is a strictly positive, continuously differentiable function and ψ is a diffeomorphism. Then it is clear that the LE and KS entropy are invariant under space diffeomorphism.

Now we will calculate the LE using proper time from

$$\lambda = \pm \sqrt{\frac{(\dot{r}^2)''}{2}}. \quad (8.5)$$

where \dot{r}^2 represents the radial potential. Here we will ignore the \pm sign and we shall take only positive Lyapunov exponent. The circular orbit is stable when λ is imaginary and circular orbit is unstable when λ is real and when $\lambda = 0$, the circular orbit

8. Lyapunov exponent, ISCO and Kolmogorov-Senai entropy for Kerr-Kiselev black hole

is marginally stable or saddle point.

Following Pretorius and Khurana ([Pretorius and Khurana \[2007\]](#)), we can define critical exponent

$$\gamma = \frac{\Omega}{2\pi\lambda} = \frac{T_\lambda}{T_\Omega} \quad (8.6)$$

where, T_λ represents the Lyapunov time scale, T_Ω represents the orbital time scale and Ω represent the angular velocity. Also here $T_\lambda = \frac{1}{\lambda}$ and $T_\Omega = \frac{2\pi}{\Omega}$. Now the critical exponent can be written, in terms of second order derivative of the square of radial velocity (\dot{r}^2), as

$$\gamma = \frac{1}{2\pi} \sqrt{\frac{2\Omega^2}{(\dot{r}^2)''}}. \quad (8.7)$$

Also the reciprocal of critical exponent is given by

$$\frac{1}{\gamma} = \frac{T_\Omega}{T_\lambda} = 2\pi \sqrt{\frac{(\dot{r}^2)''}{2\Omega^2}}. \quad (8.8)$$

8.3 Lyapunov exponent and Kolmogorov-Senai entropy:

Kolmogorov-Senai (h_{ks}) entropy ([Chierchia \[2009\]](#)) is an important quantity which is connected to the Lyapunov exponents. When the chaotic orbit evolves, this entropy gives a measurement about information lost or gained. Another way it can be explored that when $h_{ks} > 0$ then the system is chaotic or disorder and when $h_{ks} = 0$ then the system non-chaotic.

Following Pesin ([Pesin \[2020\]](#)) the Kolmogorov-Senai (h_{ks}) entropy is the sum of all positive Lyapunov exponent, that is,

$$h_{ks} = \sum_{\lambda_j > 0} \lambda_j. \quad (8.9)$$

8.4. Rotating Black hole:

There are two Lyapunov exponent in 2-dimensional phase-space, so in terms of effective radial potential the Kolmogorov -senai entropy can be written as

$$h_{ks} = \sqrt{\frac{(\dot{r}^2)''}{2}}. \quad (8.10)$$

When this entropy evolves with time it play an important role in dynamical system to examine whether a trajectory is in disorder or not. It is different from the statistical entropy or physical entropy. In fact, it assumes a partition of phase space.

8.4 Rotating Black hole:

There are many choices of rotation axis and a multitude of angular momentum parameter in higher dimension whereas, only possible rotation axis with only one angular momentum for an axisymmetric in four dimension. Here we consider the metric of a Rotating black hole surrounding with quintessence ([Toshmatov et al. \[2017\]](#)) is,

$$\begin{aligned} ds^2 = & - \left[1 - \frac{(2Mr + cr^{1-3w})}{\Sigma} \right] dt^2 + \frac{\Sigma dr^2}{\Delta} - 2a \sin^2 \theta \left[\frac{2Mr + cr^{1-3w}}{\Sigma} \right] dt d\phi \\ & + \Sigma d\theta^2 + \sin^2 \theta \left[r^2 + a^2 + a^2 \sin^2 \theta \left(\frac{2Mr + cr^{1-3w}}{\Sigma} \right) \right] d\phi^2. \end{aligned} \quad (8.11)$$

where c is a new parameter, which describes the hair of the black hole and w represents a quintessential equation of state parameter. Also these rotating black hole is always bounded from above by $w = \frac{1}{3}$, which was first considered by Schee & Stuchlik ([Schee and Stuchlík \[2016\]](#)) and also by Slany & Stuchlik ([Slany and Stuchlík \[2020\]](#)), with

$$\begin{aligned} \Delta &= r^2 + a^2 - 2Mr - c \equiv (r - r_+)(r - r_-), \\ \Sigma &= r^2 + a^2 \cos^2 \theta. \end{aligned} \quad (8.12)$$

The metric is similar to Kerr-Newman black hole when $w = \frac{1}{3}, c = -Q^2$, Reissner-Nordström black hole when $w = \frac{1}{3}, c = -Q^2, a = 0$, Kerr black hole $w = \frac{1}{3}, c = 0$ and Schwarzschild black hole when $w = \frac{1}{3}, c = 0, a = 0$. The horizon take place at

8. Lyapunov exponent, ISCO and Kolmogorov-Senai entropy for Kerr-Kiselev black hole

$g_{rr} = \infty$ or $\Delta = 0$ *i.e.*

$$r_{\pm} = M \pm \sqrt{M^2 - a^2 + c}, \quad (8.13)$$

here r_+ is called event horizon and r_- is called Cauchy horizon.

The BH solution considered in this work is the rotational version of the Kiselev static quintessence BH. Originally, Kiselev used quintessence surrounding the BH characterized by the EMT of the quintessence. Here, the scalar field couples to gravity through a Lagrangian of the form

$$\mathcal{L} = -\frac{1}{2} g^{\mu\nu} \partial_\mu \phi \partial_\nu \phi - V(\phi), \quad (8.14)$$

and the stress-energy tensor $T_{\mu\nu}$ for the matter field took as perfect fluid. The complete action and the field equations can be given as

$$S = \int d^2x \sqrt{-g} \left[R - \frac{1}{2} g^{\mu\nu} \partial_\mu \phi \partial_\nu \phi - V(\phi) \right], \quad (8.15)$$

$$R_{\mu\nu} - \frac{1}{2} g_{\mu\nu} R = -8\pi T_{\mu\nu} - 8\pi \left[\partial_\mu \phi \partial_\nu \phi - g_{\mu\nu} \left\{ \frac{1}{2} g^{\mu\nu} \partial_\mu \phi \partial_\nu \phi + V(\phi) \right\} \right] \quad (8.16)$$

$$\frac{1}{\sqrt{-g}} \partial_\mu \left[\sqrt{-g} g^{\mu\nu} \partial_\nu \phi \right] - \frac{\partial V(\phi)}{\partial \phi} = 0. \quad (8.17)$$

The pressure and energy density of the scalar field are given by

$$p_\phi = \frac{1}{2} \dot{\phi}^2 - V(\phi) \quad , \quad \rho_\phi = \frac{1}{2} \dot{\phi}^2 + V(\phi). \quad (8.18)$$

The equation of state parameter $\omega_\phi = p_\phi/\rho_\phi$ is found to be

$$\omega_\phi = \frac{\dot{\phi}^2 - 2V(\phi)}{\dot{\phi}^2 + 2V(\phi)} \quad (8.19)$$

which lies between $-1 < \omega_\phi < 1$ and if $\dot{\phi}^2 < V(\phi)$ then $\omega_\phi < -1/3$. The rotating Kiselev BH was obtained by using Newman-Janis algorithm from Kiselev static quintessence BH, for details see (Toshmatov et al. [2017]).

8.4.1 Circular geodesics in the equatorial plane:

To calculate the geodesic equation in the equatorial plane for this space-time we

8.4. Rotating Black hole:

follow Chandrasekhar ([Chandrasekhar \[1998\]](#)). To compute the geodesics motions of the orbit in the equatorial plane we set $\dot{\theta} = 0$ and $\theta = \text{constant} = \pi/2$.

The appropriate Lagrangian for this motion is

$$\begin{aligned} 2\mathcal{L} = & \left[- \left(1 - \frac{2M}{r} - cr^{-(1+3w)} \right) \dot{t}^2 - \left[\frac{4Ma}{r} + 2acr^{-(1+3w)} \right] \dot{t}\dot{\phi} \right. \\ & \left. + \left[r^2 + \left(1 + \frac{2M}{r} + cr^{-(1+3w)} \right) a^2 \right] \dot{\phi}^2 + \frac{r^2}{\Delta} \dot{r}^2, \right. \end{aligned} \quad (8.20)$$

where ϕ is an angular coordinate. Then the generalized momenta can be derived from it as follows

$$\begin{aligned} p_t &= - \left[1 - \frac{2M}{r} - cr^{-(1+3w)} \right] \dot{t} - \left[\frac{2Ma}{r} + acr^{-(1+3w)} \right] \dot{\phi} \\ &= -E = \text{const.} \end{aligned} \quad (8.21)$$

$$\begin{aligned} p_\phi &= - \left[\frac{2Ma}{r} + acr^{-(1+3w)} \right] \dot{t} + \left[r^2 + \left(1 + \frac{2M}{r} + cr^{-(1+3w)} \right) a^2 \right] \dot{\phi} \\ &= L = \text{const.} \end{aligned} \quad (8.22)$$

$$p_r = \frac{r^2}{\Delta} \dot{r}. \quad (8.23)$$

Since Lagrangian is unhampered by both of t and ϕ , so p_t and p_ϕ preserve quantities. Solving the equations (8.21) and (8.22) for $\dot{\phi}$ and \dot{t} we get

$$\dot{\phi} = \frac{1}{\Delta} \left[\left(1 - \frac{2M}{r} - cr^{-(1+3w)} \right) L + \left(\frac{2Ma}{r} + acr^{-(1+3w)} \right) E \right], \quad (8.24)$$

$$\begin{aligned} \dot{t} &= \frac{1}{\Delta} \left[\left(r^2 + \left(1 + \frac{2M}{r} + cr^{-(1+3w)} \right) a^2 \right) E \right. \\ &\quad \left. - \left(\frac{2Ma}{r} + acr^{-(1+3w)} \right) L \right]. \end{aligned} \quad (8.25)$$

The Hamiltonian in terms of the metric is given by

$$\begin{aligned} 2\mathcal{H} &= 2p_t \dot{t} + 2p_\phi \dot{\phi} + 2p_r \dot{r} - 2\mathcal{L} \\ &= - \left(1 - \frac{2M}{r} - cr^{-(1+3w)} \right) \dot{t}^2 - \left(\frac{4Ma}{r} + 2acr^{-(1+3w)} \right) \dot{t}\dot{\phi} \\ &\quad + \left[r^2 + \left(1 + \frac{2M}{r} + cr^{-(1+3w)} \right) a^2 \right] \dot{\phi}^2 + \frac{r^2}{\Delta} \dot{r}^2. \end{aligned} \quad (8.26)$$

8. Lyapunov exponent, ISCO and Kolmogorov-Senai entropy for Kerr-Kiselev black hole

Since the Hamiltonian does not depends on 't', then we can write it as follows:

$$\begin{aligned}
2\mathcal{H} = & -\left[\left(1 - \frac{2M}{r} - cr^{-(1+3w)}\right)\dot{t} + \left(\frac{2Ma}{r} + acr^{-(1+3w)}\right)\dot{\phi}\right]\dot{t} \\
& + \frac{r^2}{\Delta}\dot{r}^2 + \left[-\left(\frac{2Ma}{r} + acr^{-(1+3w)}\right)\dot{t} \right. \\
& \left. + \left(r^2 + \left(1 + \frac{2M}{r} + cr^{-(1+3w)}\right)a^2\right)\dot{\phi}\right].
\end{aligned} \tag{8.27}$$

Which is equivalent to

$$-E\dot{t} + L\dot{\phi} + \frac{r^2}{\Delta}\dot{r}^2 = \xi = \text{constant} \tag{8.28}$$

Here $\xi = -1, 0, 1$ for time-like geodesic, null geodesic and space-like geodesic, respectively. Putting eqs.(8.24)-(8.25) in eqn.(8.28) we get

$$r^2\dot{r}^2 = r^2E^2 + \left(\frac{2M}{r} + cr^{-(1+3w)}\right)(aE - L)^2 + (a^2E^2 - L^2) + \xi\Delta \tag{8.29}$$

8.4.1.1 Circular null geodesic:

For circular null geodesics ($\xi = 0$), the radial equation (8.29) gives

$$r^2\dot{r}^2 = r^2E^2 + \left(\frac{2M}{r} + cr^{-(1+3w)}\right)(aE - L)^2 + (a^2E^2 - L^2), \tag{8.30}$$

where, E is the energy per unit mass and L is the angular momentum per unit mass of the particle express the trajectory.

At the points $r = r_o$, $E = E_o$ and $L = L_o$ the circular geodesics condition $\dot{r}^2 = (\dot{r}^2)' = 0$ gives the following radius finding equations,

$$r_o^2E_o^2 + \left(\frac{2M}{r_o} + cr_o^{-(1+3w)}\right)(aE_o - L_o)^2 + (a^2E_o^2 - L_o^2) = 0, \tag{8.31}$$

$$2r_oE_o^2 - \left(\frac{2M}{r_o^2} + c(1+3w)r_o^{-(2+3w)}\right)(aE_o - L_o)^2 = 0. \tag{8.32}$$

We can write the above equations (8.31) and (8.32) in simplified form by introducing

8.4. Rotating Black hole:

the impact parameter $D_o = \frac{L_o}{E_o}$ as

$$r_o^2 + \left(\frac{2M}{r_o} + cr_o^{-(1+3w)} \right) (a - D_o)^2 + (a^2 - D_o^2) = 0, \quad (8.33)$$

$$r_o - \left(\frac{2M}{r_o^2} + \frac{c}{2}(1+3w)r_o^{-(2+3w)} \right) (a - D_o)^2 = 0. \quad (8.34)$$

From the equation (8.34) we get

$$D_o = a \mp \frac{r_o^2}{\sqrt{Mr_o + \frac{c}{2}(1+3w)r_o^{(1-3w)}}}. \quad (8.35)$$

Notice that the equation (8.33) is valid if and only if $|D_o| > a$. In the case of counter rotating orbits, $|D_o - a| = -(D_o - a)$, which correlates to upper sign in the above equation (8.35) while in the case of co-rotating orbits, $|D_o - a| = (D_o - a)$ which correlates to the lower sign in the above equation (8.35).

Putting the equation (8.35) into (8.33), we obtain an equation for the radius of null circular geodesics

$$r_o^2 - 3Mr_o \pm 2a\sqrt{Mr_o + \frac{c}{2}(1+3w)r_o^{(1-3w)}} - \frac{c}{2}(1+3w)r_o^{(1-3w)} = 0. \quad (8.36)$$

When $c = 0$, we find the well known result (Chandrasekhar [1998]). By using equations (8.33) and (8.35), we can find an another important relation for null circular orbits as follows

$$D_o^2 = a^2 + r_o^2 \left(\frac{3Mr_o + \frac{3c}{2}(1+w)r_o^{(1-3w)}}{Mr_o + \frac{c}{2}(1+3w)r_o^{(1-3w)}} \right). \quad (8.37)$$

To analyze the null circular geodesics we will derived an important quantity is the angular frequency (Ω_σ) which is given by

$$\Omega_o = \frac{\left(1 - \frac{2M}{r} - cr_o^{-(1+3w)} D_o \right) + a \left(\frac{2M}{r} + cr_o^{-(1+3w)} \right)}{\left(r^2 + a^2 + \frac{2Ma^2}{r} + a^2 cr_o^{-(1+3w)} D_o \right) - a \left(\frac{2M}{r} + cr_o^{-(1+3w)} D_o \right)} = \frac{1}{D_o}. \quad (8.38)$$

8. Lyapunov exponent, ISCO and Kolmogorov-Senai entropy for Kerr-Kiselev black hole

With the help of the equations (8.35) and (8.33) we show that the angular frequency (Ω_o) of the equatorial null circular geodesics is inverse of the impact parameter D_o , which generalize the four dimensional result (Chandrasekhar [1998]). Also it is a general property of any stationary space-time.

8.4.1.2 Circular time-like geodesics

For time-like circular geodesics ($\xi = -1$), the radial equation (8.29) gives

$$r^2 \dot{r}^2 = r^2 E^2 + \left(\frac{2M}{r} + cr^{-(1+3w)} \right) (aE - L)^2 + (a^2 E^2 - L^2) - \Delta. \quad (8.39)$$

Now we shall focus on radial equation of ISCO which governing the circular time like geodesics in terms of reciprocal radius $u = \frac{1}{r}$, can be written as

$$\begin{aligned} \mathcal{V} = u^{-4} \dot{u}^2 &= E^2 + 2Mu^3(aE - L)^2 + cu^{3(1+w)}(aE - L)^2 \\ &+ (a^2 E^2 - L^2)u^2 - u^2(a^2 - cu^{3w-1}) + 2Mu - 1, \end{aligned} \quad (8.40)$$

where \mathcal{V} is the effective potential.

The condition for the existence of the circular orbits are at $r = r_\sigma$ or $u = u_\sigma$ is given by

$$\mathcal{V} = 0, \quad (8.41)$$

and

$$\frac{d\mathcal{V}}{du} = 0. \quad (8.42)$$

$\mathcal{V} = 0$ gives,

$$\begin{aligned} E^2 &+ 2Mu_\sigma^3(aE - L)^2 + cu_\sigma^{3(1+w)}(aE - L)^2 + (a^2 E^2 - L^2)u_\sigma^2 \\ &- u_\sigma^2(a^2 - cu_\sigma^{3w-1}) + 2Mu_\sigma - 1 = 0, \end{aligned} \quad (8.43)$$

8.4. Rotating Black hole:

and $\frac{dV}{du} = 0$ gives,

$$3Mu_\sigma^2(aE - L)^2 + \frac{3c(1+w)}{2}u_\sigma^{2+3w}(aE - L)^2 + (a^2E^2 - L^2)u_\sigma - u_\sigma(a^2 - cu_\sigma^{3w-1}) + \frac{c(3w-1)}{2}u_\sigma^{3w} + M = 0. \quad (8.44)$$

For circular orbits, let L_σ and E_σ be the value of energy and angular momentum at the radius $r_\sigma = \frac{1}{u_\sigma}$, respectively. Now putting $z = L_\sigma - aE_\sigma$, in the equations (8.43) and (8.44) we obtain the followings equations

$$cu_\sigma^{3(1+w)}z^2 + 2Mu_\sigma^3z^2 - (z^2 + 2azE_\sigma)u_\sigma^2 - u_\sigma^2(a^2 - cu_\sigma^{3w-1}) + 2Mu_\sigma - 1 + E_\sigma^2 = 0. \quad (8.45)$$

and

$$\begin{aligned} \frac{3c(1+w)}{2}u_\sigma^{(2+3w)}z^2 + 3Mu_\sigma^2z^2 - (z^2 + 2azE_\sigma)u_\sigma - u_\sigma(a^2 - cu_\sigma^{3w-1}) \\ + \frac{c(3w-1)}{2}u_\sigma^{3w} + M = 0. \end{aligned} \quad (8.46)$$

With the help of the equation (8.46), we get an equation for E_σ^2 from equation (8.45) as

$$E_\sigma^2 = 1 - u_\sigma M + Mz^2u_\sigma^3 + \frac{c(3w-1)}{2}u_\sigma^{3w+1} + \frac{c(3w+1)}{2}u_\sigma^{3(1+w)}z^2. \quad (8.47)$$

Again from the equation (8.46), we get

$$\begin{aligned} 2azE_\sigma u_\sigma = & z^2 \left(3Mu_\sigma^2 + \frac{3c(1+w)}{2}u_\sigma^{2+3w} - u_\sigma \right) \\ & - \left((a^2 - cu_\sigma^{3w-1})u_\sigma - \frac{c(3w-1)}{2}u_\sigma^{3w} - M \right). \end{aligned} \quad (8.48)$$

After eliminating E_σ from the equations (8.47) and (8.48), we can get an quadratic equation for z^2 as

$$\mathcal{P}z^4 + \mathcal{Q}z^2 + \mathcal{S} = 0. \quad (8.49)$$

8. Lyapunov exponent, ISCO and Kolmogorov-Senai entropy for Kerr-Kiselev black hole

where,

$$\begin{aligned}\mathcal{P} &= u_\sigma^2 \left[\left(3Mu_\sigma - 1 + \frac{3c(1+w)}{2} u_\sigma^{3w+1} \right)^2 - 4a^2 \left(Mu_\sigma^3 + \frac{c(1+3w)}{2} u_\sigma^{3(1+w)} \right) \right], \\ \mathcal{Q} &= -2u_\sigma \left[\left(3Mu_\sigma - 1 + \frac{3c(1+w)}{2} u_\sigma^{3w+1} \right) \left[\left((a^2 - cu_\sigma^{3w-1})u_\sigma \right. \right. \right. \\ &\quad \left. \left. - \frac{c(3w-1)}{2} u_\sigma^{3w} - M \right) + 2a^2 u_\sigma \left(1 - Mu_\sigma + \frac{c(3w-1)}{2} u_\sigma^{3w+1} \right) \right], \\ \mathcal{S} &= \left[\left((a^2 - cu_\sigma^{3w-1})u_\sigma - \frac{c(3w-1)}{2} u_\sigma^{3w} - M \right) \right]^2.\end{aligned}$$

Now, the solution of the quadratic equation (8.49) is

$$z^2 = \frac{-\mathcal{Q} \pm \mathcal{D}}{2\mathcal{P}}, \quad (8.50)$$

where, \mathcal{D} denotes the discriminant of the equation (8.49) which can be found as

$$\mathcal{D} = 4au_\sigma \Delta_{u_\sigma} \sqrt{Mu_\sigma + \frac{c(3w+1)}{2} u_\sigma^{3w+1}}, \quad (8.51)$$

and

$$\Delta_{u_\sigma} = (a^2 - cu_\sigma^{3w-1})u_\sigma^2 - 2Mu_\sigma + 1. \quad (8.52)$$

In order to write the solution of the equation (8.49) in simple form, we consider the following expression

$$X_+ X_- = \left(3Mu_\sigma - 1 + \frac{3c(1+w)}{2} u_\sigma^{3w+1} \right)^2 - 4a^2 \left(Mu_\sigma^3 + \frac{c(1+3w)}{2} u_\sigma^{3(1+w)} \right), \quad (8.53)$$

where,

$$X_\pm = \left(1 - 3Mu_\sigma - \frac{3c(1+w)}{2} u_\sigma^{3w+1} \pm 2a \sqrt{Mu_\sigma^3 + \frac{c(3w+1)}{2} u_\sigma^{3(w+1)}} \right). \quad (8.54)$$

Thus the solution reduces to

$$z^2 u_\sigma^2 = \frac{\Delta_{u_\sigma} - X_\mp}{X_\mp}. \quad (8.55)$$

8.4. Rotating Black hole:

Again we can utilize the identity

$$\Delta_{u_\sigma} - X_{\mp} = u_\sigma \left[a\sqrt{u_\sigma} \pm \sqrt{M + \frac{c(3w+1)}{2}u_\sigma^{3w}} \right]^2. \quad (8.56)$$

Hence the solution for z can be written in the following simple form as

$$z = - \frac{\left[a\sqrt{u_\sigma} \pm \sqrt{M + \frac{c(3w+1)}{2}u_\sigma^{3w}} \right]}{\sqrt{u_\sigma x_{\pm}}}. \quad (8.57)$$

Here the lower sign in the foregoing equations indicates to the co-rotating orbit whereas the upper sign indicates to the counter-rotating orbit. Inserting expression of (8.57) in the equation (8.47), we obtain following expression for E_σ as energy

$$E_\sigma = \frac{1}{\sqrt{z_{\pm}}} \left[1 - 2Mu_\sigma \mp a\sqrt{Mu_\sigma + \frac{c(3w+1)}{2}u_\sigma^{3w+1}} \right]. \quad (8.58)$$

Again with the help of eqns.(8.57), (8.58) and the relation $L_\sigma = aE_\sigma + z$, we obtain the angular momentum for the time circular geodesics as

$$\begin{aligned} L_\sigma = & \mp \frac{1}{\sqrt{u_\sigma z_{\pm}}} \left[\sqrt{M + \frac{c(3w+1)}{2}u_\sigma^{3w}} \left(1 + a^2u_\sigma^2 \pm 2au_\sigma \sqrt{Mu_\sigma + \frac{c(3w+1)}{2}u_\sigma^{3w+1}} \right) \right. \\ & \left. \mp ac\sqrt{u_\sigma^5} \right]. \end{aligned} \quad (8.59)$$

In order to find the minimum radius for a stable circular orbit, we will obtained the second derivative of \mathcal{V} with respect to r for the value of E_σ and L_σ specific to circular orbit. Here we use the equations (8.41, 8.42) with further equation

$$\left. \frac{d^2V}{du^2} \right|_{u=u_\sigma} = 0, \quad (8.60)$$

and we found that

$$\frac{d^2V}{du^2} = \frac{1}{u_\sigma} \left[6Mz^2u_\sigma^2 + 3c(w+1)(3w+1)u_\sigma^{3w+2}z^2 + 2c(3w-1)u_\sigma^{3w} - 2M \right]. \quad (8.61)$$

8. Lyapunov exponent, ISCO and Kolmogorov-Senai entropy for Kerr-Kiselev black hole

By the equation (8.55) we get

$$\begin{aligned} \frac{d^2V}{du^2}|_{u=u_\sigma} &= \frac{2}{u_\sigma X_\pm} \left[\left(3M + \frac{3c(w+1)(3w+1)}{2} u_\sigma^{3w} \right) \Delta_{u_\sigma} \right. \\ &\quad \left. - \left(\frac{3c(w+1)(3w+1)}{2} u_\sigma^{3w} + c(3w-1)u_\sigma^{3w} + 4M \right) X_\pm \right]. \end{aligned} \quad (8.62)$$

Therefore the equation of ISCO at the reciprocal radius is

$$\begin{aligned} &\frac{2}{u_\sigma X_\pm} \left[\left(3M + \frac{3c(w+1)(3w+1)}{2} u_\sigma^{3w} \right) \Delta_{u_\sigma} \right. \\ &\quad \left. - \left(\frac{3c(w+1)(3w+1)}{2} u_\sigma^{3w} + c(3w-1)u_\sigma^{3w} + 4M \right) X_\pm \right] = 0. \end{aligned} \quad (8.63)$$

or this is similar to

$$\begin{aligned} &\left(3Mu_\sigma^2 + \frac{3c(w+1)(3w+1)}{2} u_\sigma^{3w+2} \right) \left(a^2 - cu_\sigma^{3w-1} \right) + \frac{3}{4}c^2(9w^2 \\ &\quad + 18w+1)(w+1)u_\sigma^{6w+1} + \frac{3cM}{2}(3w^2+14w+3)u_\sigma^{3w+1} \pm 8a \left(M + \frac{c}{8}(9w^2 \right. \\ &\quad \left. + 18w+1)u_\sigma^{6w} \right) \sqrt{Mu_\sigma^3 + \frac{c(3w+1)}{2} u_\sigma^{3(w+1)} + 6M^2u_\sigma - M} = 0. \end{aligned} \quad (8.64)$$

Returning to the variable r_σ , we get the equation of innermost stable circular orbit (ISCO) for non extremal BH is identified by

$$\begin{aligned} &M r_\sigma^{6w+1} - 6M^2 r_\sigma^{6w} - 3Ma^2 r_\sigma^{6w-1} - \frac{3cM}{2}(3w^2+14w+3)r_\sigma^{3w} \pm 8a \left(Mr_\sigma^{3w} \right. \\ &\quad \left. + \frac{c}{8}(9w^2+18w+1) \right) \sqrt{Mr_\sigma^{6w-1} + \frac{c(3w+1)}{2} r_\sigma^{3w-1}} \\ &\quad - 3c(w+1) \left[\frac{a^2(3w+1)}{2} r_\sigma^{3w-1} + \frac{c(9w^2+12w-1)}{4} \right] = 0. \end{aligned} \quad (8.65)$$

Let the smallest root of the above equation be $r_\sigma = r_{ISCO}$ which will be innermost stable circular orbit (ISCO) of the black hole. Here (-) sign determines for direct orbit and (+) sign determines for retrograde orbit. We consider the following special cases of the quintessence parameter w , namely cosmological constant ([Slaný and Stuchlík \[2020\]](#)).

8.4. Rotating Black hole:

Special cases:

- i. When $w = \frac{1}{3}$ and $c = -Q^2$, we can get the equation of ISCO for non-extremal Kerr-Newman black hole which is given by

$$Mr_\sigma^3 - 6M^2r_\sigma^2 - 3Ma^2r_\sigma + 9MQ^2r_\sigma \mp 8a(Mr_\sigma - Q^2)^{\frac{3}{2}} + 4Q^2(a^2 - Q^2) = 0 \quad (8.66)$$

The smallest root (real) of the equation (8.66) is the radius of ISCO.

- ii. When $w = \frac{1}{3}$ and $c = 0$, the equation (8.65) is similar to the equation of ISCO for Kerr black hole which is as follows:

$$r_\sigma^2 - 6Mr_\sigma \mp 8a\sqrt{Mr_\sigma - 3a^2} = 0. \quad (8.67)$$

The radius of the ISCO is equal to the real root of the above equation.

- iii. When $w = \frac{1}{3}$ and $a = 0$, we obtained the equation of ISCO for Reissner Nordström black hole as follows

$$Mr_\sigma^3 - 6M^2r_\sigma^2 + 9MQ^2r_\sigma - 4Q^4 = 0. \quad (8.68)$$

The radius of the ISCO for the Reissner Nordström black hole can be found by obtaining the smallest real root of the previous equation.

- iv. When $w = \frac{1}{3}$ and $c = a = 0$, we obtain the radius of ISCO for Schwarzschild black hole is given by

$$r_\sigma - 6M = 0. \quad (8.69)$$

8.4.2 Lyapunov Exponent:

8.4.2.1 Time-like circular geodesics (Equation of ISCO):

Now we will calculate the Lyapunov exponent and KS entry for time-circular orbit. Using the equation (8.5), we get the Lyapunov exponent and KS entry in terms of

8. Lyapunov exponent, ISCO and Kolmogorov-Senai entropy for Kerr-Kiselev black hole

the radial equation of ISCO as follows

$$\lambda_{time} = h_{ks} = \sqrt{\frac{-\left(Mr_{\sigma}^{6w+1} - 6M^2r_{\sigma}^{6w} - 3Ma^2r_{\sigma}^{6w-1} - cMGr_{\sigma}^{3w} \pm 8aH - cT\right)}{r_{\sigma}^4\left(r_{\sigma}^{3w+1} - 3Mr_{\sigma}^{3w} - \frac{3c(1+w)}{2} \pm 2a\sqrt{Mr_{\sigma}^{3w} + \frac{c(3w+1)}{2}}\right)}} \quad (8.70)$$

where,

$$\begin{aligned} G &= \frac{3}{2}(3w^2 + 14w + 3), \\ H &= \left(Mr_{\sigma}^{3w} + \frac{c}{8}(9w^2 + 18w + 1)\right)\sqrt{Mr_{\sigma}^{6w-1} + \frac{c(3w+1)}{2}r_{\sigma}^{3w-1}}, \\ T &= 3(w+1)\left[\frac{a^2(3w+1)}{2}r_{\sigma}^{3w-1} + \frac{c(9w^2 + 12w - 1)}{4}\right]. \end{aligned} \quad (8.71)$$

The condition for existing the time-circular geodesics motion of the test particle are energy (E_{σ}) and angular momentum (L_{σ}) must be real and finite. For these we must have $r_{\sigma}^{3w+1} - 3Mr_{\sigma}^{3w} - \frac{3c(1+w)}{2} \pm 2a\sqrt{Mr_{\sigma}^{3w} + \frac{c(3w+1)}{2}} > 0$ and $r_{\sigma}^{3w} > -\frac{c(3w+1)}{2M}$.

From the above equation (8.70), we can conclude that the time-circular geodesics of non extremal black hole is stable when

$$Mr_{\sigma}^{6w+1} - 6M^2r_{\sigma}^{6w} - 3Ma^2r_{\sigma}^{6w-1} - cMGr_{\sigma}^{3w} \pm 8aH - cT > 0, \quad (8.72)$$

that is, λ_{time} or h_{ks} is imaginary, the time-circular geodesics is unstable when

$$Mr_{\sigma}^{6w+1} - 6M^2r_{\sigma}^{6w} - 3Ma^2r_{\sigma}^{6w-1} - cMGr_{\sigma}^{3w} \pm 8aH - cT < 0, \quad (8.73)$$

such that λ_{time} or h_{ks} is real and circular geodesics is marginally stable when

$$Mr_{\sigma}^{6w+1} - 6M^2r_{\sigma}^{6w} - 3Ma^2r_{\sigma}^{6w-1} - cMGr_{\sigma}^{3w} \pm 8aH - cT = 0. \quad (8.74)$$

that is, λ_{time} or h_{ks} is zero.

8.4. Rotating Black hole:

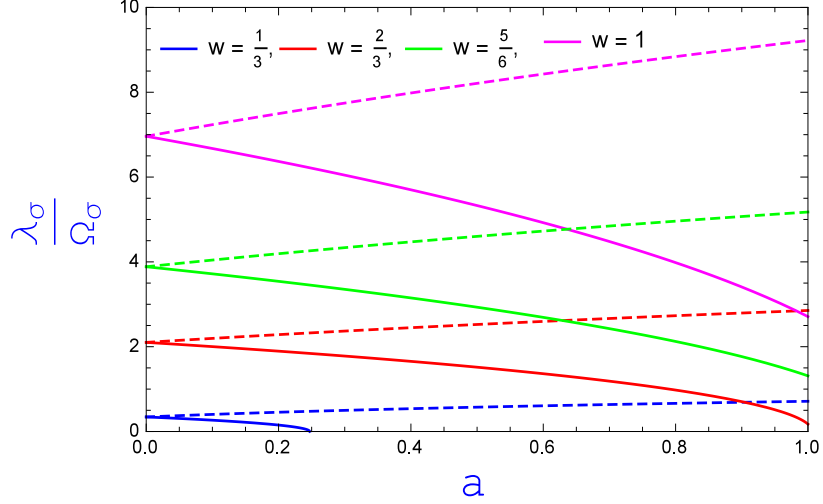


Figure 8.1: Dimensionless instability exponent $\frac{\lambda_\sigma}{\Omega_\sigma}$ as a function of rotation a for real value of Lyapunov exponent. We use units such that $M = 1, c = 2$. Solid lines refer to corotating orbits and dashed lines refer to counterrotating orbits.

Special cases:

- i. When $w = \frac{1}{3}, c = -Q^2$, we can get the Lyapunov exponent and KS entry for Kerr-Newman black hole in terms of ISCO equation are given by

$$\begin{aligned} \lambda_{KN} &= h_k s \\ &= \sqrt{\frac{-\left(Mr_\sigma^3 - 6M^2r_\sigma^2 - 3Ma^2r_\sigma + 9MQ^2r_\sigma \mp 8a(\eta_1)^{\frac{3}{2}} + 4Q^2\eta_2\right)}{r_\sigma^4\left(r_\sigma^2 - 3Mr_\sigma \mp 2a\sqrt{\eta_1} + 2Q^2\right)}} \end{aligned} \quad (8.75)$$

where, $\eta_1 = Mr_\sigma - Q^2$ and $\eta_2 = a^2 - Q^2$.

- ii. For Kerr black hole $w = \frac{1}{3}, c = 0$, the Lyapunov exponent and KS entry for circular time-like geodesics are

$$\lambda_{Kerr} = h_k s = \sqrt{\frac{-M\left(r_\sigma^2 - 6M^2r_\sigma \mp 8a\sqrt{Mr_\sigma} - 3a^2\right)}{r_\sigma^3\left(r_\sigma^2 - 3Mr_\sigma \mp 2a\sqrt{Mr_\sigma}\right)}}. \quad (8.76)$$

- iii. For the Reissner Nordström black hole $w = \frac{1}{3}, c = -Q^2, a = 0$, the Lyapunov

8. Lyapunov exponent, ISCO and Kolmogorov-Senai entropy for Kerr-Kiselev black hole

exponent and KS entry for time-like geodesics are

$$\lambda_{RN} = h_{ks} = \sqrt{\frac{-(Mr_\sigma^3 - 6M^2r_\sigma^2 + 9MQ^2r_\sigma - 4Q^4)}{r_\sigma^4(r_\sigma^2 - 3Mr_\sigma + 2Q^2)}}. \quad (8.77)$$

- iv. For Schwarzschild black hole $w = \frac{1}{3}, c = -Q^2 = 0, a = 0$, the Lyapunov exponent and KS entry for circular time-like geodesics in terms of ISCO equation are given by

$$\lambda_{Sch} = h_{ks} = \sqrt{\frac{-M(r_\sigma - 6M)}{r_\sigma^3(r_\sigma - 3M)}}. \quad (8.78)$$

8.4.2.2 Null circular geodesics:

Lyapunov exponent and KS entry for circular null geodesics are

$$\lambda_{Null} = h_{ks} = \sqrt{\frac{(L_o - aE_o)^2 \left(3Mr_o + 3c(1+w)r_o^{(1-3w)} \right)}{r_o^6}}. \quad (8.79)$$

Since $(L_o - aE_o)^2 \geq 0$ and $r_o^{3w} > \frac{-c(w+1)}{M}$ then λ_{Null} is real, so the circular null geodesics are unstable.

Special cases:

- i. When $w = \frac{1}{3}, c = -Q^2$, we can get the Lyapunov exponent and KS entry for Kerr-Newman black hole which is given by

$$\lambda_{KN} = h_{ks} = \sqrt{\frac{(L_o - aE_o)^2 (3Mr_o - 4Q^2)}{r_o^6}}. \quad (8.80)$$

- ii. When $w = \frac{1}{3}, c = 0$, the equation (8.79) is similar to the equation Kerr black hole which is as follows :

$$\lambda_{Kerr} = h_{ks} = \sqrt{\frac{3M(L_o - aE_o)^2}{r_o^5}}. \quad (8.81)$$

8.4. Rotating Black hole:

- iii. For the Reissner Nordström black hole $w = \frac{1}{3}, c = -Q^2, a = 0$, the Lyapunov exponent and KS entry for circular null geodesics are

$$\lambda_{RN} = h_k s = \sqrt{\frac{L_o^2(3Mr_o - 4Q^2)}{r_o^6}}. \quad (8.82)$$

When $r_o > \frac{4}{3}\frac{Q^2}{M}$, λ_{RN} is real which implies that null-circular geodesics for Reissner Nordström black hole is unstable.

- iv. For Schwarzschild black hole $w = \frac{1}{3}, c = 0, a = 0$, the Lyapunov exponent and KS entry for circular null geodesics are given by

$$\lambda_{Sch} = h_k s = \sqrt{\frac{3ML_o^2}{r_\sigma^5}}. \quad (8.83)$$

It can be verify that when $r_o = 3M$, λ_{Sch} is real. Hence null-circular geodesics for Schwarzschild photon sphere are unstable.

8.4.3 Angular velocity of time-like circular geodesic:

For time-like circular geodesic, the angular velocity at $r = r_\sigma$ is given by

$$\Omega_\sigma = \frac{\dot{\phi}}{\dot{t}} = \frac{\left(1 - \frac{2M}{r_\sigma} - cr_\sigma^{-(1+3w)}\right)L_\sigma + a\left(\frac{2M}{r_\sigma} + cr_\sigma^{-(1+3w)}\right)aE_\sigma}{\left(r_\sigma^2 + a^2 + \frac{2Ma^2}{r_\sigma} + a^2cr_\sigma^{-(1+3w)}\right)E_\sigma - a\left(\frac{2M}{r_\sigma} + cr_\sigma^{-(1+3w)}\right)aL_\sigma}. \quad (8.84)$$

The equation (8.84) can be written as

$$\Omega_\sigma = \frac{[L_\sigma - 2Mu_\sigma z - cu_\sigma^{(1+3w)}z]u_\sigma^2}{(1 + a^2u_\sigma^2)E_\sigma - 2Ma u_\sigma^3 z - acu_\sigma^{3(1+3w)}z}. \quad (8.85)$$

The numerator of the equation (8.85) can be written in the simplified form as

$$L_\sigma - 2Mu_\sigma z - cu_\sigma^{(1+3w)}z = \mp \frac{\sqrt{M + \frac{c(3w+1)}{2}u_\sigma^{3w}}}{\sqrt{u_\sigma z \pm}} \Delta_{u_\sigma}. \quad (8.86)$$

8. Lyapunov exponent, ISCO and Kolmogorov-Senai entropy for Kerr-Kiselev black hole

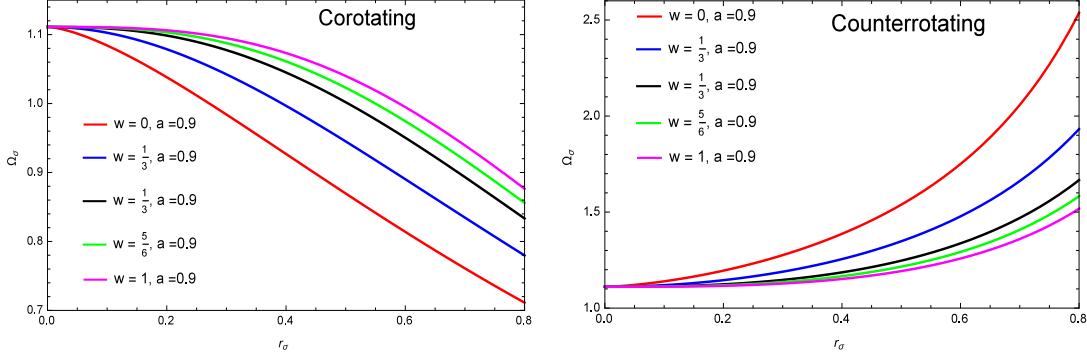


Figure 8.2: The plots shows the time-like orbital frequency Ω_σ to the radial coordinate r_σ of corotating orbits (left panel) and counterrotating orbits (right panel) for different values of w . We use units $M = 1, a = 0.9$ and $c = 2$.

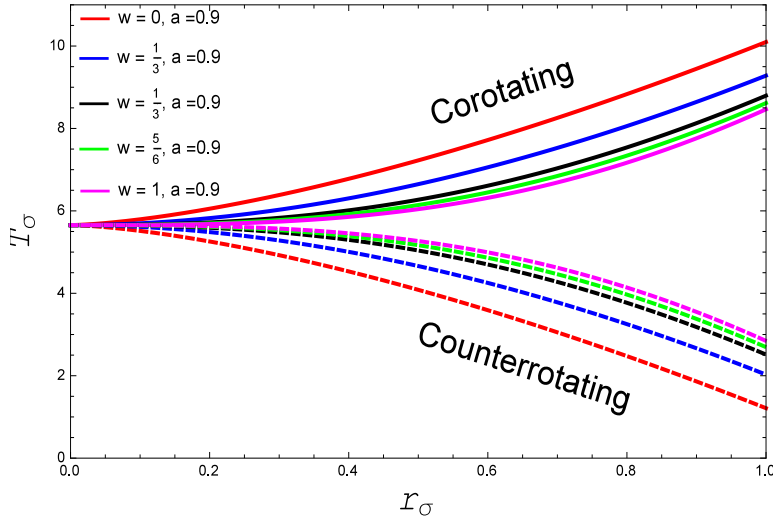


Figure 8.3: The plot shows the orbital time period of time-like circular geodesic T_σ to the radius r_σ . We use units such that $M = 1, a = 0.9$ and $c = 2$. Solid lines refer to corotating orbits and dashed lines refer to counterrotating orbits.

Similarly, the denominator can be written as

$$(1 + a^2 u_\sigma^2) E_\sigma - 2 M a u_\sigma^3 z - a c u_\sigma^{3(1+3)} z = \frac{\Delta_{u_\sigma}}{\sqrt{z_\pm}} \left(1 \mp a \sqrt{M u_\sigma^3 + \frac{c(3w+1)}{2} u_\sigma^{3(w+1)}} \right) \quad (8.87)$$

Putting eqn.(8.86) and eqn.(8.87) into eqn.(8.85), we obtain the angular velocity for

8.4. Rotating Black hole:

time circular orbit as

$$\Omega_\sigma = \mp \frac{\sqrt{Mu_\sigma^3 + \frac{c(3w+1)}{2}u_\sigma^{3(w+1)}}}{1 \mp a\sqrt{Mu_\sigma^3 + \frac{c(3w+1)}{2}u_\sigma^{3(w+1)}}}. \quad (8.88)$$

Now the angular velocity in terms of r_σ for time circular geodesics is

$$\Omega_\sigma = \mp \frac{\sqrt{Mr_\sigma^{3w} + \frac{c(3w+1)}{2}}}{r_\sigma^{\frac{3(w+1)}{2}} \mp a\sqrt{Mr_\sigma^{3w} + \frac{c(3w+1)}{2}}}. \quad (8.89)$$

Now the time period for circular time-like orbit is given by

$$T_\sigma = \frac{2\pi}{\Omega_\sigma} = \mp 2\pi \frac{\left(r_\sigma^{\frac{3(w+1)}{2}} \mp a\sqrt{Mr_\sigma^{3w} + \frac{c(3w+1)}{2}}\right)}{\sqrt{Mr_\sigma^{3w} + \frac{c(3w+1)}{2}}} \quad (8.90)$$

At the limit $w = \frac{1}{3}, c = 0, a = 0$, the above equation can be written in the form $T_\sigma^2 \propto r_\sigma^3$. This shows that the equation (8.90) satisfies relativistic Kepler's law for Schwarzschild black hole.

8.4.4 Critical Exponent:

8.4.4.1 Time-like circular geodesics:

Now we will calculate the critical exponent for equatorial time-like circular geodesics. Thus the reciprocal of critical exponent is followed by the equation (8.8)

$$\frac{1}{\gamma} = 2\pi \sqrt{\frac{-\left(Mr_\sigma^{6w+1} - 6M^2r_\sigma^{6w} - 3Ma^2r_\sigma^{6w-1} - cMGr_\sigma^{3w} \pm 8aH - cT\right)\left(r_\sigma^{\frac{3(w+1)}{2}} \mp a\eta_3\right)^2}{r_\sigma^4\eta_3\left(r_\sigma^{3w+1} - 3Mr_\sigma^{3w} - \frac{3c(1+w)}{2} \pm 2a\eta_3\right)}} \quad (8.91)$$

where, $\eta_3 = \sqrt{Mr_\sigma^{3w} + \frac{c(3w+1)}{2}}$.

Since $\left(r_\sigma^{\frac{3(w+1)}{2}} \mp a\sqrt{Mr_\sigma^{3w} + \frac{c(3w+1)}{2}}\right)^2 \geq 0$, $r_\sigma^{3w} > -\frac{c(3w+1)}{2M}$

8. Lyapunov exponent, ISCO and Kolmogorov-Senai entropy for Kerr-Kiselev black hole

$\left(r_\sigma^{3w+1} - 3Mr_\sigma^{3w} - \frac{3c(1+w)}{2} \pm 2a\sqrt{Mr_\sigma^{3w} + \frac{c(3w+1)}{2}}\right) \geq 0$,
and $Mr_\sigma^{6w+1} - 6M^2r_\sigma^{6w} - 3Ma^2r_\sigma^{6w-1} - cMG r_\sigma^{3w} \pm 8aH - cT < 0$. So $\frac{1}{\gamma}$ is real which shows that equatorial time-like circular geodesics is unstable.

Special cases:

- i. When $w = \frac{1}{3}, c = -Q^2$, we can get the equation of critical exponent for Kerr-Newman black hole in terms of ISCO which is given by

$$\frac{1}{\gamma} = 2\pi \sqrt{\frac{-(Mr_\sigma^3 - 6M^2r_\sigma^2 - 3Ma^2r_\sigma + 9MQ^2r_\sigma \mp 8a(\eta_1)^{\frac{3}{2}} + 4Q^2\eta_2(r_\sigma^2 \mp a\sqrt{\eta_1})^2)}{r_\sigma^4(\eta_1)(r_\sigma^2 - 3Mr_\sigma \mp 2a\sqrt{\eta_1} + 2Q^2)}} \quad (8.92)$$

- ii. When $w = \frac{1}{3}$ and $c = 0$, the equation (8.91) is similar to the equation of critical exponent for Kerr black hole in terms of ISCO which is as follows :

$$\frac{1}{\gamma} = 2\pi \sqrt{\frac{-\left(r_\sigma^2 - 6M^2r_\sigma \mp 8a\sqrt{Mr_\sigma} - 3a^2\right)(r_\sigma\sqrt{r_\sigma} \mp a\sqrt{M})^2}{r_\sigma^3\left(r_\sigma^2 - 3Mr_\sigma \mp 2a\sqrt{Mr_\sigma}\right)}}. \quad (8.93)$$

- iii. For the Reissner Nordström black hole $w = \frac{1}{3}, c = -Q^2$ and $a = 0$, the reciprocal of critical exponent for time-like geodesic is

$$\frac{1}{\gamma} = 2\pi \sqrt{\frac{-(Mr_\sigma^3 - 6M^2r_\sigma^2 + 9MQ^2r_\sigma - 4Q^4)}{(Mr_\sigma - Q^2)(r_\sigma^2 - 3Mr_\sigma + 2Q^2)}}. \quad (8.94)$$

- iv. When $w = \frac{1}{3}$ and $c = a = 0$, we obtained the reciprocal of critical exponent for Schwarzschild black hole in terms of ISCO equation

$$\frac{1}{\gamma} = 2\pi \sqrt{\frac{-(r_\sigma - 6M)}{r_\sigma - 3M}}. \quad (8.95)$$

8.4.4.2 Null circular geodesics:

8.4. Rotating Black hole:

The reciprocal of critical exponent associated to null circular geodesics is given by

$$\left(\frac{1}{\gamma}\right)_{Null} = 2\pi \left(r_o^{\frac{3(w+1)}{2}} \mp a \sqrt{Mr_o^{3w} + \frac{c(3w+1)}{2}} \right) \times \sqrt{\frac{(L_o - aE_o)^2 \left(3Mr_o + 3c(1+w)r_o^{(1-3w)} \right)}{r_o^6 \left(Mr_o^{3w} + \frac{c(3w+1)}{2} \right)}}. \quad (8.96)$$

Special cases:

We take following limits in the above equation (8.96):

- i. When $w = \frac{1}{3}$ and $c = -Q^2$, we can get reciprocal of critical exponent for Kerr-Newman black hole which is given by

$$\left(\frac{1}{\gamma}\right)_{Null} = 2\pi \sqrt{\frac{(L_o - aE_o)^2 (3Mr_o - 4Q^2) (r_o^2 \mp a \sqrt{Mr_o - Q^2})^2}{r_o^6 (Mr_o - Q^2)}}. \quad (8.97)$$

- ii. When $w = \frac{1}{3}$ and $c = 0$, the equation (8.96) is similar to the reciprocal of critical exponent of null-circular geodesics for Kerr black hole which is as follows :

$$\left(\frac{1}{\gamma}\right)_{null} = 2\pi \sqrt{\frac{3(L_o - aE_o)^2 (r_o \sqrt{r_o} \mp a \sqrt{M})^2}{r_o^5}}. \quad (8.98)$$

- iii. For the Reissner Nordström black hole $w = \frac{1}{3}, c = -Q^2$ and $a = 0$, the reciprocal of critical exponent for null-circular geodesic is

$$\left(\frac{1}{\gamma}\right)_{null} = 2\pi \sqrt{\frac{L_o^2 (3Mr_o - 4Q^2)}{r_o^2 (Mr_o - Q^2)}}. \quad (8.99)$$

- iv. When $w = \frac{1}{3}$ and $c = a = 0$, we obtained the reciprocal of critical exponent for Schwarzschild black hole in terms of null-circular geodesics is

$$\left(\frac{1}{\gamma}\right)_{null} = 2\pi \sqrt{\frac{3L_o^2}{r_o^2}}. \quad (8.100)$$

8.5 Marginally bound circular orbit:

It is known that for stable circular orbits the effective potential has a the local minima. Thus the condition for the existence of stable circular orbit exists is $d^2V_{eff}/dr^2 > 0$. However, for marginally stable circular orbits the condition $d^2V_{eff}/dr^2 = 0$ should be satisfied. For marginally bound circular orbit we have $E_\sigma = 1$ or $E_\sigma^2 = 1$ however, this is not true for asymptotically non-flat spacetimes (Stuchlík [2005]).

Now from equation (8.47), we get

$$z^2 u_\sigma^2 = \frac{Mu_\sigma - \frac{c(3w+1)}{2}u_\sigma^{3w+1}}{Mu_\sigma + \frac{c(3w+1)}{2}u_\sigma^{3w+1}}. \quad (8.101)$$

Again from equation (8.57), we have

$$z^2 u_\sigma^2 = \frac{\left[au_\sigma \pm \sqrt{Mu_\sigma + \frac{c(3w+1)}{2}u_\sigma^{3w+1}} \right]^2}{x_\mp}. \quad (8.102)$$

Hence from (8.101) and (8.102), we get

$$x_\mp = \left[\frac{Mu_\sigma + \frac{c(3w+1)}{2}u_\sigma^{3w+1}}{Mu_\sigma - \frac{c(3w+1)}{2}u_\sigma^{3w+1}} \right] \left[au_\sigma \pm \sqrt{Mu_\sigma + \frac{c(3w+1)}{2}u_\sigma^{3w+1}} \right]^2, \quad (8.103)$$

or the above equation can be written as

$$\begin{aligned} & \left(Mu_\sigma - \frac{c(3w-1)}{2}u_\sigma^{3w+1} \right) \left(1 - 3Mu_\sigma - \frac{3c(1+w)}{2}u_\sigma^{3w+1} \pm 2a\sqrt{Mu_\sigma^3 + \frac{c(3w+1)}{2}u_\sigma^{3(w+1)}} \right) \\ &= \left(Mu_\sigma + \frac{c(3w+1)}{2}u_\sigma^{3w+1} \right) \left[au_\sigma \pm \sqrt{Mu_\sigma + \frac{c(3w+1)}{2}u_\sigma^{3w+1}} \right]^2. \end{aligned} \quad (8.104)$$

After simplification, we get the equation of marginally bound circular orbit in terms

8.5. Marginally bound circular orbit:

of u_σ as follows:

$$\begin{aligned}
M &+ \left(a^2 + \frac{c}{2}(3w+1)u_\sigma^{3w-1} + \frac{3(3w-1)(w+1)}{2(3w+1)}u_\sigma^{3w-1} \right) - \left(4M^2u_\sigma + \frac{c}{2}(3w-1)u_\sigma^{3w} \right) \\
&- M \left(\frac{c}{2}(9w+5)u_\sigma^{3w-1} + a^2 - \frac{3c}{2}(3w-1)u_\sigma^{3w-1} \right) u_\sigma^2 - \frac{3c}{2}(3w-1)u_\sigma^{3w-1} u_\sigma^2 \\
&\mp \left(4aMu_\sigma + ac(3w+1)u_\sigma^{3w-1} \right) \sqrt{Mu_\sigma + \frac{c(3w+1)}{2}u_\sigma^{3w+1}} - \frac{c}{2}(3w+1)u_\sigma^{3w+2} = 0.
\end{aligned} \tag{8.105}$$

Now reverting to r_σ , we can get the above equation as

$$\begin{aligned}
Mr_\sigma^{6w+1} &- \left(4M^2r_\sigma^{6w} + \frac{c}{2}(3w-1)r_\sigma^{3w+1} \right) - M \left(\frac{c}{2}(9w+5)r_\sigma^{3w} + a^2r_\sigma^{6w-1} - \frac{3c}{2}(3w-1)r_\sigma^{3w} \right) \\
&\mp \left(4aMr_\sigma^{3w} + ac(3w+1) \right) \sqrt{Mr_\sigma^{6w-1} + \frac{c(3w+1)}{2}r_\sigma^{(3w-1)}} \\
&- \left(a^2r_\sigma^{3w-1} + \frac{c}{2}(3w+1) + \frac{3(3w-1)(w+1)}{2(3w+1)} \right) = 0.
\end{aligned} \tag{8.106}$$

Let $r_\sigma = r_{mb}$ be the smallest(real) root of the equation (8.106). The root will be the closest bound circular orbit to the black hole.

Special cases:

- i. When $w = \frac{1}{3}$ and $c = -Q^2$, we can get the equation of marginally bound circular orbit for Kerr-Newman black hole which is given by

$$\begin{aligned}
Mr_\sigma^3 - 4M^2r_\sigma^2 - Ma^2r_\sigma + 4MQ^2r_\sigma &\mp (4aMr_\sigma - 2aQ^2)\sqrt{Mr_\sigma - Q^2} \\
&+ Q^2(a^2 - Q^2) = 0.
\end{aligned} \tag{8.107}$$

The smallest root (real) of the equation (8.107) is the radius of marginally bound circular orbit of the black hole.

- ii. When $w = \frac{1}{3}$ and $c = 0$, the equation (8.106) is similar to the equation of Marginally bound circular orbit for Kerr black hole which is as follows :

$$r_\sigma^2 - 4Mr_\sigma \mp 4a\sqrt{Mr_\sigma - a^2} = 0. \tag{8.108}$$

The radius say $r_\sigma = r_{mb}$ can be obtained by finding real smallest root of the

8. Lyapunov exponent, ISCO and Kolmogorov-Senai entropy for Kerr-Kiselev black hole

above equation for the marginally bound circular orbit of the black hole.

- iii. For the Reissner Nordström black hole $w = \frac{1}{3}$, $c = -Q^2$ and $a = 0$, we can get the equation of marginally bound circular orbit which is as follows

$$Mr_\sigma^3 - 4M^2r_\sigma^2 + 4MQ^2r_\sigma - Q^4 = 0. \quad (8.109)$$

The radius of marginally bound circular orbit of the black hole can be found by obtaining the smallest real root of the above equation.

- iv. When $w = \frac{1}{3}$ and $c = a = 0$, we can obtained the radius of marginally bound circular orbit for Schwarzschild back hole as follows

$$r_\sigma - 4M = 0. \quad (8.110)$$

More specifically, we can say that $r_\sigma = 4M$ is the radius of marginally bound circular orbit for Schwarzschild back hole.

The static radius for the circular orbits of test particles is given by the condition $\frac{d^2V_{eff}}{dr^2} = 0$ *i.e.* correspond to local extrema of the effective potential ([Stuchlík and Hledík \[1999\]](#)). Actually, the radii of circular orbits are restricted by the static radius. The important notion of the static radius will be discussed in details in a future project.

8.6 Ratio of Angular velocity between null-circular geodesics and time-circular geodesics:

We have already computed the angular velocity for time circular geodesics ([Pradhan \[2016\]](#)) in the equation (8.89) which is given by

$$\Omega_\sigma = \mp \frac{\sqrt{Mr_\sigma^{3w} + \frac{c(3w+1)}{2}}}{r_\sigma^{\frac{3(w+1)}{2}} \mp a\sqrt{Mr_\sigma^{3w} + \frac{c(3w+1)}{2}}}. \quad (8.111)$$

Again, the similar expression of angular velocity $\Omega_o = \frac{1}{D_o}$ for null circular geodesics

8.6. Ratio of Angular velocity between null-circular geodesics and time-circular geodesics:

can be obtain from the above equation as

$$\Omega_o = \mp \frac{\sqrt{Mr_o^{3w} + \frac{c(3w+1)}{2}}}{r_o^{\frac{3(w+1)}{2}} \mp a\sqrt{Mr_o^{3w} + \frac{c(3w+1)}{2}}}. \quad (8.112)$$

Now the ratio of Angular velocity between null-circular geodesics and time-circular geodesics is

$$\frac{\Omega_o}{\Omega_\sigma} = \left(\frac{\sqrt{Mr_o^{3w} + \frac{c(3w+1)}{2}}}{\sqrt{Mr_\sigma^{3w} + \frac{c(3w+1)}{2}}} \right) \left(\frac{r_\sigma^{\frac{3(w+1)}{2}} \mp a\sqrt{Mr_\sigma^{3w} + \frac{c(3w+1)}{2}}}{r_o^{\frac{3(w+1)}{2}} \mp a\sqrt{Mr_o^{3w} + \frac{c(3w+1)}{2}}} \right). \quad (8.113)$$

- i. When the radius of time-circular geodesics is equal to the radius of null circular geodesic, the corresponding angular velocities are also equal, that is, when $r_\sigma = r_o, Q_\sigma = Q_o$ which shows that the intriguing physical phenomena could occurs in the curve space-time. For instance, it would increase the interesting possibility of exciting quasinormal frequencies of the black hole by orbiting particle, possibly leading to instabilities of the space-time ([Cardoso et al. \[2009\]](#), [Cardoso and Lemos \[2003\]](#)).
- ii. When the radius of time-circular geodesics is greater than the radius of null-circular geodesics, that is, $r_\sigma > r_o$ then $Q_o > Q_\sigma$ which implies that null-circular geodesics is characterized by the largest angular frequency than the angular frequency of time-circular geodesics as measured by asymptotic observer. Therefore, such type of space-time are characterized by

$$\Omega_{null} > \Omega_{timelike}. \quad (8.114)$$

This type of characteristic of null-circular geodesic has been graphed in the Fig. 8.4 for different values of radius r .

Thus from the above equation we may conclude that the null-circular geodesic provide the fastest way to circle of black hole ([Hod \[2011\]](#), [Cornish and Levin \[2003\]](#)). This is satisfied for the case of Spherically symmetry Schwarzschild black hole, Kerr black hole and is still much general and can be applied for the case of Stationary, Kerr-Newman, axisymmetry space-time.

8. Lyapunov exponent, ISCO and Kolmogorov-Senai entropy for Kerr-Kiselev black hole

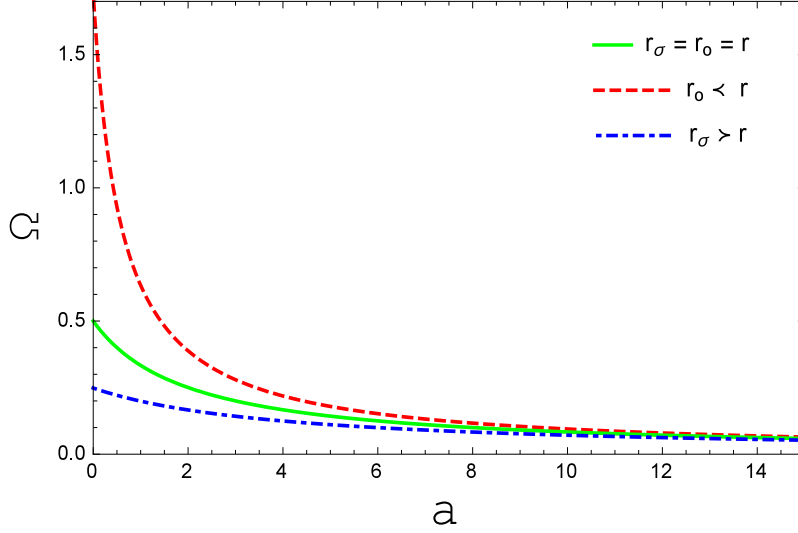


Figure 8.4: The plot shows the orbital angular frequency Ω Versus a for different values of radius r in the range $r_o \leq r \leq r_\sigma$, where r_σ and r_o are the radius of time-like geodesic and null-circular geodesic, respectively. Green (solid) color indicates for the value where the radius of time-like and null-circular geodesics are coincide, Red(Dashed) color indicates for the value of radius of null-circular geodesic and blue (Dot-Dashed) color indicates the value of radius of time-like geodesic. We use units such that $M = 1, c = 2$.

8.7 Ratio of Time period between null-circular geodesics and time-circular geodesics :

From the equation (8.90), the time period for time-like geodesics is given by

$$T_\sigma = \mp 2\pi \frac{\left(r_\sigma^{\frac{3(w+1)}{2}} \mp a \sqrt{Mr_\sigma^{3w} + \frac{c(3w+1)}{2}} \right)}{\sqrt{Mu_\sigma^{3w} + \frac{c(3w+1)}{2}}}. \quad (8.115)$$

Substituting $r_\sigma = r_o$ in the above equation, we can deduce the time period for null-circular geodesics as

$$T_o = \mp 2\pi \frac{\left(r_o^{\frac{3(w+1)}{2}} \mp a \sqrt{Mr_o^{3w} + \frac{c(3w+1)}{2}} \right)}{\sqrt{Mu_o^{3w} + \frac{c(3w+1)}{2}}}. \quad (8.116)$$

Now the ratio of Time period between null-circular geodesics and time-circular geodesics

8.7. Ratio of Time period between null-circular geodesics and time-circular geodesics :

is given by

$$\frac{T_o}{T_\sigma} = \left(\frac{\sqrt{Mr_\sigma^{3w} + \frac{c(3w+1)}{2}}}{\sqrt{Mr_o^{3w} + \frac{c(3w+1)}{2}}} \right) \left(\frac{r_o^{\frac{3(w+1)}{2}} \mp a\sqrt{Mr_o^{3w} + \frac{c(3w+1)}{2}}}{r_\sigma^{\frac{3(w+1)}{2}} \mp a\sqrt{Mr_\sigma^{3w} + \frac{c(3w+1)}{2}}} \right). \quad (8.117)$$

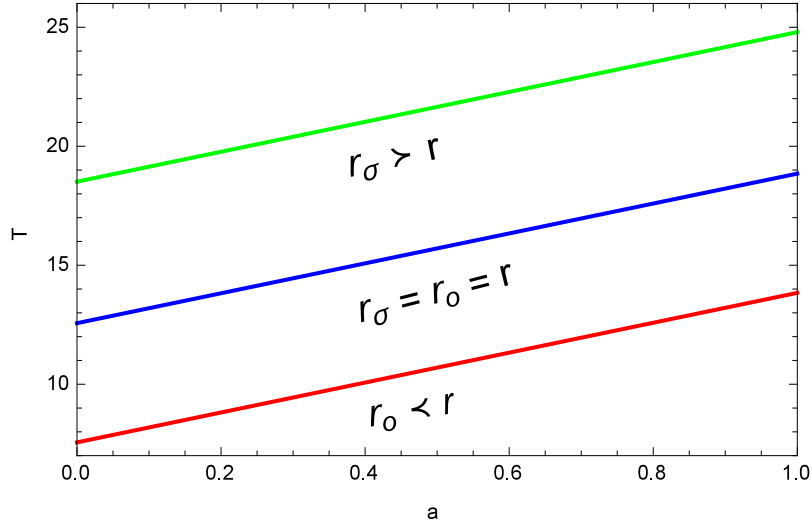


Figure 8.5: The plot shows the orbital time period T versus a for different values of radius r in the range $r_o \leq r \leq r_\sigma$, where r_σ and r_o are the radius of time-like geodesic and null-circular geodesic, respectively. Blue color indicates for the value where the radius of time-like and null-circular geodesics are coincide, green color indicates for the value of radius of time-like geodesic and red color indicates the value of radius of null-circular geodesic. We use units such that $M = 1, c = 2$.

- i. . When $r_\sigma = r_o$, the Eqn. (8.115) and the Eqn. (8.116) became identical, that is, the time period for time-like geodesics is similar to the time period of null-circular geodesics which leading to excitations of quasinormal modes.
- ii. When the radius of null- circular geodesics is smaller than the radius of time-like geodesics, orbital time period of null-circular geodesics is smaller than the orbital time period of time-circular geodesics, that is, for $r_o < r_\sigma$, $T_o < T_\sigma$. Let $r_o = r_{\text{photon}}$, $r_\sigma = r_{\text{ISCO}}$, the ratio between the orbital time period for photon

8. Lyapunov exponent, ISCO and Kolmogorov-Senai entropy for Kerr-Kiselev black hole

sphere and the orbital time period for ISCO be

$$\frac{T_{\text{photon}}}{T_{\text{ISCO}}} = \left(\frac{\sqrt{Mr_{\sigma}^{3w} + \frac{c(3w+1)}{2}}}{\sqrt{Mr_o^{3w} + \frac{c(3w+1)}{2}}} \right) \left(\frac{r_o^{\frac{3(w+1)}{2}} \mp a\sqrt{Mr_o^{3w} + \frac{c(3w+1)}{2}}}{r_{\sigma}^{\frac{3(w+1)}{2}} \mp a\sqrt{Mr_{\sigma}^{3w} + \frac{c(3w+1)}{2}}} \right). \quad (8.118)$$

which leads to

$$T_{\text{photon}} < T_{\text{ISCO}}, \quad (8.119)$$

this implies that the time-like circular geodesics provides the slowest possible orbital time period. This type of characteristic of time-like circular geodesic can be easily seen from Fig. 8.5. Therefore we conclude that among all the circular geodesics, the null-circular geodesics is characterized by the fastest way to circle of black hole.

8.8 Conclusions

In this chapter, we have clarified some aspects about principle Lyapunov exponent, KS entropy and unstable null-circular geodesics. We have shown that principle Lyapunov exponent and KS entropy can be expressed in terms of the equation of ISCO (innermost stable circular orbit). Also we have shown that Lyapunov exponent can be utilized to determine the instability of equatorial circular geodesics for both time-like and null-circular geodesics. We find the relation for null-circular geodesics that the angular frequency(Q_o) is equal to inverse of impact parameter (D_o), which is general characteristic of any stationary space-time. Also we computed the equation of ISCO in which the smallest real root give the radius of ISCO for rotating black hole and for each of the special cases black holes like Kerr-Newman, Kerr black hole, Reissner Nordström black hole and Schwarzschild black hole. We obtained that $r_{\sigma} = 6M$ is the radius of ISCO for Schwarzschild black hole.

We have computed the equations of Lyapunov exponent and reciprocal of critical exponent for both the cases of time-like and null-circular geodesics for rotating black hole and for special cases. We constructed the equation of marginally bound circular

8.8. Conclusions

orbit (MBCO) and obtained that $r_\sigma = 4M$ is the radius of MBCO for Schwarzschild black hole. We found out the ratio of angular frequency of null-circular geodesics to time-circular geodesics. In this ratio we have clarified that null circular geodesics have largest angular frequency than the time circular geodesics, that is, $Q_o > Q_\sigma$. This characteristic of null-circular geodesic can be checked by the Fig. 8.4, which is graphed by taking $M = 1$ and $c = 2$. But in the ratio of time period of null-circular geodesics to time-circular geodesics we can see that time-like circular geodesics had taken more time than null-circular geodesics, that is, $T_{timelike} > T_{photon}$. This scenario has been plotted in the Fig. 8.5, which is graphed by taking different values of radius r . In fact, we may conclude that any stable time-circular geodesics other than the ISCO traverses slowly than the null-circular geodesics.

Chapter 9

Coccluding Remarks and Future Prospectus

In the last chapter, we will conduct a comprehensive review of the research contributions made by this thesis. Additionally, we will explore potential avenues for future research in this field.

9.1 Conclusion

This thesis examines a few particular uses of modified gravity in astrophysical phenomena as well as some specific applications of general relativity. Here, we have presented a number of relativistic models of compact stars and black holes within the context of modified gravity and Einstein's gravity. To demonstrate a physically viable relativistic model, we have employed various analytical methods and graphical representations.

The following provides the respective detailed summaries of our studies:

- In the [second chapter](#), a detailed analysis of geodesic structure both null geodesics and time-like geodesics have been investigated for regular black holes. As an application of null geodesics, we calculate the radius of photon sphere, gravitational bending of light, the angle of deflection for the photons and the shadow of BH. We find the relation between null geodesics and quasinormal modes frequency in the eikonal approximation by computing the Lyapunov exponent. As an application of time-like geodesics we compute the innermost stable circular orbit (ISCO) and marginally bound circular orbit (MBCO) of

9. Cocluding Remarks and Future Prospectus

the regular BHs.

- In the [third chapter](#), we derive proper-time Lyapunov exponent (λ_p) and coordinate-time Lyapunov exponent (λ_c) for a regular Hayward class of black hole. The proper-time corresponds to τ and the coordinate time corresponds to t . Where t is measured by the asymptotic observers both for Hayward black hole and for special case of Schwarzschild black hole. We compute their ratio as $\frac{\lambda_p}{\lambda_c} = \frac{(r_\sigma^3 + 2l^2 m)}{\sqrt{(r_\sigma^2 + 2l^2 m)^3 - 3mr_\sigma^5}}$ for time-like geodesics. In the limit of $l = 0$ that means for Schwarzschild black hole this ratio reduces to $\frac{\lambda_p}{\lambda_c} = \sqrt{\frac{r_\sigma}{(r_\sigma - 3m)}}$. Using Lyapunov exponent, we investigate the stability and instability of equatorial circular geodesics. By evaluating the Lyapunov exponent, which is the inverse of the instability time-scale, we show that, in the eikonal limit, the real and imaginary parts of quasi-normal modes (QNMs) is specified by the frequency and instability time scale of the null circular geodesics. Furthermore, we discuss the unstable photon sphere and radius of shadow for this class of black hole.

- In the [fourth chapter](#), we analyze the behavior of relativistic spherical objects within the context of modified $f(R, T)$ gravity considering Tolman VI space-time, where gravitational lagrangian is a function of Ricci scalar(R) and trace of energy momentum tensor(T) *i.e.*, $f(R, T) = R + 2\beta T$, for some arbitrary constant β . For developing our model, we have chosen $\mathcal{L}_m = -p$, where \mathcal{L}_m represents matter lagrangian. For this investigation, we have chosen three compact stars namely PSR J1614-2230 [Mass= $(1.97 \pm 0.4)M_\odot$; Radius= $9.69_{-0.02}^{+0.02}$ km], Vela X-1 [Mass= $(1.77 \pm 0.08)M_\odot$; Radius= $9.560_{-0.08}^{+0.08}$ km] and 4U 1538-52 [Mass= $(9.69)M_\odot$; Radius= 1.97 km]. In this theory the equation of pressure isotropy is identical to standard Einstein's theory. So, all known metric potential solving Einsteins equations are also valid. We have investigated the effort of coupling parameter (β) on the local matter distribution. Sound of speed and adiabatic index are higher with grater values of β while on contrary mass function and gravitational redshift are lower with higher values of β . For supporting the theoretical results, graphical representation are also employed to analyze the physical viability of the compact stars.

9.1. Conclusion

- In the [fifth chapter](#), we have investigated the classical tests of General Relativity like precession of perihelion, deflection of light and time delay by considering a phenomenological astrophysical object like Sun, as a neutral regular Hayward black hole in Rastall gravity. We have tabulated all our results for some appropriate values of the parameter σ . We have compared our values with $\sigma = 0$, which correspond to the Schwarzschild case. Also the value of $\sigma = 0.7187 \times 10^{-4}$, is of particular interest as it gives some promising results.
- In the [sixth chapter](#), we have searched the existence of anisotropic and non-singular compact star in the $f(R, T)$ gravity by taking into account the non-exotic equation of state (EoS). In order to obtain the solutions of the matter content of compact object, we assume the well known barotropic form of EoS that yields the linear relation between pressures and energy density. We propose the existence of non-exotic compact star which shows the validation of energy conditions and stability with in the $f(R, T)$ extended theory of gravity perspective. The linear material correction in the extended theory the matter content of compact star remarkably able to satisfies energy condition. We discuss various physical features of compact star and show that proposed model of stellar object satisfies all regularity conditions and is stable as well as singularity-free.
- In the [seventh chapter](#), we develop a new model for a spherically symmetric dark matter fluid sphere containing two regions: **(i)** Isotropic inner region with constant density and **(ii)** Anisotropic outer region. We solve the system of field equation by assuming a particular density profile along with a linear equation of state. The obtained solutions are well-behaved and physically acceptable which represent equilibrium and stable matter configuration by satisfying the TOV equation and causality condition, condition on adiabatic index, Harrison-Zeldovich-Novikov criterion, respectively. We consider the compact star EXO 1785-248 (Mass $M = 1.3 M_{\odot}$ and radius $R = 8.8 \text{ km}$.) to analyze our solutions by graphical demonstrations.
- In the [eighth chapter](#), we calculate the principle Lyapunov exponent (LE), which is the inverse of the instability timescale associated with this geodesics and Kolmogorov-Senai (KS) entropy for our rotating Kerr-Kiselev (KK) black hole. We have investigate the existence of stable/unstable equatorial circular

orbits via LE and KS entropy for time-like and null circular geodesics. We have shown that both LE and KS entropy can be written in terms of the radial equation of innermost stable circular orbit (ISCO) for time-like circular orbit. Also, we computed the equation marginally bound circular orbit, which gives the radius (smallest real root) of marginally bound circular orbit (MBCO). We found that the null circular geodesics has larger angular frequency than time-like circular geodesics ($Q_o > Q_\sigma$). Thus, null-circular geodesics provides the fastest way to circulate KK black holes. Further, it is also to be noted that null circular geodesics has shortest orbital period ($T_{\text{photon}} < T_{\text{ISCO}}$) among the all possible circular geodesics. Even null circular geodesics traverses fastest than any stable time-like circular geodesics other than the ISCO.

9.2 Future research

The scope of our future study will encompass, but is not limited to, the following topics:

- In the [second chapter](#), we analyze the null geodesics and quasinormal mode frequency in the eikonal approximation by computing the Lyapunov exponent for regular black holes. In the future, using the geodesic properties, researcher can study pseudo-Newtonian potential so called Paczyński-Witta Potential for Ayón-Beato-García BH which are very important tools for analyzing the accretion-disk properties.
- In the [third chapter](#), we study the Hayward black hole as a most popular model of regular BHs has been chosen for investigating the geodesic stability and quasi normal modes via Lyapunov exponent. In the future work, using our result, one can extend our analysis to the thermodynamic properties of non-commutative rotating Hayward solution, providing Hawking temperature.
- In the [fourth chapter](#), we have discussed the Tolman VI fluid spheres model within the context of modified $f(R, T)$ gravity. In the future, using our result we will study a perceptible magnetic pressure influence to the equilibrium of

9.2. Future research

forces for the core of the highly compact stars as the magnetic effects calculation can give some idea of the dynamical distortion in nuclear impacts.

- In the [fifth chapter](#), we have derived three classical tests namely, the precession of perihelion, deflection of light and time delay with respect to a neutral regular black hole under the effect of the modified Rastall gravity. In future, these results can be used to study the viable cosmological dynamics of charged Einstein Æther Gravity.
- In the [sixth chapter](#), we have searched the existence of anisotropic and non-singular compact star in the $f(R, T)$ gravity by taking barotropic form of EoS. In future, one can check the viability of such solution under the specification of other valuable functional forms of $f(R, T)$ such as $f(R, T) = R + \zeta RT$ and $f(R, T) = R + \zeta R^2 + \lambda T$ where ζ and λ are arbitrary constants.
- In the [seventh chapter](#), we have introduced a new model for a spherically symmetric dark matter (DM) fluid sphere. This concept, in which stars' matter compositions are physical dark matter, is highly intriguing. Our findings will encourage future theoretical researchers to conduct fruitful, in-depth research on this subject.
- In the [eighth chapter](#), we have investigate the existence of stable/unstable equatorial circular orbits via Lyapunov exponent and Kolmogorov-Senai entropy for Kerr-Kiselev black hole for both time-like and null circular geodesics. For these rotating BHs, we focused on their ISCO and MBCO. In the future, these orbits might encourage scientists to look for observational data, deriving information about background geometry and pertinent to several astrophysical processes. In order to explore the phenomenological consequences on the generation of BHs, one can extend our investigation into extra dimensions.

References

- Abbas, G. and Sabiullah, U. (2014). Geodesic study of regular hayward black hole. *Astrophysics and Space Science*, 352, 769–774. [5](#)
- Abbott, B.P., Abbott, R., Abbott, T., Abernathy, M., Acernese, F., Ackley, K., Adams, C., Adams, T., Addesso, P., Adhikari, R., et al. (2016a). Observation of gravitational waves from a binary black hole merger. *Physical review letters*, 116(6), 061102. [1](#), [8](#)
- Abbott, B., Jawahar, S., Lockerbie, N., and Tokmakov, K. (2016b). Ligo scientific collaboration and virgo collaboration (2016) directly comparing gw150914 with numerical solutions of einstein’s equations for binary black hole coalescence. *physical review d*, 94 (6). issn 1550-2368, [http://dx. doi. org/10.1103/physrevd. 94.064035](http://dx.doi.org/10.1103/physrevd.94.064035). *PHYSICAL REVIEW D Phys Rev D*, 94, 064035. [8](#)
- Abreu, H., Hernández, H., and Núñez, L.A. (2007). Sound speeds, cracking and the stability of self-gravitating anisotropic compact objects. *Classical and Quantum Gravity*, 24(18), 4631. [7](#)
- Adhav, K. (2012). Lrs bianchi type-i cosmological model in f (r, t) theory of gravity. *Astrophysics and space science*, 339, 365–369. [1](#), [1](#)
- Agüeros, M.A., Anderson, S.F., Margon, B., Posselt, B., Haberl, F., Voges, W., Annis, J., Schneider, D.P., and Brinkmann, J. (2006). Candidate isolated neutron stars and other optically blank x-ray fields identified from the rosat all-sky and sloan digital sky surveys. *The Astronomical Journal*, 131(3), 1740. [6](#)
- Ahmed, N. and Pradhan, A. (2014). Bianchi type-v cosmology in f (r, t) gravity with λ (t). *International Journal of Theoretical Physics*, 53(1), 289–306. [1](#), [1](#)

- Akerib, D., Alsum, S., Araújo, H., Bai, X., Bailey, A., Balajthy, J., Beltrame, P., Bernard, E., Bernstein, A., Biesiadzinski, T., et al. (2017). Results from a search for dark matter in the complete lux exposure. *Physical review letters*, 118(2), 021303. [6](#)
- Al-Rawaf, A. and Taha, M. (1996a). Cosmology of general relativity without energy-momentum conservation. *General Relativity and Gravitation*, 28, 935–952. [5](#)
- Al-Rawaf, A. and Taha, M. (1996b). A resolution of the cosmological age puzzle. *Physics Letters B*, 366(1-4), 69–71.
- Alexander, S. and Yunes, N. (2009). Chern–simons modified general relativity. *Physics Reports*, 480(1-2), 1–55. [1](#)
- Alves, M., Moraes, P., De Araujo, J., and Malheiro, M. (2016). Gravitational waves in $f(r, t)$ and $f(r, t, \phi)$ theories of gravity. *Physical Review D*, 94(2), 024032. [4](#)
- Amir, M. and Ghosh, S.G. (2015). Rotating haywards regular black hole as particle accelerator. *Journal of High Energy Physics*, 2015(7), 1–17. [3](#)
- Antoniadis, J., Freire, P.C., Wex, N., Tauris, T.M., Lynch, R.S., Van Kerkwijk, M.H., Kramer, M., Bassa, C., Dhillon, V.S., Driebe, T., et al. (2013). A massive pulsar in a compact relativistic binary. *Science*, 340(6131), 1233232. [6](#)
- Aziz, A., Ray, S., and Rahaman, F. (2016). A generalized model for compact stars. *The European Physical Journal C*, 76, 1–9. [6](#)
- Azreg-Aïnou, M. (2015). Confined-exotic-matter wormholes with no gluing effect-simaging supermassive wormholes and black holes. *Journal of Cosmology and Astroparticle Physics*, 2015(07), 037. [6](#)
- Baffou, E., Kpadonou, A., Rodrigues, M., Houndjo, M., and Tossa, J. (2015). Cosmological viable $f(r, t)$ dark energy model: dynamics and stability. *Astrophysics and Space Science*, 356, 173–180. [4](#)
- Baker, J.G., Boggs, W.D., Centrella, J., Kelly, B.J., McWilliams, S.T., and van Meter, J.R. (2008). Mergers of nonspinning black-hole binaries: Gravitational radiation characteristics. *Physical Review D*, 78(4), 044046. [3](#)

References

- Bambi, C. and Modesto, L. (2013). Rotating regular black holes. *Physics Letters B*, 721(4-5), 329–334. [1](#)
- Bardeen, J. (1968a). Non-singular general relativistic gravitational collapse. In *Proceedings of the 5th International Conference on Gravitation and the Theory of Relativity*, 87. [1](#), [1](#)
- Bardeen, J. (1968b). Proceedings of the international conference gr5, ussr, tbilisi, georgia. [2](#)
- Barrow, J.D. (1981). Chaos in the einstein equations. *Physical Review Letters*, 46(15), 963. [2](#)
- Batista, C.E., Daouda, M.H., Fabris, J.C., Piattella, O.F., and Rodrigues, D.C. (2012). Rastall cosmology and the λ cdm model. *Physical review D*, 85(8), 084008.
- Batista, C., Fabris, J.C., Piattella, O.F., and Velasquez-Toribio, A. (2013). Observational constraints on rastalls cosmology. *The European Physical Journal C*, 73, 1–7. [5](#)
- Bean, R., Bernat, D., Pogolian, L., Silvestri, A., and Trodden, M. (2007). Dynamics of linear perturbations in $f(r)$ gravity. *Physical Review D*, 75(6), 064020. [4](#)
- Belinskii, V.A., Khalatnikov, I.M., and Lifshitz, E.M. (1970). Oscillatory approach to a singular point in the relativistic cosmology. *Advances in Physics*, 19(80), 525–573.
- Bell, E.F. and de Jong, R.S. (2001). Stellar mass-to-light ratios and the tully-fisher relation. *The Astrophysical Journal*, 550(1), 212. [7](#)
- Bergliaffa, S.P. (2006). Constraining $f(r)$ theories with the energy conditions. *Physics Letters B*, 642(4), 311–314. [4](#)
- Berti, E., Cardoso, V., Gonzalez, J.A., Sperhake, U., Hannam, M., Husa, S., and Brügmann, B. (2007). Inspiral, merger, and ringdown of unequal mass black hole binaries: A multipolar analysis. *Physical Review D*, 76(6), 064034. [3](#)
- Berti, E., Cardoso, V., and Starinets, A.O. (2009). Quasinormal modes of black holes and black branes. *Classical and Quantum Gravity*, 26(16), 163001. [2](#)

- Berti, E. and Kokkotas, K.D. (2005). Quasinormal modes of kerr-newman black holes: Coupling of electromagnetic and gravitational perturbations. *Physical Review D*, 71(12), 124008. 2
- Bhar, P., Rahaman, F., Manna, T., and Banerjee, A. (2016). Wormhole supported by dark energy admitting conformal motion. *The European Physical Journal C*, 76, 1–9. 5, 5
- Bhar, P., Rej, P., and Zubair, M. (2022). Tolman iv fluid sphere in f (r, t) gravity. *Chinese Journal of Physics*, 77, 2201–2212. 4
- Bharadwaj, S. and Kar, S. (2003). Modeling galaxy halos using dark matter with pressure. *Physical Review D*, 68(2), 023516. 7
- Böhmer, C.G., De Risi, G., Harko, T., and Lobo, F.S. (2010). Classical tests of general relativity in brane world models. *Classical and Quantum Gravity*, 27(18), 185013. 5, 5, 5
- Bombelli, L. and Calzetta, E. (1992). Chaos around a black hole. *Classical and Quantum Gravity*, 9(12), 2573. 3, 8
- Bondi, H. (1964). The contraction of gravitating spheres. *Proceedings of the Royal Society of London. Series A. Mathematical and Physical Sciences*, 281(1384), 39–48. 4, 6, 7
- Bowers, R. and Liang, E. (1974). 188. 657b. vol. 188. *Astrophys. J*, 657. 6
- Bronnikov, K., Fabris, J., Piattella, O., and Santos, E. (2016). Static, spherically symmetric solutions with a scalar field in rastall gravity. *General Relativity and Gravitation*, 48, 1–15. 5
- Bronnikov, K.A., Fabris, J.C., Piattella, O.F., Rodrigues, D.C., and Santos, E.C. (2017). Duality between k-essence and rastall gravity. *The European Physical Journal C*, 77, 1–9. 5
- Buchdahl, H.A. (1959). General relativistic fluid spheres. *Physical Review*, 116(4), 1027. 6, 7
- Buchdahl, H.A. (1970). Non-linear lagrangians and cosmological theory. *Monthly Notices of the Royal Astronomical Society*, 150(1), 1–8. 1, 1

References

- Burd, A. and Tavakol, R. (1993). Invariant lyapunov exponents and chaos in cosmology. *Physical Review D*, 47(12), 5336. [8](#)
- Cai, Y.F., Easson, D.A., Gao, C., and Saridakis, E.N. (2013). Charged black holes in nonlinear massive gravity. *Physical Review D*, 87(6), 064001. [1](#)
- Capozziello, S., Cardone, V., and Troisi, A. (2006). Dark energy and dark matter as curvature effects? *Journal of Cosmology and Astroparticle Physics*, 2006(08), 001. [1](#)
- Caramês, T.R., Daouda, M.H., Fabris, J.C., Oliveira, A.M., Piattella, O.F., and Stokov, V. (2014). The brans–dicke–rastall theory. *The European Physical Journal C*, 74(11), 3145. [5](#)
- Cardoso, V. and Lemos, J.P. (2003). Quasinormal modes of the near extremal schwarzschild–de sitter black hole. *Physical Review D*, 67(8), 084020. [3](#), [8](#)
- Cardoso, V., Miranda, A.S., Berti, E., Witek, H., and Zanchin, V.T. (2009). Geodesic stability, lyapunov exponents, and quasinormal modes. *Physical Review D*, 79(6), 064016. [2](#), [3](#), [3](#), [3](#), [8](#)
- Carroll, S.M., Duvvuri, V., Trodden, M., and Turner, M.S. (2004). Is cosmic speed-up due to new gravitational physics? *Physical Review D*, 70(4), 043528. [1](#)
- Casadio, R., Ovalle, J., and Da Rocha, R. (2015). Classical tests of general relativity: brane-world sun from minimal geometric deformation. *Europhysics Letters*, 110(4), 40003. [5](#), [5](#)
- Chan, R. (2003). Mfa da silva and jfv da rocha. *J. Math. Phys. D*, 12, 347. [7](#)
- Chan, R., Herrera, L., and Santos, N. (1993). Dynamical instability for radiating anisotropic collapse. *Monthly Notices of the Royal Astronomical Society*, 265(3), 533–544. [7](#)
- Chandrasekhar, S. (1965). The post-newtonian equations of hydrodynamics in general relativity. *Astrophysical Journal*, 142, 1488–1512. [6](#)
- Chandrasekhar, S. (1998). *The mathematical theory of black holes*, volume 69. Oxford university press. [1](#), [2](#), [2](#), [3](#), [3](#), [8](#), [8](#), [8](#)

- Chiba, T. and Kimura, M. (2017). A note on geodesics in the hayward metric. *Progress of Theoretical and Experimental Physics*, 2017(4), 043E01. 2, 3
- Chierchia, L. (2009). Kolmogorov-arnold-moser (kam) theory. 8
- Contopoulos, G., Voglis, N., and Efthymiopoulos, C. (1999). Chaos in relativity and cosmology. *Celestial Mechanics and Dynamical Astronomy*, 73(1-4), 1–16. 8
- Cornish, N.J. (2001). Chaos and gravitational waves. *Physical Review D*, 64(8), 084011. 3
- Cornish, N.J. and Levin, J. (2003). Lyapunov timescales and black hole binaries. *Classical and Quantum Gravity*, 20(9), 1649. 2, 3, 3, 8, 8
- Cornish, N.J. and Levin, J.J. (1997). The mixmaster universe is chaotic. *Physical Review Letters*, 78(6), 998. 2
- Cuzinatto, R., Pompeia, P., De Montigny, M., Khanna, F., and Silva, J.H.d. (2014). Classic tests of general relativity described by brane-based spherically symmetric solutions. *The European Physical Journal C*, 74(8), 3017. 5, 5
- Dahia, F. and de Albuquerque Silva, A. (2015). Classical tests of general relativity in thick branes. *The European Physical Journal C*, 75, 1–10. 5, 5
- Darabi, F., Moradpour, H., Licata, I., Heydarzade, Y., and Corda, C. (2018). Einstein and rastall theories of gravitation in comparison. *The European Physical Journal C*, 78, 1–4. 5
- Das, A., Ghosh, S., Guha, B., Das, S., Rahaman, F., and Ray, S. (2017). Gravastars in $f(r, t)$ gravity. *Physical Review D*, 95(12), 124011. 6
- Das, A., Rahaman, F., Guha, B., and Ray, S. (2016). Compact stars in $f(r, t)$ $f(r, t)$ gravity. *The European Physical Journal C*, 76, 1–10. 6, 6
- Das, A., Saha, A., and Gangopadhyay, S. (2020a). Shadow of charged black holes in gauss–bonnet gravity. *The European Physical Journal C*, 80(3), 180. 2
- Das, S., Sarkar, N., Mondal, M., and Rahaman, F. (2020b). A new model for dark matter fluid sphere. *Modern Physics Letters A*, 35(34), 2050280. 2, 4, 8

References

- Davoudiasl, H. and Denton, P.B. (2019). Ultralight boson dark matter and event horizon telescope observations of m 87. *Physical review letters*, 123(2), 021102.
- De Felice, A., Doll, A., Larrouturou, F., and Mukohyama, S. (2021). Black holes in a type-ii minimally modified gravity. *Journal of Cosmology and Astroparticle Physics*, 2021(03), 004. [1](#)
- De la Cruz-Dombriz, A. and Dobado, A. (2006). f (r) gravity without a cosmological constant. *Physical Review D*, 74(8), 087501. [4](#)
- de Mello, E.R.B., Fabris, J.C., and Hartmann, B. (2015). Abelian–higgs strings in rastall gravity. *Classical and Quantum Gravity*, 32(8), 085009. [5](#)
- Deb, D., Guha, B., Rahaman, F., and Ray, S. (2018). Anisotropic strange stars under simplest minimal matter-geometry coupling in the f (r, t) gravity. *Physical Review D*, 97(8), 084026. [4](#)
- Demorest, P.B., Pennucci, T., Ransom, S., Roberts, M., and Hessels, J. (2010). A two-solar-mass neutron star measured using shapiro delay. *nature*, 467(7319), 1081–1083. [6](#)
- Dettmann, C., Frankel, N., and Cornish, N. (1994). Fractal basins and chaotic trajectories in multi-black-hole spacetimes. *Physical Review D*, 50(2), R618. [2](#), [8](#)
- Dodelson, S. (2003). *Modern Cosmology*. Elsevier. [1](#)
- Dorfman, J.R. (1999). *An introduction to chaos in nonequilibrium statistical mechanics*. 14. Cambridge University Press. [3](#)
- Dreyer, O. (2003). Quasinormal modes, the area spectrum, and black hole entropy. *Physical Review Letters*, 90(8), 081301. [2](#)
- Eddington, A.S. (1923). *The mathematical theory of relativity*. The University Press. [1](#)
- Edery, A. and Paranjape, M.B. (1998). Classical tests for weyl gravity: deflection of light and time delay. *Physical Review D*, 58(2), 024011. [5](#), [5](#)
- Efstathiou, G., Sutherland, W.J., and Maddox, S. (1990). The cosmological constant and cold dark matter. *Nature*, 348(6303), 705–707. [7](#)

- Einasto, J., Kaasik, A., and Saar, E. (1974). Dynamic evidence on massive coronas of galaxies. *Nature*, 250(5464), 309–310. [7](#)
- Eingorn, M. and Zhuk, A. (2010). Classical tests of multidimensional gravity: negative result. *Classical and Quantum Gravity*, 27(20), 205014. [5](#)
- Einstein, A. (1911). ÜOn the influenceß of gravity on the propagation of light. *Annals of Physics*, 340(10), 898–908. [5](#)
- Eisberg, J. (1990). Eddington’s stellar models. *Publications of the Astronomical Society of the Pacific*, Vol. 102, No. 657, p. 1336, 102, 1336. [1](#)
- Fabian, A., Thomas, P., Fall, S., and White III, R. (1986). A lower limit to the binding mass of early-type galaxies. *Monthly Notices of the Royal Astronomical Society*, 221(4), 1049–1056. [7](#)
- Fabris, J., Daouda, M.H., and Piattella, O. (2012a). Note on the evolution of the gravitational potential in rastall scalar field theories. *Physics Letters B*, 711(3-4), 232–237. [5](#)
- Fabris, J.C., Piattella, O.F., Rodrigues, D.C., Batista, C.E., and Daouda, M.H. (2012b). Rastall cosmology. In *International Journal of Modern Physics: Conference Series*, volume 18, 67–76. World Scientific. [5](#)
- Fan, Z.Y. and Wang, X. (2016). Construction of regular black holes in general relativity. *Physical Review D*, 94(12), 124027. [2](#), [2](#)
- Fay, S. (2004). Scalar fields properties for flat galactic rotation curves. *Astronomy & Astrophysics*, 413(3), 799–805. [7](#)
- Fernando, S. and Clark, T. (2014). Black holes in massive gravity: quasi-normal modes of scalar perturbations. *General Relativity and Gravitation*, 46, 1–22. [2](#)
- Fierz, M. and Pauli, W.E. (1939). On relativistic wave equations for particles of arbitrary spin in an electromagnetic field. *Proceedings of the Royal Society of London. Series A. Mathematical and Physical Sciences*, 173(953), 211–232. [1](#)
- Fiorini, F. and Ferraro, R. (2009). A type of born-infeld regular gravity and its cosmological consequences. *International Journal of Modern Physics A*, 24(08n09), 1686–1689. [1](#)

References

- Fort, B. and Mellier, Y. (1994). Arc (let) s in clusters of galaxies. *The Astronomy and Astrophysics Review*, 5, 239–292. 7
- Freire, W.H., Bezerra, V., and Lima, J. (2001). Cosmological constant, conical defect and classical tests of general relativity. *General Relativity and Gravitation*, 33, 1407–1414. 5
- Frolov, V.P. (2016). Notes on nonsingular models of black holes. *Physical Review D*, 94(10), 104056. 3
- Frye, C. and Efthimiou, C.J. (2013). Stringy corrections to the classical tests of general relativity. *arXiv preprint arXiv:1306.4869*. 5
- Gangopadhyay, T., Ray, S., Li, X.D., Dey, J., and Dey, M. (2013). Strange star equation of state fits the refined mass measurement of 12 pulsars and predicts their radii. *Monthly Notices of the Royal Astronomical Society*, 431(4), 3216–3221. 6
- Ganguly, A., Gannouji, R., Goswami, R., and Ray, S. (2014). Neutron stars in the starobinsky model. *Physical Review D*, 89(6), 064019. 4
- Ghosh, S.G. and Maharaj, S.D. (2015). Radiating kerr-like regular black hole. *The European Physical Journal C*, 75, 1–9. 1
- Ghosh, S.G., Sheoran, P., and Amir, M. (2014). Rotating ayón-beato-garcía black hole as a particle accelerator. *Physical Review D*, 90(10), 103006. 2
- Gibbons, G.W. and Maeda, K.i. (1988). Black holes and membranes in higher-dimensional theories with dilaton fields. *Nuclear Physics B*, 298(4), 741–775. 1
- Goswami, R., Nzioki, A.M., Maharaj, S.D., and Ghosh, S.G. (2014). Collapsing spherical stars in f (r) gravity. *Physical Review D*, 90(8), 084011. 4
- Graca, J.M. and Lobo, I.P. (2018). Scalar qnms for higher dimensional black holes surrounded by quintessence in rastall gravity. *The European Physical Journal C*, 78, 1–7. 5
- Greenstein, J.L., Oke, J.B., and Shipman, H. (1971). Effective temperature, radius, and gravitational redshift of sirius b. *The astrophysical journal*, 169, 563. 1
- Gupta, Y. and Maurya, S.K. (2011). A class of regular and well behaved relativistic super-dense star models. *Astrophysics and Space Science*, 332, 155–162. 4

- Güver, T., Wroblewski, P., Camarota, L., and Özel, F. (2010a). The mass and radius of the neutron star in 4u 1820- 30. *The Astrophysical Journal*, 719(2), 1807. 6, 6
- Güver, T., Wroblewski, P., Camarota, L., and Özel, F. (2010b). The mass and radius of the neutron star in 4u 1820- 30. *The Astrophysical Journal*, 719(2), 1807. 6
- Halilsoy, M., Ovgun, A., and Mazharimousavi, S.H. (2014). Thin-shell wormholes from the regular hayward black hole. *The European Physical Journal C*, 74(3), 1–7. 5
- Hansraj, S. and Banerjee, A. (2018). Dynamical behavior of the tolman metrics in $f(r, t)$ gravity. *Physical Review D*, 97(10), 104020. 4
- Harko, T. and Lobo, F.S. (2011). Two-fluid dark matter models. *Physical Review D*, 83(12), 124051. 7
- Harko, T., Lobo, F.S., Nojiri, S., and Odintsov, S.D. (2011). $f(r, t)$ gravity. *Physical Review D*, 84(2), 024020. 1, 1, 4, 6, 6, 6
- Harko, T., Lobo, F.S., Otalora, G., and Saridakis, E.N. (2014). Nonminimal torsion-matter coupling extension of $f(t)$ gravity. *Physical Review D*, 89(12), 124036. 1
- Harrison, B.K., Thorne, K.S., Wakano, M., and Wheeler, J.A. (1965). Gravitation theory and gravitational collapse. *Gravitation Theory and Gravitational Collapse*. 7
- Hawking, S.W. and Ellis, G.F. (2023). *The large scale structure of space-time*. Cambridge university press. 1, 7
- Hayward, S.A. (2006). Formation and evaporation of nonsingular black holes. *Physical review letters*, 96(3), 031103. 2, 3, 3, 5
- Hendi, S. and Nemati, A. (2019). Thermodynamics, shadow and quasinormal modes of black holes in five-dimensional yang-mills massive gravity. *arXiv preprint arXiv:1912.06824*. 2
- Hendi, S., Panah, B.E., Panahiyan, S., Liu, H., and Meng, X.H. (2018). Black holes in massive gravity as heat engines. *Physics Letters B*, 781, 40–47. 1
- Herrera, L. (1992). Cracking of self-gravitating compact objects. *Physics Letters A*, 165(3), 206–210. 6, 7

References

- Herrera, L., Di Prisco, A., Martin, J., Ospino, J., Santos, N., and Troconis, O. (2004). Spherically symmetric dissipative anisotropic fluids: a general study. *Physical Review D*, 69(8), 084026. [6](#)
- Herrera, L. and Santos, N.O. (1997). Local anisotropy in self-gravitating systems. *Physics Reports*, 286(2), 53–130. [7](#)
- Hewish, A., Bell, S.J., Pilkington, J.D., Frederick Scott, P., and Collins, R.A. (1979). Observation of a rapidly pulsating radio source. In *A Source Book in Astronomy and Astrophysics, 1900–1975*, 498–504. Harvard University Press. [6](#)
- Heydarzade, Y. and Darabi, F. (2017). Black hole solutions surrounded by perfect fluid in rastall theory. *Physics Letters B*, 771, 365–373. [5](#)
- Hinshaw, G., Spergel, D., Verde, L., Hill, R., Meyer, S., Barnes, C., Bennett, C., Halpern, M., Jarosik, N., Kogut, A., et al. (2003). First-year wilkinson microwave anisotropy probe (wmap)* observations: The angular power spectrum. *The Astrophysical Journal Supplement Series*, 148(1), 135. [4](#)
- Hobill, D., Burd, A., and Coley, A.A. (2013). *Deterministic chaos in general relativity*, volume 332. Springer Science & Business Media. [2](#)
- Hochberg, D. and Visser, M. (1998). Dynamic wormholes, antitrapped surfaces, and energy conditions. *Physical Review D*, 58(4), 044021. [6](#)
- Hod, S. (2011). Fastest way to circle a black hole. *Physical Review D*, 84(10), 104024. [3](#), [8](#)
- Houndjo, M. (2012). Reconstruction of $f(r, t)$ gravity describing matter dominated and accelerated phases. *International Journal of Modern Physics D*, 21(01), 1250003. [4](#)
- Islam, J. (1983). The cosmological constant and classical tests of general relativity. *Physics Letters A*, 97(6), 239–241. [5](#)
- Ivanov, B. (2002). Static charged perfect fluid spheres in general relativity. *Physical Review D*, 65(10), 104001. [7](#)
- Iyer, S. and Will, C.M. (1987). Black-hole normal modes: A wkb approach. i. foundations and application of a higher-order wkb analysis of potential-barrier scattering. *Physical Review D*, 35(12), 3621. [3](#), [3](#), [8](#)

- Jalalzadeh, S., Mehrnia, M., and Sepangi, H. (2009). Classical tests in brane gravity. *Classical and Quantum Gravity*, 26(15), 155007. 5, 5
- Jusufi, K. (2020). Quasinormal modes of black holes surrounded by dark matter and their connection with the shadow radius. *Physical Review D*, 101(8), 084055. 2
- Kalligas, D., Wesson, P.S., and Everitt, C. (1995). The classical tests in kaluza-klein gravity. *The Astrophysical Journal, Part 1 (ISSN 0004-637X)*, vol. 439, no. 2, p. 548–557, 439, 548–557. 5, 5
- Kanti, P., Mavromatos, N., Rizos, J., Tamvakis, K., and Winstanley, E. (1998). Dilatonic black holes in higher curvature string gravity. ii. linear stability. *Physical Review D*, 57(10), 6255. 1
- Kanti, P., Mavromatos, N.E., Rizos, J., Tamvakis, K., and Winstanley, E. (1996). Dilatonic black holes in higher curvature string gravity. *Physical Review D*, 54(8), 5049. 1
- Karas, V. and Vokrouhlický, D. (1992). Chaotic motion of test particles in the ernst space-time. *General relativity and gravitation*, 24, 729–743. 3
- Kerr, R.P. (1963). Gravitational field of a spinning mass as an example of algebraically special metrics. *Physical review letters*, 11(5), 237. 1
- Kiselev, V. (2003). Quintessence and black holes. *Classical and Quantum Gravity*, 20(6), 1187. 8
- Klein, M., Kox, A., and Schulmann, R. (1995). Einstein and bello: Manuscript on the motion of the perihelion of mercury. *The collected papers of Albert Einstein*, 4, 1912–1914. 5
- Knop, R.A., Aldering, G., Amanullah, R., Astier, P., Blanc, G., Burns, M., Conley, A., Deustua, S., Doi, M., Ellis, R., et al. (2003). New constraints on ω_m , ω_λ , and w from an independent set of 11 high-redshift supernovae observed with the hubble space telescope. *The Astrophysical Journal*, 598(1), 102. 1, 4
- Kokkotas, K.D. and Schmidt, B.G. (1999). Quasi-normal modes of stars and black holes. *Living Reviews in Relativity*, 2, 1–72. 2, 3

References

- Kološ, M., Stuchlík, Z., and Tursunov, A. (2015). Quasi-harmonic oscillatory motion of charged particles around a schwarzschild black hole immersed in a uniform magnetic field. *Classical and Quantum Gravity*, 32(16), 165009. [8](#)
- Kološ, M., Tursunov, A., and Stuchlík, Z. (2017). Possible signature of the magnetic fields related to quasi-periodic oscillations observed in microquasars. *The European Physical Journal C*, 77, 1–17. [8](#)
- Konno, K., Matsuyama, T., and Tanda, S. (2009). Rotating black hole in extended chern-simons modified gravity. *Progress of Theoretical Physics*, 122(2), 561–568. [1](#)
- Konoplya, R. and Stuchlík, Z. (2017). Are eikonal quasinormal modes linked to the unstable circular null geodesics? *Physics Letters B*, 771, 597–602.
- Konoplya, R. and Zhidenko, A. (2011). Quasinormal modes of black holes: From astrophysics to string theory. *Reviews of Modern Physics*, 83(3), 793. [2](#), [3](#), [8](#)
- Konoplya, R.A. and Zhidenko, A. (2005). Decay of massive scalar field in a schwarzschild background. *Physics Letters B*, 609(3-4), 377–384. [2](#)
- Krauss, L.M. (2001). Einsteins unfinished symphony: Listening to the sounds of space-time. *Physics Today*, 54(6), 59–59. [1](#)
- Krori, K. and Barua, J. (1975). A singularity-free solution for a charged fluid sphere in general relativity. *Journal of Physics A: Mathematical and General*, 8(4), 508. [6](#), [6](#)
- Kumar, R. and Ghosh, S.G. (2018). Rotating black hole in rastall theory. *The European Physical Journal C*, 78, 1–13. [1](#), [5](#)
- Kumar Yadav, A. (2014). Bianchi-v string cosmology with power law expansion in f (r, t) gravity. *The European Physical Journal Plus*, 129(9), 194. [6](#), [6](#)
- Lanczos, C. (1938). A remarkable property of the riemann-christoffel tensor in four dimensions. *Annals of Mathematics*, 842–850. [1](#)
- Le Verrier, U.J. (1859). Theorie du mouvement de mercure. *Annales de l’Observatoire imperial de Paris; t. 5; Annales de l’Observatoire de Paris. Memoires; t. 5., Paris: Mallet-Bachelier, 1859., 195 p.; 28 cm., 5.* [5](#)

- Lense, J. and Thirring, H. (1918). Über den einfluss der eigenrotation der zentralkörper auf die bewegung der planeten und monde nach der einsteinschen gravitationstheorie. *Physikalische Zeitschrift*, 19, 156. [1](#)
- Letelier, P.S. (1980). Anisotropic fluids with two-perfect-fluid components. *Physical Review D*, 22(4), 807. [7](#)
- Letelier, P.S. and Alencar, P.S. (1986). Anisotropic fluids with multifluid components. *Physical Review D*, 34(2), 343. [7](#)
- Levin, J. (2003). Fate of chaotic binaries. *Physical Review D*, 67(4), 044013. [8](#)
- Levin, J., O'Reilly, R., and Copeland, E. (2000). Gravity waves from homoclinic orbits of compact binaries. *Physical Review D*, 62(2), 024023. [8](#)
- Li, B. and Barrow, J.D. (2007). Cosmology of $f(R)$ gravity in the metric variational approach. *Physical Review D*, 75(8), 084010. [4](#)
- Licata, I., Moradpour, H., and Corda, C. (2017). The commutator algebra of covariant derivative as general framework for extended gravity. the rastall theory case and the role of the torsion. *International Journal of Geometric Methods in Modern Physics*, 14(11), 1730003. [5](#)
- Lin, K., Li, J., and Yang, S. (2013). Quasinormal modes of hayward regular black hole. *International Journal of Theoretical Physics*, 52, 3771–3778. [3](#), [5](#)
- Lin, K. and Qian, W.L. (2019). Neutral regular black hole solution in generalized rastall gravity. *Chinese Physics C*, 43(8), 083106. [5](#), [5](#), [5](#)
- Lobo, I.P., Moradpour, H., Morais Graça, J., and Salako, I. (2018). Thermodynamics of black holes in rastall gravity. *International Journal of Modern Physics D*, 27(07), 1850069. [5](#)
- Lyapunov, A.M. (1992). *General problem of the stability of motion*, volume 55. CRC Press. [3](#)
- Ma, M.S. and Zhao, R. (2017). Noncommutative geometry inspired black holes in rastall gravity. *The European Physical Journal C*, 77, 1–7. [5](#)

References

- Manna, T., Rahaman, F., Molla, S., Bhadra, J., and Shah, H.H. (2018). Strong lensing of a regular black hole with an electrodynamics source. *General Relativity and Gravitation*, 50, 1–18. [5](#), [5](#)
- Manna, T., Rahaman, F., and Mondal, M. (2020). Solar system tests in rastall gravity. *Modern Physics Letters A*, 35(07), 2050034. [2](#), [3](#), [4](#), [8](#)
- Markevitch, M., Gonzalez, A., Clowe, D., Vikhlinin, A., Forman, W., Jones, C., Murray, S., and Tucker, W. (2004). Direct constraints on the dark matter self-interaction cross section from the merging galaxy cluster 1e 0657–56. *The Astrophysical Journal*, 606(2), 819. [7](#)
- Martins, C.F. and Salucci, P. (2007). Analysis of rotation curves in the framework of r n gravity. *Monthly Notices of the Royal Astronomical Society*, 381(3), 1103–1108. [1](#)
- Mashhoon, B. (1985). Stability of charged rotating black holes in the eikonal approximation. *Physical Review D*, 31(2), 290. [2](#)
- Matos, T., Guzmán, F.S., and Nunez, D. (2000). Spherical scalar field halo in galaxies. *Physical Review D*, 62(6), 061301. [7](#)
- Maurya, S., Gupta, Y., Dayanandan, B., and Ray, S. (2016a). A new model for spherically symmetric anisotropic compact star. *The European Physical Journal C*, 76, 1–9. [6](#)
- Maurya, S., Gupta, Y., Rahaman, F., Rahaman, M., and Banerjee, A. (2017). Compact stars with specific mass function. *Annals of Physics*, 385, 532–545. [6](#)
- Maurya, S., Gupta, Y., Ray, S., and Dayanandan, B. (2015). Anisotropic models for compact stars. *The European Physical Journal C*, 75(5), 225. [6](#)
- Maurya, S., Gupta, Y., Ray, S., and Deb, D. (2016b). Generalised model for anisotropic compact stars. *The European Physical Journal C*, 76, 1–12. [6](#), [7](#)
- Milgrom, M. (1983). A modification of the newtonian dynamics as a possible alternative to the hidden mass hypothesis. *Astrophysical Journal, Part 1 (ISSN 0004-637X)*, vol. 270, July 15, 1983, p. 365–370. Research supported by the US-Israel Binational Science Foundation., 270, 365–370. [7](#)

- Miraghaei, H. and Nouri-Zonoz, M. (2010). Classical tests of general relativity in the newtonian limit of the schwarzschild–de sitter spacetime. *General relativity and gravitation*, 42, 2947–2956. 5
- Misner, C.W. (1969). Mixmaster universe. *Physical Review Letters*, 22(20), 1071. 8
- Momeni, D., Faizal, M., Myrzakulov, K., and Myrzakulov, R. (2017). Compact stars in vector–tensor–horndeski theory of gravity. *The European Physical Journal C*, 77, 1–9. 6
- Mondal, M., Pradhan, P., Rahaman, F., and Karar, I. (2020). Geodesic stability and quasi normal modes via lyapunov exponent for hayward black hole. *Modern Physics Letters A*, 35(30), 2050249. 2, 4, 8
- Mondal, M., Rahaman, F., Singh, K., et al. (2021a). Lyapunov exponent, isco and kolmogorov–senai entropy for kerr–kiselev black hole. *The European Physical Journal C*, 81(1), 1–16. 2, 4
- Mondal, M., Yadav, A.K., Pradhan, P., Islam, S., and Rahaman, F. (2021b). Null geodesics and qnms in the field of regular black holes. *International Journal of Modern Physics D*, 30(12), 2150095. 4, 8
- Moradpour, H., Heydarzade, Y., Darabi, F., and Salako, I.G. (2017a). A generalization to the rastall theory and cosmic eras. *The European Physical Journal C*, 77, 1–9. 5
- Moradpour, H., Sadeghnezhad, N., and Hendi, S. (2017b). Traversable asymptotically flat wormholes in rastall gravity. *Canadian Journal of Physics*, 95(12), 1257–1266. 5
- Moraes, P.H. (2015). Cosmological solutions from induced matter model applied to 5d $f(r, t)$ gravity and the shrinking of the extra coordinate. *The European Physical Journal C*, 75, 1–8. 6, 6
- Moraes, P. and Sahoo, P. (2017). Modeling wormholes in $f(r, t)$ gravity. *Physical Review D*, 96(4), 044038. 6, 6, 6, 6
- Moraes, P. and Sahoo, P. (2018). Nonexotic matter wormholes in a trace of the energy-momentum tensor squared gravity. *Physical Review D*, 97(2), 024007. 4, 6

References

- Motl, L. and Neitzke, A. (2003). Asymptotic black hole quasinormal frequencies. [2](#)
- Motter, A.E. (2003). Relativistic chaos is coordinate invariant. *Physical review letters*, 91(23), 231101. [3](#), [8](#), [8](#)
- Nojiri, S. and Odintsov, S.D. (2007). Unifying inflation with λ cdm epoch in modified f (r) gravity consistent with solar system tests. *Physics Letters B*, 657(4-5), 238–245. [1](#)
- Nojiri, S. and Odintsov, S.D. (2008). Modified f (r) gravity unifying r m inflation with the λ cdm epoch. *Physical Review D*, 77(2), 026007. [1](#)
- Nollert, H.P. (1999). Quasinormal modes: the characteristicsound’of black holes and neutron stars. *Classical and Quantum Gravity*, 16(12), R159. [2](#), [3](#)
- Ohanian, H.C. and Ruffini, R. (2013). *Gravitation and spacetime*. Cambridge University Press. [1](#)
- Oliveira, A., Velten, H., Fabris, J., and Casarini, L. (2015). Neutron stars in rastall gravity. *Physical Review D*, 92(4), 044020. [5](#)
- Oort, J. (1970). Galaxies and the universe: Properties of the universe are revealed by the rotation of galaxies and their distribution in space. *Science*, 170(3965), 1363–1370. [7](#)
- Oppenheimer, J.R. and Volkoff, G.M. (1939). On massive neutron cores. *Physical Review*, 55(4), 374.
- Ostriker, J., Peebles, P., and Yahil, A. (1974). The size and mass of galaxies and the mass of the universe. [7](#)
- Overduin, J.M. and Wesson, P.S. (2004). Dark matter and background light. *Physics Reports*, 402(5-6), 267–406. [7](#)
- Pani, P. and Cardoso, V. (2009). Are black holes in alternative theories serious astrophysical candidates? the case for einstein-dilaton-gauss-bonnet black holes. *Physical Review D*, 79(8), 084031. [1](#)
- Pánis, R., Kološ, M., and Stuchlík, Z. (2019). Determination of chaotic behaviour in time series generated by charged particle motion around magnetized schwarzschild black holes. *The European Physical Journal C*, 79(6), 479. [8](#)

- Pant, R., Gedela, S., Bisht, R.K., and Pant, N. (2019). Core-envelope model of super dense star with distinct equation of states. *The European Physical Journal C*, 79, 1–11. [7](#), [7](#)
- Percival, W.J., Reid, B.A., Eisenstein, D.J., Bahcall, N.A., Budavari, T., Frieman, J.A., Fukugita, M., Gunn, J.E., Ivezić, Ž., Knapp, G.R., et al. (2010). Baryon acoustic oscillations in the sloan digital sky survey data release 7 galaxy sample. *Monthly Notices of the Royal Astronomical Society*, 401(4), 2148–2168. [4](#)
- Pesin, J.B. (2020). Ljapunov characteristic exponents and ergodic properties of smooth dynamical systems with an invariant measure. In *Hamiltonian Dynamical Systems*, 512–515. CRC Press. [8](#)
- Pesin, Y.B. (1977). Characteristic lyapunov exponents and smooth ergodic theory. *Russian Mathematical Surveys*, 32(4), 55. [8](#)
- Pesin, Y.B. (1976). Ljapunov characteristic exponents and ergodic properties of smooth dynamical systems with an invariant measure. In *Doklady Akademii Nauk*, volume 226, 774–777. Russian Academy of Sciences.
- Pfister, H. (2007). On the history of the so-called lense-thirring effect. *General Relativity and Gravitation*, 39, 1735–1748. [1](#)
- Pope, A.C., Matsubara, T., Szalay, A.S., Blanton, M.R., Eisenstein, D.J., Gray, J., Jain, B., Bahcall, N.A., Brinkmann, J., Budavari, T., et al. (2004). Cosmological parameters from eigenmode analysis of sloan digital sky survey galaxy redshifts. *The Astrophysical Journal*, 607(2), 655. [7](#)
- Pradhan, P. (2016). Stability analysis and quasinormal modes of reissner–nordstrøm space-time via lyapunov exponent. *Pramana*, 87, 1–9. [3](#), [8](#)
- Pradhan, P. and Majumdar, P. (2011). Circular orbits in extremal reissner–nordstrom spacetime. *Physics Letters A*, 375(3), 474–479. [3](#), [3](#)
- Prasobh, C. and Kuriakose, V. (2014). Quasinormal modes of lovelock black holes. *The European Physical Journal C*, 74(11), 3136. [2](#)
- Press, W.H. (1971). Long wave trains of gravitational waves from a vibrating black hole. *The Astrophysical Journal*, 170, L105. [3](#)

References

- Pretorius, F. and Khurana, D. (2007). Black hole mergers and unstable circular orbits. *Classical and Quantum Gravity*, 24(12), S83. 2, 3, 3, 8
- Pugliese, D., Quevedo, H., and Ruffini, R. (2011). Circular motion of neutral test particles in reissner-nordström spacetime. *Physical Review D*, 83(2), 024021. 3
- Rahaman, F., Kalam, M., and Chakraborty, S. (2007). Gravitational lensing by stable c-field wormhole. *arXiv preprint arXiv:0705.0740*.
- Rahaman, F., Kalam, M., and Rahman, K. (2008). Some new class of chaplygin wormholes. *Modern Physics Letters A*, 23(16), 1199–1211. 6
- Rahaman, F., Nandi, K., Bhadra, A., Kalam, M., and Chakraborty, K. (2010a). Perfect fluid dark matter. *Physics Letters B*, 694(1), 10–15. 7
- Rahaman, F., Banerjee, A., Jamil, M., Yadav, A.K., and Idris, H. (2014a). Non-commutative wormholes in f (r) gravity with lorentzian distribution. *International Journal of Theoretical Physics*, 53(6), 1910–1919. 6
- Rahaman, F., Chakraborty, K., Kuhfittig, P., Shit, G., and Rahman, M. (2014b). A new deterministic model of strange stars. *The European Physical Journal C*, 74(10), 3126. 6
- Rahaman, F., Kuhfittig, P., Ray, S., and Islam, N. (2014c). Possible existence of wormholes in the galactic halo region. *The European Physical Journal C*, 74(2), 2750. 5, 5
- Rahaman, F., Manna, T., Shaikh, R., Aktar, S., Mondal, M., and Samanta, B. (2021). Thin accretion disks around traversable wormholes. *Nuclear Physics B*, 972, 115548. 4
- Rahaman, F., Maulick, R., Yadav, A.K., Ray, S., and Sharma, R. (2012). Singularity-free dark energy star. *General Relativity and Gravitation*, 44, 107–124. 6, 6, 6
- Rahaman, F., Molla, S., Ali, A., and Ray, S. (2018). Solar system tests in constraining parameters of dyon black holes. *The European Physical Journal C*, 78, 1–6. 5, 5
- Rahaman, F., Ray, S., Jafry, A.K., and Chakraborty, K. (2010b). Singularity-free solutions for anisotropic charged fluids with chaplygin equation of state. *Physical Review D*, 82(10), 104055. 7

- Rastall, P. (1972). Generalization of the einstein theory. *Physical Review D*, 6(12), 3357. 5
- Rastall, P. (1976). A theory of gravity. *Canadian Journal of Physics*, 54(1), 66–75. 5
- Ray, S. and Das, B. (2004). Relativistic gravitational mass in tolmán-vi type solution. *arXiv preprint astro-ph/0409527*. 4
- Reddy, D. and Santhi Kumar, R. (2013). Some anisotropic cosmological models in a modified theory of gravitation. *Astrophysics and Space Science*, 344, 253–257. 6
- Reddy, D., Santhi Kumar, R., and Pradeep Kumar, T. (2013). Bianchi type-iii dark energy model in $f(r, t)$ gravity. *International Journal of Theoretical Physics*, 52, 239–245. 1, 1
- Rej, P. and Bhar, P. (2021). Charged strange star in $f(r, t)$ gravity with linear equation of state. *Astrophysics and Space Science*, 366(4), 35. 4
- Riess, A.G., Filippenko, A.V., Challis, P., Clocchiatti, A., Diercks, A., Garnavich, P.M., Gilliland, R.L., Hogan, C.J., Jha, S., Kirshner, R.P., et al. (1998). Observational evidence from supernovae for an accelerating universe and a cosmological constant. *The astronomical journal*, 116(3), 1009. 1, 4
- Riess, A.G., Strolger, L.G., Tonry, J., Casertano, S., Ferguson, H.C., Mobasher, B., Challis, P., Filippenko, A.V., Jha, S., Li, W., et al. (2004). Type ia supernova discoveries at $z \lesssim 1$ from the hubble space telescope: Evidence for past deceleration and constraints on dark energy evolution. *The Astrophysical Journal*, 607(2), 665. 1, 4, 6
- Rindler, W. (2012). *Essential relativity: special, general, and cosmological*. Springer Science & Business Media. 1
- Roberts, M.S. and Whitehurst, R.N. (1975). The rotation curve and geometry of m31 at large galactocentric distances. *Astrophysical Journal*, Vol. 201, p. 327–346, 201, 327–346. 7
- Rosen, N. (1973). A bi-metric theory of gravitation. *General Relativity and Gravitation*, 4, 435–447. 1
- Rosen, N. (1974). A theory of gravitation. *Annals of Physics*, 84(1-2), 455–473. 1

References

- Rosen, N. (1975). A bi-metric theory of gravitation. ii. *General Relativity and Gravitation*, 6, 259–268. [1](#)
- Rosen, N. (1978). Bimetric gravitation theory on a cosmological basis. *General Relativity and Gravitation*, 9, 339–351. [1](#)
- Rubin, V.C. and Ford Jr, W.K. (1970). Rotation of the andromeda nebula from a spectroscopic survey of emission regions. *Astrophysical Journal*, vol. 159, p. 379, 159, 379. [7](#)
- Salako, I.G., Houndjo, M., and Jawad, A. (2016). Generalized mattigs relation in brans–dicke–rastall gravity. *International Journal of Modern Physics D*, 25(07), 1650076. [5](#)
- Santos, A. and Ulhoa, S. (2015). On gödel-type solution in rastall’s gravity. *Modern Physics Letters A*, 30(09), 1550039. [5](#)
- Schee, J. and Stuchlík, Z. (2015). Gravitational lensing and ghost images in the regular bardeen no-horizon spacetimes. *Journal of Cosmology and Astroparticle Physics*, 2015(06), 048.
- Schee, J. and Stuchlík, Z. (2016). Silhouette and spectral line profiles in the special modification of the kerr black hole geometry generated by quintessential fields. *The European Physical Journal C*, 76, 1–8. [8](#)
- Schnittman, J.D. and Rasio, F.A. (2001). Ruling out chaos in compact binary systems. *Physical review letters*, 87(12), 121101. [2](#)
- Schutz, B.F. and Will, C.M. (1985). Black hole normal modes: a semianalytic approach. *The Astrophysical Journal*, 291, L33–L36. [3](#)
- Semerák, O. and Karas, V. (1999). Pseudo-newtonian models of a rotating black hole field. *arXiv preprint astro-ph/9901289*. [2](#)
- Setare, M. and Momeni, D. (2011). Geodesic stability for kehagias-sfetsos black hole in hořava-lifshitz gravity via lyapunov exponents. *International Journal of Theoretical Physics*, 50, 106–113. [3](#)
- Shabani, H. and Farhoudi, M. (2013). f (r, t) dark energy models in phase space. *Phys. Rev. D*, 88(arXiv: 1306.3164), 044048. [6](#)

- Shabani, H. and Farhoudi, M. (2014). Cosmological and solar system consequences of $f(r, t)$ gravity models. *Physical Review D*, 90(4), 044031. [6](#)
- Shapiro, I.I. (1964). Fourth test of general relativity. *Physical Review Letters*, 13(26), 789. [5](#)
- Shapiro, S.S., Davis, J.L., Lebach, D.E., and Gregory, J. (2004). Measurement of the solar gravitational deflection of radio waves using geodetic very-long-baseline interferometry data, 1979–1999. *Physical Review Letters*, 92(12), 121101. [1](#)
- Sharif, M. and Zubair, M. (2014). Study of bianchi i anisotropic model in $f(r, t)$ gravity. *Astrophysics and Space Science*, 349, 457–465. [6](#)
- Sharma, R., Mukherjee, S., and Maharaj, S. (2001). General solution for a class of static charged spheres. *General Relativity and Gravitation*, 33, 999–1009. [6](#)
- Singh, C. and Kumar, P. (2014). Friedmann model with viscous cosmology in modified $f(r, t)$ gravity theory. *The European Physical Journal C*, 74(10), 1–11. [6](#)
- Singha, K., Mauryab, S., Errehymyc, A., Rahamand, F., and Daoude, M. (2020). Tolman vi fluid sphere in $f(r, t)$ gravity. *Phys. Dark Universe*, 30, 10062. [4](#)
- Slaný, P. and Stuchlík, Z. (2020). Equatorial circular orbits in kerr–newman–de sitter spacetimes. *The European Physical Journal C*, 80, 1–15. [8](#), [8](#)
- Sotiriou, T.P. and Liberati, S. (2007). Metric-affine $f(r)$ theories of gravity. *Annals of Physics*, 322(4), 935–966. [1](#)
- Spallucci, E. and Smailagic, A. (2018). Gaussian black holes in rastall gravity. *International Journal of Modern Physics D*, 27(02), 1850003. [5](#)
- Sperhake, U., Cardoso, V., Pretorius, F., Berti, E., and Gonzalez, J.A. (2008). High-energy collision of two black holes. *Physical review letters*, 101(16), 161101. [3](#)
- Stairs, I.H. (2003). Testing general relativity with pulsar timing. *Living Reviews in Relativity*, 6, 1–49. [1](#)

References

- Starobinsky, A.A. (1980). A new type of isotropic cosmological models without singularity. *Physics Letters B*, 91(1), 99–102. [1](#), [1](#)
- Stefanov, I.Z., Yazadjiev, S.S., and Gylchev, G.G. (2010). Connection between black-hole quasinormal modes and lensing in the strong deflection limit. *Physical review letters*, 104(25), 251103.
- Steklain, A. and Letelier, P. (2009). Stability of orbits around a spinning body in a pseudo-newtonian hill problem. *Physics Letters A*, 373(2), 188–194. [2](#)
- Stierwalt, S., Liss, S.E., Johnson, K.E., Patton, D.R., Privon, G.C., Besla, G., Kallivayalil, N., and Putman, M. (2017). Direct evidence of hierarchical assembly at low masses from isolated dwarf galaxy groups. *Nature Astronomy*, 1(2), 0025. [7](#)
- Stuchlík, Z. and Hledík, S. (1999). Some properties of the schwarzschild–de sitter and schwarzschild–anti-de sitter spacetimes. *Physical Review D*, 60(4), 044006. [8](#)
- Stuchlík, Z. (1983). The motion of test particles in black-hole backgrounds with non-zero cosmological constant. *Astronomical Institutes of Czechoslovakia, Bulletin (ISSN 0004-6248), vol. 34, no. 3, 1983, p. 129-149.*, 34, 129–149. [8](#)
- Stuchlík, Z. (2005). Influence of the relict cosmological constant on accretion discs. *Modern Physics Letters A*, 20(08), 561–575. [8](#), [8](#)
- Stuchlík, Z. and Kološ, M. (2016). Acceleration of the charged particles due to chaotic scattering in the combined black hole gravitational field and asymptotically uniform magnetic field. *The European Physical Journal C*, 76, 1–21. [8](#)
- Stuchlík, Z. and Schee, J. (2019). Shadow of the regular bardeen black holes and comparison of the motion of photons and neutrinos. *The European Physical Journal C*, 79(1), 44.
- Su, K.Y. and Chen, P. (2009). Comment on modeling galaxy halos using dark matter with pressure. *Physical Review D*, 79(12), 128301. [7](#)
- Suzuki, S. and Maeda, K.i. (1997). Chaos in schwarzschild spacetime: The motion of a spinning particle. *Physical Review D*, 55(8), 4848. [8](#)
- Tegmark, M., Blanton, M.R., Strauss, M.A., Hoyle, F., Schlegel, D., Scoccimarro, R., Vogeley, M.S., Weinberg, D.H., Zehavi, I., Berlind, A., et al. (2004a). The

- three-dimensional power spectrum of galaxies from the sloan digital sky survey. *Astrophys. J*, 606(2), 702–740. [7](#)
- Tegmark, M., Strauss, M.A., Blanton, M.R., Abazajian, K., Dodelson, S., Sandvik, H., Wang, X., Weinberg, D.H., Zehavi, I., Bahcall, N.A., et al. (2004b). Cosmological parameters from sdss and wmap. *Physical review D*, 69(10), 103501. [7](#)
- Tolman, R.C. (1939). Static solutions of einstein’s field equations for spheres of fluid. *Physical Review*, 55(4), 364. [4](#), [4](#)
- Tonry, J.L., Schmidt, B.P., Barris, B., Candia, P., Challis, P., Clocchiatti, A., Coil, A.L., Filippenko, A.V., Garnavich, P., Hogan, C., et al. (2003). Cosmological results from high- z supernovae. *The Astrophysical Journal*, 594(1), 1. [4](#)
- Torii, T., Yajima, H., and Maeda, K.i. (1997). Dilatonic black holes with a gauss-bonnet term. *Physical Review D*, 55(2), 739. [1](#)
- Toshmatov, B., Abdujabbarov, A., Stuchlík, Z., and Ahmedov, B. (2015). Quasi-normal modes of test fields around regular black holes. *Physical Review D*, 91(8), 083008. [2](#)
- Toshmatov, B., Ahmedov, B., Abdujabbarov, A., and Stuchlík, Z. (2014). Rotating regular black hole solution. *Physical Review D*, 89(10), 104017. [1](#)
- Toshmatov, B., Stuchlík, Z., and Ahmedov, B. (2017). Rotating black hole solutions with quintessential energy. *The European Physical Journal Plus*, 132, 1–21. [8](#), [8](#)
- Toshmatov, B., Stuchlík, Z., Ahmedov, B., and Malafarina, D. (2019). Relaxations of perturbations of spacetimes in general relativity coupled to nonlinear electrodynamics. *Physical Review D*, 99(6), 064043.
- Tursunov, A., Stuchlík, Z., and Kološ, M. (2016). Circular orbits and related quasiharmonic oscillatory motion of charged particles around weakly magnetized rotating black holes. *Physical Review D*, 93(8), 084012. [8](#)
- Tursunov, A., Stuchlík, Z., Kološ, M., Dadhich, N., and Ahmedov, B. (2020). Supermassive black holes as possible sources of ultrahigh-energy cosmic rays. *The Astrophysical Journal*, 895(1), 14. [8](#)
- Tzikas, A.G. (2019). Bardeen black hole chemistry. *Physics Letters B*, 788, 219–224.

References

- Vieira, W.M. and Letelier, P.S. (1997). On the integrability of halo dipoles in gravity. *Physics Letters A*, 228(1-2), 22–24. [8](#)
- Vieira, W.M. and Letelier, P.S. (1999). Relativistic and newtonian core-shell models: analytical and numerical results. *The Astrophysical Journal*, 513(1), 383.
- Visser, M. (2018). Rastall gravity is equivalent to einstein gravity. *Physics Letters B*, 782, 83–86. [5](#)
- Wald, R.M. (1986). Spin-two fields and general covariance. *Physical Review D*, 33(12), 3613. [7](#)
- Wei, S.W. and Liu, Y.X. (2014). Establishing a universal relation between gravitational waves and black hole lensing. *Physical Review D*, 89(4), 047502.
- Wheeler, J.T. (2014). Weyl gravity as general relativity. *Physical Review D*, 90(2), 025027. [1](#)
- Wu, X., Huang, T.Y., and Zhang, H. (2006). Lyapunov indices with two nearby trajectories in a curved spacetime. *Physical review D*, 74(8), 083001. [8](#)
- Wu, X. and Huang, T.y. (2003). Computation of lyapunov exponents in general relativity. *Physics Letters A*, 313(1-2), 77–81. [8](#)
- Yadav, A.K. (2019). Transitioning scenario of bianchi-i universe within $f(r, t)$ formalism. *Brazilian Journal of Physics*, 49(2), 262–270. [6](#), [6](#)
- Yadav, A.K. and Ali, A.T. (2018). Invariant bianchi type i models in $f(r, t)$ gravity. *International Journal of Geometric Methods in Modern Physics*, 15(02), 1850026. [6](#), [6](#)
- Yadav, A.K., Mondal, M., and Rahaman, F. (2020). Singularity-free non-exotic compact star in $f(r, t)$ gravity. *Pramana*, 94, 1–9. [3](#), [4](#), [8](#)
- Yuan, F.F. and Huang, P. (2017). Emergent cosmic space in rastall theory. *Classical and Quantum Gravity*, 34(7), 077001. [5](#)
- Yunes, N. and Pretorius, F. (2009). Dynamical chern-simons modified gravity: Spinning black holes in the slow-rotation approximation. *Physical Review D*, 79(8), 084043. [1](#)

- Zeldovich, Y.B. and Novikov, I.D. (1971). Relativistic astrophysics. vol. 1: Stars and relativity. *Chicago: University of Chicago Press.* 7
- Zhang, S.N., Cui, W., and Chen, W. (1997). Black hole spin in x-ray binaries: observational consequences. *The Astrophysical Journal*, 482(2), L155. 2
- Zhao, S.S. and Xie, Y. (2017). Strong deflection gravitational lensing by a modified hayward black hole. *The European Physical Journal C*, 77, 1–10. 5
- Zhou, S.W. and Liu, W.B. (2012). Three classical tests of hořava-lifshitz gravity theory. *Astrophysics and Space Science*, 337, 779–784. 5, 5
- Zubair, M., Abbas, G., and Noureen, I. (2016a). Possible formation of compact stars in $f(r, t)$ gravity. *Astrophysics and Space Science*, 361(1), 8. 6
- Zubair, M., Waheed, S., and Ahmad, Y. (2016b). Static spherically symmetric worm-holes in $f(r, t)$ gravity. *The European Physical Journal C*, 76(8), 1–13. 6
- Zwicky, F. (1933). Die rotverschiebung von extragalaktischen nebeln. *Helvetica Physica Acta*, Vol. 6, p. 110-127, 6, 110–127. 7
- Zwicky, F. (1979). On the masses of nebulae and of clusters of nebulae. In *A Source Book in Astronomy and Astrophysics, 1900–1975*, 729–737. Harvard University Press. 7